

PET Respiratory Motion Correction in Simultaneous PET/MR

Richard Manber

A dissertation submitted in partial fulfillment
of the requirements for the degree of
Doctor of Philosophy
of
Medical Physics.

Department of Medical Physics
University College London

December 4, 2016

I, Richard Manber, confirm that the work presented in this thesis is my own. Where information has been derived from other sources, I confirm that this has been indicated in the thesis.

Abstract

In Positron Emission Tomography (PET) imaging, patient motion due to respiration can lead to artefacts and blurring, in addition to quantification errors. The integration of PET imaging with Magnetic Resonance (MR) imaging in PET/MR scanners provides spatially aligned complementary clinical information, and allows the use of high spatial resolution and high contrast MR images to monitor and correct motion-corrupted PET data.

In this thesis, we form a methodology for respiratory motion correction of PET data, and show it can improve PET image quality. The approach is practical, having minimal impact on clinical PET/MR protocols, with no need for external respiratory monitoring, using standard MR sequences and minimal extra acquisition time.

First we validate the use of PET-derived respiratory signal to use for motion tracking, that uses raw PET data only, via Principal Component Analysis (PCA), then set up the tools to carry out PET Motion Compensated Image Reconstruction (MCIR). We introduce a joint PET-MR motion model, using one minute of PET and MR data to provide a motion model that captures inter-cycle and intra-cycle breathing variations. Different motion models (one/two surrogates, linear/polynomial) are evaluated on dynamic MR data sets.

Finally we apply the methodology on 45 clinical PET-MR patient datasets. Qualitative PET reconstruction improvements and artefact reduction are assessed with visual analysis, and quantitative improvements are calculated using Standardised Uptake Value (SUV) changes in avid lesions. Lesion detectability changes are explored with a study where two radiologists identify lesions or 'hot spots', with confidence levels, in uncorrected and motion-corrected images.

In summary, we developed a methodology for motion correction in PET/MR by using a joint motion model and demonstrated the capability of a joint PET-MR motion

model to predict respiratory motion by showing significantly improved image quality of PET data, with one minute of extra scan time, and no external hardware.

Acknowledgements

First I would like to thank my supervisors and other academic staff for their tireless efforts in helping this thesis come to fruition. I am immensely grateful to Prof Brian Hutton, Dr Anna Barnes, and especially Dr Kris Thielemans and Dr David Atkinson, for providing support, guidance and answers to endless technical questions whenever I needed.

This work would not have been possible without the help of countless clinical staff at UCLH; especially radiographers David Brown, Steve Burn and Celia O'Meara, who went above and beyond in collecting a vast amount of clinical data. A special thanks to radiologists Dr Francesco Fraioli and Dr Simon Wan who put in hours and hours of extra work in assessing the images that came out of this work, and also to Dr Chloe Hutton and Dr Jerome Declerck at Siemens, for always providing enthusiastic and insightful assistance.

Thanks also for the support and ongoing discussions of the whole PET/MR group, and the INM research team who I've had the pleasure to share an office with for the last 3 years, especially Hasan Sari, Alexandre Bousse, Ottavia Bertolli, Beverley Holman and Débora Salvado.

Final gratitude must go to my loving family, and to Dr Kirsten Christensen Jeffries, for inspiring me to undertake the PhD, providing constant support throughout, and helping me get over the line at the end. Thank you all.

I acknowledge support from: Siemens/UCL IMPACT studentship, the EPSRC (EP/K005278/1) and The National Institute for Health Research University College London Hospitals Biomedical Research Centre.

Publications

Journal Papers

1. **Manber, R.**, Thielemans, K., Hutton, B. F., Barnes, A., Ourselin, S., Arridge, S., O'Meara, C., Wan, S., and Atkinson, D. (2015). Practical PET Respiratory Motion Correction in Clinical PET/MR. *J. Nucl. Med.*, 56(6):890-896.
2. **Manber, R.**, Thielemans, K., Hutton, B., Wan, M. Y. S., McClelland, J. R., Barnes, A., Arridge, S., Ourselin, S., and Atkinson, D. (2016). Joint PET-MR Respiratory Motion Models for Clinical PET Motion Correction. *Phys. Med. Biol.*, 6515(17):6515-6530.

Conference Papers

1. **Manber, R.**, Thielemans, K., Hutton, B., Barnes, A., Ourselin, S., Arridge, S., O'Meara, C., and Atkinson, D. (2014). Initial evaluation of a practical PET respiratory motion correction method in clinical simultaneous PET/MRI. *EJNMMI Phys.*, 1(Suppl 1):A40.
2. Markiewicz, P., Thielemans, K., Burgos, N., **Manber, R.**, Jiao, J., Barnes, A., Atkinson, D., Arridge, S. R., Hutton, B. F., and Ourselin, S. (2014). Image reconstruction of mMR PET data using the open source software STIR. *EJNMMI Phys.*, 1(ii):3-5
3. **Manber, R.**, Thielemans, K., Hutton, B., Barnes, A., Ourselin, S., Arridge, S., Wan, M. Y. S., O'Meara, C., and Atkinson, D. (2015). MR Image-based PET Respiratory Motion Correction in PET/MR. *J. Nucl. Med.*, 56:98.
4. **Manber, R.**, Atkinson, D., Thielemans, K., Hutton, B., Barnes, A., O'Meara, C., Wan, S., Ourselin, S., and Arridge, S. (2015a). Practical PET respiratory

motion correction in clinical simultaneous PET/MR. *Proc. - Int. Symp. Biomed. Imaging, IEEE*, volume 2015-July, pages 1580-1583.

Conference Abstracts

1. **Manber, R.**, Atkinson, D., Hutton, B., Barnes, A., Ourselin, S., Arridge, S., O'Meara, C., and Thielemans, K. (2014). Validation of a PET-derived Respiratory Signal by Comparison with an MRI Pencil-Beam Navigator Signal in Simultaneous PET/MR. *ISMRM Conf. Proc.*, volume 44, page 1396.

Glossary

μ	attenuation coefficient
AC	attenuation correction
AP	anterior-posterior
APD	avalanche photo diodes
CT	computed tomography
FBP	filtered back projection
FDG	fluorodeoxyglucose
FLASH	fast low-angle shot (MR image)
FOV	field of view
FROC	free-response receiver operating characteristic
FT	Fourier transform
FWHM	full-width-half-maximum
GRE	gradient echo (MR image)
G-RPE	golden-radial phase encoding (MR image)
ED	Euclidean distance
EPI	echo planar imaging (MR image)
LL	lesion localisation
LOR	line of response
LSO	lutetium oxyorthosilicate
MC	motion corrected (image)
MCIR	motion-compensated image reconstruction
MI	mutual information
MIP	maximum intensity projection
MLEM	maximum likelihood expectation maximisation
MR	magnetic resonance

NAC	non attenuation-corrected
NLL	non-lesion localisation
OSEM	ordered subset expectation maximisation
PET	positron emission tomography
PCA	principal component analysis
ROI	region of interest
RTA	reconstruct-transform-average
SI	superior-inferior
SNR	signal-to-noise ratio
SSD	sum of squared differences
SSRB	single-slice rebinning
STIR	Software for Tomographic Image Reconstruction
SUV	standard uptake value
T	Tesla
TE	echo time
TR	repetition time
TrueFISP	true fast imaging with steady state precession (MR image)
U	uncorrected (image)
VOI	volume of interest

Contents

1	Introduction	24
1.1	Motivation	24
1.2	Thesis Outline	26
1.3	Contribution	28
2	Theory	30
2.1	Principles of PET	30
2.1.1	Data Acquisition	32
2.1.2	Data Corrections	33
2.1.3	Image Reconstruction	35
2.1.4	Noise	36
2.2	Principles of MRI	37
2.2.1	Data Acquisition	38
2.2.2	Image Reconstruction	39
2.3	Multi-Modality Imaging	40
2.3.1	PET/CT	40
2.3.2	PET/MR	40
2.4	Clinical PET/MR Protocol	43
2.5	The Role of PET in Oncology	43
3	Background	47
3.1	Why Is Motion Correction Necessary?	47
3.2	Respiratory Mechanics	49
3.3	Tracking Motion: Respiratory Signals	51
3.4	Image Registration	52

3.4.1	Sum of Squared Differences	53
3.4.2	Mutual Information	53
3.5	PET Framing and Gating	54
3.6	Measuring Motion	55
3.6.1	Measuring Motion: PET	56
3.6.2	Measuring Motion: MR	56
3.7	PET Image Reconstruction with Motion Correction	59
3.8	Motion Models	60
3.9	Recent PET/MR Respiratory Motion Correction Literature	61
3.10	Summary	63
4	Validation of a PET-derived Respiratory Signal	66
4.1	Motivation	66
4.2	PET Data-driven Signal Extraction	66
4.3	Other Respiratory Signals for Validation	68
4.3.1	MR Pencil-Beam Navigator Signal Extraction	68
4.3.2	Respiratory Cushion Signal Extraction	68
4.4	Pilot Study - Comparison with Respiratory Cushion	69
4.5	Validation Study: Comparison with MR Pencil-beam Navigator	70
4.5.1	Methods	71
4.5.2	Analysis	71
4.6	Results	72
4.6.1	Signal Correlation	72
4.6.2	Parameter Choice	75
4.6.3	Gating comparison	75
4.7	Discussion	76
5	Simple MR Image-based PET Respiratory Motion Correction	80
5.1	Motivation	80
5.2	Choice of MRI sequence	82
5.3	Data Acquisition	85
5.3.1	Patient Data	85
5.3.2	Protocol	85

5.4	Data Processing	87
5.4.1	Respiratory Signal Extraction	87
5.4.2	MR Data Binning	87
5.4.3	Deformation Field Formation	88
5.4.4	PET Data Binning	89
5.4.5	PET Corrections	89
5.4.6	Attenuation Correction	90
5.4.7	Motion Compensated PET Reconstruction	90
5.5	Analysis	91
5.6	Results	91
5.7	Discussion	94
6	Joint PET-MR Respiratory Motion Models	99
6.1	Motivation	99
6.2	Overview	100
6.3	Data	101
6.4	Joint PET-MR Motion Model	101
6.4.1	PET-derived Respiratory signal as a Model Surrogate	102
6.4.2	MR Model Imaging Data	102
6.4.3	Model Setup	102
6.4.4	Visualising the Models	105
6.5	PET-MR Clock Synchronisation	106
6.5.1	Clock Drift	106
6.5.2	Clock Shift	108
6.6	Improving Model Robustness	109
6.6.1	Least-squares	112
6.6.2	Iterative Least-Squares	113
6.7	Validation Study: Model Comparison on MR data	113
6.7.1	Methods	115
6.7.2	Analysis	115
6.7.3	Statistical Analysis	116
6.8	Results	116

6.8.1	Model Performance: Global Analysis	116
6.8.2	Model Performance: Spatial Analysis	118
6.8.3	Model Performance: Extrapolation Analysis	119
6.8.4	Model Performance: Failure Analysis	120
6.9	Discussion	122
7	PET Respiratory Motion correction via Joint PET-MR Motion Models	124
7.1	Motivation	124
7.2	PET Gating in the Continuous PET-MR Model Context	125
7.3	How Many Bins is Enough?	127
7.3.1	Methods	127
7.3.2	Results	128
7.3.3	Discussion	128
7.4	Flexible Binning Scheme	131
7.5	Evaluation of Motion Models on PET data	133
7.5.1	Protocol	133
7.5.2	Methods	133
7.6	Results	134
7.6.1	Individual Lesion Analysis	134
7.6.2	Overall Patient Analysis	134
7.7	Discussion	137
8	Clinical Validation of Motion-Compensated PET: Pilot Study	140
8.1	Overview	140
8.2	Detectability Studies in PET	141
8.3	Data	142
8.3.1	Patients	142
8.3.2	Protocol	143
8.3.3	Data Processing	143
8.4	Methods	144
8.4.1	Global sharpness	144
8.4.2	SUV Analysis	144
8.4.3	Lesion Detectability Study	144

8.4.4	Statistical Analysis	145
8.5	Results	145
8.5.1	Global sharpness	145
8.5.2	SUV Analysis	147
8.5.3	Lesion Detectability	147
8.5.4	Cross-study Correlation	151
8.6	Clinical Case Studies	151
8.6.1	Case Study 1: New Lesions Detected with MR confirmation . .	151
8.6.2	Case Study 2: New Lesions Detected with PET Follow-up confirmation	153
8.6.3	Case Study 3: Lesion Localisation Change	154
8.6.4	Case Study 4: Lesion Shape Change	157
8.6.5	Case Study 5: Artefact Reduction	158
8.6.6	Case Study 6: Improved Cardiac Uptake	158
8.6.7	Case Study 7: Motion-correction Induced Artefact	159
8.7	Discussion	159
9	Conclusions and Future Work	165
9.1	Conclusions	165
9.2	Future Work	167
9.2.1	Potential Improvements to Methodology	167
9.2.2	Development of Clinical Workflow	169
9.2.3	Improving the PET-derived Signal	172
9.2.4	Multi-surrogate Motion Model	172
9.2.5	Other	173
	References	176

List of Figures

2.1	Annihilation process: unstable radioisotope decaying to emit a positron e^+ , which travels and loses energy, annihilates with an electron e^- , emitting a pair of gamma rays γ in opposite directions.	31
2.2	Sinogram formation: a projection $p(r, \theta)$ is formed by integration across all LORs at a certain θ , forming one row in the sinogram.	32
2.3	Types of measured coincidence events.	34
2.4	Randomly aligned protons realign to be parallel or anti-parallel with the scanner's magnetic field B_0 , precessing about the longitudinal axis, at a frequency proportional to that of B_0	38
2.5	Fast Fourier transform used to convert k-space data from frequency space to image space.	40
2.6	Schematic of the components that make up the Siemens Biograph mMR scanner, from [Quick et al., 2011].	41
2.7	Typical clinical PET/MR workflow for a whole body scan, image adapted from [Quick et al., 2011]. A minimum duration of approximately 30 minutes consists of patient setup, localiser acquisitions and multiple 3 minute bed positions.	44
3.1	Static and motion-corrupted PET images from [Ullisch et al., 2012] . . .	47
3.2	A lesion is mislocalised at the bottom of the lung in the attenuation corrected image (left) although it is actually located at the dome of the liver as visible on the non-attenuation corrected image (right). PET images from [Sureshbabu and Mawlawi, 2005]	48
3.3	Diagram of breathing mechanics [Teppema and Berendsen, 2014]. . . .	49

3.4	PET gating schemes to form 5 gates by (a) phase gating and (b) amplitude gating.	55
4.1	Method for derivation of an MR-derived respiratory signal, (a) pencil-beam navigator image, (b) image with liver edge detected, (c) resulting respiratory signal.	69
4.2	Patient respiratory signal data for two cases, (a) PET (red), cushion (green), (b) PET (red), MR (blue), cushion (green).	70
4.3	PET reconstructions, view 1 of 1st PC, and MR-derived (blue line) vs. PET-derived (dotted red line) respiratory signals for 5 patients with various moving anatomies - (a) Patient 8 - liver/spleen, ^{68}Ga -DOTATATE, (b) Patient 2 - lung lesion, ^{18}F -FDG, (c) Patient 5 - heart, ^{18}F -FDG, (d) Patient 7 - liver/spleen, ^{68}Ga -DOTATATE, (e) Patient 6 - liver/spleen, ^{68}Ga -DOTATATE. Each PC is shown with a grey scale from minimum to maximum, resulting in a different scale for each patient. Reconstructed images are also displayed with different scales for visualisation.	73
4.4	Effect of parameter variations on correlation between MR and PET-derived signals, for (a) patient 2 and (b) patient 7.	75
4.5	Uncorrected PET reconstruction from patient 8 (^{68}Ga -DOTATATE) with VOI extracted from 5 gates.	76
4.6	Rigid displacements between 5 gates for PET (red) and MR (blue) -based gating schemes - (a) Amplitude gating - x,y,z displacements, (b) Amplitude gating - total displacements, (c) Phase gating - x,y,z displacements, (d) Phase gating - total displacements.	77
4.7	Maximum inter-gate displacements found by gating (with 5 gates) per patient with MR and PET derived signals via, (a) Amplitude Gating, (b) Phase Gating.	78
5.1	Proposed clinical workflow from PET-MR data acquisition to motion incorporated PET reconstruction.	82

- 5.2 Selection of tested MR sequences. (a) 3D TrueFISP, (b) 2D TrueFISP, (c) 2D TrueFISP at cardiac contraction, (d) 2D GRE, (e) 2D GRE at cardiac contraction. 84
- 5.3 Patient data protocol: multi-bed position clinical PET/MR scan, followed by motion model PET/MR sequence: MRAC, pencil beam navigator NAV, and multi-slice GRE sequence. 86
- 5.4 Overview of data workflow: building motion models, then using them in PET recon-structions. NAV represents MR pencil-beam navigator. . . 87
- 5.5 Section of respiratory signal showing amplitude based binning and rejection scheme, with a close up of how one respiratory cycle is divided by amplitude and gradient sign. 88
- 5.6 Comparison of MR-based motion corrected and uncorrected reconstructions of PET_{model} , where motion fields are taken from $model_{long}$. For each image pair, uncorrected images are top with purple line profiles, and corrected images are bottom with green line profiles. (a) Patient 1 - liver lesions, reconstructions of PET_{model} , with an ROI around lesion 1, (b)-(d) line profiles through liver lesions 1-3, (e) line profile through 1 lung lesion. 93
- 5.7 Comparison of uncorrected and motion-corrected reconstructions of PET_{model} (column 1), with line profiles through ROIs for PET_{model} (column 2) and $PET_{clinical}$ (column 3) on patients 2-4. For each image pair, uncorrected images are top with purple line profiles, and corrected images are bottom with dotted green line profiles. Arrows in the bottom row show where the liver starts in the μ -map. 95
- 5.8 Respiratory signals from two acquisitions on one patient, separated by 45 minutes 97

- 6.1 Model training data and deformation estimation at one slice location. (a) shows respiratory signal and a single voxel marked on slices with arrows representing the size of d^y . Blue dots are real d^y deformations at one voxel and slice position, and red dots are the model d^y predictions for models b) 1D-linear, c) 2D-linear, d) 1D-poly, e) 2D-poly. f) and g) show 3D plots for 2D-linear and 2D-poly models. 107
- 6.2 Effects of PET/MR clock drift over a 4 minute scan. (a) respiratory signal with marked slice acquisition times, and deformations d^y at one voxel (b) before drift correction and (c) after drift correction. 108
- 6.3 Effect of shift and drift correction on d^y and d^x deformation plots. Top row: one voxel marked at each slice location. (a) no corrections, (b) shift correction only, (c) shift and drift correction. 110
- 6.4 Dynamic line profiles through original uncorrected, registered, and model-warped images (with the 2D-linear model), with and without clock synchronisation correction, at two different slice locations in (a) and (b). 111
- 6.5 Model fitting performance of estimated deformations d^y (red) to registration-based deformations (blue) with different regression schemes - (a) plain least-squares, (b) iterative least-squares with 'bisquare' weighting, (c) iterative least-squares with 'fair' weighting. . . 112
- 6.6 Model coefficient images found with the 3 regression schemes - (a) plain least-squares, (b) iterative least-squares with 'bisquare' weighting, (c) iterative least-squares with 'fair' weighting. Arrows in (b) indicate areas of non-smooth coefficients. 114
- 6.7 Performance index $\xi(MI)$ as a % compared to registration, for (a) model-fit, (b) model-prediction. High values show best model performance. 117
- 6.8 Mean voxel-wise Euclidean distance for (a) model-fit, (b) model-prediction. Low values show best model performance 117

- 6.9 Mean performance index ξ for MI and SSD, and mean vector field ED over all 45 patients, (a) model-fit, (b) model-prediction. Good improvement compared to warping by registration is indicated by high values for MI and SSD, and by low values for ED. 118
- 6.10 Model prediction errors in areas of non-respiratory motion. Top row: slices with arrows in stomach/bowel. Second row: mean registration-based deformation fields $\| \mathbf{D} \|$, bottom row: mean difference between registration-deformations and model-deformations $\| \hat{\mathbf{D}} - \mathbf{D} \|$ 119
- 6.11 MRAC acquired at deep inhale, for patient 13. (a) Respiratory signal, reference exhale MR, acquired MRAC at same slice position, and warped MRAC. (b) All acquired MRAC and exhale MR slices, overlay images of: acquired MRAC and exhale MR, warped MRAC and exhale MR. 121
- 6.12 Two patient examples, respiratory signal, 2 MR slices at the same signal value, and image difference. (a) and (b) patient where bulk motion occurs during acquisition, (c) and (d) patient with no bulk motion. . . . 122
- 7.1 Proposed clinical workflow from PET-MR data acquisition to motion incorporated PET reconstruction. The MR acquisition consists of the normal MRAC and clinical MR, plus one min of extra dynamic GRE for the motion model. 125
- 7.2 (a) Surrogate signals plot against time, (b) Trajectory map, plotting surrogate signals against each other, throughout a four minute patient scan, (c) gating of PET data into 12 bins. 126
- 7.3 Coronal view of each lesion in PET motion-compensated reconstructions with 1, 2, 5, 10, 20 and 50 bins, using the 1D linear model, with line profiles through each. Blue is low voxel intensity and red is high voxel intensity. 129
- 7.4 Comparison of MCIR NAC PET reconstruction with 1D-linear model and various bin numbers, to uncorrected reconstruction. (a) VI_{peak} (b) VI_{max} , (c) ΔTVS 130

7.5	Method for automatic calculation of PET gate size. (a) Respiratory trajectory, (b) Respiratory perimeter, (c) Deformation ranges in each direction, (d) Largest deformation ranges in each direction, (e) Deformation ranges histogrammed, (f) Final gating scheme.	132
7.6	Mean SUV_{peak} and SUV_{max} changes in lesions in AC PET reconstructions. (a) and (b) Patient A, SUV_{peak} and SUV_{max} , (c) and (d) Patient C, SUV_{peak} and SUV_{max}	136
7.7	Mean SUV_{peak} and SUV_{max} changes in lesions in 5 patients. (a) SUV_{peak} AC, (b) SUV_{max} AC, (c) VI_{peak} NAC, (d) VI_{max} NAC	137
7.8	Uncorrected and motion-corrected (2D-linear model) PET reconstructions for patient A. Top row shows coronal slices and bottom row shows sagittal slices.	138
7.9	Uncorrected and motion-corrected (2D-linear model) PET reconstructions for patient B. Top row shows coronal slices and bottom row shows sagittal slices.	138
8.1	ΔTVS for all 44 patients. (a) box plot of all data points, (b) histogram with 3 outliers cut out. Positive change in TVS indicates an increase in image sharpness after motion correction.	146
8.2	ΔSUV_{peak} and ΔSUV_{max} . (a) histogram of all 162 lesions, (b) histogram with some outliers removed.	148
8.3	Change in confidence χ scores for true-positives (LL), for (a) reader 1 only and reader 2 only, (b) all reader 1 and 2 scores, (d) sum of reader 1 and 2 scores for each lesion. Green bars represent the number of lesions with specific values score changes. Pink bars represent the total number of lesions with negative or positive score changes, where positive change is 'good' - true lesions are more detectable after motion correction.	149
8.4	True-positive (LL) consensus scores (both positive or both negative change). The asterix (*) denotes lesions which were not detected in the U image, then detected to some degree in the MC image by both readers.	150

8.5	Change in confidence χ scores for false-positives (NLL) after motion correction. Green bars represent the number of lesions with specific values score changes. Pink bars represent the total number of lesions with negative or positive score changes, where negative change is 'good' - false lesions are less detectable after motion correction.	150
8.6	Case study 1. Lesion 1, coronal and axial slices of U and MC PET images, and fused with T1 Dixon VIBE MR.	152
8.7	Absolute SUV_{peak} and ΔSUV_{max} values in U and MC images for three lesions.	152
8.8	Case study 2. PET maximum intensity projection (MIP) image showing 3 pancreas lesions and axial views of U and MC PET images in both the baseline and follow-up PET scans, and fused with T1 Dixon VIBE MR.	154
8.9	Absolute SUV_{peak} and ΔSUV_{max} values in U and MC images for six lesions in (a) baseline scan, and (b) follow-up scan.	155
8.10	Case study 3. (a) MIP images for NAC and AC U images, and AC MC image. (b) axial PET slice with three lesions which wrongly appear in the lung in the U image and correctly in the liver in the MC image, and fused with T2 HASTE MR.	156
8.11	Case study 4. Coronal and axial slices of U and MC PET images, and fused with T1 VIBE SPAIR MR, showing change in shape of uptake in necrotic lesion.	157
8.12	Case study 5. Coronal slice of U and MC PET images, and fused with T1 VIBE MR, showing a reduction in attenuation misalignment artefacts.	158
8.13	Case study 6. Axial slice of U and MC PET images, and fused with T2 HASTE MR, showing increased cardiac uptake.	159
8.14	Case study 7. Coronal slice of U and MC PET images, and fused with T1 VIBE MR, showing an artefact introduced by motion correction. . .	159
8.15	Sagittal PET slice from Case study 7, with the difference between coefficients for forward and backwards motion models.	161

8.16	Examples of limitations in detectability study. (a) showing human error, where lesion given lower confidence score in MC image, and (b) area of high uptake marked as 1 lesion rather than 2.	163
8.17	Lung lesion falsely 'added' to the uncorrected AC PET image image due to segmentation error in the MRAC image. The CT image shows the location of the true lesion.	163
9.1	Proposed whole-body clinical workflow with extended PET bed position durations for motion model acquisitions.	170
9.2	Typical 4 min PET/MR scan for a single bed position. Four different MR sequences acquired at either inhale breath-hold, exhale breath-hold or free breathing. Values of PET-derived signals can be used to warp motion-corrected PET images to spatially align with each MR acquisition.	171
9.3	Multiple PET-derived signals for cardiac scan, (a) Principal components 1-5, (b) Associated weights for PC1 (top) and PC2 (bottom), (c) Frequency distribution of signals for PC1 (top) and PC2 (bottom).	174

List of Tables

3.1	Mean and standard deviation (SD) organ displacements through respiration, from all studies summarised by [Langen and Jones, 2001].	50
4.1	PET vs MR derived signal results, with parameters optimising correlation. ^{68}Ga represents ^{68}Ga -DOTATATE.	74
5.1	Overview of MR sequence parameters for TrueFisp (True Fast Imaging with Steady state Precession) and GRE (Gradient Echo) sequences.	85
5.2	Overview of four patients with varying regions of interest and administered tracer. ^{68}Ga represents ^{68}Ga -DOTATATE.	85
5.3	Increase in SUV_{peak} and SUV_{max} in $\text{PET}_{\text{model}}$ and $\text{PET}_{\text{clinical}}$, for lesions in patient 1 (multiple liver/lung lesions) and patient 2 (multiple pancreatic lesions).	92
7.1	Changes in SUV_{peak} and SUV_{max} in all lesions, Patients A and C, and all types of model in AC PET.	135
8.1	Lesion summary in patient cohort.	143
8.2	Quantitative results summary. Image sharpness includes all data sets, SUV metrics include all lesions, and detectability metrics include all non-excluded data sets. The LL and NLL numbers are out of 84 data sets (42 patients \times 2 readers). Statistical significance is based on paired scores from uncorrected and motion-corrected data sets.	146

Chapter 1

Introduction

1.1 Motivation

Positron Emission Tomography (PET) is a form of functional imaging, providing a 3D view of physiological processes inside the human body. PET offers quantitative analysis, allowing monitoring of biological function through blood flow and metabolism, using radio labelled tracers.

One of the main clinical PET applications is in oncology. Lesions can be assessed by morphological features with Computed Tomography (CT) or Magnetic Resonance (MR) imaging, but often shape and voxel intensity information is not enough to evaluate malignancy [Rohren et al., 2004]. The most utilised tracer is ^{18}F fluorodeoxyglucose (^{18}F -FDG), an analogue of glucose which accumulates in most tumours more than it does in normal tissue. PET images produce a map of tracer distribution throughout the body, helping with disease staging, characterisation of aetiology, providing information for monitoring of response to therapy, and to help delineate functional lesion boundaries and calculate lesion volumes for radiotherapy planning [Nehmeh et al., 2002, Acton et al., 2004, Tomasi et al., 2012]. Quantification of uptake is also important, and is often assessed in the form of a standard uptake value (SUV).

Due to long acquisition duration (typically 3-15 minutes per bed position), motion during PET acquisition may lead to blurring in resulting images and errors in quantification. The already limited spatial resolution of PET, around 4.5 mm full width half maximum (FWHM), is effectively reduced when motion occurs during acquisition. In oncology, tumours in the upper abdomen and thorax are particularly

adversely affected by respiratory motion, due to a movement of the diaphragm of around 20 mm on average in one breathing cycle [Martinez-Möller et al., 2007]. Lesions at anatomy boundaries such as between the liver and lung can also be mispositioned on images when compared to the anatomical reference MR or CT image. Quantification is also affected as moving lesions show an apparent increase in size and decrease in uptake as the lesion appears smeared. Motion may also cause problems with attenuation correction, where a static attenuation map does not correlate spatially with the PET emission data, due to moving anatomies [Sureshbabu and Mawlawi, 2005].

PET respiratory motion correction can be achieved by gating (splitting data into respiratory states), reconstructing separate images and registering to a common respiratory state [Klein et al., 1996, Boucher et al., 2004, Bai and Brady, 2011]. This technique requires a good signal-to-noise ratio (SNR) in each gated image for accurate registration results. This becomes difficult as there is competing interest to reduce scan time for increased patient throughput and to reduce tracer activity injected for reduced patient dose, leading to low count statistics and lower SNR in each gate.

The recent advent of PET/MR scanners allows us to exploit the simultaneity of the modalities by using high spatial resolution and high contrast MR images to track respiratory motion and correct PET data, without additional radiation exposure. Tagged MR is one such technique, which uses a special pulse sequence to create temporary features (tags) in tissue, which deform and can be tracked in subsequent MR images as the anatomy deforms [Guérin et al., 2011, Chun et al., 2012]. An alternative technique is to acquire quick 'motion-capturing' multislice 2D MR images of the thorax and calculate deformation fields by registration of the images [Würslin et al., 2013]. A similar method has also been proposed using 3D dynamic low resolution MR images, where a patient-specific MR motion model is built to capture breathing patterns linked to a 2D image navigator, with the method tested on simulated PET/MR data [King et al., 2012]. These methods are explained in more detail in sections 3.6.2 and 3.9.

Although current methods for respiratory motion correction in PET/MR show an improvement in PET image quality, all require a change to the otherwise intended PET/MR protocol to be able to collect the respiratory signal and/or MR-derived

motion model in a clinical setting. Measuring the respiratory signal using external monitoring devices, such as the RPM (Real-time Position Management, Varian Medical Systems Inc.), spirometer, or pressure belt require time for set-up and readjustment, and can fail due to mispositioning, patient movement, poor calibration, or signal drift and clipping. Another respiratory measure, the 'gold-standard' MR pencil-beam navigator needs to either run continuously or be inserted into the MR sequence running parallel with the PET, but this needs to be set up in advance of the scan, can create artefacts in MR images near the diaphragm, and may increase scan time. Furthermore, any bespoke 'motion-capturing' MR sequence has to be acquired separately to any clinical diagnostic MR so may increase overall scan time further.

We propose a respiratory motion correction method that requires no external hardware to provide a respiratory signal and no change to the imaging examination except for the addition of a short PET/MR sequence after the clinical acquisition. We propose that sufficient data for respiratory correction can be acquired in just one minute. The acquisition is used to build a patient-specific respiratory motion model, which is then used to motion-correct the clinical PET data of any duration. Our method uses only standard MR sequences and image registration techniques. The approach is practical and anatomically general, applicable to any type of thorax/abdomen related motion caused by respiration, for example, lung/liver/pancreatic lesions and cardiac data.

1.2 Thesis Outline

In Chapter 2 the theory for this thesis is presented, covering the general principles of PET and MR imaging modalities, along with the emergence of the simultaneous PET/MR scanner, on which all data for this thesis was acquired. Clinical PET/MR protocols are outlined, as the work in this thesis is informed with the aim of methodologies being practical for clinical use. Furthermore, the role of PET imaging in oncology is briefly explained.

Chapter 3 describes the tools required for PET motion correction, including respiratory mechanics, respiratory signals, PET gating, and image registration. This chapter also includes a literature review of the relevant areas, including motion tracking methods used in MRI, general PET motion correction, and recent specific

simultaneous PET/MR correction strategies.

In Chapter 4, we describe a methodology for a PET-derived respiratory signal, then perform a validation by comparison with a respiratory cushion, and with an absolute measure of diaphragmatic displacement using an MR pencil-beam navigator, on nine patients. The PET-derived signal is formed via low spatial resolution framing and Principal Component Analysis (PCA). A selection of the work in this chapter was presented at The International Society for Magnetic Resonance in Medicine (ISMRM) conference [Manber et al., 2014a].

We then set up the tools to carry out full PET respiratory motion correction in Chapter 5, using an MR binning scheme based on the PET-derived signal tested in the previous chapter. All steps in the process are described; PET and MR data acquisition and processing, binning, deformation field formation via non-rigid image registration and motion-compensated PET reconstruction including attenuation, scatter and randoms correction. Data was collected on a number of patients to test two main hypotheses. First, that motion captured by a full (2 min 40 s) dynamic MR sequence can successfully motion-correct simultaneously acquired PET data, and second, that only one minute of the MR sequence is required to capture enough motion to motion-correct PET data acquired earlier during the clinical scan. Analysis methods to measure the effect of motion correction are introduced, qualitatively with PET reconstruction improvements and artefact reduction assessed with visual analysis, and quantitatively using SUV changes in avid lesions. Various sections of the work in this chapter were presented at the PET, SPECT and MR (PSMR) conference [Manber et al., 2014b], the International Symposium on Biomedical Imaging (ISBI) [Manber et al., 2015a], and the Society of Nuclear Medicine and Molecular Imaging (SNMMI) conference [Manber et al., 2015b]. The full methodology and results were published in the Journal of Nuclear Medicine (JNM) [Manber et al., 2015c].

A methodology for a joint PET-MR continuous motion model is outlined in Chapter 6, using only one minute of simultaneously acquired PET and MR data to provide a respiratory motion correspondence model that captures inter-cycle and intra-cycle breathing variations. In the model setup, 2D multi-slice MR provides the dynamic imaging component, and the PET-derived respiratory signal provides the model surrogate. Different motion models (either one or two surrogate signals, linear

or polynomial system) are evaluated on a dynamic MR image data set of 45 patients.

In Chapter 7, the one minute joint PET-MR motion model is used to estimate deformations during the PET scan, and the motion is accounted for in the PET reconstruction. As in Chapter 6, we compare the effect of different types of model, but on motion corrected PET images. We also explore how the number of bins chosen for PET gating affects the resulting reconstruction, and outline a novel strategy to gate PET data depending on the breathing range of the patient during the scan. The work on a joint PET-MR motion model covered in this and the previous chapter is to be published in *Physics in Medicine and Biology* (PMB), currently in print [Manber et al., 2016].

We then apply the motion model methodology on a large patient cohort of 45 clinical PET/MR patient datasets in Chapter 8. A full quantitative assessment is carried out on avid lesions, whilst lesion detectability changes are explored with a detection study carried out by accredited radiologists. A number of case studies are then presented in detail to demonstrate the potential change to patient diagnosis and care that can occur from proper respiratory PET motion correction.

Finally, Chapter 9 summaries the findings of the thesis and outlines directions for future areas for research.

1.3 Contribution

All work in this thesis was my own, except for methods outlined here.

All data were acquired using an integrated 3T PET/MR system (Biograph mMR, Siemens Healthcare, Erlangen, Germany), at University College London Hospital (UCLH), London, UK. Additional data were acquired as part of calibration and service development protocols. Patients consented to the use of their data for research purposes.

In general, PET data processing (unlisting, reconstruction etc.) was carried out with STIR (Software for Tomographic Image Reconstruction) [Thielemans et al., 2007]. The MIRT (Medical Image Registration Toolbox) [Myronenko and Song, 2010] was used in Matlab for registration. All other analysis was performed with Matlab (Mathworks, Inc.).

The algorithm for extraction of a PET-derived respiratory signal was written in

Matlab based on a method outlined in [Thielemans et al., 2012].

Test data was collected on the PET/MR scanner by UCLH radiographers, with sequence development and parameter testing carried out by myself, with assistance from David Atkinson. Clinical data was collected by the radiographers, and patients were pre-selected using the hospital PACS (picture archiving and communication system).

Chapter 2

Theory

In this chapter we present a brief overview of the imaging modalities PET and MRI, considering how data is acquired and reconstructed in both, then go on to discuss the recently emerging technology of the multi-modality PET/MR scanner. A brief discussion of the clinical PET/MR workflow is also included, with an overview of the role of PET imaging in oncology.

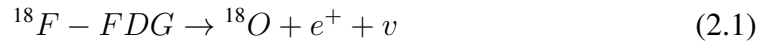
2.1 Principles of PET

Although the principles of PET imaging have been understood since the 1950s, the first commercial scanners were produced in the late 1960s to generate sliced images. Usage moved from research to clinical use in the 1970s when resolution improved due to technological advances producing more sensitive detectors, and by the 1990s PET had become an important diagnostic tool [Rohren et al., 2004]. An original emphasis of PET lay in cardiac imaging, where PET is the gold-standard for techniques such as assessment of myocardial blood flow and tissue viability for detection of coronary artery disease [Matsunari et al., 2003, Kaufmann and Camici, 2005]. PET imaging is now substantially used in oncology in all parts of the body, and more recently in neuroimaging for characterisation of disorders such as epilepsy and Alzheimer disease.

PET images are created by detection of radioactivity from a radioactive substance injected into the body intravenously. These substances are radioactive, having been tagged with a positron emitting, usually short half life radioactive isotope such as Oxygen-15, Fluorine-18 or Carbon-11. Isotopes are often formed using a cyclotron.

One of the most common techniques with PET is the measurement of glucose

consumption. The tracer used for this measurement is radiolabelled glucose analogue fluorodeoxyglucose, ^{18}F -FDG. Once this is injected into the body it will accumulate in cells with fast glucose metabolism, such as malignant tumours, though glycolysis does not occur as the oxygen required for glucose metabolism has been replaced with ^{18}F in FDG, and it therefore remains trapped in the cell until after the PET acquisition. This uptake in all parts of the body can be measured and quantified. The unstable radioisotope will emit positrons as protons are converted to neutrons, through radioactive decay. In the case of ^{18}F -FDG, it decays to 18-oxygen (^{18}O), whilst emitting a positron e^+ and a neutrino ν :



The positron has a certain kinetic energy which dissipates as it travels a short distance (in the order of a millimetre) through nearby tissue. When the kinetic energy of the positron reaches almost zero it annihilates with an electron e^- in the tissue and mass is converted to energy in the form of a pair of photons (also known as gamma rays γ), emitted in opposite directions (almost 180° apart) each with an energy of 511keV:



Scintillation crystals placed in detectors in a ring formation in the scanner detect the photons by absorbing them, and producing light, which is converted into an electrical signal. A schematic of this process is provided in Figure 2.1. By detecting these photon pairs, a 3D image of radio tracer distribution in the body can be reconstructed.

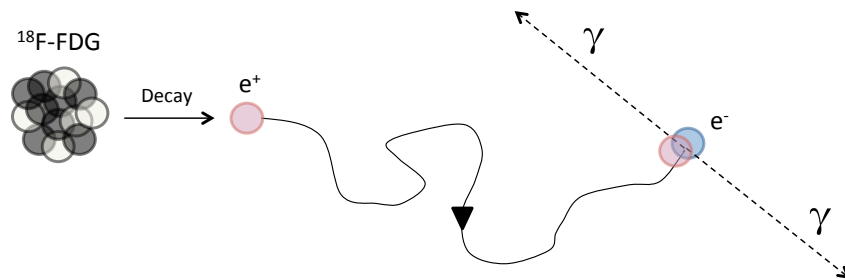


Figure 2.1: Annihilation process: unstable radioisotope decaying to emit a positron e^+ , which travels and loses energy, annihilates with an electron e^- , emitting a pair of gamma rays γ in opposite directions.

2.1.1 Data Acquisition

Each time a pair of photons is detected in opposite detectors, this is recorded as a coincidence event. Coincidence events occur when a detector pair detects photons and produces signals within a finite time interval in the order of 4-12 ns. In the first instance, it is assumed that the annihilation occurred somewhere along a straight line in space connecting the two detectors. This line is known as a line of response (LOR). Many coincidence events are stored during a scan, either in list-mode, where every event is stored along with the time of detection in a list, or in a histogrammed format as a matrix, known as a sinogram.

In a 2D sinogram, the x-axis describes the distance from the centre of the scanner field of view r , and the y-axis describes the projection angle θ . Considering one ring of detectors, LORs are grouped by θ , for $0 \leq \theta < \pi$, so those in one group are all parallel. The projection $p(r, \theta)$ is formed by integration across all LORs at this value of θ , as a histogram of the total number of detected events. Each projection at a certain θ then fills a single row in the sinogram (see Figure 2.2), and the full set of projections over all angles forms the radon transform. A single point in the field of view (FOV) traces a sinusoid shape across all values of θ , providing the sinogram with its name.

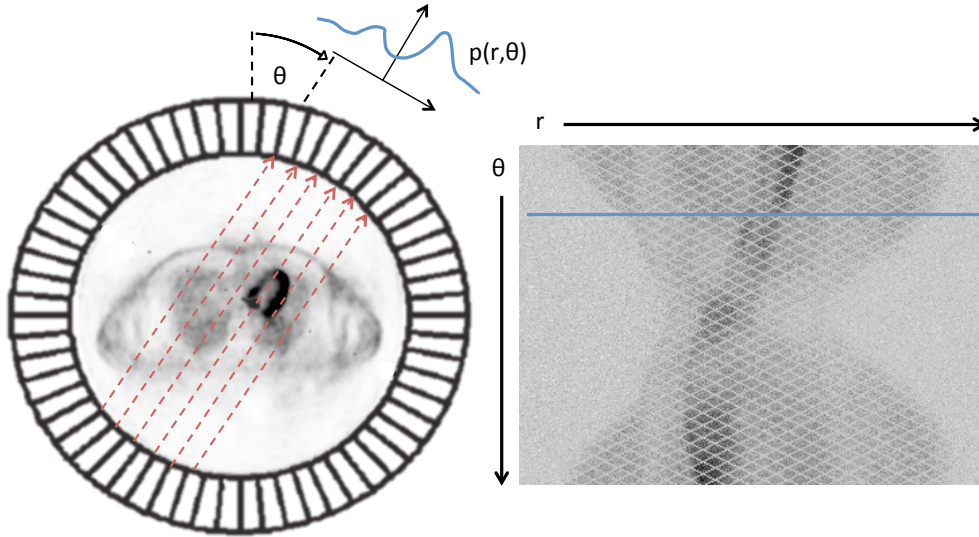


Figure 2.2: Sinogram formation: a projection $p(r, \theta)$ is formed by integration across all LORs at a certain θ , forming one row in the sinogram.

Sinograms formed from each detector ring at different axial positions (normal to head-foot direction) in the scanner are known as direct planes, and are used alone for

2D PET. Stacking them to capture multiple parallel planes is a type of 3D imaging. For fully 3D PET, oblique LORs that involve pairs of detectors lying in different ring (at different axial positions), forming planes that cross the direct planes must be considered. 3D PET increases sensitivity and increases the signal-to-noise ratio (SNR) in resulting images.

2.1.2 Data Corrections

2.1.2.1 Randoms

When two photons are detected within the defined time interval, a true coincidence event is assumed (Figure 2.3a). However, as many annihilations occur almost simultaneously throughout data acquisition, if two photons are detected within the time interval but were omitted from different annihilations, a coincidence event is still (wrongly) recorded (Figure 2.3b) [Shukla and Kumar, 2006]. These are known as random events. Decreasing the coincidence time interval will reduce the likelihood of unrelated photons to be recorded as a coincidence event and therefore reduce the randoms rate, but the interval is limited by the timing resolution of the detectors.

A common method to correct for randoms that is built into most commercial scanners is to measure randoms using a delayed coincidence window. If only random and not true coincidences are recorded, these can be subtracted from the PET data before reconstruction.

2.1.2.2 Scatter

After an annihilation, photons can be diverted from their original paths, due to Compton scatter, giving way to a mispositioned line of coincidence that does not pass through the point of annihilation (Figure 2.3c). If the scattered photon(s) still get detected, this is known as a scattered event. The scattered photon will also lose energy, and this loss of energy could be used to identify scattered coincidence events. However, detectors have a limited energy resolution, therefore many scattered events cannot be distinguished from true events which have a higher energy as the detector cannot perceive this difference in energy.

One common method to correct for scatter analytically is by assuming the distribution of scatter varies gradually over the PET FOV. A Gaussian curve is fitted to the counts that occur outside of the body where it is assumed that only scatter and no

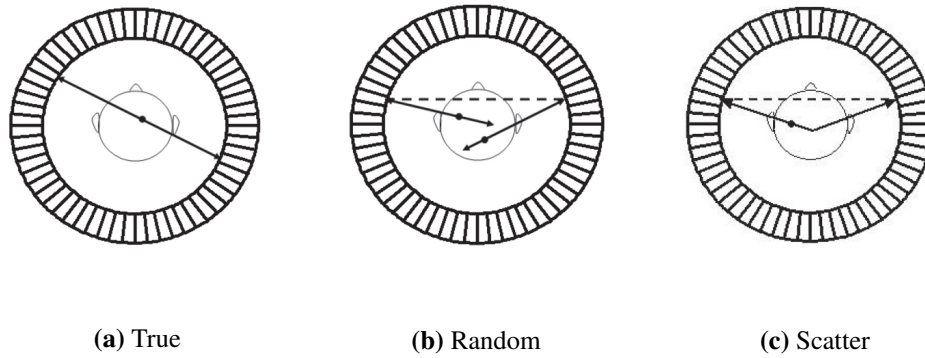


Figure 2.3: Types of measured coincidence events.

true events are recorded. This curve is then used to also estimate scattered events inside the body. A more recent widely used method uses a model-based simulation of the distribution of scattered events in the sinogram [Watson, 2000].

2.1.2.3 Attenuation

Attenuation refers to the reduction in detected coincidence events due to either the scattering of photons diverted out of the detector ring FOV, or by absorption in tissues (or other apparatus inside the FOV). The fraction of attenuated photons depends on the total length of travel within the tissue of the two photons along the LOR, and the attenuation coefficient of the tissue, μ .

This can be accounted for by defining an attenuation correction (AC) map (also known as a μ -map), applying attenuation factors to different tissues within the FOV. This map can be directly derived with CT images in combined PET/CT scanners, or with segmentation based on specialised MR sequences in combined PET/MR scanners. For accurate attenuation correction, the AC map must be spatially aligned with the tissue, which is a problem for scans of the abdomen/thorax where tissue is deforming throughout with respiration.

2.1.2.4 Normalisation

Normalisation is necessary to account for differences in coincidence detection efficiencies based on detector electronics/efficiencies and geometric variations.

A simple method to find normalisation correction factors is to use the inverse of the measured counts when scanning a uniformly radioactive PET source, therefore measuring the efficiency of each LOR [Badawi et al., 1998]. The second more

common, component-based method, separates the process into parts, calculating geometric variations and crystal efficiencies with a rotating rod or cylindrical source [Badawi et al., 2000]. With modern scanners such as the Siemens Biograph mMR, a normalisation scan is carried out daily to keep the system calibrated in case of changes over time.

2.1.2.5 Dead time

The time after which a coincidence event is recorded, before the detectors can detect another event is known as dead time, and this is intrinsic to the system electronics. A dead time model can be used to account for this affect by repeatedly measuring count rate from a decaying source and estimating the true count rate from the measured rate.

2.1.3 Image Reconstruction

Sinograms are reconstructed into images that show tracer distribution throughout the body. The most commonly used approaches are analytic or iterative methods.

2.1.3.1 Filtered Back Projection

Filtered Back Projection (FBP) is an analytic method that reconstructs an image by using the inverse radon transform of projections $p(r, \theta)$. In FBP, projections are fourier transformed, filtered in frequency space, inverse fourier transformed, then back projected into image space.

2.1.3.2 Maximum Likelihood Expectation Maximisation

Maximum Likelihood Expectation Maximisation (MLEM) is a commonly used statistical iterative reconstruction method, based on looking for the solution image most consistent with the measured PET data. A system model H is needed which relates the image to the data including attenuation and normalisation effects. Each element H_{ij} in the model represents the probability that the activity leads to an unscattered event.

With MLEM, an initial guess is made where the whole image is set to a constant value. Then, the image is forward projected into the projection domain and compared with the actual measured projections. This produces a correction factor for each projection, which is back projected into the image domain to provide a correction factor in the image domain, which is multiplied by the current image estimate and

divided by a weighting term based on the system model. The resulting image is then entered as the next starting image estimate and the process is iterated a user-defined number of times. In equation form, estimating the activity at each voxel:

$$\hat{f}_j^{(n+1)} = \frac{\hat{f}_j^{(n)}}{\sum_{i'} H_{i'j}} \sum_i H_{ij} \frac{p_i}{\sum_k H_{ik} \hat{f}_k^{(n)} + B_i} \quad (2.3)$$

where p_i is detected projection i , $\hat{f}_j^{(n+1)}$ is the next estimate of voxel j based on the current estimate $\hat{f}^{(n)}$, and B_i is background including scatter and randoms. In vector form, considering all voxels and all projections, this becomes:

$$\hat{f}^{(n+1)} = \frac{\hat{f}^{(n)}}{H^T \mathbf{1}} H^T \frac{p}{H \hat{f}^{(n)} + B} \quad (2.4)$$

The MLEM method is slower than FBP but does provide better control of noise.

2.1.3.3 Ordered Subset Expectation Maximisation

Ordered Subset Expectation Maximisation (OSEM) is a variation of MLEM, using only subsets of the data set for each image update, to reduce reconstruction time. The modified equation becomes:

$$\hat{f}_j^{(n+1)} = \frac{\hat{f}_j^{(n)}}{\sum_{i' \in S_k} H_{i'j}} \sum_{i \in S_k} H_{ij} \frac{p_i}{\sum_k H_{ik} \hat{f}_k^{(n)} + B_i} \quad (2.5)$$

where the back projection step sums over only a subset of projections S_k out of a total of K subsets. The method is equal to MLEM when $K=1$. Subsets are most commonly formed by grouping projections into sets containing different values of projection angle θ in each.

2.1.4 Noise

Statistical noise in measured data occurs due to a combination of Poisson noise which characterises positron emission, and other characteristic noise from electronic components [Tsui et al., 1981, Vardi et al., 1985, Teymurazyan et al., 2013]. Noise from components is influenced by the sensitivity of detectors, inherent to the scanner, determined by the detector arrangement and absorption efficiency, and also the bore diameter, where decreasing the distance between detectors increases sensitivity. Noise

is also influenced by the amount of radioactive tracer administered, limited by safety consideration, which directly affects count statistics. The noise distribution is then altered based on the choice of data correction and image reconstruction schemes.

Considering only the Poisson distribution of positron emission for a high number of expected counts, the variance is equal to the mean number of events N , so the noise, defined as standard deviation of N is equal to \sqrt{N} . Increasing scan times therefore increases SNR but is limited by cost and patient comfort. Effective scan time is reduced when data is grouped into 'static' motion states, causing a loss of SNR in each group. Noise can be reduced with spatial filtering but at a cost of reduced spatial resolution, with most commonly used post-processing schemes assuming the overall noise can be characterised as Gaussian [Alessio and Kinahan, 2006, Teymurazyan et al., 2013].

2.2 Principles of MRI

Clinical MRI scanners have strong primary magnetic fields B_0 , with strengths of either 1.5 or 3 Tesla (T), 5×10^5 times greater than the Earth's magnetic field. The human body is composed of 70% water, and MRI makes use of the protons in hydrogen atoms in this water when a person lies inside the machine's own magnetic field to produce images.

Each hydrogen nucleus consists of a spinning charged proton producing a magnetic moment. As there are many protons and they are all randomly oriented, the net magnetisation is usually zero. When in the B_0 field they reorient into one of two available energy states - 'spin up' (parallel to B_0) and 'spin down' (antiparallel to B_0). Each proton now precesses with a frequency proportional to the magnetic field strength, known as the Larmor frequency, about the longitudinal Z axis parallel with B_0 (see Figure 2.4). A small majority reorient to align with the primary field in the 'spin up' state, producing a net magnetisation in this longitudinal direction. As the precession from protons are out of phase, the net magnetisation in the transverse (X-Y) plane is zero.

An extra magnetic field can be applied in the form of a radiofrequency (RF) pulse, also oscillating at the Larmor frequency, through transmitter coils which excite the protons. This causes a resonant effect, aligning the phase of the spins and tipping protons from being aligned in the longitudinal direction to give a component in the

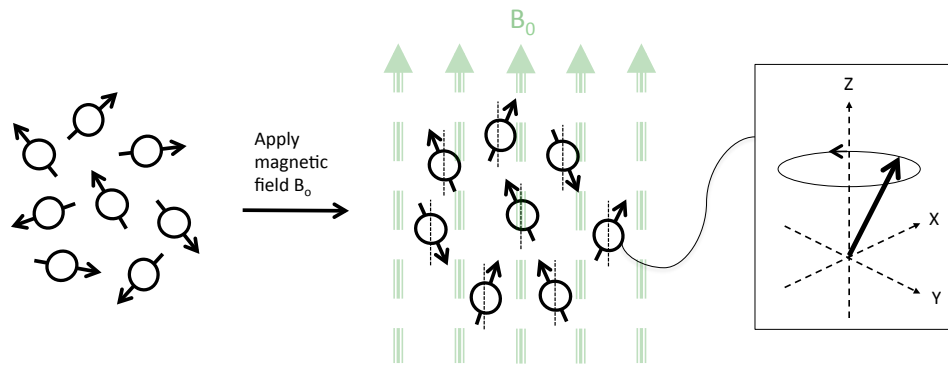


Figure 2.4: Randomly aligned protons realign to be parallel or anti-parallel with the scanner's magnetic field B_0 , precessing about the longitudinal axis, at a frequency proportional to that of B_0 .

perpendicular transverse plane.

After protons are tipped into the transverse plane by the RF pulse, they undergo a relaxation processes in two different forms. The fastest is T2 relaxation - dephasing of spins in the transverse plane, reducing the net magnetisation in the transverse plane. The other is T1 relaxation - recovery of spins back to their original longitudinal direction, restoring the net magnetisation in this direction.

Different tissues, depending on factors such as viscosity, have different T1 and T2 relaxation rates. This leads to different signal intensities from various tissues after RF excitation, visualised in resulting MR images as greyscale differences.

2.2.1 Data Acquisition

When an RF pulse is applied to excite protons, gradient coils in the scanner bore are used to vary the spin rotation frequency and phase as a function of position. Three gradient coils are used to change the magnetic field in the X, Y and Z directions through the scanner bore. This varies the spin rotation frequency and phase of protons depending on their 3D positions, allowing localisation - known as spatial encoding. Spins precess at a frequency proportional to the local field. With no gradients switched on, this is proportional to the B_0 field. Application of an extra linear field G_x causes the spin frequency to vary linearly with position x across the scanner. This is frequency encoding. A phase encoding gradient G_y is applied to cause the phase of the spins to vary linearly with position y , and a second phase encoding gradient G_z is applied to vary the phase in the z direction. The phase encode and frequency encode

gradients can be applied in any 3D orientation by applying currents to the physical X, Y and Z gradient coils. By utilising all three gradients, each point in 3D space can be characterised by a unique phase angle and procession frequency in 3D MRI.

Alternatively, many MR sequences are acquired as 2D planes, stacked to create a 3D volume. In a 2D acquisition, first a slice selection gradient and RF pulse is applied along the Z axis to only excite spins that lie in a particular plane in the scanner. Then, a phase encoding gradient is applied in the Y direction and finally a frequency encoding gradient in the X axis.

After each RF pulse excitation, spins are tipped into the transverse plane and a coherent signal from the transverse plane can be detected by receiver coils. Receiver coils lie in the scanner bore, but also come in various shapes and sizes, each bespoke to different anatomies, to boost signal depending on the anatomy being imaged.

The RF pulse is applied repeatedly, whilst changing the phase encoding gradient amplitude each time. This time interval between RF excitation pulses is known as the repetition time (TR). The time between each RF pulse and receiving the signal in the receiver coils is known as the echo time (TE). Adjusting the parameters TR and TE can help to enhance the contrast between certain tissues in the resulting images due to their differing inherent T1 and T2 values.

Raw data received by MRI coils are saved in the complex spatial frequency domain of k-space.

2.2.2 Image Reconstruction

The Fourier transform (FT), or fast Fourier Transform (FFT) is integral to all modern imaging, and is particularly important in MRI. The signal received is a complex signal made of a large number of constituent frequencies. This can be visualised as multiple sine and/or cosine waves along a time-axis. The Fourier transform represents the same data over a frequency axis, where frequency corresponds to image position. Each pixel in the resultant image is encoded by information in all points in the k-space plane as a weighted sum, where central regions contain contrast information and outer regions contain spatial information.

In 2D MR, each plane 2D k-space is transformed into an image slice with the FFT in the frequency and phase encoding directions. In 3D, this FFT is applied in three

dimensions, once in frequency, and twice in each of two phase encoding directions. Figure 2.5 shows a 2D k-space alongside the image of the brain that is formed once a FFT is applied.

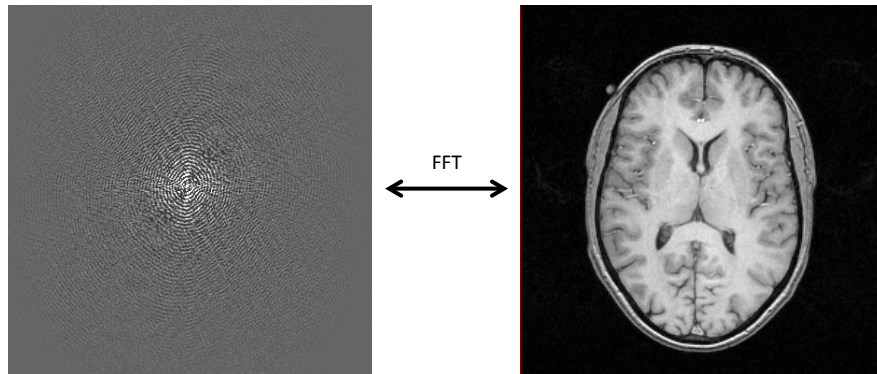


Figure 2.5: Fast Fourier transform used to convert k-space data from frequency space to image space.

2.3 Multi-Modality Imaging

2.3.1 PET/CT

With quickly advancing technologies and miniaturisation, eventually multi-modality hybrid imaging became possible, with technology to acquire images with different modalities, built into one piece of hardware. This allows fusion images without the need for registration. Multi-modality imaging allows collection of more information in a shorter period of time, whilst also minimising patient discomfort. The most commonly used system in clinics today is the hybrid PET/CT scanner, which combines the functional imaging of PET with the high resolution anatomical images of CT. The first standalone PET/CT scanner was developed in the late 1990s, with the first commercial system in use by 2001 [Weissman et al., 2013].

2.3.2 PET/MR

The hybrid PET/MR scanner is a more recent multi-modality imaging platform, with the first whole body clinical scanners installed in hospitals in the USA and Europe in 2010. The MR side provides excellent soft tissue resolution, whilst the PET is sensitive to the pico-molar concentrations of metabolic imaging, resulting in a scanner that can study anatomy and metabolism/pathophysiology, with radioactive tracers that

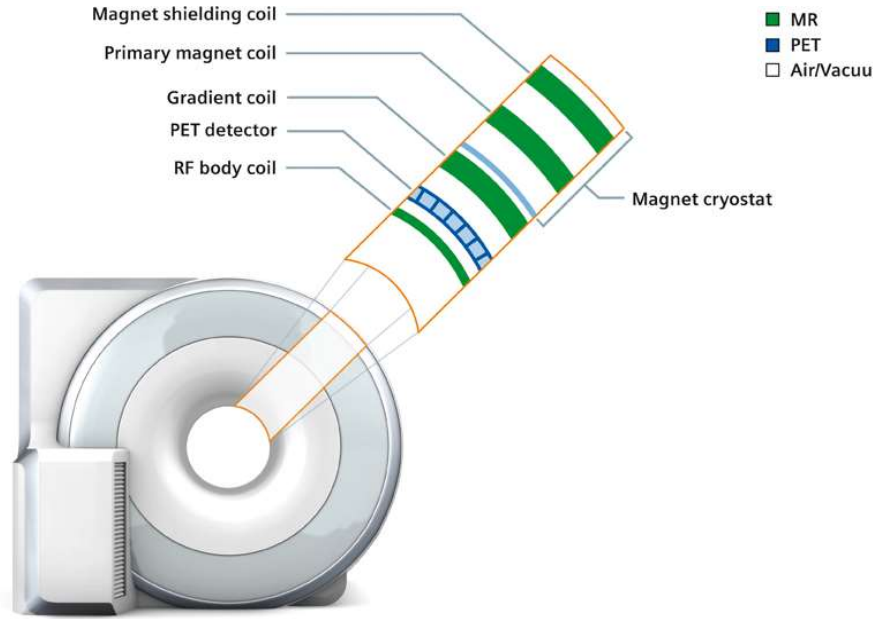


Figure 2.6: Schematic of the components that make up the Siemens Biograph mMR scanner, from [Quick et al., 2011].

do not disturb normal physiology [Daftary, 2010]. There are two main types of PET/MR scanner. The first has two separate gantries for PET and MR, with a common patient table between the two, so PET and MR data are acquired sequentially without any patient repositioning between acquisitions. The second type is a fully integrated PET/MR scanner, where a PET detector ring is within the MR scanner, allowing simultaneous acquisition.

Experimental work in this thesis was performed with the Siemens Biograph mMR simultaneous PET/MR scanner. The PET detectors used are a combination of lutetium oxyorthosilicate (LSO) crystals (each $4 \times 4 \times 20 \text{ mm}^3$) and avalanche photo diodes (APD), which convert the detected events from scintillation light to electrical signals, whilst being non-sensitive to the magnetic field. 56 LSO-APD detector blocks, each with a block area of $32 \times 32 \text{ mm}^2$ are aligned to form a detector ring, and eight rings form the full PET detector system. The scanner has a 60 cm bore, whilst the PET system has an axial FOV of 25.8 cm and a transaxial FOV of 59.4 cm. The average spatial resolution full-width-half-maximum (FWHM) is 4.3 mm [Delso et al., 2011]. The schematic in Figure 2.6 shows how the MR primary magnetic coil, gradient coils and body coil all lie in the scanner bore with the PET detector ring lying in between.

MR has many advantages over CT, including the ability for functional imaging techniques such as diffusion and spectroscopy. Unlike CT, MRI does not involve use of radiation. Contrast agents in MRI are mostly gadolinium based and have a different safety and side effect profile compared to iodine based CT contrast agents. MR, like CT, also has the capability for rapid imaging and with the added benefit of lack of radiation burden. This makes it useful for dynamic sequences to study either functionality with contrast agents, or to study movement in the body for motion correction [Torigian et al., 2013].

A number of key applications have started to emerge since the introduction of the simultaneous PET/MR scanner to clinics. In oncology, tumour detection, and tumour, node and metastasis staging have shown potential [Ratib and Beyer, 2011, Torigian et al., 2013]. In cases such as brain, head and neck, spinal cord, liver, pelvis, breast and musculoskeletal system, tissue contrast is not optimal with CT so volumetric delineation of tumours with PET/MR in these areas shows promise. The combination of PET with functional MR can also improve assessment of prognosis, biopsy and treatment planning and patient selection for response prediction and drug development. PET scans for patients where radiation can be dangerous, such as paediatric, is now safer in PET/MR due to a lower radiation dose required for PET/MR over PET/CT, especially for cases where multiple PET scans are required for therapy response [Chawla et al., 2010]. In neurology, applications include multi-parametric structural and functional assessment of the central and peripheral nervous system, as well as of various neurodegenerative, vascular and psychiatric conditions [Schwenzer et al., 2012]. In the cardiovascular area, quantitative assessment of myocardial viability, ventricular function and myocarditis have all surfaced as potential applications. In the musculoskeletal area, PET/MR has shown promise for diagnosis and assessment of response to a number of disorders such as Charcot neuroarthropathy, osteomyelitis, spinal disorders and arthritides [Chen et al., 2008].

One limitation of current PET/CT scanners is that although data from both modalities are spatially correlated, they are not temporally correlated as data is acquired sequentially rather than simultaneously. Currently both sequential and simultaneous PET/MR scanners are in use clinically, with the latter having the

advantage of spatial alignment between the two modalities without relying on inter-modality registration. This acquisition simultaneity is important for imaging parts of the body that move non-rigidly such as in the thorax and abdomen, where movements occur due to movement of food through the intestines and filling of the bladder. Furthermore, for dynamic techniques such as analysing temporal response to MR contrast agents or PET tracers, this simultaneity ensures correlation of PET and MR signals over time as well as spatial localisation [Bolus et al., 2009, Yankeelov et al., 2012].

2.4 Clinical PET/MR Protocol

Each clinical protocol run on the PET/MR is bespoke to the context of the scan, from hour long single bed position scans, to 30 minute full body scans, with up to 6-7 three minute bed positions. A bed position is the name given to a PET acquisition covering a certain section of the body, for example, head and neck, thorax, abdomen etc. The bed that the patient lies on moves between each acquisition so the part of the body being imaged is inside the PET detector ring.

Figure 2.7 shows an example of the individual PET and MR images acquired for each bed position in a 30 minute whole-body scan, which are then put together to form a whole-body fused PET/MR image. At each bed position, PET is acquired continuously for three minutes, whilst multiple diagnostic MR images are acquired simultaneously. Some of these are breath-hold scans (the patient is asked to hold their breath at an exhale position) and some are free breathing, with the MR data either being continuously collected, or 'triggered'; where data is only collected at the exhale sections of the breathing cycle, with respiration tracked with an MR pencil-beam navigator or respiratory cushion (see Section 3.3).

2.5 The Role of PET in Oncology

Qualitative visual PET image assessment plays a large role in staging and diagnosis in oncology. Cancer staging directly affects patient care, by identifying if a patient is suitable for resection, chemotherapy or radiotherapy. TNM staging is a widely used cancer staging system and has been validated to be predictive of treatment effect and outcome; T refers to the size of the main tumour, N refers to the number of cancerous

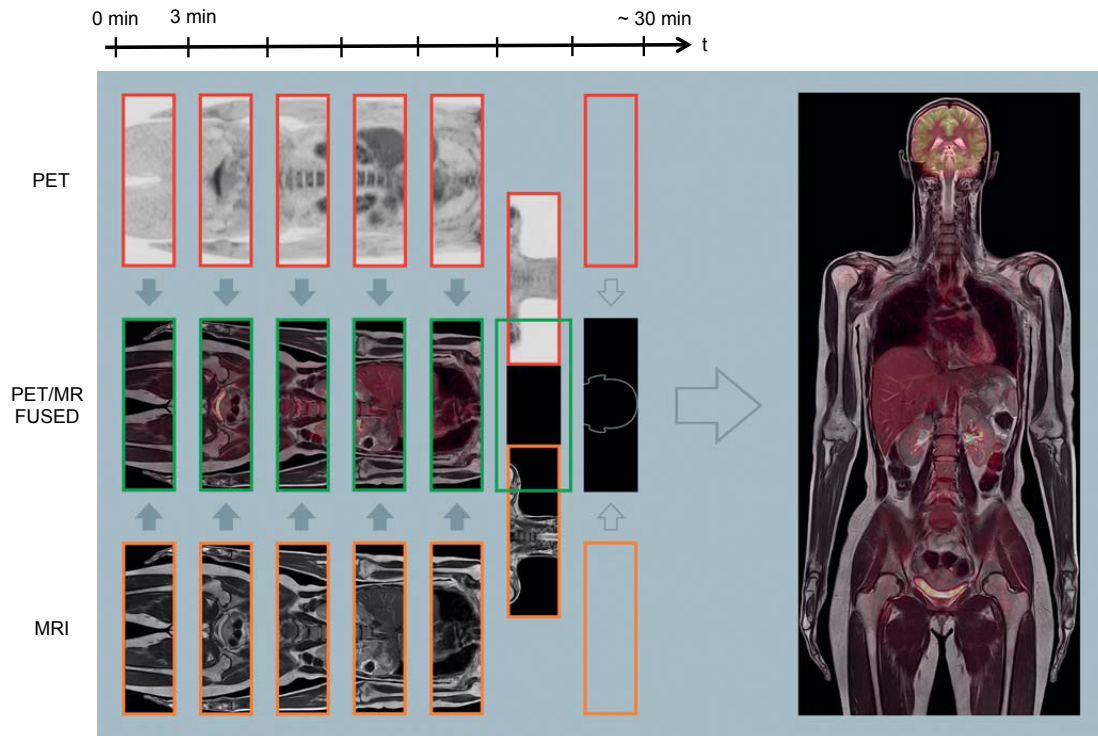


Figure 2.7: Typical clinical PET/MR workflow for a whole body scan, image adapted from [Quick et al., 2011]. A minimum duration of approximately 30 minutes consists of patient setup, localiser acquisitions and multiple 3 minute bed positions.

nearby nodes, and M refers to whether the cancer has metastasised (spread to other organs). In a wide range of tumour types and contexts, PET imaging has been shown to be more accurate compared to anatomical imaging with CT and MR. For instance, FDG PET has been shown to be more accurate in nodal and metastatic disease staging of head and neck, lung, oesophageal, neuroendocrine cancers, staging and response assessment of lymphoma, and the re-staging and follow up surveillance of these cancers. The appearance and number of lesions visible in PET image therefore has a big role to play in staging [NCI Breast Cancer, 2013].

As well as providing an image of tracer uptake distribution for qualitative assessment, PET can also provide quantitative information, which provides an additional dimension for the study of pathological and physiological processes. Standard uptake value (SUV) is a semiquantitative measure widely used to measure metabolic activity in avid lesions [Acton et al., 2004, Tomasi et al., 2012]. SUV normalises the uptake in a region of interest (ROI) or lesion, to injected dose per unit

body weight, considering radioactive decay, so:

$$\text{SUV} = \frac{\text{Activity (MBq/mL)} \times \text{decay factor}}{\text{Dose (MBq)} / \text{body weight (g)}} \quad (2.6)$$

where decay factor = $2^{-T/\lambda}$, where T is the time between the measurement of the injected dose and the start of the scan (s), and λ is the tracer half life (s). Measures often used are SUV_{max} , defined as the maximum voxel SUV value inside a ROI, SUV_{mean} , defined as the mean voxel SUV value within a ROI, and SUV_{peak} , defined as the maximum average activity concentration within a 12 mm diameter sphere inside the ROI [Boellaard R, Delgado-Bolton R, Krause B, 2015]. SUV_{peak} is more reproducible than SUV_{max} as it is less susceptible to noise.

It has been suggested by some studies that absolute SUV thresholds may help to distinguish between benign (non-cancerous) and malignant (cancerous) lesions, which in turn affects patient diagnosis and management [Patz et al., 1993, Hubner et al., 1996, Rohren et al., 2004]. However, SUV measures have some downfalls. Administered tracer dose may be less than planned if any inadvertent subcutaneous (not intravenous) extravasation occurs, causing an overestimation of SUV. SUV for FDG PET may be underestimated in hyperglycaemic patients [Higashi et al., 2003], where blood glucose levels are high, or in lesions smaller than the PET spatial resolution, due to partial volume (PV) effects [Hickeson et al., 2002]. SUV variations also occur depending on settings such as scatter and attenuation correction schemes, as well as the reconstruction algorithm itself, making it difficult to compare results between sites in large studies. It has also been reported that SUV is sensitive to the time interval between injection and acquisition, but measuring at more than one time point can provide diagnostic benefit [Hamberg et al., 1994]. SUV is also sensitive to motion, and SUV underestimation occurs if the activity within an area of tracer uptake is spread out over a larger area, for example in a focal lesion moving due to respiration. More detail is provided in Section 3.1.

PET is also useful for surgical and radiation planning. For example, SUV measures can be used to help delineate malignant regions with automatic threshold based approaches, especially useful for lesions with non-homogeneous uptake or when the tumour is not visible on anatomical imaging (MR/CT)

[Acton et al., 2004, Krak et al., 2005]. Assessment of response to treatment and assessment of drug efficacy can also be made with information from SUVs, by a quantitative comparison between results from before and after treatment.

Further additional quantitative metrics such as SUV (minimum, maximum, mean, standard deviation etc.) and metabolic lesion volume can be used as features for differentiation of healthy/tumour tissue, or treatment outcome prediction, with a growing research area known as texture analysis [El Naqa et al., 2009]. One method forms a histogram of voxel intensities inside an ROI, then numerical values can be found for parameters such as alignment of voxels with similar intensities, and difference between neighbouring voxels. These numerical values describe ROI heterogeneity for each parameter. [Tixier et al., 2011]

Chapter 3

Background

3.1 Why Is Motion Correction Necessary?

Motion artefacts caused by any kind of patient movement during acquisition lead to a loss of information in the resulting image in all types of imaging modalities. The type of artefact that appears in the image will depend on the imaging modality, acquisition type, the source of motion - from anatomies that move rigidly or non-rigidly, and the type of motion, either involuntary such as sneezing, twitching, muscle relaxation, slow pillow compression, head movement etc., or periodic such as respiratory and cardiac cycles.

In PET imaging specifically, any areas which move during acquisition will be adversely affected in resulting images. A blurring effect is seen on brain scans if there is head motion during acquisition, as shown in Figure 3.1.

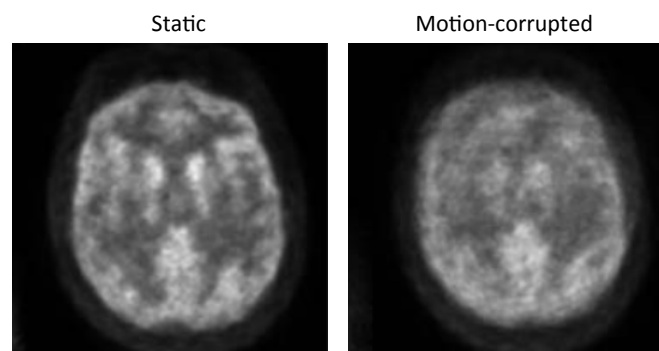


Figure 3.1: Static and motion-corrupted PET images from [Ullisch et al., 2012]

In the thorax/abdomen, due to a movement of the diaphragm of around 20 mm on average in one breathing cycle, areas of high tracer uptake may appear blurred, and in extreme cases may not be visible at all, potentially affecting staging and treatment

planning [Martinez-Möller et al., 2007] (see Section 2.5). Lesions located at anatomy boundaries such as at the lung/liver interface can also be mispositioned in resulting PET images, for example a lesion at the top of the liver could appear to sit at the bottom of the lung or vice versa. Quantification can also be affected, with motion causing underestimation of SUV, potentially affecting diagnosis and tumour staging.

Motion may also cause problems with attenuation correction. The AC map is either acquired during shallow breathing in PET/CT, or at breath-hold in PET/MR. First, as breathing is irregular and the AC map acquisition time is much lower than the length of free-breathing PET scan, an inherent spatial mis-match will occur, which may cause artefacts [Sureshbabu and Mawlawi, 2005]. Figure 3.2 shows an example where mispositioning of a lesion at the top of the liver is caused by attenuation mismatch from respiratory motion, resulting in an image artefact.

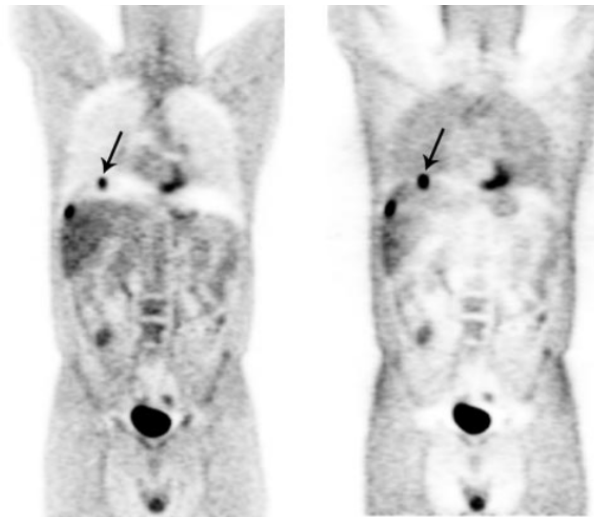


Figure 3.2: A lesion is mislocalised at the bottom of the lung in the attenuation corrected image (left) although it is actually located at the dome of the liver as visible on the non-attenuation corrected image (right). PET images from [Sureshbabu and Mawlawi, 2005]

A large number of motion correction techniques have been proposed in the literature to reduce the effect of respiratory motion. Many are currently used in clinical research and some are now available for diagnostic purposes, for example, Q.Static and Q.Freeze systems (GE Healthcare, Milwaukee, WI, USA), and HD Chest and BodyCOMPASS systems (Siemens Healthcare, Erlangen, Germany).

This chapter provides an overview of the tools required for PET motion correction; respiratory mechanics and tracking, general image registration, measuring motion in

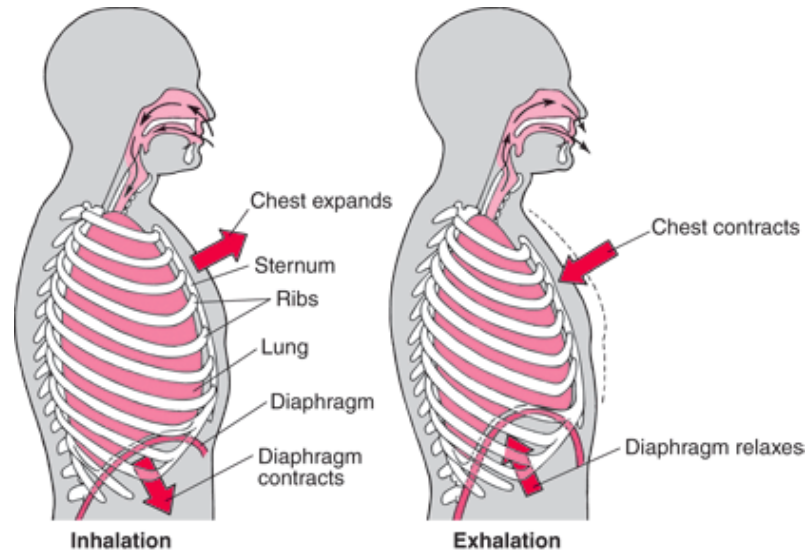


Figure 3.3: Diagram of breathing mechanics [Teppema and Berendsen, 2014].

MR and PET, PET gating, and motion-compensated PET reconstruction. Furthermore, recent methods proposed that specifically utilise the simultaneity of the two modalities in hybrid PET/MR scanners are discussed.

3.2 Respiratory Mechanics

The breathing process is carried out mostly by the diaphragm, a dome-shaped muscle sheet at the thorax/abdomen interface, attached to the base of the sternum and lower section of ribs. The intercostal muscles, situated between the ribs also contribute. During inhalation, the diaphragm contracts and moves down, whilst the inter costal muscles contract and push the chest wall out, causing an increase in chest cavity size. This in turn increases lung volume, reducing the air pressure inside the lungs causing air to flow in. Exhalation occurs when the diaphragm relaxes and moves back up, and the increases in pressure in the lungs pushes air back out. This process is depicted in Figure 3.3.

Though triggered by diaphragm and chest wall movement, the breathing process causes motion in many parts of the thorax and abdomen, including lungs, liver, pancreas, kidneys, spleen, heart and prostate. Langen et al. summarised the results of many patient studies measuring organ displacement. Combining results from all studies examined, normal/deep breathing average displacements are 14/71 mm for the diaphragm, 15/46 mm for the liver, 20/43 mm for the pancreas, and 16/24 mm for the

Anatomy	Normal breathing	Deep breathing
	mean \pm SD (mm)	mean \pm SD (mm)
Diaphragm	14 \pm 6	71 \pm 35
Liver	15 \pm 6	46 \pm 13
Pancreas	20 \pm 2	43 \pm 0
Kidney	16 \pm 4	24 \pm 14

Table 3.1: Mean and standard deviation (SD) organ displacements through respiration, from all studies summarised by [Langen and Jones, 2001].

kidneys [Langen and Jones, 2001]. Table 3.1 provides the mean and standard deviation of all average displacements from these studies.

Displacement of lung lesions is harder to generalise as more movement occurs in the lower lung rather than the upper lung, and mobility of lesions is reduced when attached to structures such as the chest wall or vertebrae. In a study with 20 patients, average lesion displacement was reported to be 6 mm over all lesions, compared to 12 mm in the lower lung lesions only [Seppenwoolde et al., 2002]. The study also reported that on average, lesion motion was 5.5 mm in the superior-inferior (SI) direction, 2.2 mm in the anterior-posterior (AP) direction, and only 1.2 mm in the lateral direction.

The heart also moves due to respiration, as it sits just above the diaphragm. Translation in the SI direction is the dominant motion, with a mean ratio of heart-to-liver displacement found to be 0.57 (range of 0.17-0.93) [Danas et al., 1999]. Another study reports mean absolute maximum translation of the heart during respiration at 17 mm [Wang et al., 1995]. Small non-rigid deformations of the heart are also reported, with an average of 3-4 mm in some areas, and up to 7 mm in some subjects [McLeish et al., 2002]. Respiration can also cause motion of the prostate, reportedly 3.3 mm on average with a maximum of 10.2 mm in one study [Malone et al., 2000], although in this case patients were immobilised in thermoplastic shells.

The respiratory cycle is quasi-periodic, with an approximate period of five seconds [Nehmeh et al., 2004, Ruan et al., 2008], whilst the depth of breathing varies greatly across the population. The nature of the internal motion that takes place via

respiration depends on many factors, such as type of breathing (more from diaphragm or chest wall), breathing style (tidal or deep), posture, gender, and proximity to the diaphragm and chest wall [Wade, 1954]. Variable contributions from both the diaphragm and chest wall means that the respiratory cycle is not repeatable from cycle to cycle, and this is known as inter-cycle variation. The difference in motion of internal organs followed between inhalation and exhalation is known as intra-cycle variation, or hysteresis [McClelland et al., 2013].

3.3 Tracking Motion: Respiratory Signals

A respiratory, or surrogate signal, is required to track a patient's breathing, which in this work we define as a 1D high temporal resolution signal. A direct method of collecting a respiratory signal is by measuring absolute diaphragmatic displacement, in the form of an MR pencil-beam navigator image. This is a 1D MR image, collecting a signal by excitation of only a vertical column of voxels passing through the diaphragm, acquired at high temporal resolution [Danas et al., 1997]. This provides an accurate way of tracking the SI movement of the diaphragm over time, but extends scan time, requires bespoke sequence development for interleaving the navigator into other clinical MR sequences, and gives artefacts in the clinical sequence. An MR-based signal can also be acquired by extracting the central k-space lines from other 3D MR data, forming a 1D projection via a Fourier transform [Odille et al., 2010, Buerger et al., 2012].

Another method of measuring respiration is tracking movement of the chest wall, which can be done in a number of ways. One is the Real-time Position Management (RPM) device (Varian Medical Systems, Palo Alto, California), which is a small block placed on top of the patient chest, tracked by an infrared camera to measure the displacement in three dimensions. Another method is using a respiratory belt, or pneumatic bellows, placed around the abdomen, such as the Anzai AZ-733V (Anzai Medical Co, Ltd., Tokyo, Japan), which monitors change in pressure inside the belt as it stretches during respiration. For experimental work in this thesis, a respiratory cushion is used (Siemens AG, Erlangen, Germany), which sits between the patient chest and an MR coil sitting on top, measuring pressure changes as the cushion is compressed with respiration.

A signal may also be obtained with a temperature-sensitive device which tracks

respiration based on the temperature of exhaled air [Boucher et al., 2004]. It is possible to monitor respiration by measuring the flow of air in and out of the lungs, with a spirometer. However, with this method there is often a drift in the signal due to escaping air.

These methods come at a monetary and time cost due to the initial purchase and careful setup before each patient scan. It has also been found that a phase difference may exist between such external signals and internal motions [Ozhasoglu and Murphy, 2002, Gierga et al., 2005].

A respiratory signal can also be found by analysis of internal motion with PET data, which overcomes the problem of phase differences between internal and external motion. One such method is by computing a centre-of-mass in a ROI, in PET sinograms [Bundschuh et al., 2007]. Another method is analysing time activity curves in ROIs placed over moving anatomy edges, either by manually selecting ROIs in image space [Visvikis et al., 2003] or by automatically detecting ROIs in sinogram space with frequency analysis to find dominant respiratory frequencies [Schleyer et al., 2009]. A practical approach is to measure the varying number of total counts in PET time frames, which changes as areas of contrast move in and out of the FOV, if motion in the SI direction occurs [He et al., 2008]. Another practical approach is to use principal component analysis (PCA) to detect changes in sinogram frames, with no need for ROIs [Thielemans et al., 2012]. This method will be explained in more detail in Chapter 4 .

3.4 Image Registration

To account for motion during data acquisition, physical warping between different motion states or images needs to be estimated. To find a transformation that will align one image to another, image registration is used. A similarity measure is used to compare images. One image can then be warped, and the similarity measured again. This is done in an iterative process to find the best warping that aligns the images, by minimising or maximising an energy function containing the similarity measure and a warping transformation.

Optimisation schemes such as gradient descent or conjugate gradient method are commonly used to find the best warping of one image to align with another, and this

can be in the form of a displacement at each voxel, or for a set of control points. This depends on the type of warping required. Rigid registration uses only rotation and translation, whilst affine adds sheering and scaling. For motion of solid bodies such as the brain, only rigid (and sometimes affine) warping is necessary. However, to find the internal motion between images at different respiratory states, nonrigid warping is needed to account for more complex motions. For non-rigid motion, a deformation field can be produced where each voxel is assigned its own displacement vector.

Two types of commonly used similarity measures that compare two images on a voxel-by-voxel basis are detailed here as they are used as metrics to compare pairs of images later in the thesis.

3.4.1 Sum of Squared Differences

Sum of Squared Differences (SSD) is an intensity based measure, describing the difference in corresponding individual voxel intensities between two greyscale images A and B , with voxels a_i and b_i :

$$SSD(A, B) = \sum_i (a_i - b_i)^2 \quad (3.1)$$

3.4.2 Mutual Information

Mutual Information (MI) is an entropy based measure, describing the amount of information that is shared between two signals. MI accounts for a difference in voxel intensities between images so is often used for bi-modality registration. Applied to 2D images A and B , MI is defined as:

$$MI(A, B) = H(A) + H(B) - H(A, B) \quad (3.2)$$

where $H(A, B)$ is the joint entropy between images:

$$H(A, B) = - \sum_i p_{AB}(a_i, b_i) \log p_{AB}(a_i, b_i)$$

and $H(A)$ and $H(B)$ are the individual image entropies, for example

$$H(A) = - \sum_i p_A(a_i) \log p_A(a_i)$$

where p_{AB} is the joint probability distribution function of A and B , and p_A is the marginal probability distribution function of A .

Image registration is widely used in methodologies for motion correction to find deformations between motion states with both MR and PET images. Various methods that utilise registration are covered in the next sections.

3.5 PET Framing and Gating

Typical PET acquisitions last between 3-15 minutes for clinical images, or even over an hour for research scans. Due to long scan times and the ability to collect raw data in a constant stream as list-mode, most motion correction techniques rely on grouping data together that is collected at a similar motion state, with motion correction applied retrospectively. This can be in the form of framing, where data is grouped in intervals over time (usually non-periodic motions), or in the form of gating, where data is grouped periodically, for cyclic motion such respiratory or cardiac. Once motion has been grouped into sections of different motion states, they can either be reconstructed separately then warped and added, or the motion can be incorporated into the reconstruction to form one motion-free image.

PET framing was used by Picard et al. in 1997, who tested their method on a moving Hoffman brain phantom. Head position was monitored during the scan with two video cameras, and when the head displacement from original position was over a set threshold, a new frame of data was started [Picard and Thompson, 1997]. Fulton et al. described a similar methodology, tested on a volunteer, where data was framed every 30 seconds and the volunteer was asked to move their head at various points to coincide with the start of a new frame. Here, the Polaris optical-tracking system (Northern Digital Inc., Waterloo, ON, Canada) was used to track head motion [Fulton et al., 2002].

A disadvantage of framing at predetermined time intervals is that intra-frame motion is not accounted for. One way to avoid intra-frame motion is to frame the PET data according to when movement occurs, either by tracking motion with a tracking system [Montgomery et al., 2006], or by getting this information from the raw PET data itself using PCA [Thielemans et al., 2013].

Respiratory motion is cyclic, so rather than framing data throughout an

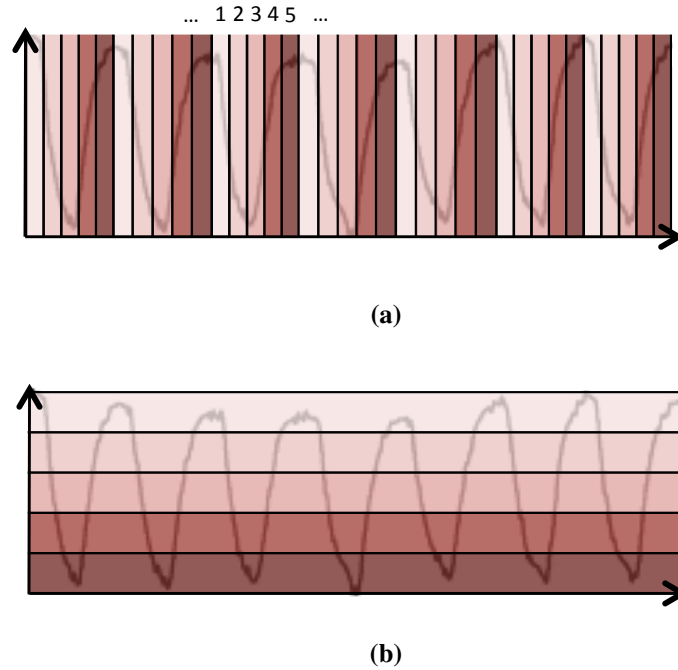


Figure 3.4: PET gating schemes to form 5 gates by (a) phase gating and (b) amplitude gating.

acquisition, data acquired at similar respiratory positions can be combined. Once a respiratory signal has been collected, PET data can be binned, or gated, so data in a single gate is assumed to be acquired when anatomy was in a similar position. The main methods are gating by amplitude or phase [Rahmim et al., 2007, Pépin et al., 2014].

Phase gating splits the data within each respiratory cycle into a predetermined number of bins between each inhalation peak (Figure 3.4b). This method ensures the same time duration of each gate and similar count statistics, but neglects inter-cycle variations in breathing amplitude.

Amplitude gating splits the data based on the value of respiratory signal (Figure 3.4a). This method accounts for inter-cycle variations as divisions are made based on absolute values of the signal, but gates will vary in time length and count number, and hysteresis effects are neglected as no division is made between inhalation and exhalation for the same value of respiratory signal.

3.6 Measuring Motion

Once PET data has been split into different 'motion-free' states, a static image can be produced by either using data from one gate only, or by combining data from all

gates, once the physical deformation between each motion state is known. In PET motion correction literature, finding deformations between motion states is typically done using PET images themselves, but with the simultaneous PET/MR scanner, the use of MR data to determine physical motion is also a possibility.

3.6.1 Measuring Motion: PET

Most motion determination in PET literature is done by binning data into different motion states, reconstructing an image in each bin, then registering images to a common reference image. This method has been widely used for rigid motion where PET data framing is carried out to form the separate images [Picard and Thompson, 1997, Fulton et al., 2002, Montgomery et al., 2006, Thielemans et al., 2013]. The same method can be used for non-rigid motion such as respiration [Nehmeh et al., 2002, Boucher et al., 2004, Bai and Brady, 2011].

The aim of gating is to minimise intra-gate motion in the data, with each bin representing a different part of the respiratory cycle, assuming a periodic relationship between the reparatory signal and all moving anatomies. Higher gate temporal resolution (higher number of gates) therefore minimises intra-gate motion, but decreases the number of counts in each gate, and therefore SNR, which is required for good registration results. A trade-off must be considered between having a total gate duration high enough to provide good contrast in resulting images, and having gate duration short enough that intra-gate motion is minimised. Also, depending on the type of framing/gating method chosen, if the duration of each frame/gate varies (and therefore the number of counts in each frame/gate varies), this may have detrimental effects on the image registration results.

3.6.2 Measuring Motion: MR

Rigid body motion, such as head motion, occurring between MR acquisitions can be found by analysing k-space as the motion has well defined influence on raw k-space data. Physical translations in image space affect only the phase, and rotations cause a rotation of k-space that can be detected in the k-space magnitude data. For translations, change in k-space is known from the Fourier shift theorem. If the Fourier transform of the function $f(x)$ is $F(k)$, then the Fourier transform of the shifted function $f(x - a)$ is $F(k)e^{-iak}$. Physical rotations in image space cause a rotation of the k-space magnitude

data about the k-space centre. These two separate effects mean a rigid body motion between two sets of k-space data can be deduced retrospectively after an acquisition. To exploit this, specific k-space trajectories, called 'navigators' have been developed to sparsely sample k-space in such a way to provide enough information for motion measurement when repeat measurements are taken.

One type is the 'Spherical Navigator'. This samples a spherical surface in 3D k-space using a spiral trajectory. The spherical shape is good for rotation estimation as whatever the centre of axis of rotation in image space, there are sampled k-space points far away, and estimation of rotation requires these points far from the axis centre. Another is the 'Cloverleaf Navigator', whose trajectory follows three quarter arcs, each perpendicular to a k-space axis about the k-space centre, connected by line navigators which follow each axis. The arcs are useful for rotation estimation whilst the lines are useful for translation estimation. The acquisition time of the cloverleaf navigator is much lower than that of the sphere [Ullisch, 2012].

To determine non-rigid motion, MR tagging is one possible technique, used to create temporary features, or tags in tissue which deform in images as anatomy deforms. It was originally proposed as a means of tracking myocardial motion and techniques have been developed for more complex motion such as respiratory motion [Zerhouni et al., 1988]. It is built on the theory that when a selective RF pulse is applied in the presence of the normal magnetic field gradients, the magnetisation of protons in a section of tissue is perturbed, and these protons retain a memory of the pulse for a time dependant on the T1 of the tissue. Then, if an image of the area is obtained orthogonal to the tagged plane before full magnetisation recovery, tagged tissue will look different to non-tagged tissue. When consecutive images are acquired, warping of the tagged region can be inferred as it appears to move in the images.

Harmonic Phase (HARP) MRI was developed as an image processing technique for automated analysis of tagged images [Osman et al., 2000]. Spectral peaks of tagged MR images are found with the Fourier transform. Single peaks can be isolated and the inverse Fourier transform of the spectral contents within this peak can be found to yield the harmonic image split into magnitude and phase images. The harmonic phase depends on the underlying motion, and each spectral peak contains information about motion in a distinct direction. Motion can be found between 2 harmonic phase images

by exploiting the fact that the harmonic phase of a point in the tissue is time invariant so is constant throughout deformation. As tags are not usually visible for more than 1 second after the RF pulse, motion estimation with tagging has proven successful for cardiac motion, but is more challenging for respiratory motion as tags would not last for a whole period of the respiratory cycle.

Another way of determining motion is to use dynamic MR images, and to find deformations through image registration. One way is through 'snapshot' imaging, where MR images are acquired with a high enough temporal resolution to capture inter-frame motion. This has been proposed using low spatial resolution dynamic 3D MR images [King et al., 2012, Fayad et al., 2015]. A binning approach to MR data, similar to that of PET gating may also be used to build up bins of MR data over time, rather than acquiring images in real time in a 'snapshot' approach. One way is to acquire high spatial resolution 2D MR images, and bin to form a 3D image in each bin [Würslin et al., 2013]. In this work a pencil beam navigator is acquired in between each 2D slice to provide the respiratory signal on which the gating is based.

Another approach of increasing interest is the golden-radial phase encoding (G-RPE) MR k-space trajectory. This uses cartesian sampling in the readout direction and radial sampling in the phase direction, acquiring each k-space radial line through the k-space centre. The golden ratio is used as the angle between consecutive k-space lines, which provides global k-space coverage and isotropic resolution in the phase encoding plane [Buerger et al., 2012, Moghari et al., 2013, Rank et al., 2015]. For gated k-space data, scan time must be long enough to ensure a homogenous k-space line distribution within each bin, which can be reached by setting a maximum allowed angle between consecutive lines [Buerger et al., 2012]. One advantage of G-RPE is that as each k-space line passes through the k-space centre, it acts as a projection of the excited volume in the SI direction, so provides the respiratory signal for binning.

Many methodologies have been proposed to jointly estimate motion and perform MR image reconstruction at the same time for rigid motion [Atkinson et al., 1997, Manduca et al., 2000], and non-rigid motion [Batchelor et al., 2005], but as deformation fields are not explicitly calculated with these methods, they are not discussed here.

3.7 PET Image Reconstruction with Motion Correction

Once data has been split into individual 'static' motion states, there are multiple methods to form a single motion-corrected PET image. The most simple approach, and one that is used in clinical practice is to reconstruct only one gate, for example Q.Static (GE Healthcare, Milwaukee, WI, USA), normally at exhale position, but this is inefficient as only uses a fraction of the collected data. An image of a single gate will also suffer from low count statistics and high noise unless scan duration is increased.

Methods to use all acquired data require finding deformation fields between gates as described in the previous section. The deformation fields can then be used either before, during or after reconstruction. Pre-correction of lines of response (LORs) before reconstruction is possible, for rigid or affine motion, so suitable for brain imaging [Livieratos et al., 2005, Rahmim et al., 2007].

Many motion correction techniques use the reconstruct-transform-average (RTA) method of reconstructing each frame then warping images back to the exhale position with the deformation fields, and forming a weighted average of all images [Nehmeh et al., 2002, Boucher et al., 2004, Bai and Brady, 2011]. It is also possible to use the deformation fields directly in the system matrix as part of a motion-compensated image reconstruction (MCIR) with an iterative expectation maximisation algorithm [Qiao et al., 2006, Polycarpou et al., 2012, Tsoumpas et al., 2013]. The MCIR implementation used in this thesis is described in Section 5.4.7.

Polycarpou et al. compared the RTA and MCIR methods, with motion information obtained from dynamic MR acquired previously on a human volunteer applied to simulated PET data. The study found that MCIR quantitatively outperforms RTA, recovering true intensity values, and RTA has high bias in the gated images due to low count statistics in each gate potentially giving rise to issues related to convergence [Polycarpou et al., 2012]. With RTA, interpolation errors could occur due to warping the images after reconstruction, leading to degradation of resolution and possible image artefacts. On the other hand, noise increases with iteration number for MCIR whereas noise is small and stable in RTA. As RTA is simple and easy to implement it is a useful tool for motion correction but if quantification of lesions etc.

is important then MCIR is better, but noise must be treated with a regularised reconstruction or post-filtering. The RTA and MCIR methods have also been compared on real PET data [Fayad et al., 2015]. This work also found MCIR to be superior, in terms of lesion contrast improvement, changes in mean lesion position and lesion FWHM.

3.8 Motion Models

A motion model can be defined as taking surrogate data as input and estimating motion as an output [McClelland et al., 2013]. Model coefficients are calculated from a set of training data taking surrogate and motion data as inputs. These model coefficients allow motion estimation from new surrogate data when motion data cannot be captured. Formally, a direct correspondence model can be written as:

$$\mathbf{M} = \phi(\mathbf{s}) = \mathbf{A}\mathbf{s} \quad (3.3)$$

where \mathbf{M} is a motion estimate, ϕ is the model, and \mathbf{s} is a matrix containing input surrogate data. The model is made of a matrix \mathbf{A} of scalar coefficients, the size of which depends on the number of surrogates used and the number of motion parameters (i.e. the sizes of \mathbf{s} and \mathbf{M}).

Motion models are useful to infer motion estimates when a simple surrogate signal can be acquired but motion-capturing images cannot be acquired due to acquisition of other diagnostic images, or through image-guided interventions. Wang et. al proposed the basic idea of a motion model by demonstrating that the translation of the coronary arteries is linearly related to the diaphragm displacement [Wang et al., 1995]. In this example the displacement of the diaphragm is the surrogate signal and the dynamic images covering the coronary arteries provide the motion estimate in the model. Aside from image formation, motion models have been extensively explored with many applications such as proton therapy [Bert and Durante, 2011] and radiotherapy, with the Cyberknife system (Accuray Inc., Sunnyvale, CA) currently in clinical use.

Motion models have been used for motion correction in MR imaging. Generalised Reconstruction by Inversion of Coupled Systems (GRICS) is a method

used to reconstruct non-rigidly motion corrupted k-space data [Odille et al., 2008]. A model of motion at acquisition is however needed, along with collection of a surrogate signal throughout. The method iteratively updates the motion model and reconstruction as a coupled problem, and positive results were shown for moving phantoms and in cardiac and abdominal images in healthy volunteers [Odille et al., 2010].

Motion models have been used to some extent in PET/CT image acquisition [Fayad et al., 2010, Ambwani et al., 2011, Kruis et al., 2013], but their use has increased recently in the context of the simultaneous PET/MR scanner, where a model can be built with MR data, with the motion subsequently applied to the PET data.

3.9 Recent PET/MR Respiratory Motion Correction Literature

The recent advent of PET/MR scanners allows us to exploit the simultaneity of the modalities by using high spatial resolution and high contrast MR images to track respiratory motion and correct PET data, without additional radiation exposure. Many methods rely on MR sequences to retrospectively provide motion information to guide motion correction of PET data. Below is an outline of some recent research in the literature.

One method utilised for PET motion correction is with 'snapshot' MR, simultaneously acquiring PET data, binned at the same temporal resolution as the MR. Motion occurring between MR images can then be retrospectively applied to the PET data, either with RTA or MCIR methods. For rigid motion, this method has been applied to brain imaging, obtaining deformation information from either registration of low resolution echo planar imaging (EPI) images, or from cloverleaf navigators interleaved into the TR of a high resolution 3D-encoded fast low-angle shot (FLASH) sequence [Catana et al., 2011]. For the first method, scan time is extended as the EPI images are not clinical diagnostic images, and are acquired purely to determine motion. Both methods were tested with a physical phantom and two human volunteers. Results showed reduced blurring of all brain structures and boosted grey matter uptake, but the navigator-based correction appeared to not work as well as the

EPI-based correction, possibly due to the fact that motion estimates based on cloverleaf navigators are less accurate for larger movements (over 10 mm translation or 10° rotation).

This 'snapshot' imaging method can also be applied to non-rigid respiratory motion. In work proposed by King et al., low spatial resolution dynamic 3D MR images were acquired, then a motion model formed from the 3D deformation fields with 2D images used as the surrogate [King et al., 2012, Polycarpou et al., 2014]. In both pieces of work, model-estimated deformation fields were then used to warp reconstructed simulated PET data, framed in parallel with each MR image.

A similar approach of gating MR and PET data, and determining motion from the MR data can also be applied to cyclic non-rigid motion. Wurslin et al. described a methodology to form 3D MR volumes from binned 2D MR, then non-rigid deformation fields were found between each and the reference volume by registration. PET data were also gated using the same respiratory signal and binning scheme as applied to the MR, reconstructed into images, then warped and added using the MR-derived motion fields. The method was tested on five patients with lesions in the thorax or upper abdomen, and results showed improvements in images, with higher apparent SUV and lower FWHM in lesions, due to a decrease in blurring. For static lesions, SNR suffered slightly due to interpolation with the RTA approach of combining gated data [Würslin et al., 2013]. Fayad et al. also formed 3D MR images from 2D data binning, for formation of deformation fields in the motion correction of real PET data gated through respiration, on 11 oncology patients [Fayad et al., 2015]. Results showed significant mean increases in lesion SNR, contrast and position, and significant decrease in lesion size. The G-RPE MR technique has also been used to form 3D MR volumes, with deformation fields applied to PET data simulated from real dynamic MR data [Rank et al., 2015].

Forming deformation fields between motion states is also possible with MR tagging (see Section 3.6.2), and these can also be applied to motion correction of gated PET data. MR tagging was used to track motion of the lower abdomen in simulated PET/MR with a moving digital phantom, and on a physical deforming phantom [Guérin et al., 2011]. Tagging was also used on free-breathing primates and rabbits [Chun et al., 2012]. A methodology using tagged MR to correct for cardiac

PET data has also been proposed [Petibon et al., 2013]. MR tagging was used to derive non-rigid deformation fields of myocardial wall motion on a physical beating cardiac phantom, and the motion fields used in the PET reconstruction with the MCIR approach.

Some work has demonstrated the use of deformation information found from both PET and MR images. One method has been proposed with an MR motion model, using results from registration of gated PET images to choose which MR-derived deformation fields to use [Balfour et al., 2015]. The method was tested on MR data from four human volunteers, with simulated PET data. Results were similar to using only MR data to form deformation fields, but the proposed method only required a short MR acquisition to form the model, rather than acquiring throughout the whole PET scan. In this methodology, the gated PET data acts as the surrogate to the motion model, though in practice with real data, a respiratory signal would need to be acquired in order to gate the PET data. Another approach used PET and MR data together to form the deformation fields, by utilising both sets of data in a registration cost function [Fieseler et al., 2014]. This work shows some local improvements over using MR-derived deformations only, though it was tested with simulation data only.

3.10 Summary

PET imaging of the thorax and/or abdomen can be adversely affected by patient respiration, potentially causing quantification errors, blurring of tracer-avid regions, and image artefacts. This Chapter has explained the mechanics that cause this motion through breathing, and some of the tools currently used to try to correct for this motion.

The various methods used to track breathing with a respiratory signal were evaluated, from imaging methods that directly measure diaphragmatic displacement, to external hardware devices and data-driven approaches. Different methods to measure physical displacements with PET and MR imaging were also covered, along with tools such as image registration and PET gating. Once deformations throughout a PET scan have been estimated, and PET data has been grouped into different motion states, a motion-corrected PET reconstruction can then be carried out with one of two methods, either in image space after gated reconstructions (RTA), or during

reconstruction (MCIR).

In the last few years, many methods to utilise the simultaneity of MR with PET in the simultaneous PET/MR scanner have been proposed. Although work has shown promising results, the main limitation of other proposed methods is the issue of applicability for clinical use. One issue is scan time, and the need to keep this low for high patient throughput in hospitals. For 'snapshot' imaging or use of bespoke MR sequences such as tagging, MR images are acquired throughout the PET scan to track motion, meaning useful diagnostic MR images cannot be acquired at the same time. This means scan time must be extended to accommodate diagnostic imaging, and extended further if the method is used at multiple bed positions.

Use of motion models partly overcome this problem by collecting motion information in a short space of time, then using this information to infer deformations throughout the PET scan without the use of motion-capturing MR. However, to use motion models, a surrogate signal is required. An MR pencil-beam navigator can provide the signal, but this requires sequence development by insertion into each clinical MR sequence, can't be continuously acquired, may introduce artefacts in the MR images, and extends scan time. External hardware may also be used, but at a monetary and time cost, with methods requiring careful set up prior (and often during) each patient scan. Data-driven methods may overcome this issue, with PET-derived respiratory signals possible to acquire from the PET data with no need to extend scan time or change imaging protocol. Anatomical location is also an issue, as some motion-capturing MR techniques are designed for motion of a specific anatomy, whereas in clinical practice there is a need to motion-correct all areas as often the diseased area is unknown prior to the patient scan.

Another limitation of recent PET/MR motion correction literature is the lack of clinical validation on patient data. Many studies have been conducted on simulated and physical moving phantoms, which is useful for comparing computational methods such as types of reconstruction, but they do not account for the complex motion of real breathing. For example, with simulated PET data, the deformation fields used to apply respiratory motion are often taken from registration results of 3D low resolution MR images, but these are often unrealistic as these are only an estimation of complex non-rigid diffeomorphic motions. This type of motion will be more easily recovered

by generic registration methods than real respiratory motions. Some studies have been conducted with primates and human patients, but often subject number is low, and there is still a need to test methods on a large patient cohort.

In this thesis many of these limitations of previous work are addressed. We demonstrate the capability of a joint PET-MR motion model to predict respiratory motion, and use this to motion-correct any length of PET acquisition with minimal extra scan time and no external hardware used, and finally, test the method on a large patient cohort.

Chapter 4

Validation of a PET-derived Respiratory Signal

4.1 Motivation

In this chapter, we introduce a technique devised by Thielemans et al. to extract a respiratory signal from raw PET data alone [Thielemans et al., 2012]. In this chapter, the signal was used for PET gating only, and compared with RPM data. We perform a validation of the PET-derived respiratory signal, by comparison with an absolute measure of diaphragmatic displacement using an MR pencil-beam navigator. The aim of this study is to find if the PET-derived signal can provide an accurate measure of diaphragmatic displacement, and therefore be used as a respiratory signal for motion monitoring and correction. We also explore the use of a respiratory cushion for a measure of chest wall displacement, for comparison with the PET-derived signal.

4.2 PET Data-driven Signal Extraction

It has been shown that a respiratory signal can be extracted from raw PET list-mode data with Principal Component Analysis (PCA) [Thielemans et al., 2012] with no extra hardware or scanning time required. PCA is a form of dimensional reduction used to find change in a data set. Thielemans et al. used this mathematical technique to exploit the fact that if areas of sufficient contrast in a PET scan are moving, this movement will be detectable in the raw PET data. If respiration is the main source of change in a data set then the first Principal Component (PC) should reflect this.

First, the PET list-mode file is unlisted into N short (~ 0.5 s duration) low spatial

resolution sinogram frames. To reduce the size of data, axial compression, or single-slice rebinning (SSRB), which is an approximation used to assign LORs between a detector pair to the transaxial sinogram at the half-way point in the axial direction between the detectors [Daube-Witherspoon and Muehllehner, 1987], is used during the unlisting. This process produces a 3D stack of sinograms at each time point, with one 2D sinogram at each axial position. As most respiratory motion occurs in the inferior-superior direction, the number of projection angles, or views, is also reduced with angular compression, or view mashing. Each view sums sinogram data in the angular direction. With this method, 9 different angles were used, creating projections in 9 different views. View 1 is similar to looking at the data in a 'coronal-like' orientation.

Sinogram stacks are then spatially smoothed with a Gaussian filter to reduce the effect of noise. To normalise for low-frequency changes so that each time frame contains approximately the same number of total counts, scale factors are applied to the sinogram series to normalise for changes in radioactive tracer concentration (due to radioactive decay or tracer kinetics). The Freeman-Tukey transformation is applied to approximately convert Poisson noise to Gaussian, then finally PCA is executed. With PCA, each sinogram stack in the 4D time series is approximated as

$$s_i \approx \bar{s} + \sum_{k=1}^K w_{i,k} p_k \quad (4.1)$$

where s_i is sinogram frame $i \in 1 \dots N$, \bar{s} is the mean of all sinogram frames, p_k is the k -th PC, $k \in 1 \dots K$ and $w_{i,k}$ is the scalar weight factor for sinogram frame i , PC k . For one PC, each sinogram frame in the time series therefore has a single weight factor, calculated as the sum of a voxel-wise multiplication of the PC with the difference between the sinogram and sinogram mean,

$$w_{i,k} = p_k \cdot (s_i - \bar{s}) \quad (4.2)$$

These weights $w_{i,1}$ for Principal Component $k = 1$ are then temporally smoothed, and these then provide the respiratory signal. As the sign of the weight factors are arbitrary, inhalation direction is chosen manually by flipping the sign if necessary, by

either visual analysis (looking for more prominent peaks at inhale than exhale), or by comparison with MR data where available.

Note: for work in this chapter, the first three principal components were computed, and the associated signal that matched best with the MR-based respiratory signal was used, picked by visual comparison. For all data sets, the first principal component provided the most 'respiratory-like' signal. Although heart-beat would in principle affect the data, its influence on time frames of 0.4s is likely to be small.

4.3 Other Respiratory Signals for Validation

To test if the PET-derived signal would provide a good measure of respiratory displacement, two available alternative methods, a respiratory cushion and a MR pencil-beam navigator, were explored for comparison.

4.3.1 MR Pencil-Beam Navigator Signal Extraction

An MR pencil-beam navigator 1D signal can be acquired to measure diaphragmatic displacement in the SI direction, by positioning it on the right hemi-diaphragm at the lung-liver interface and acquiring signal from a column of voxels. On the Siemens mMR, this was implemented with 'scout mode', with repetition time of 150ms. A typical MR navigator image, as output by the scanner, for a patient free-breathing is provided in Figure 4.1a.

An automatic edge detection method was used to find the liver edge, by applying a threshold when searching each column of voxels in the SI direction. Blue dots are plotted where this edge is detected in Figure 4.1b. Using the spatial and temporal resolution information, this edge can be converted into a respiratory signal of amplitude of the diaphragm (mm) against time (s), with the peaks representing inhalations, as seen in Figure 4.1c.

4.3.2 Respiratory Cushion Signal Extraction

A respiratory cushion was used (Siemens AG, Erlangen, Germany), measuring pressure changes as the cushion is pressed against the MR body coil through respiration. Respiratory cushion data was output from the scanner as a text file, and the numbers were converted into a signal with a Matlab script.

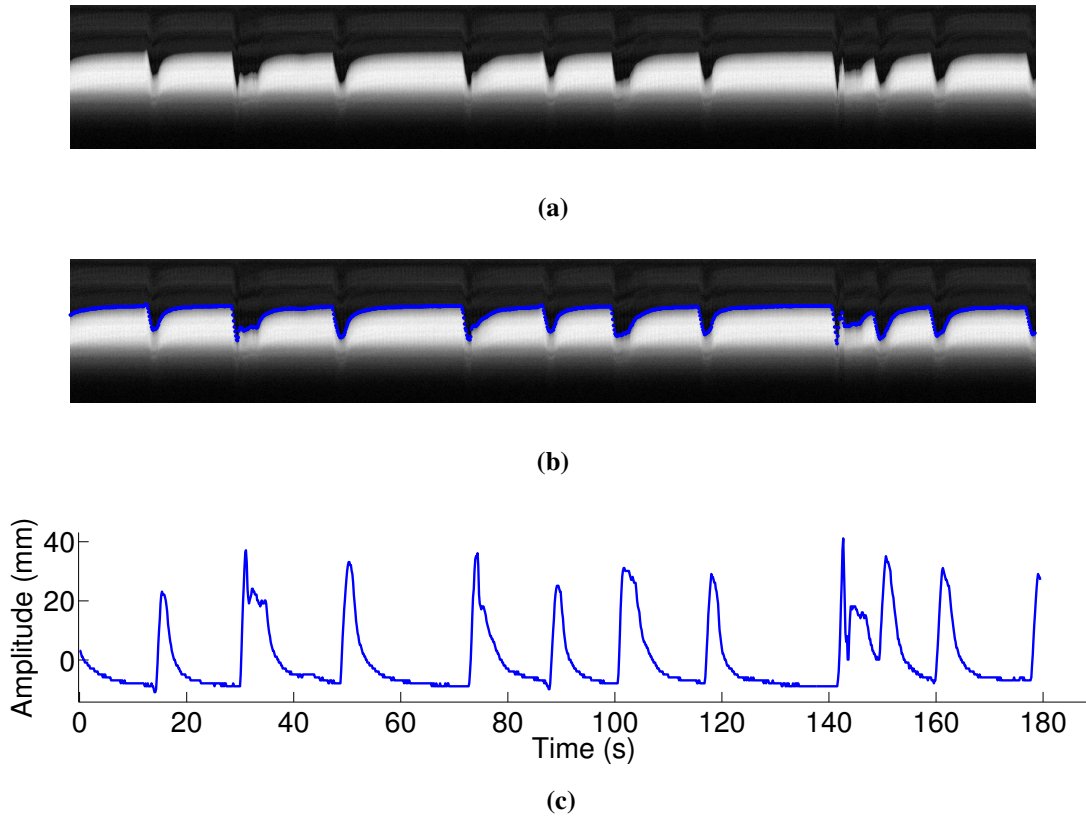


Figure 4.1: Method for derivation of an MR-derived respiratory signal, (a) pencil-beam navigator image, (b) image with liver edge detected, (c) resulting respiratory signal.

4.4 Pilot Study - Comparison with Respiratory Cushion

The PET-derived respiratory signal and respiratory cushion signal were compared in one patient dataset. Figure 4.2a shows a comparison of the cushion and PET signals, demonstrating a good visual correlation between the two. In this case there are no values on the y-axis as both signals are scale-less.

Figure 4.2b shows a comparison for another patient, of the respiratory cushion with both MR and PET derived signals. In this case the signals have been manually scaled to match the MR-derived signal as this has an absolute scale (mm). The signals have also been manually aligned temporally, due to the PET and MR system clocks being asynchronous. This example demonstrates the limitations of using the respiratory cushion. Whilst the PET and MR signals seem to correlate well, the cushion signal drops down to negative values at many of the inhalations. This occurs if there is too much pressure on the cushion and it hits a maximum, resulting in the signal dropping

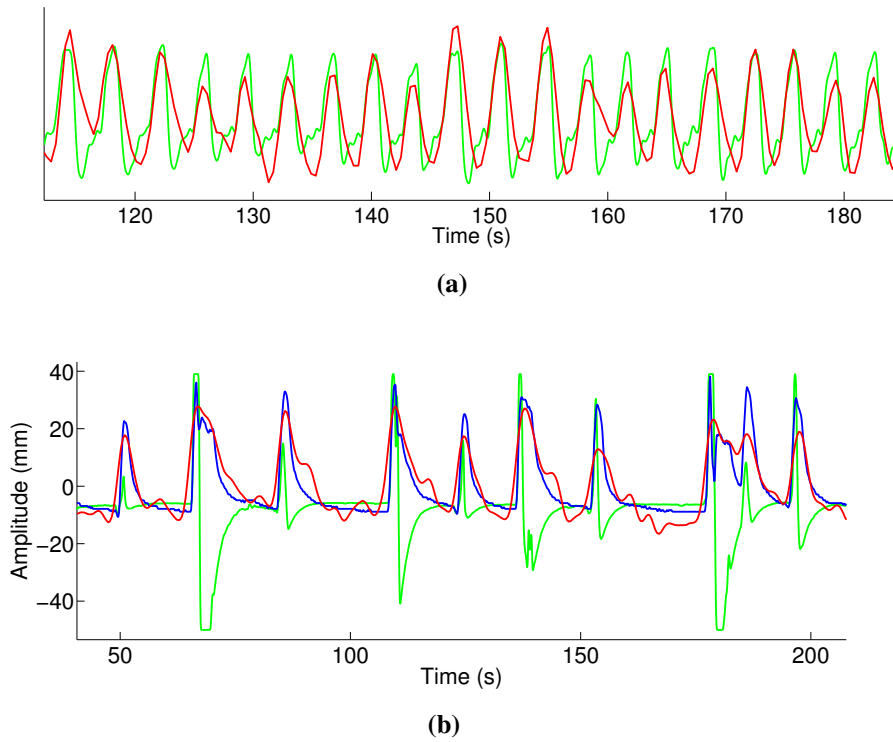


Figure 4.2: Patient respiratory signal data for two cases, (a) PET (red), cushion (green), (b) PET (red), MR (blue), cushion (green).

and taking a few seconds to level out again.

This problem occurred with multiple patients when being tested, and careful setup of the cushion (up to five minutes) was needed to make sure there was not too much or too little pressure on the cushion to allow it to work properly. As many patient datasets were desirable for a full validation, it was not practical to keep collecting the cushion data, and it was decided to continue collecting only MR and PET data to produce signals for comparison.

4.5 Validation Study: Comparison with MR Pencil-beam Navigator

For this validation study, a full comparison of our PET-derived respiratory signal with an absolute measure of diaphragmatic displacement using a 'gold-standard' MR pencil-beam navigator was carried out, on nine subjects. The respiratory signal was extracted from the PET data itself as described in Section 4.2, and a range of variables used to form the signal were tested to optimise the correlation between PET and MR derived signals on each patient data set. The aim was to assess how well the derived signal

matched with the MR navigator signal, on what types of avid moving regions the signal can be extracted for, and how tracer choice and count rate (relating to time between injection and scan) may have an affect on correlation.

4.5.1 Methods

Data were collected on nine patients (age range, 34-80 years; mean, 60 ± 15 years) immediately after the clinical PET/MR scan. These patients had a range of diseases (related to lung, cardiac, liver, pancreas, spleen, kidney), with one of two radiotracers used (six ^{18}F -FDG, three ^{68}Ga -DOTATATE). All patient information is included in Table 4.1.

The protocol used consists of PET list-mode with an MR pencil-beam navigator, acquired concurrently (overlap time range 93-180 s, mean 144 ± 22 s).

4.5.2 Analysis

4.5.2.1 Signal Correlation

The PET signal was extracted from the list-mode data according to equations 4.1 and 4.2 from each PET acquisition. Variables used to for the PET-derived signal were varied, along with a time shift constant δ between the PET and MR clocks, which is unknown and specific to each scan. This is due to the fact that there is a small gap (up to 1 second) between the MR and PET systems beginning to acquiring data, when set up to start at the same time. An error of 1 second is important, considering an average respiratory period of around 4 seconds. The signal was extracted multiple times for all permutations of the following variables:

- Sinogram frame duration = 0.1:0.9 s (0.1 s increments).
- Sinogram Gaussian spatial smoothing kernel standard deviation $\sigma = 5:50$ mm (5 mm increments).
- Signal temporal smoothing kernel standard deviation $\sigma = 0:0.7$ s (0.1 s increments).
- Time shift $\delta = -1:1$ s (0.1 s increments).

For each patient data set, the PET-derived signal was extracted using all permutations of the above variables, and compared with the MR-derived signal with

the 1D Pearson Correlation Coefficient. For each pair of PET and MR signals, the two signals were first interpolated to a temporal resolution of 0.1s then correlation $\rho_{p,m}$ was found with

$$\rho_{p,m} = \frac{COV(p, m)}{\sigma_p \sigma_m} \quad (4.3)$$

where σ_p and σ_m are the standard deviations of the PET and MR-derived signals respectively and COV is the covariance of the two signals. For each patient, the best correlation is quoted as the signal extracted with the set of variables that maximises $\rho_{p,m}$.

4.5.2.2 Gating comparison

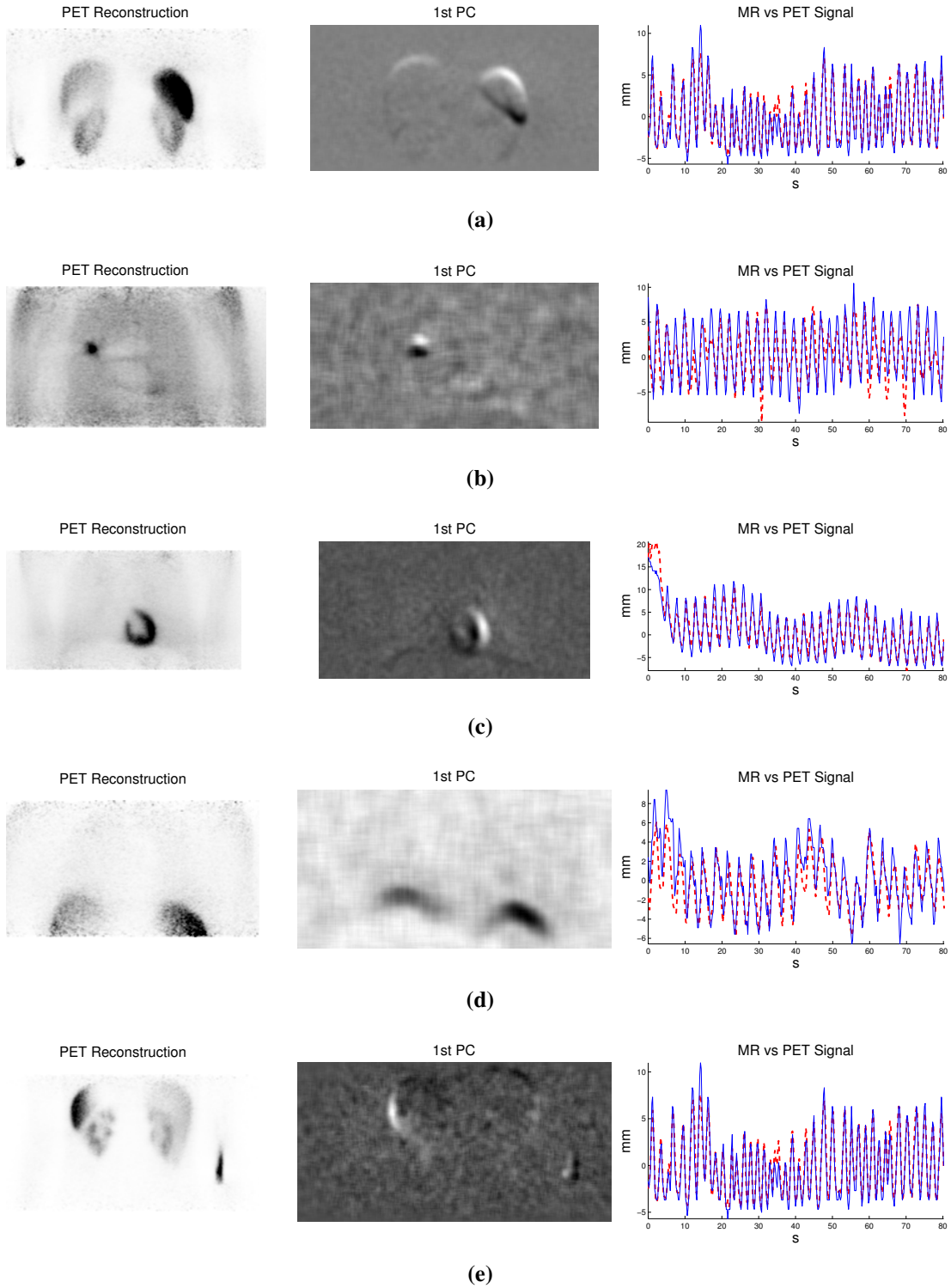
Once the PET-derived signal with the best correlation to the MR-derived signal had been found, gating of the PET data according to a binning scheme based on both signals was also compared. The PET data were grouped into five respiratory gates based on two different binning schemes using the PET and MR derived signals - by amplitude of the signals, and phase of the signals. PET images for each bin were reconstructed (OSEM, 7 subsets, 1 iteration, no attenuation or randoms correction). Volumes of interest (VOIs) were identified for each dataset manually; choosing a region of high tracer uptake expected to move due to respiration (e.g. spleen, lung/liver lesion, heart etc). VOIs in each gate were then registered (rigid, translation only) to a reference gate (chosen at exhale position) and the maximum displacement between gates recorded.

4.6 Results

4.6.1 Signal Correlation

Figure 4.3 shows the non-attenuation corrected reconstructed image, view 1 of the 1st PC, and an 80 second section of the MR and PET-derived signals for a range of patients. The PET-derived signals were formed with optimal parameters. The PET-derived signal was scaled to match the MR-derived absolute (mm) signal for visual analysis.

Table 4.1 summarises the results, with parameters providing the best correlation between PET and MR derived respiratory signals, as well as gating results. Over all patients there was a very strong correlation between MR and PET-derived signals (mean, 0.89 ± 0.09 ; range, 0.70-0.98).



Patient	Tracer	Avid VOI	Time since injection	Count rate (10^4 counts/sec)	Optimal Parameters				Results	
					Frame duration (s)	Spatial smoothing σ (mm)	Temporal smoothing σ (s)	Time shift δ (s)	Correlation $\rho_{p,m}$	Max displacement (mm)
1	^{18}F -FDG	lung lesion	2h 54m	38	0.2	15	0.4	-0.2	0.96	72
2	^{18}F -FDG	lung lesion	2h 31m	55	0.4	10	0.2	-0.3	0.82	35
3	^{18}F -FDG	lung lesion	2h 28m	84	0.2	5	0.3	-0.4	0.96	98
4	^{18}F -FDG	lung lesion	2h 51m	58	0.5	15	0.3	-0.2	0.88	27
5	^{18}F -FDG	cardiac	1h 41m	89	0.4	5	0.1	-0.9	0.94	88
6	^{68}Ga	pancreas lesions	2h 19m	35	0.4	10	0.1	-0.1	0.94	54
7	^{68}Ga	rib lesions	6h 02m	36	0.9	15	0.3	0	0.82	133
8	^{68}Ga	liver lesions	2h 36m	85	0.2	5	0.1	-0.7	0.97	154
9	^{18}F -FDG	liver lesions	4h 22m	6	0.4	45	0.2	0	0.70	15

Table 4.1: PET vs MR derived signal results, with parameters optimising correlation. ^{68}Ga represents ^{68}Ga -DOTATATE.

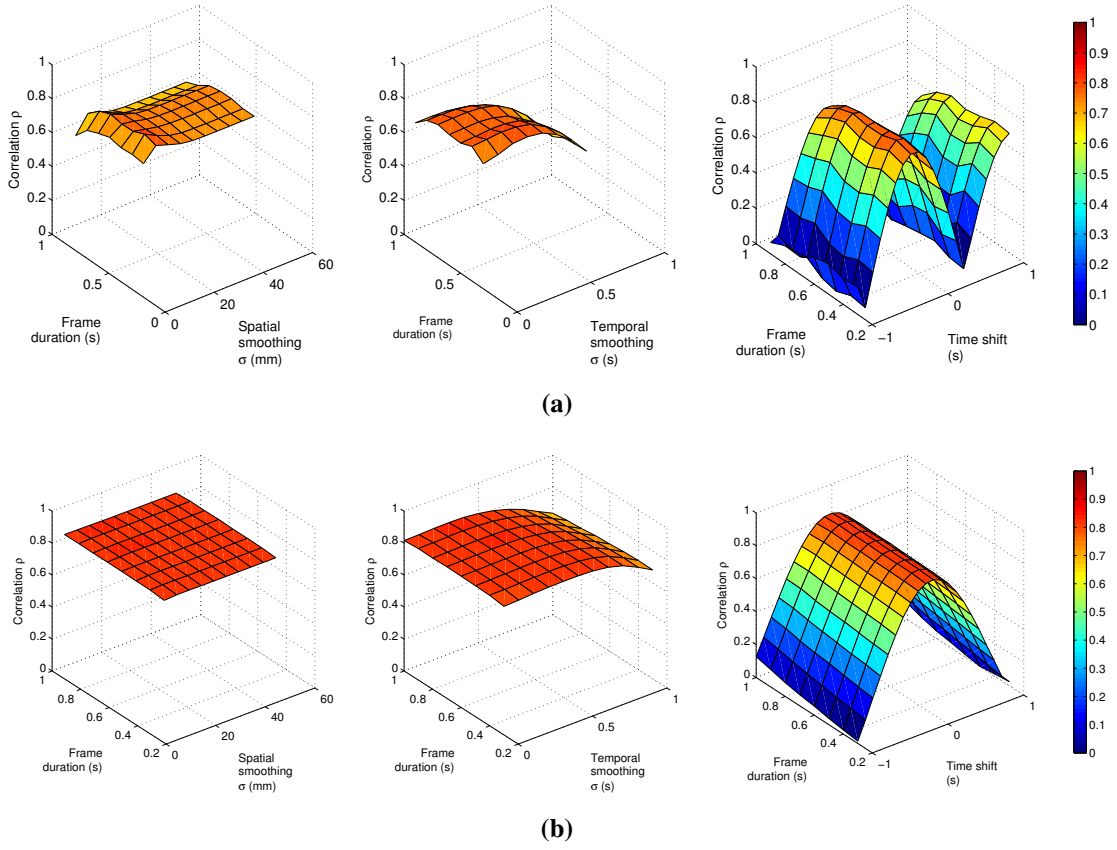


Figure 4.4: Effect of parameter variations on correlation between MR and PET-derived signals, for (a) patient 2 and (b) patient 7.

4.6.2 Parameter Choice

The table shows variation in parameters used to maximise correlation between MR and PET-derived signals, but some parameters have more effect than others. Figure 4.4 shows how correlation $\rho_{p,m}$ varies by plotting against frame duration and each other variable for patients 2 (4.4a) and 7 (4.4b). Spatial smoothing of the sinograms has little effect on both data sets, whilst too much temporal smoothing of the signal decreases $\rho_{p,m}$. Patient 2 has a shorter respiratory period cycle (~ 1 s) than patient 7, so high frame durations cause a slight decrease in $\rho_{p,m}$ as intra-cycle motion cannot be captured. Time shift affects $\rho_{p,m}$ the most, with patient 2 showing periodic changes in $\rho_{p,m}$ as the signals roughly re-align with every ~ 1 s shift.

4.6.3 Gating comparison

For each patient, PET data were binned and reconstructed into 5 gates based on both the MR and PET- derived signals, using amplitude and phase gating. Figure 4.5 shows the PET reconstruction and the same VOI extracted from each gated reconstruction

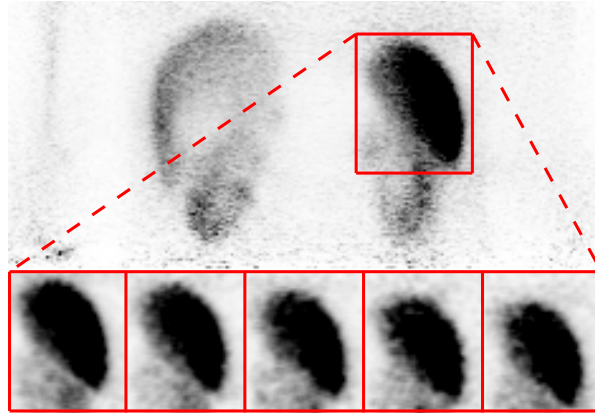


Figure 4.5: Uncorrected PET reconstruction from patient 8 (^{68}Ga -DOTATATE) with VOI extracted from 5 gates.

for the amplitude gating regime based on the PET-derived signal for a patient with high ^{68}Ga -DOTATATE uptake in the spleen. Each of gates 2-5 were registered to the reference gate (chosen as gate 1 - exhale). The separate x (AP), y (lateral) and z (SI) displacements needed to align the gates are displayed in figures 4.6a (amplitude gating) and 4.6c (phase gating). Figures 4.6b and 4.6d show respective total displacements between each gate and gate 1.

The maximum displacements recorded between gates for each patient are displayed in 2 bar charts; figures 4.7a (amplitude gating) and 4.7b (phase gating). Both gating methods gave comparable results for inter-gate displacements by registration between PET (red) and MR (blue) signal based gating schemes over all nine patients.

4.7 Discussion

We have demonstrated that a respiratory signal can be obtained from raw PET data, comparable with a 'gold-standard' MR pencil-beam navigator. Table 4.1 shows the applicability of the technique, with good results from two tracers, and range of moving anatomies and maximum displacements measured by registration.

Variation in the optimal frame duration, spatial smoothing and temporal smoothing parameters in forming the PET-derived signal showed optimal correlation results were found with different parameter values across all patient data sets. There was not enough data to draw conclusions on correlation between these values and other data variables such as count rate. Although table 4.1 shows a variation in the optimal values of the

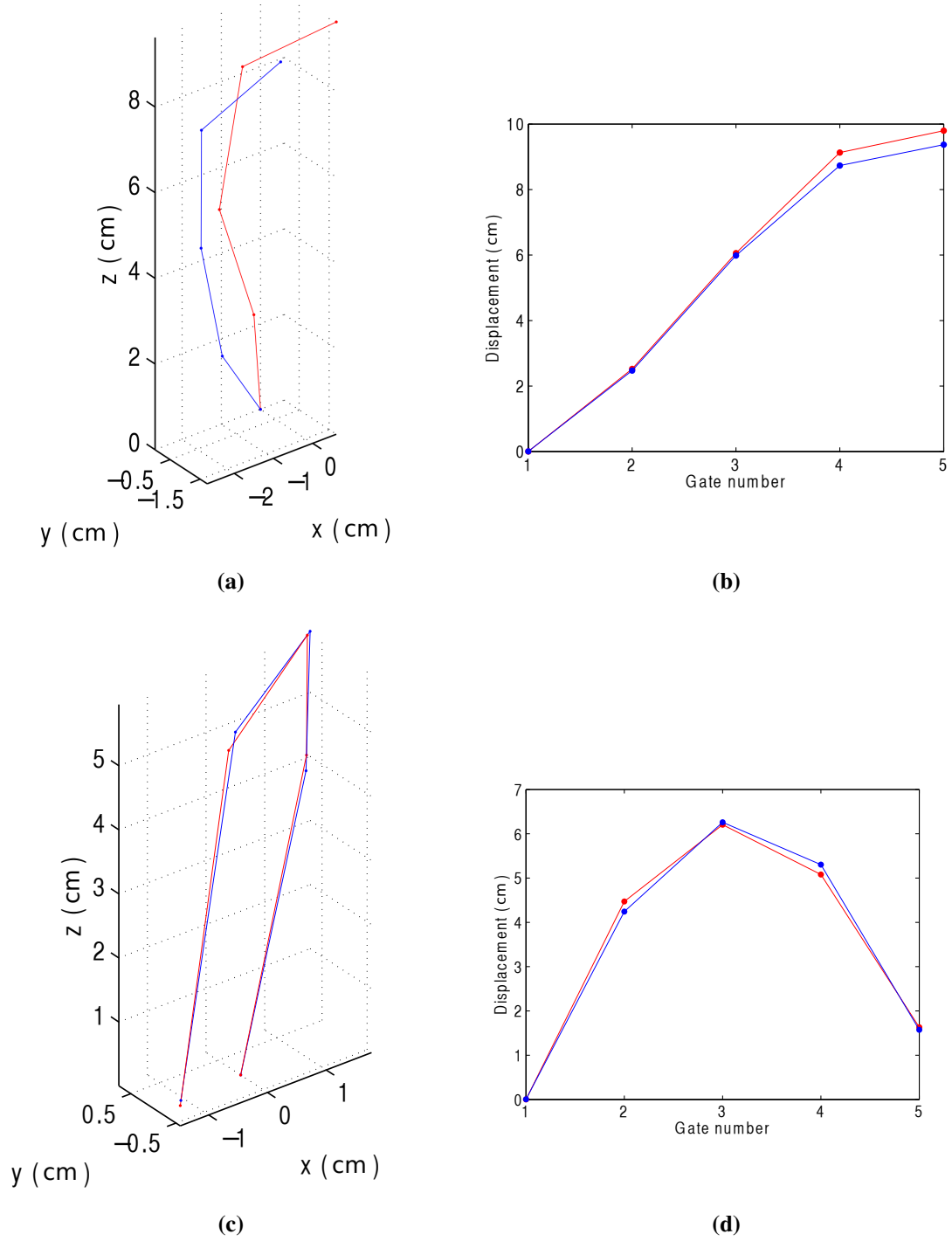


Figure 4.6: Rigid displacements between 5 gates for PET (red) and MR (blue) -based gating schemes - (a) Amplitude gating - x,y,z displacements, (b) Amplitude gating - total displacements, (c) Phase gating - x,y,z displacements, (d) Phase gating - total displacements.

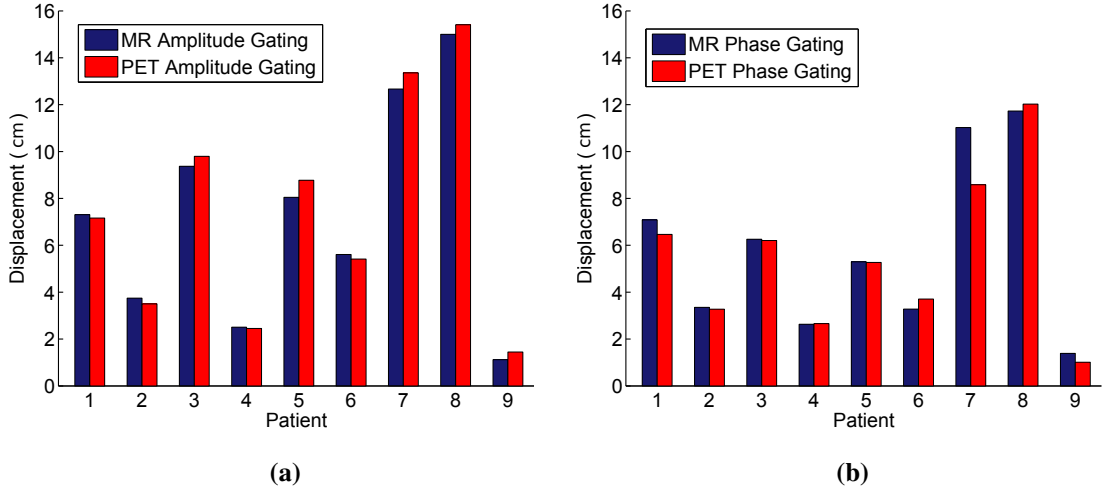


Figure 4.7: Maximum inter-gate displacements found by gating (with 5 gates) per patient with MR and PET derived signals via, (a) Amplitude Gating, (b) Phase Gating.

tested variables, the variation in correlation depending on parameter choice is minimal and, therefore, a decision was made to choose values in the middle of the ranges (frame duration = 0.4 s, spatial smoothing $\sigma = 10$ mm, temporal smoothing $\sigma = 0.2$ s) to extract the signals in the following chapters. These results also showed that choosing the correct time shift δ was important, and this will need to be found for each patient scan independently in subsequent work. The results also show that gating of data based on PET and MR derived signals give comparable results.

The work with the pilot study showed with limited data, that the PET derived signal gave comparable results to a respiratory cushion based signal. It also reiterated the fact that careful setup of the cushion is essential for it to work, and as this can take up to five minutes, it is not a practical solution for motion tracking of clinical patients when scanner throughput is large.

Using a signal derived from PET data has possible advantages and disadvantages. It could be seen as a superior measure of respiration as it measures internal anatomy warping rather than just stimuli from the outside of the body such as measured with a pressure cushion or sensors. This can be a positive as sometimes during respiration the chest/belly surface can move out of phase with the diaphragm [Gierga et al., 2005]. One limitation of assessing the PET-derived signal by comparison with diaphragmatic displacement is that a moving region such as a lung lesion may not correlate directly with the diaphragm. However, this could be a positive if the signal is derived from a

moving area to be motion corrected, and as long as any signal is derived from respiration, it could still be used to track motion and split data into respiratory states.

Overall, the work in this chapter provides sufficient grounding for use of the PET-derived respiratory signal for respiratory tracking, and will be used in the following chapters to bin data, and build motion models.

Chapter 5

Simple MR Image-based PET Respiratory Motion Correction

5.1 Motivation

The aim of this chapter is to introduce a methodology for a simple, MR image-based motion-compensated PET reconstruction. We use our PET-derived respiratory signal, validated in Chapter 4, to bin MR imaging data into separate respiratory states, then find deformations between states. We then use this deformation information directly in the PET reconstruction to reduce the effects of respiratory motion.

This chapter will cover the full methodology, from data acquisition, MR and PET data processing and binning, and deformation field formation with non-rigid registration, to PET data corrections such as randoms, scatter and attenuation, and finally motion-compensated PET reconstruction. We also consider the choice of MR acquisition used to model motion. The method presented here uses only standard MR sequences and image registration techniques, to keep the approach practical and anatomically general, applicable to any type of thorax/abdomen related motion caused by respiration e.g. lung/liver/pancreatic lesions and cardiac data.

In this chapter, we model motion by splitting the respiratory signal into a discrete number of bins, as this is a simple method to use whilst testing a new set of computational tools. Using this patient-specific 'discrete motion model', PET data of any duration can be motion-corrected, although usually durations of three, five or 15 minutes in a clinical setting. We aim to test the feasibility of using a short 1 minute additional PET/MR acquisition to build a patient-specific respiratory motion model to

motion-correct the clinical PET data acquired earlier during the same patient scan. An additional four minute acquisition at the end of the scan was used, including MR sequences for validation and test purposes and enough dynamic MR data to build two motion models: one with 2 min 40 s of MR data ($\text{model}_{\text{long}}$) and one with only one min of MR data ($\text{model}_{\text{short}}$). This allowed us to test the performance of our motion correction methodology with two hypotheses: First, that motion captured by the full dynamic MR sequence ($\text{model}_{\text{long}}$) can successfully motion-correct simultaneously acquired PET data ($\text{PET}_{\text{model}}$), where acquisition duration is long enough to ensure good count statistics in PET. Second, that only one minute of the MR sequence ($\text{model}_{\text{short}}$) is required to capture enough motion to motion-correct PET data acquired earlier during the clinical scan ($\text{PET}_{\text{clinical}}$) (in our case with an interval of up to one hour between acquisitions).

The steps below outline the workflow of data from acquisition to reconstruction. All steps will be explained in detail throughout this chapter. A pictorial description is presented in Figure 5.4.

1. Acquire 4 min PET-MR sequence.
2. Extract respiratory signal from raw PET data.
3. Form 10 bin binning scheme.
4. Unlist raw PET data into 10 gates according to step 3.
5. Bin dynamic MR slices according to step 3, select 1 exhale image per bin.
6. Perform non-rigid registration between MR bin slices and exhale image to provide binned deformations.
7. Calculate 3D deformation fields with binned deformations.
8. Warp μ -map to form 10 gated μ -maps.
9. Motion compensated image reconstruction (MCIR).

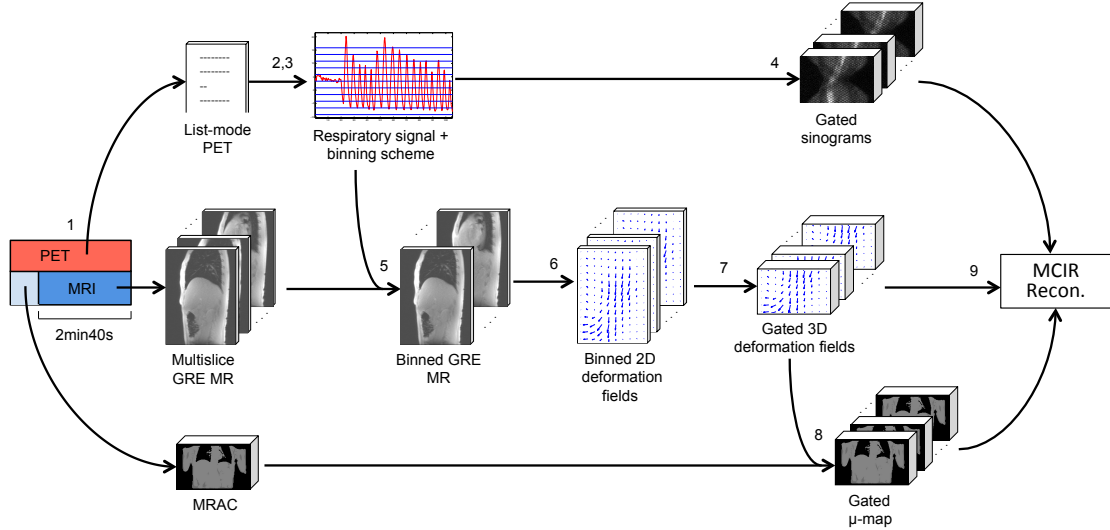


Figure 5.1: Proposed clinical workflow from PET-MR data acquisition to motion incorporated PET reconstruction.

5.2 Choice of MRI sequence

To capture respiratory motion, various MR sequences were tested on the scanner to obtain good contrast in all anatomies of interest such as lung, liver and pancreas. A sequence was desired that would provide good images in all areas of the thorax and abdomen, to allow the same general sequence protocol to be used on all patients, independent of the specific anatomy of interest.

In MRI, a trade off exists between spatial and temporal resolution. High spatial resolution is desirable in order to capture detail in moving anatomy, but this is at a cost in temporal resolution. For example, a detailed image could be acquired with high spatial resolution, but if it takes too long to acquire then there will be intra-frame motion, where motion occurs during image acquisition. A good temporal resolution is required in order to capture a 'static' image so motion can be found between images during free-breathing. Ideally, for motion modelling, a 3D sequence would be used to capture a full imaging volume, but there is again a spatial-temporal resolution trade off. Figure 5.2a shows a slice from a 3D image volume, with high spatial resolution, but takes around 18 seconds to acquire, which is too long to avoid intra-frame motion during free-breathing. With imaging parameter changes, a volume could potentially be acquired in under one second but this would have a much lower spatial resolution, meaning it would not contain enough detail to be useful for motion capturing. It is for these reasons that we decided to use 2D imaging - to acquire high resolution images

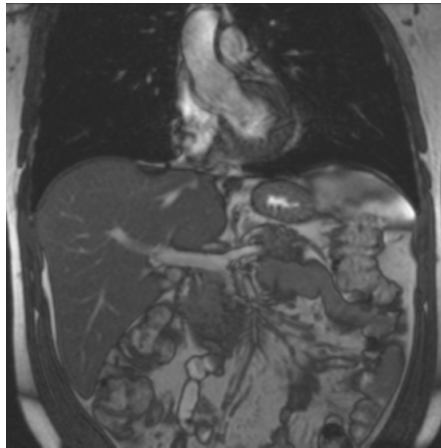
quickly.

The Siemens TrueFISP (True Fast Imaging with Steady state Precession) sequence was tested first, as this has very good tissue contrast. TrueFISP is a balanced sequence, which gets signal from the current longitudinal magnetisation, as well as the previous transverse magnetisation. The use of balanced gradients refocuses both components simultaneously. Figure 5.2a shows a coronal slice from a full 3D TrueFISP breath-hold image volume, and Figure 5.2b shows a 2D TrueFISP image. Both have good contrast in the lung and liver, with blood vessels visible in both. These features are useful for image registration. However, the 2D TrueFISP is susceptible to flow artefacts at 3T, so 'flashing' caused by the pulsatile in-flow of unsaturated blood due to the cardiac cycle is visible, as seen in Figure 5.2c. Artefacts like this will degrade the subsequent registration results, resulting in inaccurate deformation fields. Balanced sequences also give rise to "banding" artefacts due to magnetic field inhomogeneities. These bands do not necessarily move with the tissue so can also lead to inaccurate motion determination.

The GRE (Gradient Echo) MR sequence was then examined. This sequence uses a frequency encode gradient twice quickly in opposite directions. First it is used to apply a dephasing gradient, then to apply a frequency encoding (readout) gradient. By using a low flip angle, a pseudo steady state with measurable transverse magnetisation can be achieved with repetition times of the order ms, even though the tissue T1 recovery time is of the order 1 s. Figure 5.2d shows an example of a GRE image, whilst Figure 5.2e shows the image that is acquired during a heart beat. Due to the quick acquisition time (300 ms as opposed to 500 ms for the TrueFISP) and the fact that signal is collected from only the previous RF pulse, the only side effect from cardiac blood flow is a brightening of the vessels, with no unwanted image artefacts. This means that GRE images should provide better co-registrations than TrueFISP images.

A temporal resolution of 300 ms for the GRE sequence ensures a good temporal-spatial resolution trade off, where intra-frame motion is minimised and inter-frame motion is captured. All sequence parameters for the TrueFISP and GRE sequence were optimised with human volunteers and the parameters that were used to produce the images shown are provided in Table 5.2.

Although test images are presented in the coronal plane, the sagittal imaging plane



(a)



(b)



(c)



(d)



(e)

Figure 5.2: Selection of tested MR sequences. (a) 3D TrueFISP, (b) 2D TrueFISP, (c) 2D TrueFISP at cardiac contraction, (d) 2D GRE, (e) 2D GRE at cardiac contraction.

	TrueFISP	GRE
Echo Time	1.5 ms	2.18 ms
Repetition Time	491 ms	4.8 ms
Pixel Size	$1.9 \times 1.2 \times 10$ mm	$1.6 \times 1.6 \times 10$ mm
Pixel Bandwidth	1028 Hz	965 Hz
Flip Angle	35°	10°
Temporal Resolution	0.5 s	0.3 s

Table 5.1: Overview of MR sequence parameters for TrueFisp (True Fast Imaging with Steady state Precession) and GRE (Gradient Echo) sequences.

was then chosen to be used for motion modelling as most motion due to respiration occurs in this plane (see Section 3.2).

5.3 Data Acquisition

5.3.1 Patient Data

Data were acquired on four patients undertaking clinical PET/MR scans, covering a range of diseases and tracers (^{18}F -FDG and ^{68}Ga -DOTATATE), and varying length, from multi-bed position whole-body scans to cardiac-only scans (see Table 5.2).

Patient	Sex	Age (y)	ROIs	Tracer
1	M	41	5 liver lesions, 1 lung lesion	^{68}Ga
2	F	48	4 pancreatic lesions	^{68}Ga
3	M	69	cardiac	^{18}F -FDG
4	M	66	lung/liver edge artefact	^{68}Ga
mean \pm SD		56 ± 14		

Table 5.2: Overview of four patients with varying regions of interest and administered tracer. ^{68}Ga represents ^{68}Ga -DOTATATE.

5.3.2 Protocol

Figure 5.3 shows a typical clinical workflow with the additional acquired 4 minute PET/MR sequences, consisting of:

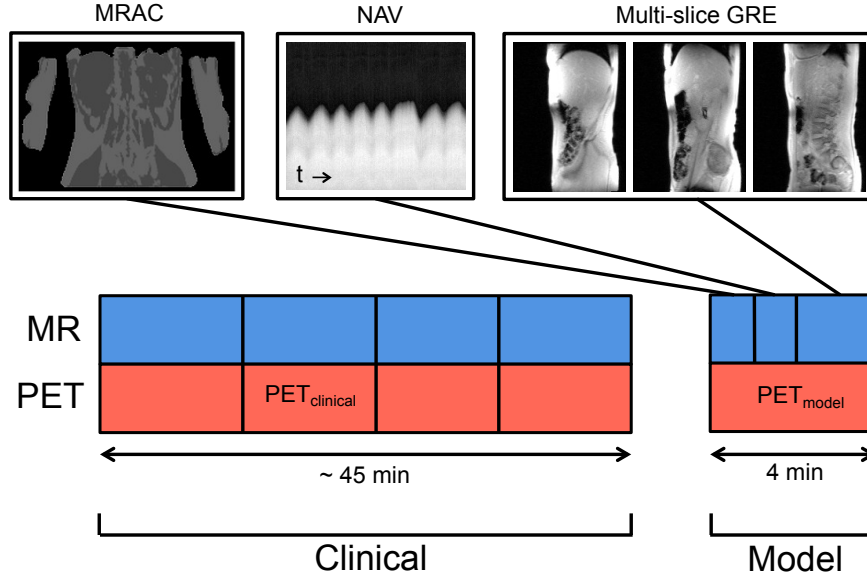


Figure 5.3: Patient data protocol: multi-bed position clinical PET/MR scan, followed by motion model PET/MR sequence: MRAC, pencil beam navigator NAV, and multi-slice GRE sequence.

- PET list-mode - PET_{model} (4 min), in same bed position as previous PET_{clinical} (chosen as the clinical scan bed position affected by respiratory motion).
- MR Dixon (18 s), used by the manufacturer's software to produce an MRAC (MR Attenuation Correction) μ -map, patient instructed to hold their breath at end-expiration.
- MR pencil-beam navigator (30 s), later used to temporally align the PET and MR-derived signals for compensation of differences in PET and MR system clocks.
- MR 2D multi-slice gradient echo (GRE) (2 min 40 s), sagittal slices at nine slice locations, covering the thorax and abdomen (including lungs, liver, pancreas etc.) repeated 60 times. Scan parameters: slice thickness 10 mm, gap between slice centres 25 mm, repetition time 5.1 ms, echo time 2.5 ms, flip angle 10°, pixel bandwidth 965 Hz, matrix size 192×144, FOV 262×349 mm, in-plane resolution 1.8×1.8 mm², IPAT (integrated Parallel Acquisition Technique) 3, acquisition time per image 0.3 s.

5.4 Data Processing

To take the data from PET/MR acquisition to PET reconstruction, many different computational tools and software packages are used. This section outlines each step. The main steps are shown in Figure 5.4.

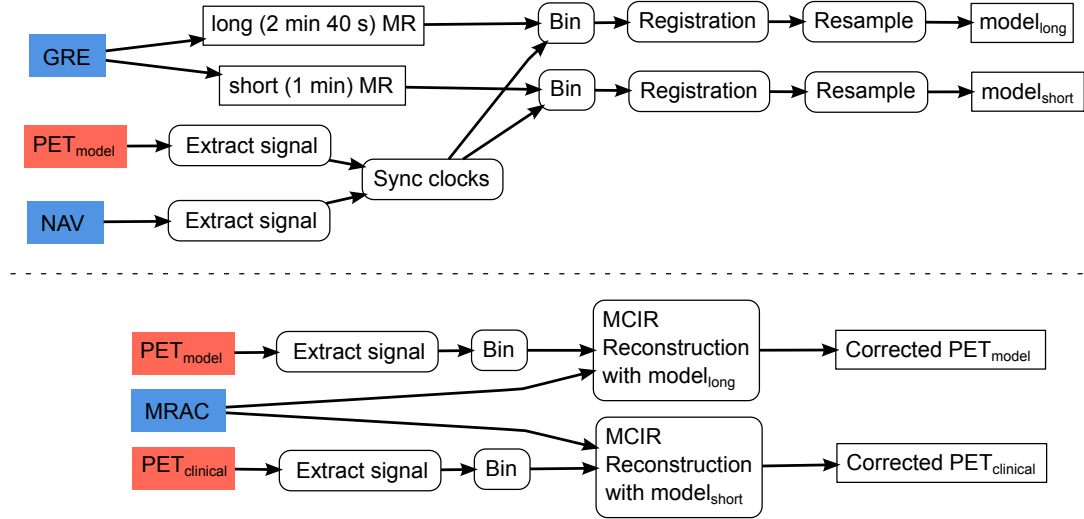


Figure 5.4: Overview of data workflow: building motion models, then using them in PET reconstructions. NAV represents MR pencil-beam navigator.

5.4.1 Respiratory Signal Extraction

A respiratory signal was extracted from the whole 4 minute PET_{model} acquisition with PCA as described in Section 4.2. A signal was also extracted from the MR pencil-beam navigator image as in Section 4.5.2.1 in order to synchronise the timing between the PET and MR systems, by manually aligning inhale peaks by visual analysis.

5.4.2 MR Data Binning

A binning scheme was chosen, using five amplitude bins whilst discriminating between inhalation and exhalation via gradient sign (Figure 5.5), to provide 10 bins. This was chosen as a simple initial method, using amplitude based binning, whilst using an element of phase based binning, to accommodate hysteresis (intra-cycle variation in breathing), which is known to be a normal feature of breathing patterns [Seppenwoolde et al., 2002, McClelland et al., 2013]. The range of signal values at which to bin the data were chosen manually for each patient data set, discarding data that fell outside of the breathing range of the patient during the model-building section of the scan. The MR images were collected at nine different slice locations and first

sorted automatically according to location l , then put into 10 respiratory bins. At each location l and each respiratory bin n , images were averaged; then one image was chosen that minimises the difference between the image and the mean image, to form one image $I_{l,n}$ per location and bin. This method was used to form both $\text{model}_{\text{short}}$ and $\text{model}_{\text{long}}$.

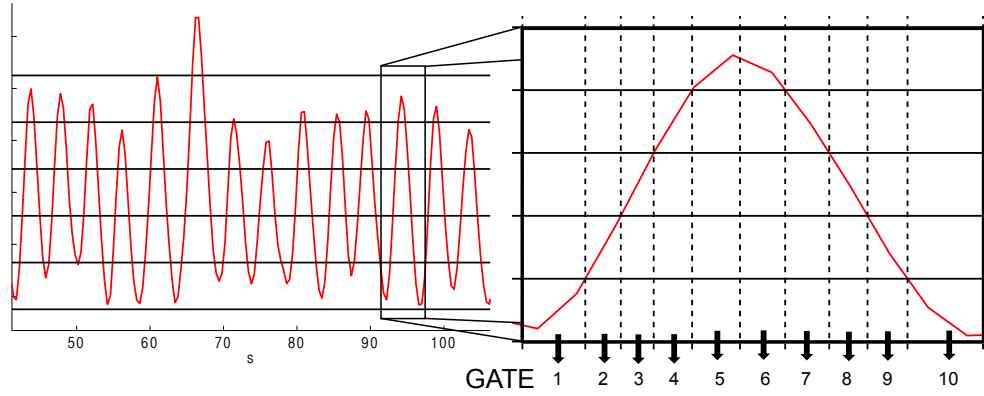


Figure 5.5: Section of respiratory signal showing amplitude based binning and rejection scheme, with a close up of how one respiratory cycle is divided by amplitude and gradient sign.

5.4.3 Deformation Field Formation

The MIRT (Medical Image Registration Toolbox) [Myronenko and Song, 2010] was used in Matlab for registration. This toolbox implements image registration based on many different similarity measures, some intensity based such as sum of squared difference (SSD) and correlation coefficient (CC), and some entropy based such as mutual information (MI). It uses a free form deformation model with cubic B-spline transformation model, with an implicit Euler gradient-based optimisation method. Tuning of parameters such as mesh size of grid control points, and regularisation weight to control displacement of control points is also possible.

In the GRE data sequence, vessel intensity is non-homogeneous throughout the series, and spatial intensity distortions may occur within slices, meaning a cost function that is robust to intensity changes is necessary. Residual complexity (RC) utilises intensity correction between the two images to be registered, which visually showed the most accurate results for GRE MR data, when compared with other similarity measures, providing a degree of robustness to vessel intensity changes and spatial intensity distortions that were present in the GRE MR images. The following

parameters were used: b-spline control point grid size = 5 voxels, λ (regularization weight) = 0.05, and α (trade off parameter controlling the sparseness of coefficients) = 0.01. For cases with very large deformations, λ was reduced to 0.01.

Nonrigid 2D registration with RC was used to find deformation fields $D_{l,n}$ between images $I_{l,n}$ ($n \in 2...10$) and $I_{l,1}$ (exhalation), chosen as the reference image, at each slice location l . Registrations were performed independently to form deformation fields for forward (reference to moving) motion $D_{l,n}$, and to form backward (moving to reference) motion, $D_{l,n}^{-1}$, as both directions will be used in the PET reconstruction. These 2D deformation fields were then resampled into the 3D PET FOV, with linear interpolation used to generate deformation vectors for between-slice voxels. This formed a full forward and backward 3D deformation field for each gate D_g and D_g^{-1} , with a 2D vector at each voxel (the 3rd vector orthogonal to the sagittal plane was set to zero as motion information in this lateral direction was unknown. This process was carried out for both $\text{model}_{\text{short}}$ and $\text{model}_{\text{long}}$.

5.4.4 PET Data Binning

For each patient data set, a respiratory signal was extracted from the $\text{PET}_{\text{model}}$ and $\text{PET}_{\text{clinical}}$ data. Both datasets were then gated using the same scheme as applied to the MR data, meaning PET data that fell outside the range of breathing during the model-building section of the scan was discarded. The binning was performed by unlisting the PET data into 10 sets of emission sinograms. Full 3D PET was used including oblique LORs, with no SSRB. $\text{PET}_{\text{model}}$ data were selected as the 2 min 40 s of PET that was acquired simultaneously to the motion-capturing MR data, and $\text{PET}_{\text{clinical}}$ as the previously acquired clinical PET data at the same bed position. The duration of each PET gate was recorded as a fraction of the total duration of the ungated PET, called duration fraction.

5.4.5 PET Corrections

A number of steps are made before reconstruction to correct for normalisation, randoms and scatter. A normalisation sinogram is acquired every day to account for variations of detector crystal efficiencies. Randoms and scatter estimation was also carried out with STIR, calculated with data from the whole PET acquisition. These were added together and multiplied by the normalisation sinogram to form a background sinogram

for the whole acquisition. This was multiplied by the duration fraction to form 10 gated background sinograms.

5.4.6 Attenuation Correction

A two-point Dixon VIBE MR sequence was acquired, producing in-phase, out-of-phase, water and fat images. Automatic threshold-based segmentation is used with Siemens proprietary software to separate tissues into four classes of air (background), lung, fat and soft tissue [Dixon, 1984, Coombs et al., 1997, Martinez-Möller et al., 2009]. Attenuation coefficients are assigned to each tissue class, producing an MRAC image. Due to the MR FOV being narrower than the PET FOV, the arms are cut off in this MRAC. These truncation artefacts were accounted for with an algorithm for estimating the missing part of this attenuation data from the PET emission data, known as Maximum Likelihood simultaneous Activity and Attenuation reconstruction (MLAA) [Nuyts et al., 2013]. Siemens proprietary software was also used for this step.

Before the original Dixon MR was acquired, the radiographer asked the patient to take a breath in and out, then hold their breath, to acquire an exhale-breath-hold image. However, if the patient did not follow instructions, the acquisition may not be at exhale, so a visual comparison of the MRAC was carried out with the gated MR slices, and the μ -map was assigned to one of bin 1-10. If the μ -map did not align with exhale bin one, an exhale μ -map was formed by warping with the forward motion deformation field. This exhale μ -map was then warped to match the motion states of each respiratory bin by warping with the backward motion deformation fields.

Each warped μ -map was then projected to form an attenuation sinogram, and multiplied by the normalisation sinogram and duration fraction to form 10 attenuation coefficient sinograms.

5.4.7 Motion Compensated PET Reconstruction

Motion Compensated Image Reconstruction (MCIR) was used to form motion corrected PET images with randoms, attenuation, scatter processes and motion incorporated in the system matrix of the reconstruction [Polycarpou et al., 2012, Tsoumpas et al., 2013]. Motion can be added to the MLEM

equation 2.4 (Section 2.1.3.2) by incorporating warping matrices W_g :

$$\hat{f}^{(n+1)} = \frac{\hat{f}^{(n)}}{\sum_{g'} W_{g'}^\top H^\top 1} \sum_g W_g^\top H^\top \frac{p_g}{HW_g \hat{f}^{(n)} + B} \quad (5.1)$$

where W_g are warping matrices defined by the deformation field D_g and the interpolation [Jacobson and Fessler, 2003]. With the method of Tsoumpas et al [Tsoumpas et al., 2013], W_g^\top is approximated as the backwards warping matrix W_g^{-1} .

This process was carried out with an OSEM reconstruction algorithm in the STIR software, with 21 subsets, 5 iterations and 4 mm Gaussian post-filtering. The MCIR method is chosen over Reconstruct-Transform Average (RTA - where each frame is reconstructed separately then images are warped back to the reference state and averaged) as it has been shown that MCIR is superior in terms of quantification, as long as noise is treated with post-filtering [Polycarpou et al., 2012]. Both PET acquisitions were reconstructed with and without motion correction. PET_{model} was corrected with deformation fields from $\text{model}_{\text{long}}$, and PET_{clinical} was reconstructed with deformation fields from $\text{model}_{\text{short}}$.

5.5 Analysis

Quantifying the performance of motion correction in real data is difficult, without the reference standard available with phantom and simulation studies. It is therefore common to use measures that suggest a positive effect of motion correction, such as an increase in sharpness of PET-avid ROIs, correlating with an increase in voxel intensities or SUV metrics. This problem is revisited in Chapter 8.

Motion-corrected images were therefore compared to uncorrected images visually, with line profiles, and quantitatively with changes in SUV in a ROI containing areas of high tracer uptake. Measures used were SUV_{max} , and SUV_{peak} . Focal lesions were identified and highlighted by a PET accredited radiologist from the original clinical images of the PET/MR study.

5.6 Results

First the methodology was tested on patient 1, just acquiring PET_{model} and applying motion correction with deformation fields from $\text{model}_{\text{long}}$. There was an increase in

Patient	Lesion	PET _{model}		PET _{clinical}	
		$\Delta\text{SUV}_{\text{peak}}$ (%)	$\Delta\text{SUV}_{\text{max}}$ (%)	$\Delta\text{SUV}_{\text{peak}}$ (%)	$\Delta\text{SUV}_{\text{max}}$ (%)
1	1	10.1	17.6	-	-
	2	6.2	2.8	-	-
	3	11.9	48.0	-	-
	4	14.6	24.9	-	-
	5	7.0	9.3	-	-
	6	16.9	22.0	-	-
mean \pm SD		11.1 \pm 4.2	20.8 \pm 15.6		
2	1	31.9	42.9	25.0	49.7
	2	9.9	13.9	8.7	4.5
	3	36.9	57.1	29.8	36.1
	4	13.7	24.0	6.9	8.4
mean \pm SD		23.1 \pm 13.3	34.5 \pm 19.3	17.6 \pm 11.5	24.7 \pm 21.8

Table 5.3: Increase in SUV_{peak} and SUV_{max} in PET_{model} and PET_{clinical}, for lesions in patient 1 (multiple liver/lung lesions) and patient 2 (multiple pancreatic lesions).

SUV_{peak} and SUV_{max} across all six lesions, whilst Figure 5.6 demonstrates increased sharpness in a selection of these lesions with line profiles.

For patient 2 with 4 pancreatic lesions, PET_{model} and PET_{clinical} were acquired and corrected with model_{long} and model_{short} respectively. Increase in SUV_{peak} and SUV_{max} in lesions in patients 1 and 2 are given in Table 5.3.

Figure 5.7 shows a comparison of uncorrected/corrected reconstructions in both PET_{model} and PET_{clinical} for patients 2-4, where PET_{clinical} acquisitions have been corrected with motion information from 1 minute's worth of MR data. The top row shows the uncorrected and corrected reconstruction for patient 2 in PET_{model}. As apparent in line profiles through one lesion in both PET_{model} and PET_{clinical}, blurring in the original images has been reduced in the motion-corrected images.

Figure 5.7 middle row shows the uncorrected/corrected reconstruction for patient 3 in PET_{model}. These images show an increase in sharpness and decrease in blurring of the heart. The line profiles through the heart for both PET_{model} and PET_{clinical} also show

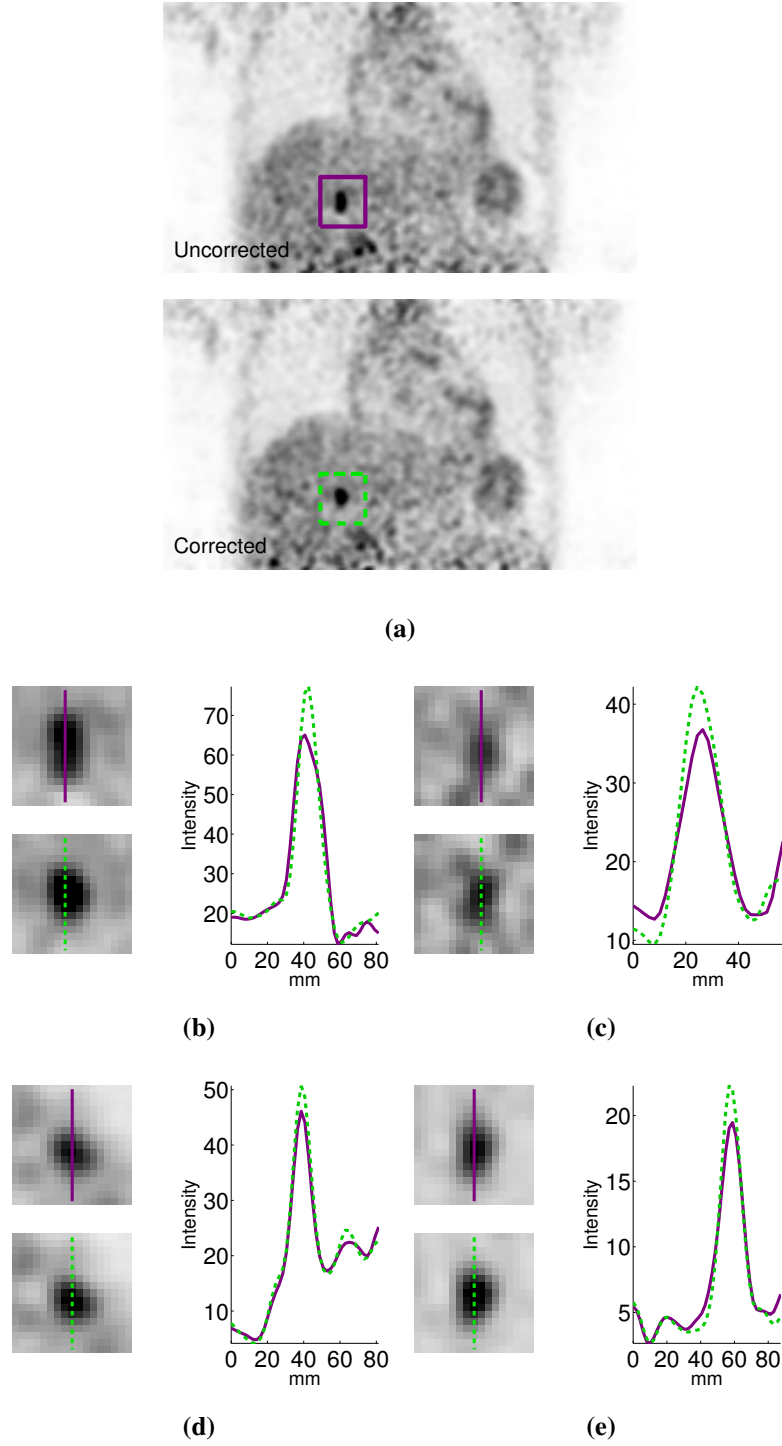


Figure 5.6: Comparison of MR-based motion corrected and uncorrected reconstructions of PET_{model} , where motion fields are taken from $model_{long}$. For each image pair, uncorrected images are top with purple line profiles, and corrected images are bottom with green line profiles. (a) Patient 1 - liver lesions, reconstructions of PET_{model} , with an ROI around lesion 1, (b)-(d) line profiles through liver lesions 1-3, (e) line profile through 1 lung lesion.

this increase in sharpness in motion-corrected images.

Figure 5.7 bottom row shows the uncorrected/corrected reconstructions for patient 4 in PET_{model} , where there are no avid lesions present, but there is a significant motion artefact at the lung/liver edge in the uncorrected image. This artefact, often known as the 'banana artefact', occurs where there is a mismatch in respiratory position between MRAC acquisition and emission data. This can occur when the MRAC is acquired at inhale position, rather than exhale as requested by the radiographer. This artefact is removed due to motion correction as the workflow allows the μ -map to be assigned to the most appropriate gate. The hump marked with arrows on the uncorrected line profiles in PET_{model} and PET_{clinical} show the top of the liver in the μ -map, at different points to the actual top of the liver (in emission data).

Processing time for one motion correction PET reconstruction performed offline (using non-optimised MATLAB code and STIR) was ~ 6 hours in total.

5.7 Discussion

Increases in sharpness and quantitative changes have been demonstrated in PET images with a practical motion correction scheme in a number of patients. These have the potential to improve lesion delineation and quantitation accuracy, and may also contribute to improved lesion detectability. The methodology also demonstrated respiratory artefact reduction, such as evident in patient four at the lung/liver edge, where the common 'banana artefact' is observed.

A possible source of error exists within the choice of MR sequence and registration scheme used for the motion model. By only examining motion in the sagittal plane, we assume no lateral motion during respiration. Motion in this direction has been shown in general, to be as low as 1.2 mm for lung lesions [Seppenwoolde et al., 2002]. For an application of MR motion correction, this could be a source of error as MR can potentially have a much higher spatial resolution (of under 1 mm), whereas PET scanners have a higher typical resolution of around 4.5 mm, so this motion could be considered negligible, considering the application of PET motion correction. A 2D multi-slice acquisition scheme was used to ensure good spatial resolution, but with a gap between slices to keep scan time to a minimum. A full 3D motion model including lateral motion could be found by acquiring

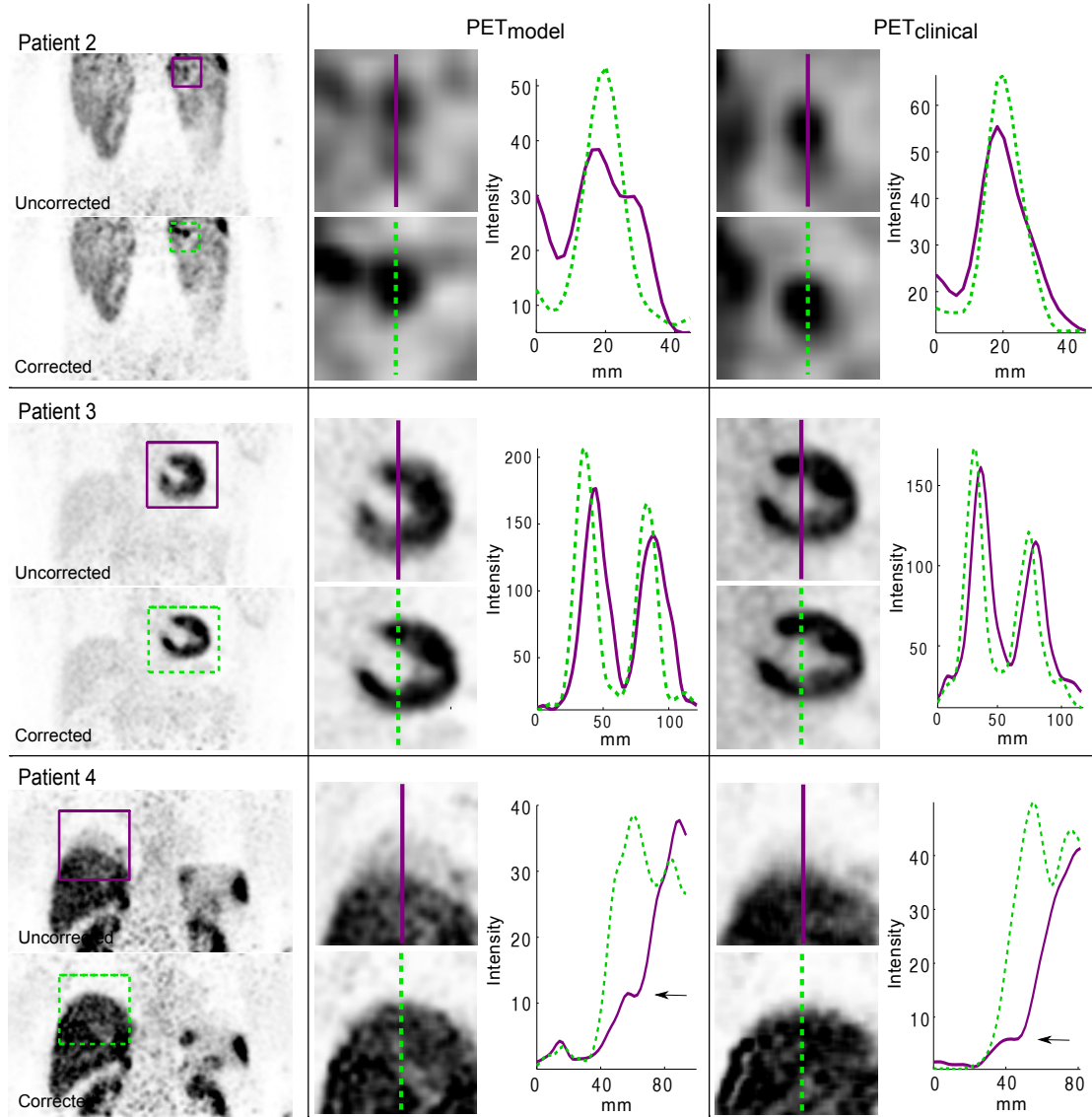


Figure 5.7: Comparison of uncorrected and motion-corrected reconstructions of PET_{model} (column 1), with line profiles through ROIs for PET_{model} (column 2) and PET_{clinical} (column 3) on patients 2-4. For each image pair, uncorrected images are top with purple line profiles, and corrected images are bottom with dotted green line profiles. Arrows in the bottom row show where the liver starts in the μ -map.

contiguous slices [Würslin et al., 2013, McClelland et al., 2014] but this would extend the scan time. A general, easy to use, open-source registration scheme was utilised, which was chosen as a practical method, but it cannot deal with non-diffeomorphic transformations (sliding motion), as would occur between the liver and the ribs. Regardless of these possible limitations of the MR sequence and registration scheme we still see promising results, so we continue to use these in the subsequent chapters as the MR sequence is quick and practical in a clinical setting, and both the MR sequence and registration would be easy to implement in other centres.

We have only examined SUV changes in lesions that were already avid and detected in the uncorrected images by the radiologist. Detectability becomes a more important issue for smaller lesions that go undetected in uncorrected images but have the potential to become visible with motion correction. This will be further explored in Chapter 8.

There are a number of limitations with the methodology presented. The three examples of PET_{clinical} for patients 2-4 were acquired between 50-61 minutes prior to the motion model sequence acquisition. For each patient-specific motion model to be applicable an hour prior to formation, it is assumed that the patient is in the same position in the scanner and breathing style is consistent. Another issue with the respiratory signal is the fact that it is being extracted from two separate PET acquisitions, during the clinical scan then at the end for the motion model building section, and these two signals may not be directly comparable. It is important for the motion model acquired at the end of the scan to be applicable to the respiratory signal gathered throughout the clinical scan. By plotting the two signals for a single patient scan alongside each other it is clear the signals do not have the same amplitude (figure 5.8). As the extracted signals with the PCA method have a zero mean and a scale which is not immediately related to the amount of motion, it is hard to determine whether the drop in amplitude is due to shallower patient breathing, or for another reason, such as a natural drop in count statistics and contrast over time due to washout. With the current methodology, if the amplitude of respiration is larger in PET_{clinical} than PET_{model} then data that falls outside of pre-determined amplitude range are currently rejected, leading to a loss of count statistics.

Only a single respiratory signal was collected, which does not discriminate

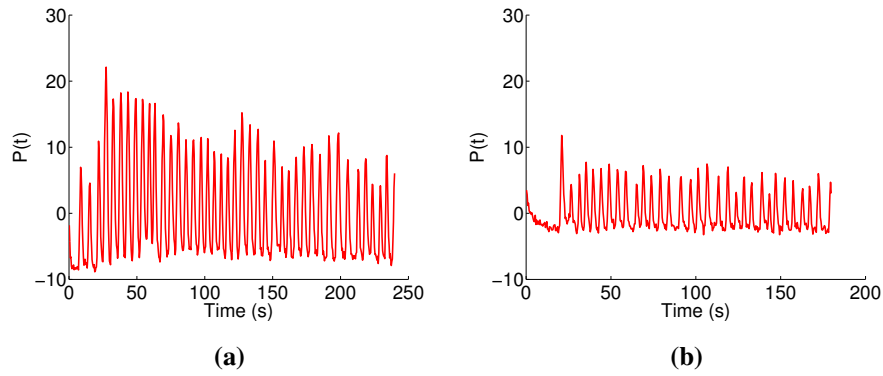


Figure 5.8: Respiratory signals from two acquisitions on one patient, separated by 45 minutes

between types of breathing. Other methods have been proposed in the literature that collect data during different types of breathing to account for inter-cycle variability [King et al., 2012], but this increases scan time and can cause extra patient discomfort by forcing different types of breathing. The motion modelling relies on only one image per bin, which may not be a fair representation of that respiratory state, and if a single registration fails it will affect all data within that bin.

Physical relaxation of the patient laying down in the scanner could cause a slight drift in breathing pattern as a scan progresses. To increase the chances of repeatable respiratory motion, respiratory-affected bed position acquisitions should be acquired after localisers and non-respiratory-affected bed positions (head, neck, etc.), allowing the patient to relax before acquisitions of the thorax/abdomen.

The main issues of using motion information gathered much later after the main clinical scan, only using a single respiratory signal, and relying on one image per bin to represent a whole respiratory state will all be minimised in the next chapter, where a continuous motion model methodology is described.

In this chapter we have proposed a practical, anatomy-independent MR-based correction strategy for PET data affected by respiratory motion, and have shown it can improve image quality for PET acquired simultaneously to the motion-capturing MR, and furthermore for PET acquired earlier during a clinical scan whilst any other free-breathing or breath-hold diagnostic MR is being acquired. Quantitatively, mean increase in SUV_{peak} and SUV_{max} was demonstrated in patients with PET-avid lesions. The method does not require changing the clinical protocol except for an additional short (1 minute) acquisition at the end of a clinical protocol, and with no external

hardware required. We also developed a set of tools required to perform MR image-based PET motion correction, which will be used in the next chapters whilst improving on the methodology.

Chapter 6

Joint PET-MR Respiratory Motion Models

6.1 Motivation

In this chapter we investigate the use of a continuous correspondence model, rather than using discrete MR bins, as in Chapter 5. There are a number of key advantages of using a continuous motion model.

With the previous method, only one MR image was chosen per slice location per respiratory bin, as a representative of the moving anatomy at a certain point in the respiratory cycle. This proved to be sub-optimal because empty bins may occur where no MR image was acquired at a certain slice location within the defined bin amplitude window. Continuous motion models allow all MR images to be used without the need to discard redundant images, and motion estimates can be made with interpolation at any value of the model surrogate, even for surrogate values at which no MR image was acquired. This also means a higher number of PET gates can be used, minimising intra-gate motion, without risking empty bins.

The continuous motion model allows extrapolation, estimating deformation fields at values of the surrogate signal that were not used as input to the model-building sequence, which has two advantages. First, for motion correction with the previous method, any PET data that fell outside of surrogate signal values that were not used during model-building had to be discarded, leading to less counts and therefore noisier images. With the continuous model, all of the PET data can be used in the image reconstruction by model extrapolation. Secondly, the attenuation μ -map can be used

in the PET reconstruction even when the surrogate during acquisition is outside of the normal breathing range. An example of this is shown later in the chapter.

Another advantage of using a continuous motion model is that by not relying on one image per bin, it is more robust to registration errors [McClelland et al., 2013]. With the previous method and binning based schemes, deformation fields that mapped any motion state back to the reference state were provided by a single non-rigid registration. Now with a continuous model, all MR images are registered back to a reference image and all deformation fields are used in the model. This means if any single registration fails, it has little effect on the overall model performance. Extra care is taken in the fitting method chosen to make sure failed registrations do not have a detrimental effect on the model, which is explained later in the chapter.

Additional methodology is also described in this chapter to ensure more practicality in a clinical setting. The PET and MR systems run on two separate clocks, so to temporally align the data, we previously collected extra MR sequences for clock-syncing purposes, as shown in the previous chapter. The time shift and drift between the PET and MR system clocks is now accounted for as part of the optimisation scheme to build the motion model so only one minute of extra data is needed to capture respiratory motion, with no extra sequences acquired for clock-syncing.

Another limitation of the discrete MR binning method from the previous chapter is that it could not accommodate more complicated relations between the motion and the respiratory signal, i.e. hysteresis. Previously, data was put into inhale and exhale states, but with a continuous model we can split data depending on the value of gradient in a continuous fashion, again without risking bins containing no MR data.

6.2 Overview

In this chapter we present a novel methodology to build a patient specific motion model using PET and MR data only. We set up a general framework of the model, then specifically consider four different types of models, using either one or two surrogate signals, with a linear or polynomial model. We also explain the regression techniques used to form the models, and how clock shift and drift are accounted for. To evaluate our method we perform a validation study, applying the PET-MR motion models to

MR data acquired during and outside of the model-building acquisition to test model-fit and model-prediction accuracy on 45 patients. The aim of this study was to find the type of model which can estimate motion most accurately, keeping an eventual clinical application of PET motion correction in mind. Due to the higher spatial resolution of MR data compared to PET, we test the models on a large cohort of MR data first. The use of the models for PET motion correction is covered in the next chapter.

6.3 Data

In order to use real patient data sets as examples to explain the theory described in the coming sections, the data acquisition is briefly outlined here. The same protocol as described in the previous chapter was used again on patients undertaking clinical whole-body PET-MR scans, with only the list-mode PET, MR Dixon and dynamic GRE MR used:

- PET list-mode (4 min).
- MR Dixon (18 s), used by the manufacturer's software to produce an MRAC (MR Attenuation Correction) μ -map, nominally acquired at end-expiration.
- MR 2D multi-slice gradient echo (GRE) (2 min 40 s), sagittal slices at 9 slice locations. Scan parameters: slice thickness 10 mm, gap between slice centres 25 mm, repetition time 5.1 ms, echo time 2.5 ms, flip angle 10° , pixel bandwidth 965 Hz, matrix size 192×144 , FOV 262×349 mm, in-plane resolution 1.8×1.8 mm², IPAT 3. Only data from the last minute of the acquisition are used to form the motion models (model slices) and the rest are for validation purposes (test slices).

6.4 Joint PET-MR Motion Model

The motion models explored in this chapter build on the theory from Section 3.8, but consist of only PET and MR data as input. Four different correspondence models are tested, limited to only one or two surrogate signals and either a linear or polynomial system up to an order of 2. Higher number of surrogate signals and higher model complexity lead to a larger coefficient matrix \mathbf{A} , and this can lead to over-fitting of data and increased risk of extrapolation errors.

6.4.1 PET-derived Respiratory signal as a Model Surrogate

To use our PET-derived respiratory signal as a surrogate for a continuous motion model, equations 4.1 and 4.2 from Chapter 4 need to be re-framed as functions of time rather than discrete frames, such that:

$$\mathbf{s}(t) \approx \bar{\mathbf{s}} + \sum_{k=1}^K \mathbf{w}_k(t) \mathbf{c}_k \quad (6.1)$$

where $\mathbf{s}(t)$ is the sinogram acquired at time t , t is the time at the middle of the frame, $\bar{\mathbf{s}}$ is the mean of all sinograms, \mathbf{c}_k is principal component (PC) k and $\mathbf{w}_k(t)$ is the scalar weight factor for sinogram $\mathbf{s}(t)$, PC k . Our PET-derived respiratory signal is then defined as the weights corresponding to Principal Component $k = 1$:

$$\mathbf{P}(t) = w_1(t) \quad (6.2)$$

and the gradient of the respiratory signal can be approximated as $\mathbf{P}'(t)$.

6.4.2 MR Model Imaging Data

MR images $\mathbf{I}(t)$ can be grouped by slice location $l \in 1 \dots L$, where t represents the acquisition times of slices at slice location l . At each slice location, one reference image \mathbf{I}_r is chosen by binning all images based on the value of the respiratory signal $\mathbf{P}(t)$ to find a single dynamic slice at the 'exhale' position. The same non-rigid registration scheme as described in Section 5.4.3 is used to find voxel-wise deformation fields $\mathbf{D}(t)$, that map each $\mathbf{I}(t) \rightarrow \mathbf{I}_r$. The reverse deformation fields $\mathbf{D}(t)^{-1}$ that warp $\mathbf{I}_r \rightarrow \mathbf{I}(t)$ are found by separate registrations, and are only used in the PET motion correction methodology in the next chapter.

6.4.3 Model Setup

In the case of our PET-MR motion model, the PET-derived respiratory signal $\mathbf{P}(t)$ is the main surrogate, however we also define 'inferred' surrogates such as the gradient $\mathbf{P}'(t)$ and $\mathbf{P}(t)^2$ etc., also as surrogates. Using the gradient as the second surrogate allows modelling of inter- and intra-cycle variation (hysteresis) [Low et al., 2005, McClelland et al., 2013]. The four different models are therefore:

- 1 surrogate linear (1D-linear)

$$\phi(\mathbf{P}(t)) = \mathbf{A} \begin{bmatrix} \mathbf{P}(t) \\ 1 \end{bmatrix} \quad (6.3)$$

- 2 surrogates linear (2D-linear)

$$\phi(\mathbf{P}(t), \mathbf{P}'(t)) = \mathbf{A} \begin{bmatrix} \mathbf{P}(t) \\ \mathbf{P}'(t) \\ 1 \end{bmatrix} \quad (6.4)$$

- 1 surrogate 2nd order (1D-poly)

$$\phi(\mathbf{P}(t)) = \mathbf{A} \begin{bmatrix} \mathbf{P}(t)^2 \\ \mathbf{P}(t) \\ 1 \end{bmatrix} \quad (6.5)$$

- 2 surrogates 2nd order (2D-poly)

$$\phi(\mathbf{P}(t), \mathbf{P}'(t)) = \mathbf{A} \begin{bmatrix} \mathbf{P}(t)^2 \\ \mathbf{P}'(t)^2 \\ \mathbf{P}(t) \\ \mathbf{P}'(t) \\ \mathbf{P}(t)\mathbf{P}'(t) \\ 1 \end{bmatrix} \quad (6.6)$$

where the size of matrix \mathbf{A} is different in each case, depending on the number of surrogates used. The model construction is now explained using the two-surrogate linear model (2D-linear) at only one slice location as illustration. Training data comprising of PET-derived signals $\mathbf{P}(t)$ and $\mathbf{P}'(t)$, and MR-derived deformation fields $\mathbf{D}(t)$, are used as input to the model. Each $\mathbf{D}(t)$ can be split into its constituent

parts $\mathbf{D}^x(t)$ and $\mathbf{D}^y(t)$, and each reshaped into column vectors, such that:

$$\mathbf{D}^x(t) = \begin{bmatrix} d_1^x \\ d_2^x \\ \vdots \\ d_V^x \end{bmatrix}, \mathbf{D}^y(t) = \begin{bmatrix} d_1^y \\ d_2^y \\ \vdots \\ d_V^y \end{bmatrix} \quad (6.7)$$

where V is the total number of voxels in each MR image slice. We define MR acquisitions times as t_n , where n is the MR slice number, $n \in 1 \dots N$, and N is the total number of slices acquired at each slice location. Putting deformation fields at all time points t_n alongside each other in a matrix, this becomes:

$$\mathbf{D}^x(t_n) = \begin{bmatrix} d_{1,1}^x & d_{1,2}^x & \cdots & d_{1,N}^x \\ d_{2,1}^x & d_{2,2}^x & \cdots & d_{2,N}^x \\ \vdots & \vdots & \ddots & \vdots \\ d_{V,1}^x & d_{V,2}^x & \cdots & d_{V,N}^x \end{bmatrix}, \mathbf{D}^y(t_n) = \begin{bmatrix} d_{1,1}^y & d_{1,2}^y & \cdots & d_{1,N}^y \\ d_{2,1}^y & d_{2,2}^y & \cdots & d_{2,N}^y \\ \vdots & \vdots & \ddots & \vdots \\ d_{V,1}^y & d_{V,2}^y & \cdots & d_{V,N}^y \end{bmatrix} \quad (6.8)$$

We denote \mathbf{A}_i as a section of coefficient matrix \mathbf{A} that corresponds to each surrogate signal, for $i \in 1 \dots (k+1)$, where k is the number of surrogate signals. For our 2D linear model, 3 coefficient matrices are therefore used per slice location. Each \mathbf{A}_i can then be split into x and y direction components and reshaped into column vectors:

$$\mathbf{A}_i^x = \begin{bmatrix} a_1^x \\ a_2^x \\ \vdots \\ a_V^x \end{bmatrix}, \mathbf{A}_i^y = \begin{bmatrix} a_1^y \\ a_2^y \\ \vdots \\ a_V^y \end{bmatrix} \quad (6.9)$$

Values of the surrogate signals $\mathbf{P}(t)$ and $\mathbf{P}'(t)$ can then be found at the times of each MR slice at the slice location with linear interpolation:

$$\mathbf{P}(t_n) = \begin{bmatrix} \mathbf{P}(t_1) & \mathbf{P}(t_2) & \cdots & \mathbf{P}(t_N) \end{bmatrix} \quad (6.10)$$

$$\mathbf{P}'(t_n) = \begin{bmatrix} \mathbf{P}'(t_1) & \mathbf{P}'(t_2) & \cdots & \mathbf{P}'(t_N) \end{bmatrix} \quad (6.11)$$

Model coefficients can be found by minimising the least squares fitting error to the training data:

$$\arg \min \left[\begin{pmatrix} D^x(t_n) \\ D^y(t_n) \end{pmatrix} - \begin{pmatrix} A_1^x & A_2^x & A_3^x \\ A_1^y & A_2^y & A_3^y \end{pmatrix} \begin{pmatrix} P(t_n) \\ P'(t_n) \\ 1 \end{pmatrix} \right]^2 \quad (6.12)$$

where the vector $\mathbf{1}$ is a vector of 1s of the same length as $P(t_n)$ and $P'(t_n)$. The expression can also be written in a simpler form by combining all x and y components of vector and coefficient matrices:

$$\arg \min \left[D(t_n) - A \begin{pmatrix} P(t_n) \\ P'(t_n) \\ 1 \end{pmatrix} \right]^2 \quad (6.13)$$

Considering all slice locations, model coefficients A_l can be found at each slice location $l \in 1 \dots L$, where MR acquisition times at each slice location are denoted by t_{nl} :

$$\arg \min \sum_{l=1}^L \left[D(t_{nl}) - A_l \begin{pmatrix} P(t_{nl}) \\ P'(t_{nl}) \\ 1 \end{pmatrix} \right]^2 \quad (6.14)$$

The minimisation can be solved to find each A_l , then new deformation fields \hat{D}_l at each slice location can be estimated using the model with new input surrogate values \hat{p} and \hat{p}' and the model coefficient matrices A_l :

$$\hat{D}_l = A_l \begin{bmatrix} \hat{p} \\ \hat{p}' \\ 1 \end{bmatrix} \quad (6.15)$$

6.4.4 Visualising the Models

Figure 6.1a shows GRE MR slices $I(t_{nl})$ for one slice location $l = 3$ in one patient dataset. The interpolated values of respiratory signal $P(t_{nl})$ at the time of each slice acquisition are marked on the signal. One voxel on each image in the liver is marked with an arrow representing the d^y deformation at that voxel. The scatter plots 6.1b-e

show the d^y deformations of each $D(t_{nl})$ at this voxel, along with the deformations that each of the four models predict at the same voxel. Figure 6.1b shows deformations for the 1D linear model, where the estimated deformations plot a straight line through the real deformations. Figure 6.1c shows deformations for the 1D polynomial model, where the estimated deformations plot a 1st order polynomial line through the real deformations. Figure 6.1d shows deformations for the 2D linear model, where the estimated deformations plot a narrow ellipse through the real deformations, allowing different paths for inhale and exhale (hysteresis). Figure 6.1e shows deformations for the 2D polynomial model, where the estimated deformations plot a curved ellipse through the real deformations. Figures 6.1f and 6.1g show real and estimated deformations against both surrogate signals $P(t)$ and $P'(t)$ in 3D plots for 2D-linear and 2D-polynomial models respectively. The estimated deformations lie on a plane for the 2D-linear model, and on a curved 2D surface for the 2D-polynomial model.

6.5 PET-MR Clock Synchronisation

In the previous chapter, differences in MR and PET system clocks were accounted for by acquiring an extra 30 second pencil-beam navigator MR image to manually synchronise the clocks. To avoid the need for this extra acquisition, and to provide a more accurate synchronisation and therefore better motion correction, the difference in clocks can be accounted for in the optimisation by building it into the model functional.

6.5.1 Clock Drift

First, a constant drift λ between the two clocks was sought, i.e. one clock running at a constant factor slower than the other, within a patient dataset. In Figure 6.2a a respiratory signal $P(t)$ is plotted, with the points marked at which each MR image and deformation field $D(t_l)$ at one slice location is acquired. The deformations d^y at one voxel in each image is marked against the value of the signal in Figure 6.2b, with the colour of each point taken from the colour of the signal at that point in Figure 6.2a. It is clear that as the acquisition goes on and the colour of the signal moves from blue to red, the points which are initially spread move further towards a straight line. When a constant drift factor of $\lambda=0.996$ is applied to the data, all the points fall roughly onto

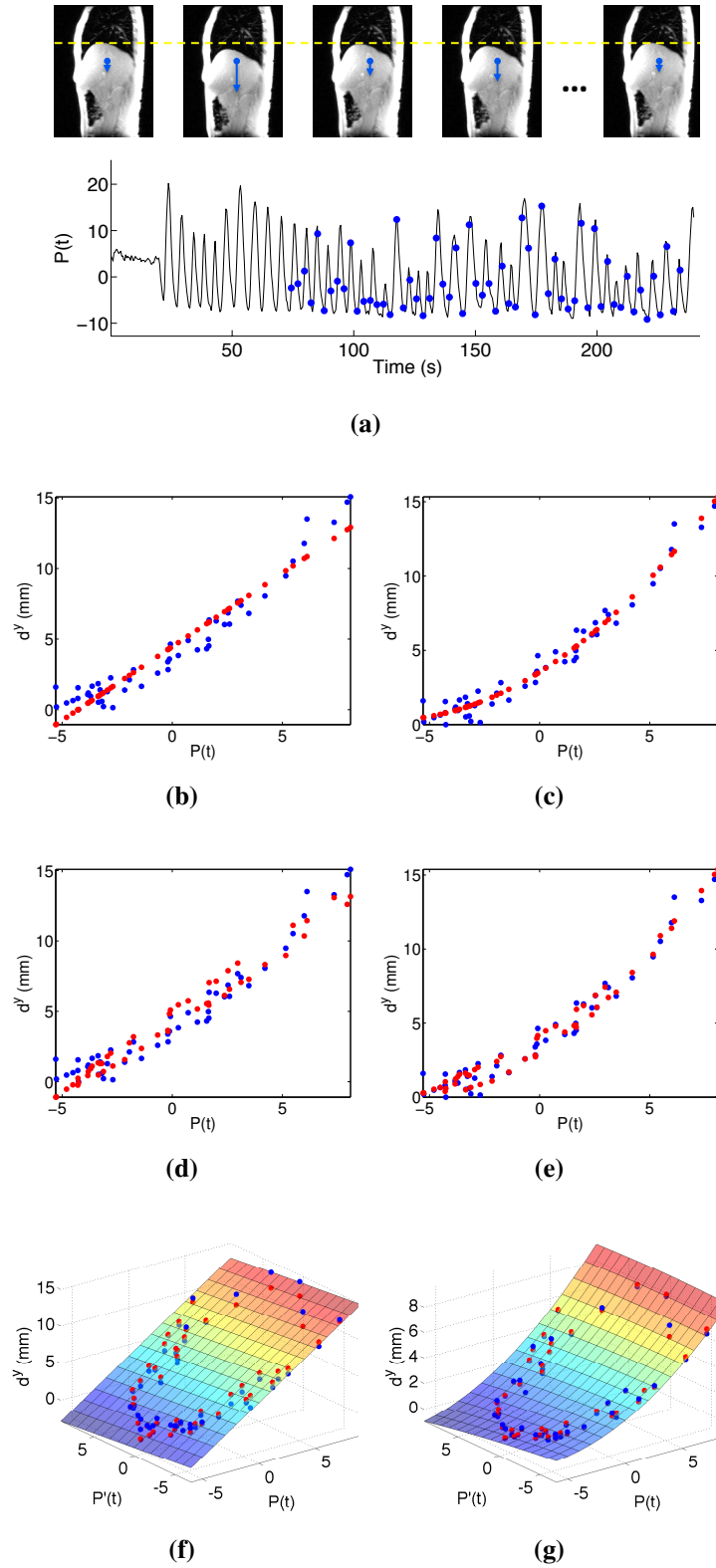


Figure 6.1: Model training data and deformation estimation at one slice location. (a) shows respiratory signal and a single voxel marked on slices with arrows representing the size of d^y . Blue dots are real d^y deformations at one voxel and slice position, and red dots are the model d^y predictions for models b) 1D-linear, c) 2D-linear, d) 1D-poly, e) 2D-poly. f) and g) show 3D plots for 2D-linear and 2D-poly models.

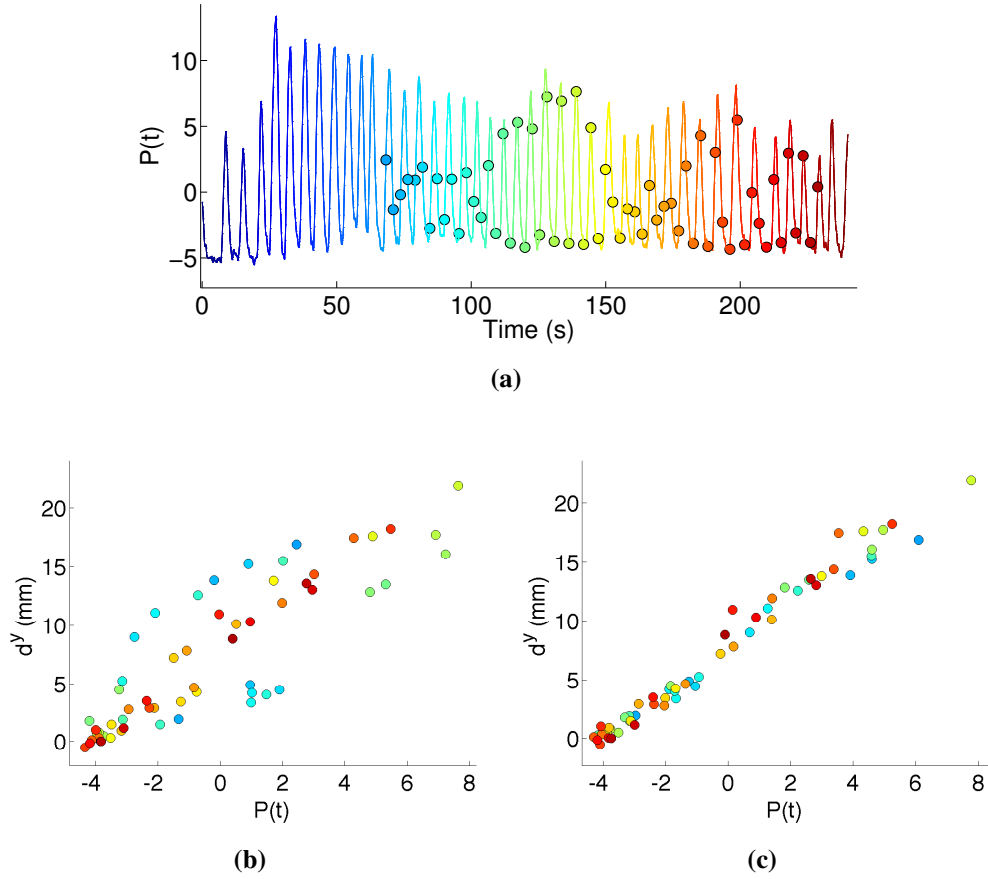


Figure 6.2: Effects of PET/MR clock drift over a 4 minute scan. (a) respiratory signal with marked slice acquisition times, and deformations d^y at one voxel (b) before drift correction and (c) after drift correction.

a straight line (see Figure 6.2c). In this case the MR clock runs 0.4% slower than the PET clock (which equated to almost 1 second slower over a 4 minute acquisition). A clock drift of this order has been confirmed by the manufacturer, and we used this value of $\lambda=0.996$ for subsequent model calculations.

6.5.2 Clock Shift

It is also possible to account for an unknown time shift constant δ between the PET and MR clocks, which is unknown and specific to each scan. It can therefore be included as an unknown in the functional to be minimised by addition to equation 6.15, which now becomes:

$$\arg \min \sum_{l=1}^L \left[D(t_{nl}) - A_l \begin{pmatrix} P(\lambda t_{nl} + \delta) \\ P'(\lambda t_{nl} + \delta) \\ 1 \end{pmatrix} \right]^2 \quad (6.16)$$

The effects of both drift and shift are possible to visualise by plotting deformations against respiratory signal values again. Figure 6.3a plots the deformations d^y and d^x at one voxel at each slice location against the respiratory signal value. Figure 6.3b shows the same plot once a clock shift of $\delta=0.4$ s is applied, and Figure 6.3c shows the same plot once the known drift of $\lambda=0.996$ is also applied.

The minimisation in Equation 6.16 can be solved to find A_l with a nonlinear optimisation. The Matlab function 'lsqnonlin' was used, which uses the interior-reflective Newton method [Coleman and Li, 1996], with constraints, setting an initial starting estimate of $\delta=0$ s and an upper and lower bound of 1s and -1s respectively. These bounds were found to provide a sufficient window, considering results by manually applying synchronising the clocks the work in the Chapter 5. As respiration is cyclic, without these constraints, solutions can otherwise be found at local minima, especially when breathing is periodic and steady.

To provide further evidence that the drift and shift correction improves the motion model, each MR image (model slices and test slices) can be deformed by either estimated deformation fields \hat{D} , or by the deformation fields found via registration, $D(t)$. Figure 6.4 shows dynamic line profiles at two different slice locations through the original uncorrected images, images warped by registration deformation fields, images warped by deformation fields predicted by the model without clock synchronisation, and images warped by deformation fields predicted by the model with clock synchronisation. The 2D-linear model was used for deformation estimation in each case. The two different slice locations are chosen to show a slice through the right lung and liver, and another slice through the left lung and pancreas. The images show on both sides, the extent that clock synchronisation improves the model performance, with a flatter dynamic line profile at the lung/liver interface, and at other interfaces in the abdomen.

6.6 Improving Model Robustness

The example shown above with patient data shows that a motion model can be formed and deformation fields can be predicted, providing an estimate of motion from surrogate signal value alone. In this example, the registration results used to form the model seemed by visual analysis to provide good results. However, in some cases, the

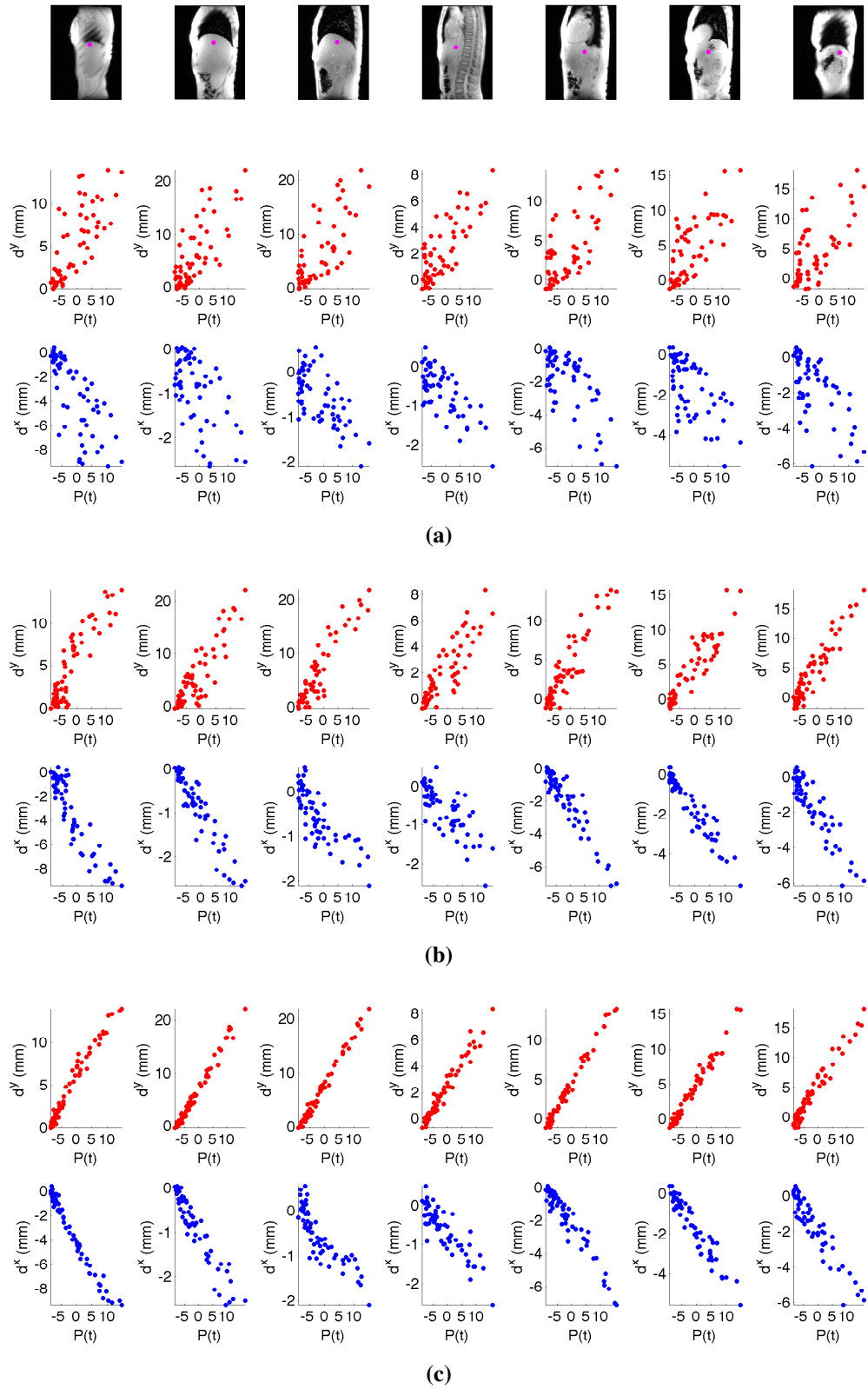


Figure 6.3: Effect of shift and drift correction on d^y and d^x deformation plots. Top row: one voxel marked at each slice location. (a) no corrections, (b) shift correction only, (c) shift and drift correction.

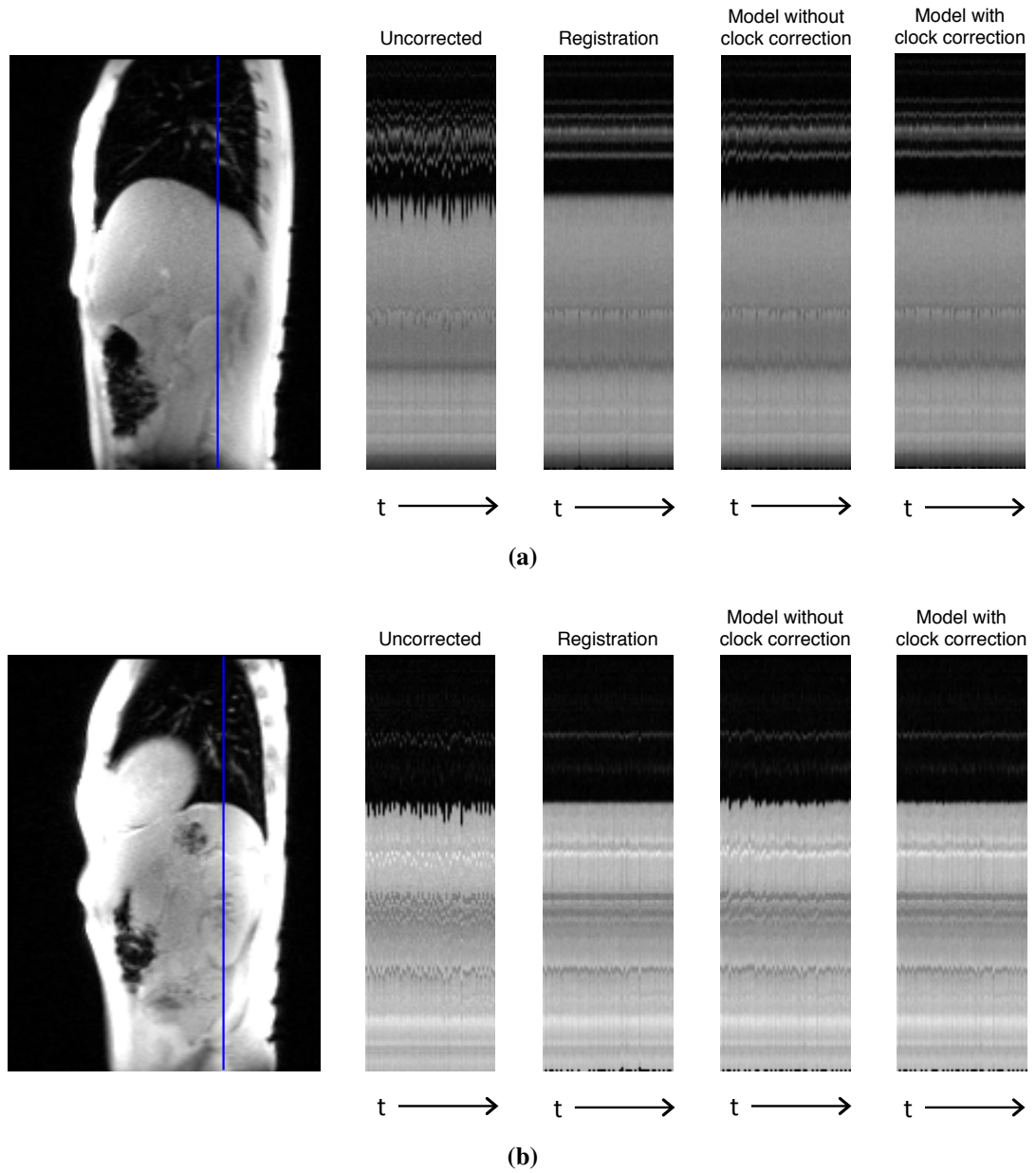


Figure 6.4: Dynamic line profiles through original uncorrected, registered, and model-warped images (with the 2D-linear model), with and without clock synchronisation correction, at two different slice locations in (a) and (b).

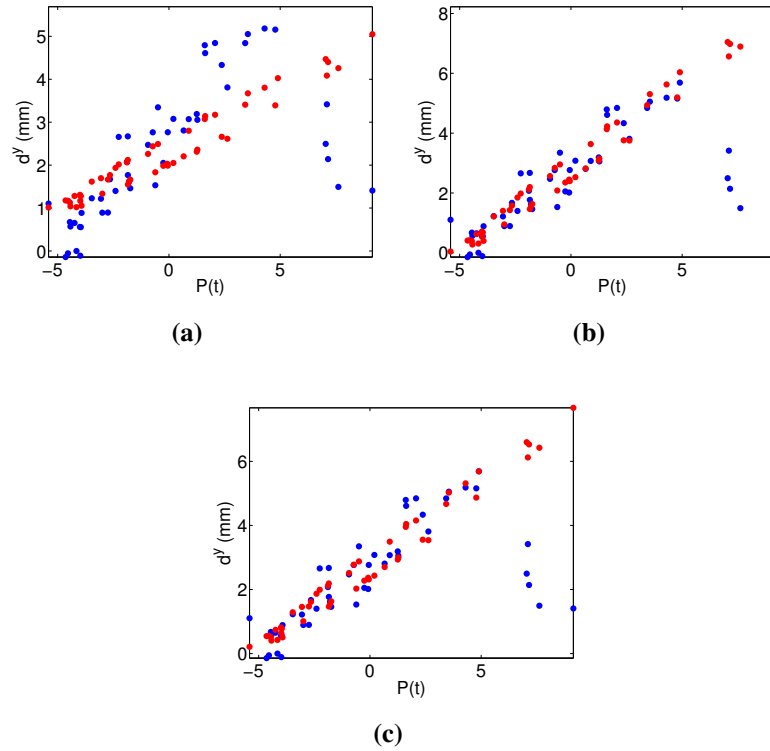


Figure 6.5: Model fitting performance of estimated deformations d^y (red) to registration-based deformations (blue) with different regression schemes - (a) plain least-squares, (b) iterative least-squares with 'bisquare' weighting, (c) iterative least-squares with 'fair' weighting.

registrations can fail, and this can cause problems when finding model coefficients to fit the data and provide the model. In this section, the various regression schemes are explained and tested along with the scheme chosen to make the model robust to registration errors.

6.6.1 Least-squares

Figure 6.5a shows how the model performs with the least-squares method when a registration failure had occurred. The blue points show real deformations d^y (based on registration) at one voxel and one slice location, whilst the red dots show the model-estimated deformations. The blue dots on the right of the plot appear to be outliers, where registration may have failed for images where the respiratory signal is large, i.e. at deep inhale. The least-squares fit to this data considers these points and influences the model-predicted deformations, as can be seen by the skewed estimated deformations. Figure 6.6a shows the model coefficient matrices at each slice location.

6.6.2 Iterative Least-Squares

To fit model coefficients that are less sensitive to outlier data points from registration failures, an iterative reweighted robust multilinear regression scheme with the least-squares equation can be used [Holland and Welsch, 1977]. To test this method, the Matlab function 'robustfit' was used, where weights determine how much each data point influences the coefficient estimates, and good quality data influence the fit more than low quality (outlier) data. The weighting function must be carefully selected. For example a 'bisquare' weighting function can be used:

$$w(r) = \begin{cases} (1 - r^2)^2 & |r| < 1 \\ 0 & |r| \geq 1 \end{cases} \quad (6.17)$$

where r depends on the residual error and error standard deviation from the last iteration. Figure 6.5b shows that this scheme gives a better fit to the data without being affected by outliers, but Figure 6.6b shows that model coefficient matrices are not smooth with this solution. Non-smooth coefficient maps would lead to non-smooth deformation fields, giving rise to unrealistic motions and possible imaging artefacts in resulting PET reconstructions.

Figure 6.5c shows the model fit using a different ('fair') weighting:

$$w(r) = 1/(1 + |r|) \quad (6.18)$$

This also gives a good fit without being influenced by the outliers, and this time provides much smoother coefficient matrices, as seen in Figure 6.6c, and was chosen to be used in our methodology. This weighting is similar to an L1 norm, which is less prone to outliers, unlike the L2 norm, which magnifies their effect.

6.7 Validation Study: Model Comparison on MR data

A validation study was performed using 45 patient data sets. The aim was to find which type of PET-MR motion model performs best when estimating respiratory deformations from surrogate data alone.

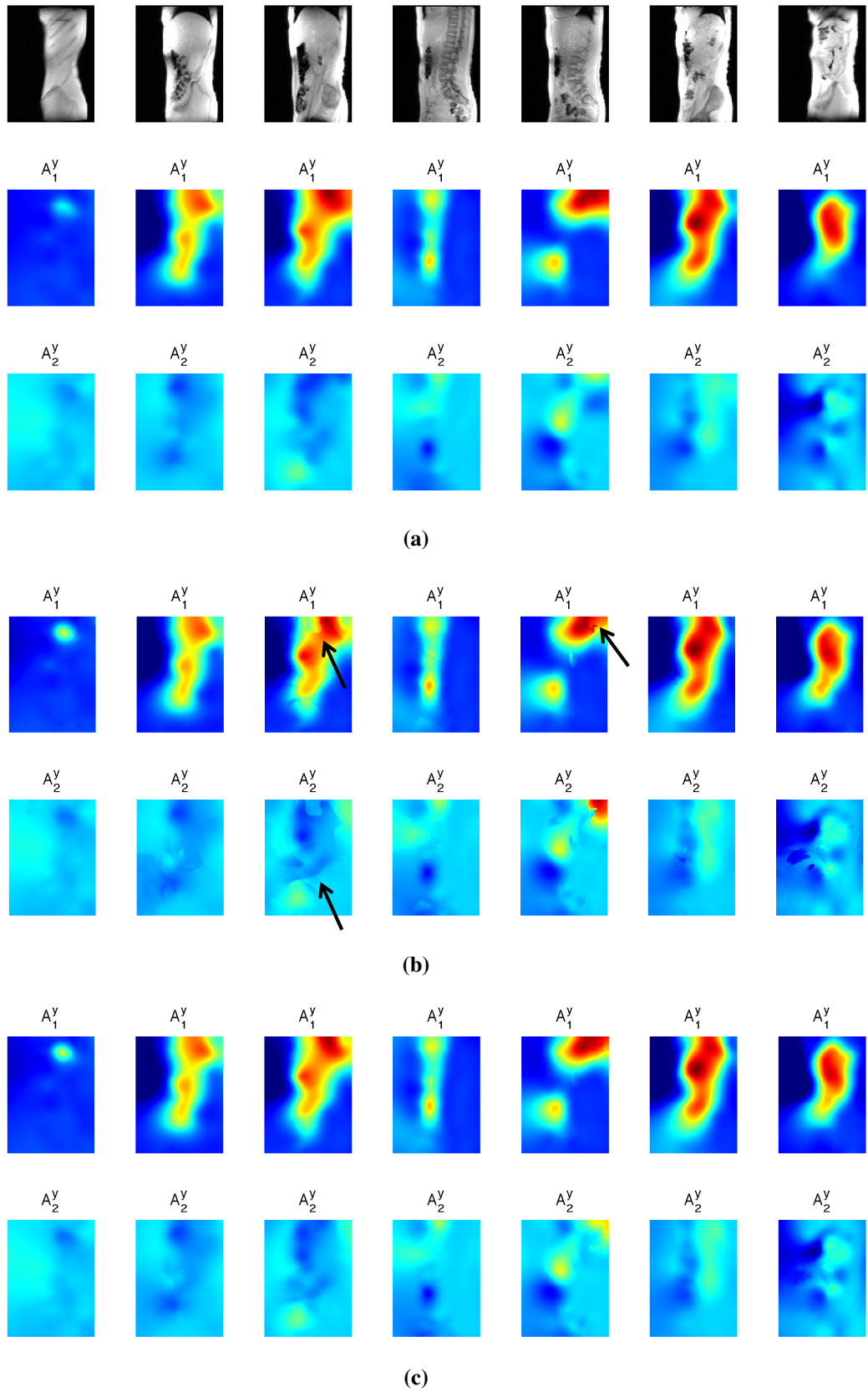


Figure 6.6: Model coefficient images found with the 3 regression schemes - (a) plain least-squares, (b) iterative least-squares with 'bisquare' weighting, (c) iterative least-squares with 'fair' weighting. Arrows in (b) indicate areas of non-smooth coefficients.

6.7.1 Methods

The protocol used is described in Section 6.3. First, a respiratory signal was extracted from the PET data according to equation 6.1, and clock drift correction applied. At each slice location, images were binned based on signal value (as per the methodology in the previous chapter) and a single image from bin 1 was chosen as an exhale reference, $I_{r,l}$, for the registration of all other images. All images I were registered to their slice location reference image $I_{r,l}$ to provide warped images I_w and associated deformation field D , using the same non-rigid registration scheme as described previously. These deformation fields were assumed to provide a 'perfect' registration and so become the reference-standard. Deformation fields \hat{D} were estimated using each type of model. Each image I can therefore also be warped to an estimated 'exhale' position to form image \hat{I}_w .

6.7.2 Analysis

The performance of each model was assessed by comparing results to 'reference-standard' results from registrations i.e. comparing images I_w to \hat{I}_w with mutual information (MI) and sum of squared difference (SSD) metrics, and comparing deformation fields D to \hat{D} by calculating Euclidean distance (ED). The two image based similarity measures MI and SSD were chosen to provide a fair test, with one being an intensity based metric, and the other an entropy based metric (see Section 3.4). All metrics were used to compare how each model performed regarding model-fit error (testing the same 1 minute set of MR images that were used to form the model) and model-prediction error (testing using the set of MR images not used as input to the model - acquired prior to the last 1 minute model-building section).

MI and SSD were explained in Chapter 3, whilst ED is explained as follows. For 2D deformation fields A and B , comprising of vectors $\mathbf{a}_i = [a_i^x, a_i^y]$ and $\mathbf{b}_i = [b_i^x, b_i^y]$, Euclidean distance is described as:

$$ED(A, B) = \|A - B\| = \sum_i \sqrt{(a_i^x - b_i^x)^2 + (a_i^y - b_i^y)^2} \quad (6.19)$$

The performance index $\xi(M)$ of an image-based metric M was defined as percentage improvement by dividing the improvement from model-warping by

improvement from registration-warping:

$$\xi(M) = \sum_n \frac{M(\hat{\mathbf{I}}_w, \mathbf{I}_{r,l}) - M(\mathbf{I}, \mathbf{I}_{r,l})}{M(\mathbf{I}_w, \mathbf{I}_{r,l}) - M(\mathbf{I}, \mathbf{I}_{r,l})} \quad (6.20)$$

where n is the frame number in the set to be evaluated - either test slices or model slices, and M is either metric MI or SSD. A high value of 100% of index $\xi(M)$ shows the model performs as well as registration in predicting the correct warping of all images back to their respective exhale reference images.

When using the ED metric, model-based deformation fields were compared with registration-based deformation fields. The voxel-wise ED was calculated as the sum between each $\hat{\mathbf{D}}$ and \mathbf{D} as absolute values in mm :

$$Mean\ ED = \sum_n \frac{\|\hat{\mathbf{D}} - \mathbf{D}\|}{V} \quad (6.21)$$

where V is the total number of voxels in all frames in the set (either test slices or model slices). A simple thresholding mask was applied to each deformation field so only deformations within the body were included in the analysis.

6.7.3 Statistical Analysis

A Wilcoxon signed rank test was used to test the statistical significance of the results, with a threshold of 0.0001 (99.99% confidence), so p -values below this were considered significant.

6.8 Results

6.8.1 Model Performance: Global Analysis

Figures 6.7 and 6.8 show model performance for each patient in terms of MI and mean ED respectively, for both model-fit and model-prediction. For model-fit error, the 2D-poly model performed best in terms of MI, SSD and ED, in 98%, 93% and 100% of patients respectively. For model-prediction error, the 2D-linear model performed best in terms of MI, SSD and ED, in 82%, 78% and 65% of patients respectively.

Figure 6.9 shows average performance index for all metrics over all 45 patients, in terms of both model-fit (Figure 6.9a) and model-prediction (Figure 6.9b). Overall, for model-fit, the 2D-poly model performed best, and for model-prediction, the 2D-

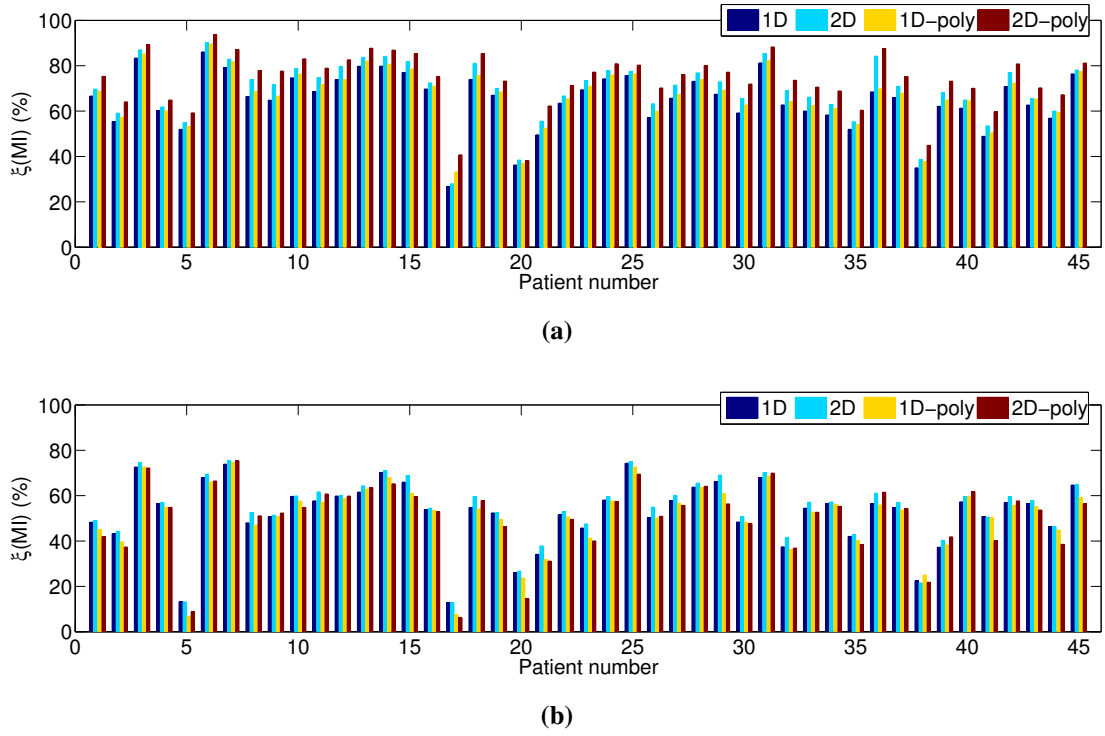


Figure 6.7: Performance index $\xi(MI)$ as a % compared to registration, for (a) model-fit, (b) model-prediction. High values show best model performance.

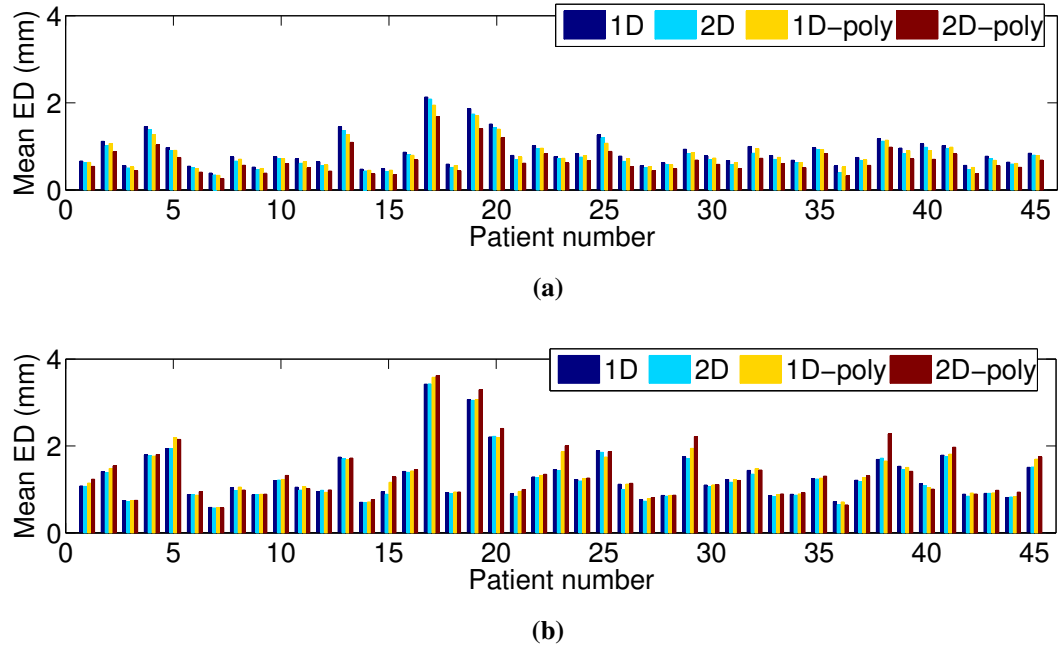


Figure 6.8: Mean voxel-wise Euclidean distance for (a) model-fit, (b) model-prediction. Low values show best model performance

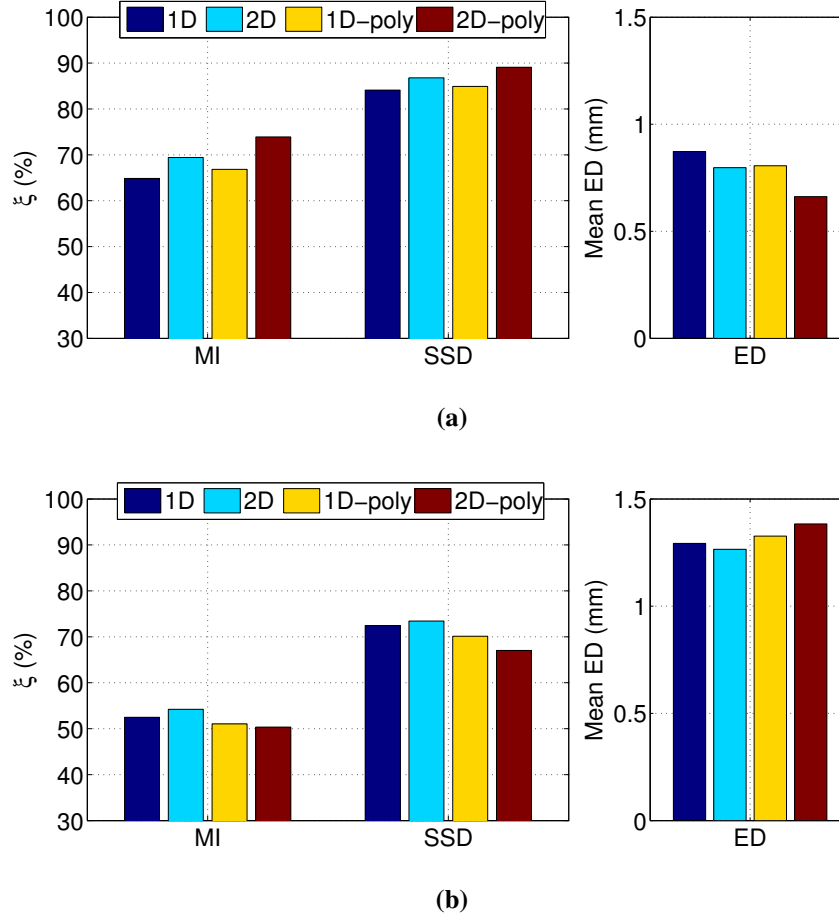


Figure 6.9: Mean performance index ξ for MI and SSD, and mean vector field ED over all 45 patients, (a) model-fit, (b) model-prediction. Good improvement compared to warping by registration is indicated by high values for MI and SSD, and by low values for ED.

linear model performed best, and these were statistically significant ($p < 0.0001$) when comparing with each other model, for each of the 3 metrics.

6.8.2 Model Performance: Spatial Analysis

As can be seen on Figure 6.9a, even when using the image-based metrics on model slices, and using the best performing (2D-poly) model, the model only performed about 74-90% as well as using direct registration. However, as the image-based metrics used were global (across every voxel position at every slice location), it can be expected that a respiratory motion model will not perform well in areas affected by other types of non-respiratory motion. For example, the stomach and bowels are sporadically moving during respiration, but this motion will not correlate with the respiratory signal surrogate that the model is built upon, unlike the motion of the

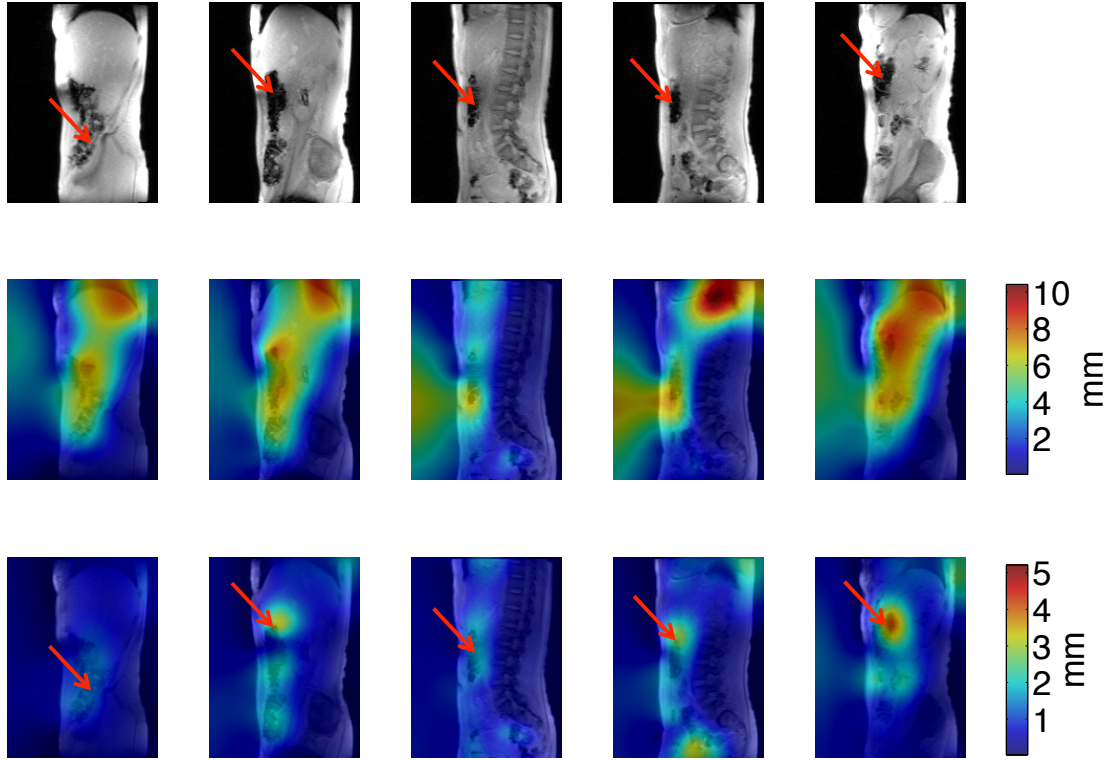


Figure 6.10: Model prediction errors in areas of non-respiratory motion. Top row: slices with arrows in stomach/bowel. Second row: mean registration-based deformation fields $\|D\|$, bottom row: mean difference between registration-deformations and model-deformations $\|\hat{D} - D\|$.

diaphragm, liver, pancreas etc.

The top row of Figure 6.10 shows an image from the five central slice locations with arrows marking such areas in the stomach and bowel. The second row shows the mean of registration-provided deformations $\|D\|$, and the bottom shows the mean ED at each voxel between registration and model-provided deformations, $\|\hat{D} - D\|$. It is clear from the bottom row that areas showing the highest error (up to 5 mm) are the same areas identified with arrows in the stomach/bowel, and areas such as the liver and pancreas which move with respiration have low errors.

6.8.3 Model Performance: Extrapolation Analysis

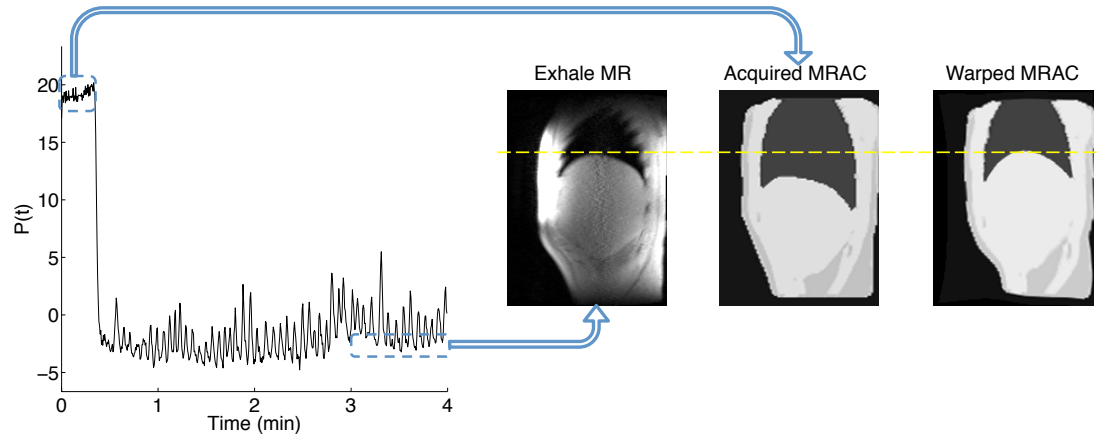
It is important for the model to perform well in extrapolation to allow for changes in breathing style and amplitude outside of the model-building section of the scan. Extrapolation is also vital for PET reconstruction when the MRAC is acquired at a breath-hold state outside of the range of breathing during the model-building sequence, for example when the MRAC is acquired at deep inhale instead of at the

exhale position. By examining the original signal $P(t)$ for patient 13 where this occurred, it is clear that a deep inhalation was taken at the start of the scan where the MRAC was acquired, as visible in Figure 6.11a. This figure shows the mis-match between an exhale reference image and the corresponding slice in the MRAC. Also shown in Figure 6.11b is the alignment of the MRAC with each reference exhale image before and after warping. In this example, the respiratory signal value is much larger at MRAC acquisition than during the model-building phase, nevertheless, the MRAC matches the exhale reference images reasonably well after warping with the model at extrapolated input signal values.

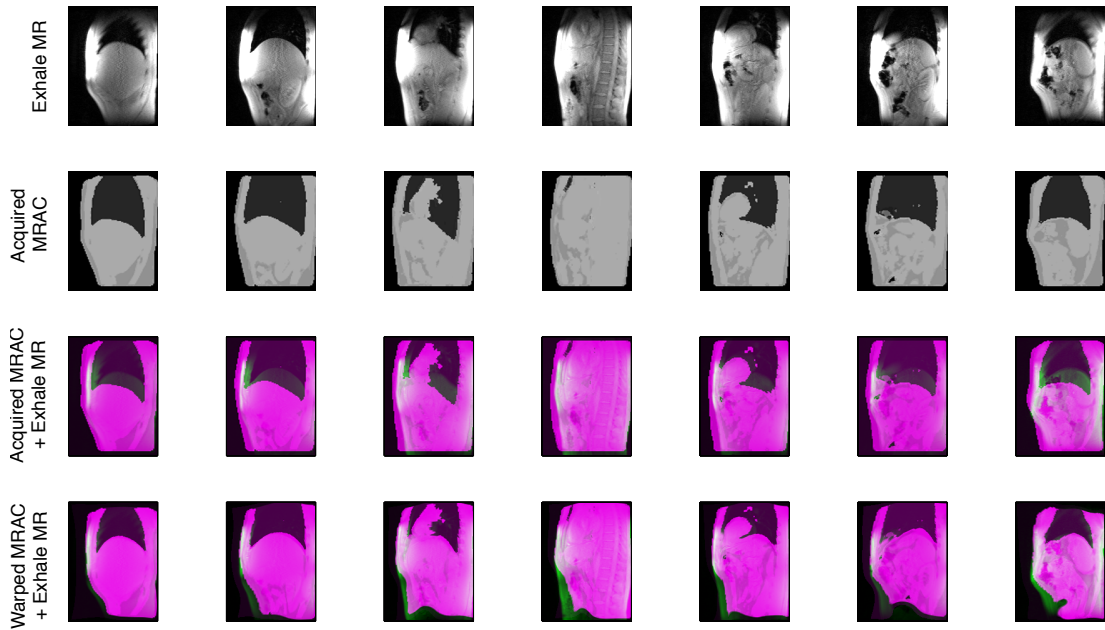
6.8.4 Model Performance: Failure Analysis

The patient-by-patient MI results in Figure 6.7 show that there is a big drop in performance between model-fit and model-prediction for patient 5. When examining the dynamic MR images for this patient, it became clear that bulk motion occurred during the scan. Figure 6.12a shows the respiratory signal for this patient, with red dots marking two MR acquisitions; one in the last minute at an exhale position, and one in the first two minutes at the same signal value. It can be seen that the first red dot is not at an exhale position of the signal, and the trough of the signal is not at a steady position throughout the scan. Furthermore, by examining these two MR images and the difference between them in Figure 6.12b, the diaphragm and chest wall are in different positions. This suggests that bulk motion took place at one or more points during this scan, and this has a knock-on effect on model-prediction performance.

In contrast, Figures 6.12c and 6.12d show the respiratory signal and the difference between MR images in the first and second half of the scan for patient 7, where there is only a small drop in performance between model-fit and model-prediction MI. In this example, both images are acquired at the same value of the respiratory signal, both are at signal troughs, and the images show minimal difference in diaphragm and chest wall position, suggesting no bulk motion has occurred throughout the scan, and therefore model-prediction performance is only slightly lower than model-fit performance.



(a)



(b)

Figure 6.11: MRAC acquired at deep inhale, for patient 13. (a) Respiratory signal, reference exhale MR, acquired MRAC at same slice position, and warped MRAC. (b) All acquired MRAC and exhale MR slices, overlay images of: acquired MRAC and exhale MR, warped MRAC and exhale MR.

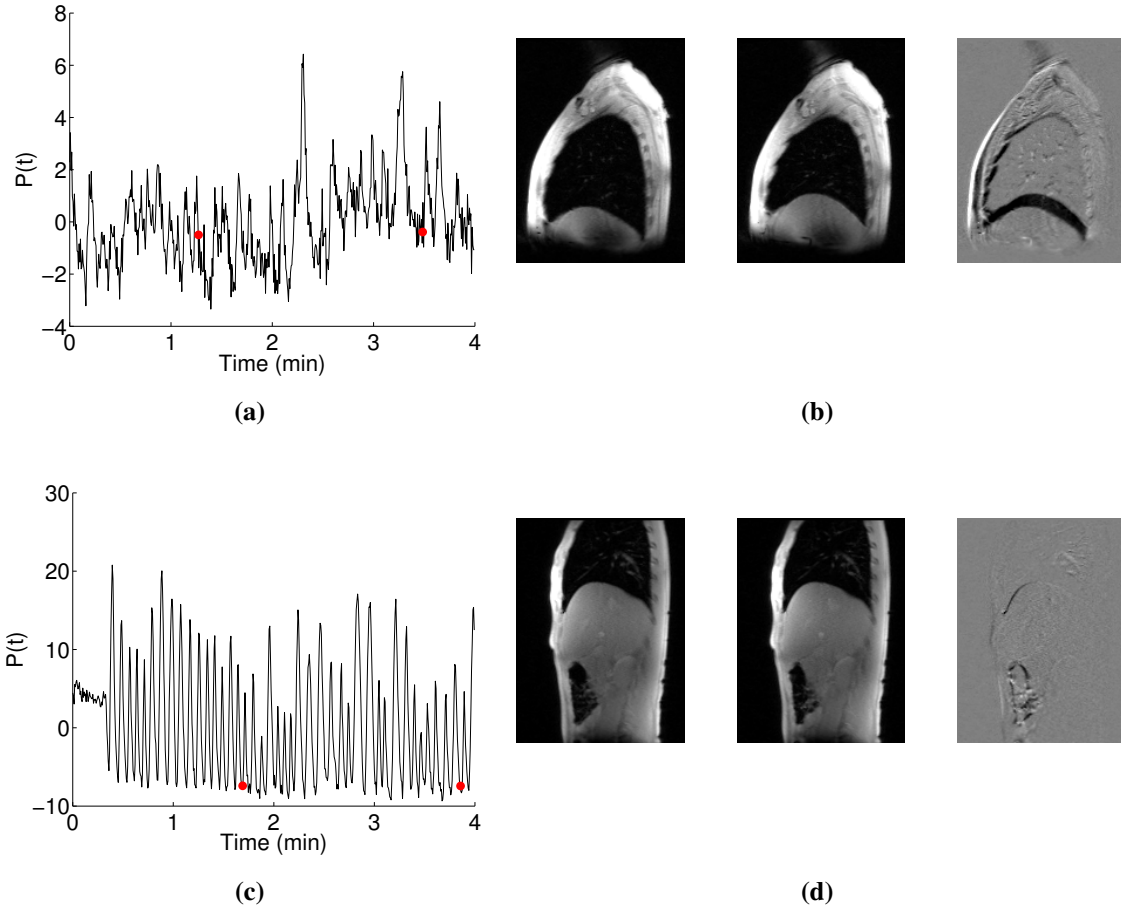


Figure 6.12: Two patient examples, respiratory signal, 2 MR slices at the same signal value, and image difference. (a) and (b) patient where bulk motion occurs during acquisition, (c) and (d) patient with no bulk motion.

6.9 Discussion

The theory and results in this chapter have demonstrated the feasibility of building and applying a motion model with MR and PET data only; using only one minute of data with no external devices to build a correspondence model capable of estimating respiratory motion. Various ways to set up the model were explored, with different numbers of surrogate signals and different levels of complexity, with each model tested on 45 MR patient data sets. The methodology presented builds a robust continuous motion model with the capability of interpolation and extrapolation, by predicting motion outside of what was visible in the model data, thus allowing potential use of 100% of PET data throughout a clinical scan during the same PET bed.

The overall results from all metrics indicated that the 2D-poly model performed

the best in terms of model-fit (Figure 6.9a). This was to be expected, as the larger the model coefficient matrix, the better the model can fit to the data. The aim of this work was to use the model to predict motion so other clinical MR sequences can be acquired in parallel with the PET scan, so the results of the model-prediction are of more interest. The general trend shows that performance drops when using the models to predict motion (Figure 6.9b). These tests also showed that the simpler 2D (linear) model performs best in terms of motion prediction. This model is able to capture intra-cycle variability (hysteresis) as well as exhale-inhale motion.

The difference in performance of model-fit and model-prediction in the patient-by-patient MI results of Figure 6.9 give clues as to where the model can fail, and it is clear from Section 6.8.4 that bulk motion may occur during clinical scans. Currently our method cannot account for this type of bulk motion, but it could potentially be captured with intermittent MR-based checks throughout clinical scanning. Other work explores the problem of stand-alone bulk motion (without respiratory motion) in the PET-MR context [Kolbitsch et al., 2014].

There are a number of limitations to the validation study conducted in this chapter. Firstly, there are some confounding factors in interpreting the results from the metrics used on MR data. We assume that the non-rigid registrations worked perfectly to provide our motion ground truth, and performance of models rely on comparing with results from registration. Occasional registration errors may occur, and so comparing deformations predicted by the model and by registration will not provide a meaningful result. However, the robust method of model optimisation ensures that these stand-alone registration errors should not affect the model performance, and in these cases the model should predict deformations better than the registration has.

Overall, results indicate that the 2D linear PET-MR motion model performs best when predicting motion as measured by MR data, and we continue to test the models on PET data in the next chapter.

Chapter 7

PET Respiratory Motion correction via Joint PET-MR Motion Models

7.1 Motivation

In this chapter, we apply the the continuous joint PET-MR motion model methodology explored in Chapter 6, and use the model to predict deformations during the whole PET scan, accounting for this motion in the PET reconstruction. As in Chapter 6, we compare the effect of different types of model (either one or two surrogate signals, with a linear or polynomial system), but now on motion corrected PET images. We also explore how the number of bins chosen for PET gating affects the resulting reconstruction, and outline a novel strategy to gate PET data depending on the breathing range of the patient during the scan.

First, in terms of clinical application, we revisit the workflow proposed in Chapter 5. With the use of the continuous motion model, all MR images are now registered (rather than just a selection of binned images), then a trajectory map is formed to allow for PET data binning based on more than one surrogate signal. We also now assume that a three minute PET scan at a single bed position would be extended to four minutes to allow for a one minute model-building sequence, so motion information is used for reconstruction of the same PET acquisition, rather than on clinical data acquired up to one hour earlier. The PET part of the motion model acquisition can therefore not only be used to provide a respiratory signal, but can be included with the other three minutes of PET data, ensuring greater count statistics. Workflow steps are outlined below, and presented in Figure 7.1, with some steps explained in more detail in this chapter:

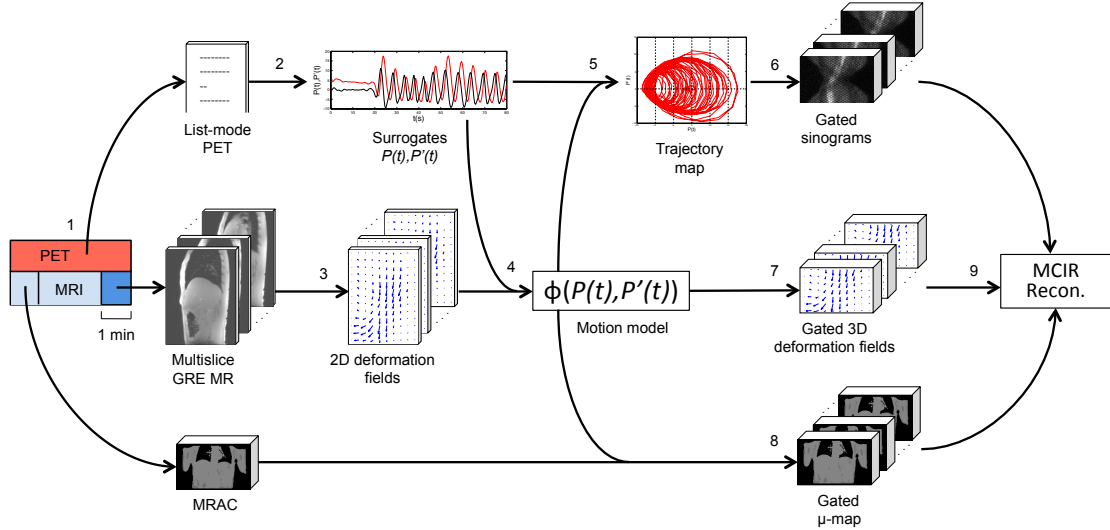


Figure 7.1: Proposed clinical workflow from PET-MR data acquisition to motion incorporated PET reconstruction. The MR acquisition consists of the normal MRAC and clinical MR, plus one min of extra dynamic GRE for the motion model.

1. Acquire 4 min PET-MR sequence.
2. Extract surrogate signals from raw PET data.
3. Bin GRE MR slices based on signal to identify an 'exhale' reference image at each slice position and perform non-rigid registration of all MR slices.
4. Form joint PET-MR motion model, providing a correspondence between deformation fields and surrogate signals.
5. Form trajectory map and plan PET data gating scheme.
6. Unlist raw PET data into several gates according to step 5.
7. Calculate 3D gated deformation fields with motion model.
8. Warp μ -map with motion model to form gated μ -maps.
9. Motion compensated image reconstruction (MCIR).

7.2 PET Gating in the Continuous PET-MR Model Context

With the discrete motion model of Chapter 5, the gating of PET data was predetermined by the gating scheme applied to the dynamic GRE MR data. The new

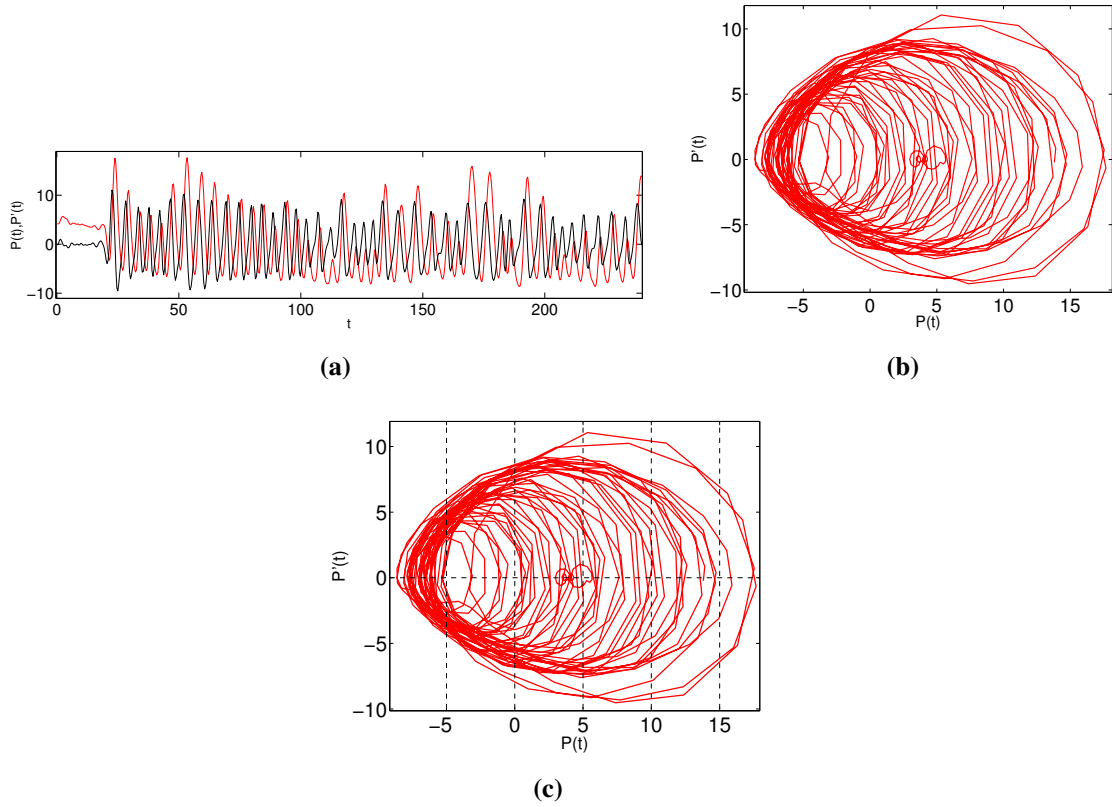


Figure 7.2: (a) Surrogate signals plot against time, (b) Trajectory map, plotting surrogate signals against each other, throughout a four minute patient scan, (c) gating of PET data into 12 bins.

continuous model allows estimation of deformation fields for any value of the surrogate(s). However, as explained in Chapter 2, computational effort for motion-compensated list-mode reconstruction is high, therefore, binning the PET data which have similar surrogate value(s) (and hence deformation fields) is still desirable.

In order to bin PET data based on the value of more than one surrogate signal, a change from a standard view of signal $P(t)$ vs. t (Figure 7.2a) to a trajectory map of $P(t)$ vs. $P'(t)$ (Figure 7.2b) is needed to track the surrogate signals throughout the scan. PET data can therefore be binned based on the values of the two signals, by grouping values with a grid. Figure 7.2c applies a grid to bin the PET data into six bins in the $P(t)$ direction and two bins in the $P'(t)$ direction (equivalent to splitting inhale/exhale data), providing 12 data bins overall. Deformation fields for each PET bin can then be estimated with the motion model using the surrogate values at the centre of each grid box, to then be used in the motion-compensated reconstruction using the same methodology as in Chapter 5.

7.3 How Many Bins is Enough?

The continuous motion model methodology allows deformation estimation for any number of PET data bins, thus providing the chance to explore how the number of bins affects the motion-compensated PET reconstruction. The issue of how many bins are enough to ensure the maximum improvement in image quality through motion correction can be tested, considering the PET system spatial resolution.

7.3.1 Methods

For one patient data set with multiple avid abdomen lesions, motion-compensated reconstructions were carried out with no attenuation correction (NAC), in order to examine how well the motion correction alone was performing, without added changes due to attenuation correction. The simplest 1D linear model was used, with reconstructions for one bin (uncorrected), and 2, 5, 10, 20 and 50 bins. Analysis is carried out by visual assessment of lesion ROIs for each NAC PET reconstruction with associated line profiles. As SUV measures are not appropriate for reconstructions without attenuation correction, changes in voxel intensity (VI) between uncorrected and each motion-compensated image are used. VI measures VI_{\max} and VI_{peak} are defined in a similar vein to the SUV measures, as:

$$\Delta VI_{\max} = MC_{\max}^{\text{ROI}} / U_{\max}^{\text{ROI}} \quad (7.1)$$

$$\Delta VI_{\text{peak}} = MC_{\text{peak}}^{\text{ROI}} / U_{\text{peak}}^{\text{ROI}} \quad (7.2)$$

where MC^{ROI} and U^{ROI} are the ROI from the motion corrected and uncorrected NAC PET reconstructions respectively. As with SUV measures, 'max' denotes the maximum voxel intensity within the ROI, and 'peak' denotes the maximum average voxel intensity within a 12 mm diameter sphere within the ROI.

The Tenengrad Variance Sharpness (TVS) metric, defined as the variance of the gradient of the volume found with the Sobel operator [Alvarez-Borrego, 2005], was used to measure changes in global sharpness between the uncorrected and motion-compensated images:

$$\Delta TVS = MC_{\text{TVS}} / U_{\text{TVS}} \quad (7.3)$$

7.3.2 Results

The ROI images in Figure 7.3 show the change in appearance of each lesion with increased bin number. Line profiles are also shown through the centre of each lesion in the SI direction for each reconstruction.

Figure 7.4 summarises the changes in voxel intensity of each lesion in each type of reconstruction with the VI_{peak} (Figure 7.4a) and VI_{max} measures (Figure 7.4b), when compared with the one bin (uncorrected) reconstructions. Global sharpness changes are also shown with the ΔTVS metric in Figure 7.4c.

7.3.3 Discussion

By visual analysis of the lesions in Figure 7.3, it is clear that lesions 1-5 decrease in volume and become sharper with increasing number of bins. At the one bin level these lesions all appear blurred in the SI direction due to respiratory motion, but this is reduced with increasing bin number. The line profiles also show this effect with voxel intensities reaching higher peaks and with steeper gradients.

The graph in Figure 7.4a quantifies this increase in voxel intensity with the increase in VI_{peak} for lesions 1-5. The maximum level of ΔVI_{peak} differs from lesion to lesion, as does the bin number at which the line plateaus. The behaviour of this line for each lesion will depend on a number of factors, including how accurately the motion model performed at the lesion location, and on the actual level of tracer uptake in that lesion compared to its surroundings. The location and how much motion occurs at the location will also have a big effect. For example, lesion 1 was located at the top of the pancreas near the diaphragm and so this lesion also experiences the highest ΔVI_{peak} . For some lesions, the values of ΔVI_{peak} and ΔVI_{max} are also still increasing between the 20 bin and 50 bin values, suggesting a bin number higher than 50 may be optimal.

Lesion six is the anomaly in this example as in the images in Figure 7.3 there is less obvious visual change in lesion appearance. The blurring seems to decrease slightly in the motion-compensated images with the lesions looking smaller, and the line profiles confirm this decrease in lesion size, but do not show much change in their peak values. The ΔVI_{peak} metric confirms this with a small negative change at each bin level, although the ΔVI_{max} metric shows a slight positive increase. The negative

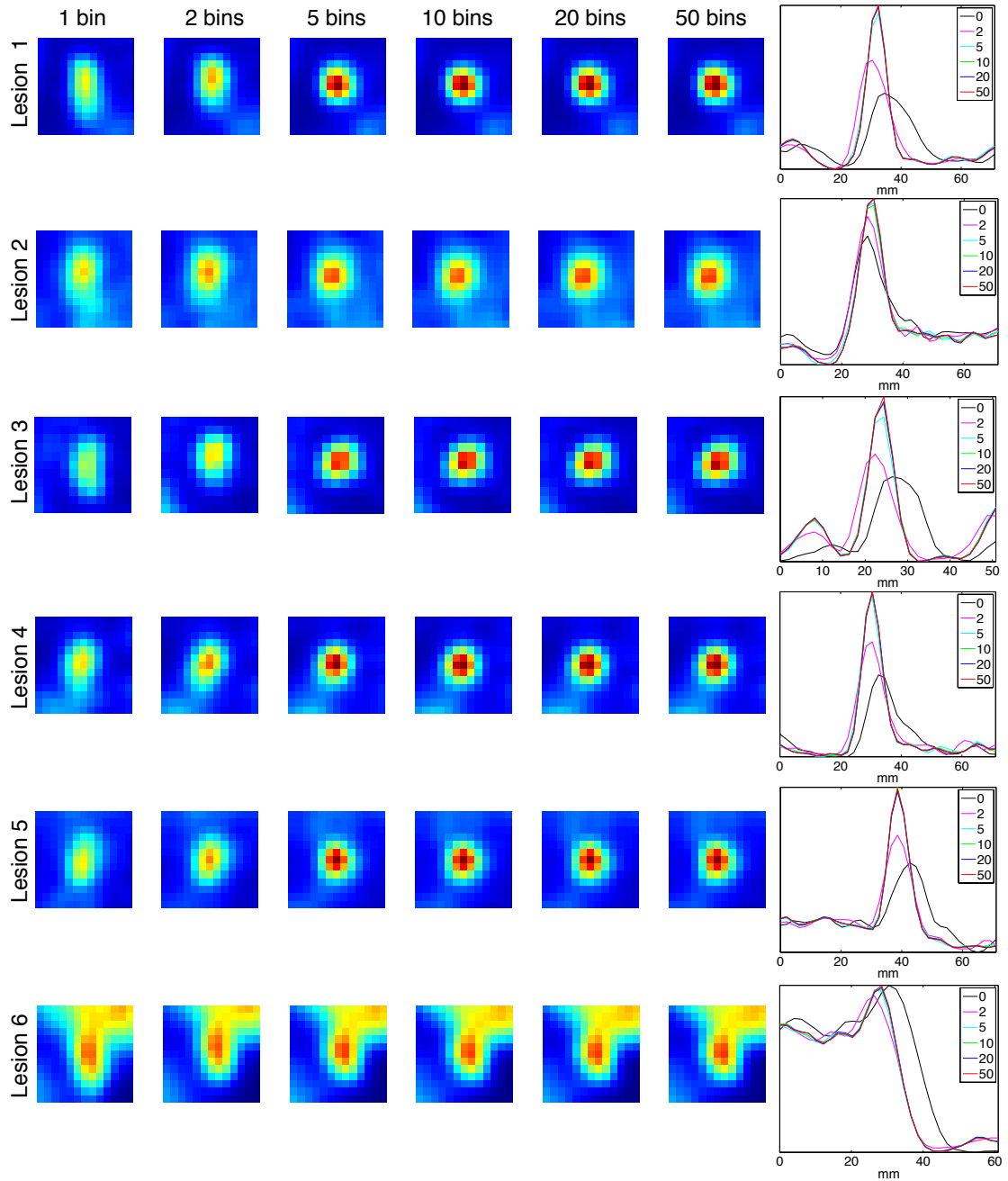


Figure 7.3: Coronal view of each lesion in PET motion-compensated reconstructions with 1, 2, 5, 10, 20 and 50 bins, using the 1D linear model, with line profiles through each. Blue is low voxel intensity and red is high voxel intensity.

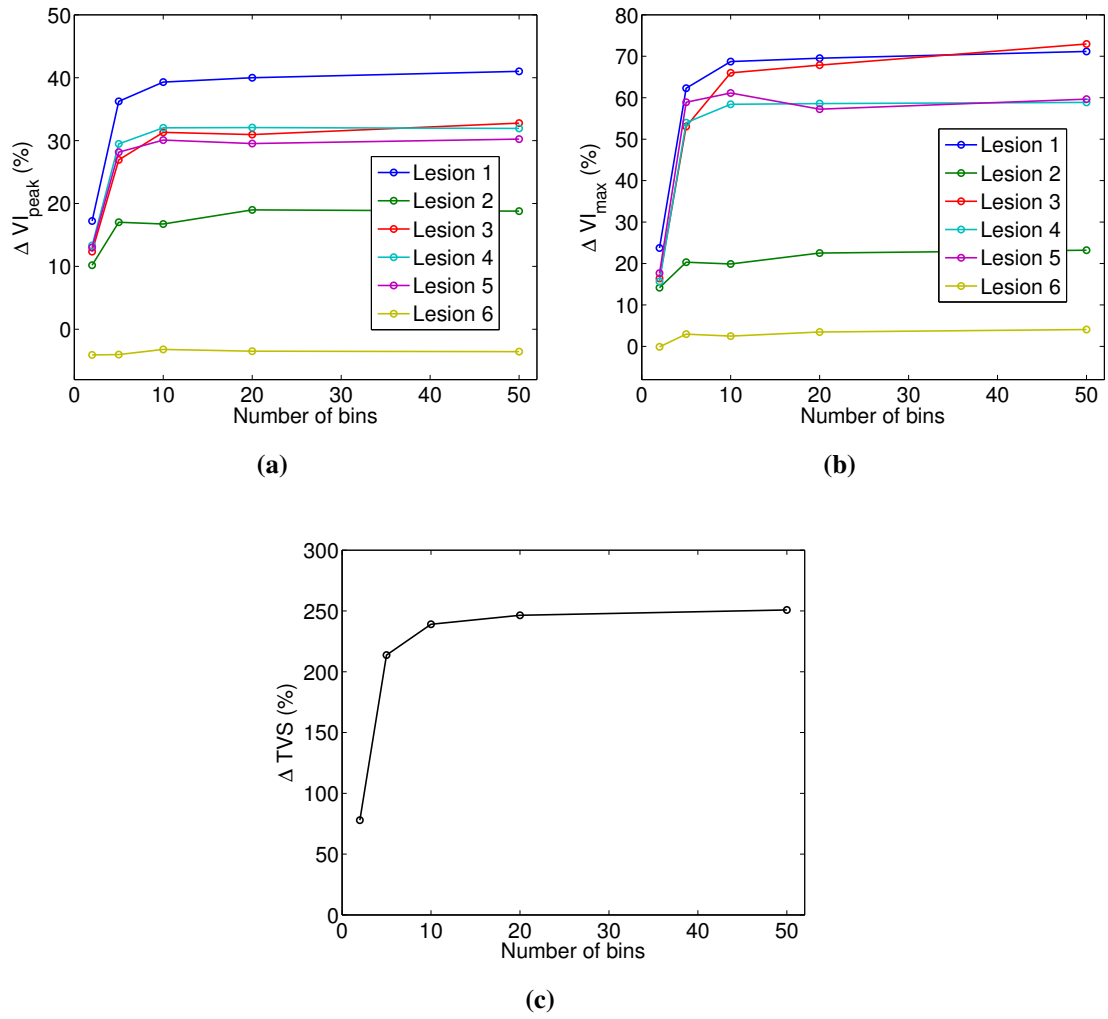


Figure 7.4: Comparison of MCIR NAC PET reconstruction with 1D-linear model and various bin numbers, to uncorrected reconstruction. (a) VI_{peak} (b) VI_{max} , (c) ΔTVS .

ΔVI_{peak} value may be due to the fact that the lesion is small and is touching the spleen, so a peak (mean based) measure may not be appropriate as the lesion is smaller than the peak search area and so uptake in the spleen will also be inside the volume. Also, as the lesion is located at the edge of the abdomen next to the ribs, the motion modelling underpinning the motion correction may be inaccurate due to the registration scheme not dealing with sliding motion, as discussed in the last chapter.

For this patient dataset, 10 bins seems to be enough to reverse the effects of motion-blurring, but the necessary bin number depends on absolute displacement of internal organs during respiration, which is patient and location specific. We now go on to formulate a methodology for a flexible patient-specific binning scheme.

7.4 Flexible Binning Scheme

It is necessary to ensure that enough bins are used to maximise the effect of motion-compensation in the PET reconstruction, whilst not using too many such that computational cost is increased beyond what is needed. In this section, a patient-specific efficient binning scheme is proposed, to group PET data based on the amplitude and range of breathing throughout a patient acquisition. This is to ensure that intra-bin motion is less than half the FWHM resolution of the scanner, which is ~ 4.5 mm [Delso et al., 2011] for the Siemens Biograph mMR. The process is outlined below and illustrated with patient data.

1. A trajectory map of P and P' is used to track the surrogate signals throughout the scan, and a fine grid is drawn across the trajectory map (Figure 7.5a).
2. Each outer square on the grid following the perimeter of the trajectory is marked (Figure 7.5b) and deformation fields at every slice location are estimated for each of these squares.
3. For each row (constant value of P') and each column (constant value of P) the deformation range is found for each voxel, between the 2 outermost squares (Figure 7.5c).
4. The deformation range with the highest sum over all voxels in both P and P' directions over all slice locations is found (Figure 7.5d).
5. In the two directions P and P' , individual voxel deformations of the maximum range images are histogrammed (Figure 7.5e). The maximum respiratory displacement is marked as the value at the 98th percentile in each of these directions. The percentile is used to disregard any local outliers in the deformation fields.
6. Bin size in both directions is then found by dividing the maximum respiratory displacement by half the FWHM resolution of the scanner (4.5 mm).

The resulting gating scheme for this patient is shown in Figure 7.5f, with bins marked on the trajectory.

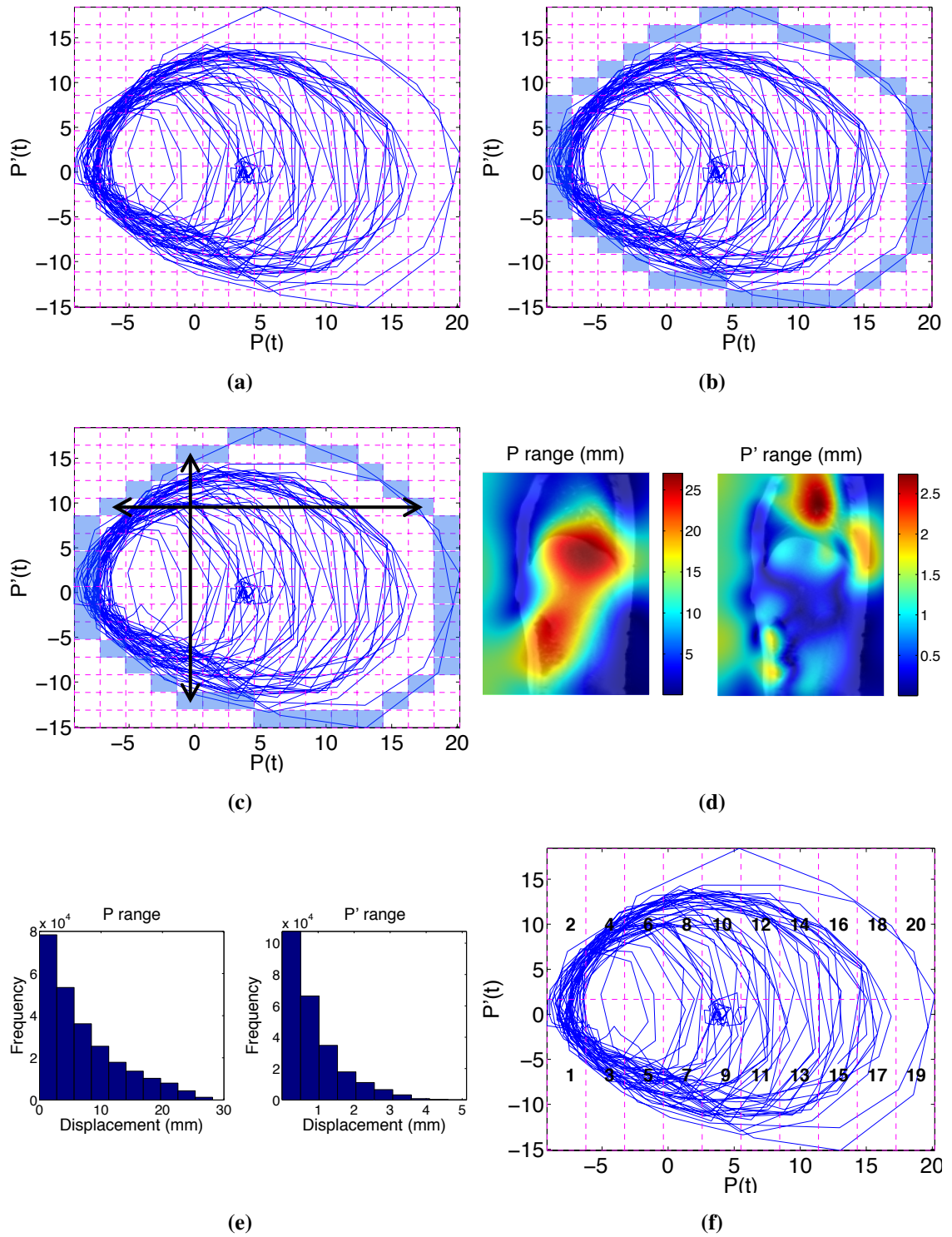


Figure 7.5: Method for automatic calculation of PET gate size. (a) Respiratory trajectory, (b) Respiratory perimeter, (c) Deformation ranges in each direction, (d) Largest deformation ranges in each direction, (e) Deformation ranges histogrammed, (f) Final gating scheme.

7.5 Evaluation of Motion Models on PET data

The aim of this section was to find which type of motion model (either 1 or 2 surrogate signals, with a linear or polynomial system), if any, would perform best when used to model motion in a motion-compensated PET reconstruction.

7.5.1 Protocol

Part of the data sets from five patients that were scanned under the protocol from the validation study in Chapter 6 was used. The following acquisitions were used:

- PET list-mode (4 min).
- MR Dixon (18 s) at end-expiration, for MRAC .
- MR 2D multi-slice gradient echo (GRE) (1 min).

7.5.2 Methods

Patients were selected from available data to have suspected/known lesions in the abdomen/thorax - Patient A (four pancreas), B (six liver), C (10 liver), D (four pancreas), E (six liver/lung).

A motion-compensated reconstruction of the four min PET acquisition was carried out using deformation fields estimated by each of the four motion models. PET data was binned using the patient-specific scheme outlined in Section 7.4, carried out independently for each of the four models. The attenuation μ -map was warped to the exhale position with deformation fields estimated by the motion model, using the mean values of the surrogate signals P and P' recorded during the time in which the MRAC sequence was being acquired. This exhale μ -map was then warped to match each of the gates. Randoms and scatter sinograms were also calculated for each gate (as explained in Section 5.4.5), and together with the μ -map at each gate, make up the background sinograms. Each PET acquisition was reconstructed without motion correction, and with motion correction four different ways using the four motion models. All reconstructions were carried out both with attenuation correction (AC) and without attenuation correction (NAC).

Motion-corrected images were compared to uncorrected images visually, and quantitatively in regions of interest (ROIs) containing areas of high tracer uptake.

Measures used were SUV_{max} and SUV_{peak} in AC PET, and VI_{max} and VI_{peak} in NAC PET. Focal lesions were identified and highlighted by a PET accredited radiologist on the original clinical images of the PET/MR study.

7.6 Results

7.6.1 Individual Lesion Analysis

Table 7.1 summarises the changes in SUV_{peak} and SUV_{max} in all lesions in patients A and C with the four different models used in motion-compensated AC PET. There is a large range of SUV changes over all lesion, which depends on the breathing of the patient and the location of the lesion, with lesions located further from the diaphragm moving less due to respiration.

The relative performance of each model varies from patient to patient. Figure 7.6 displays the results in a bar graph for patients A (top row) and patient C (bottom row). For patient A, there is little visual difference between models in SUV_{peak} and SUV_{max} changes, in any of the six lesions. This is in contrast with patient C, where there are big differences in SUV metrics depending on the model used. However, although there is not one clear model which gives the largest increases in SUV metrics over all lesions, it seems that the 2D linear and 2D polynomial models perform best the most frequently. For example, the 2D models perform best in seven out of 10 lesions for SUV_{peak} , and in eight out of 10 lesions for SUV_{max} .

By examination of the raw deformation data from the registrations for these two patients, it is clear that there is more hysteresis in breathing of Patient C than for Patient A, which would explain the increase in model performance when two surrogates are used in the model.

7.6.2 Overall Patient Analysis

Figure 7.7 summarises the mean quantitative changes in all lesions in each of the five patient data sets. In all patients, average SUV_{peak} , SUV_{max} , VI_{max} and VI_{peak} have significantly increased due to motion correction in both the AC and NAC PET images when comparing uncorrected and motion-corrected images, but no model performs statistically significantly better than all others. On average, over all lesions in all patients on both AC and NAC images, the 2D-linear model performed best compared

Patient	Lesion	$\Delta\text{SUV}_{\text{peak}}$				$\Delta\text{SUV}_{\text{max}}$			
		1D	2D	1D-poly	2D-poly	1D	2D	1D-poly	2D-poly
A	1	28.8	29.0	28.4	28.5	51.2	51.4	49.3	48.9
	2	15.8	14.9	15.8	14.8	26.2	23.0	25.9	24.6
	3	11.2	11.4	11.1	11.7	43.6	44.8	43.3	46.5
	4	22.6	22.9	22.5	21.2	46.5	47.9	46.6	41.4
	5	9.9	10.1	9.3	6.8	51.4	51.1	49.1	42.5
	6	-3.4	-4.1	-3.2	-4.1	4.6	3.2	4.1	3.5
C	1	36.7	39.2	34.6	39.5	32.0	39.8	21.0	42.3
	2	21.6	19.6	19.8	19.3	25.6	29.3	23.0	28.6
	3	25.6	33.5	23.2	26.7	31.7	44.3	27.9	27.8
	4	12.9	16.0	17.1	22.0	8.2	15.7	18.6	28.0
	5	23.3	16.6	17.6	16.4	30.9	39.2	47.5	24.5
	6	17.1	17.3	16.9	18.0	15.3	17.3	18.7	18.3
	7	33.9	34.0	40.7	41.8	50.2	44.7	54.0	54.8
	8	40.5	47.2	46.3	44.7	58.2	66.9	50.5	47.0
	9	19.6	22.1	18.2	22.3	17.9	23.1	14.9	14.8
	10	17.9	21.7	17.1	17.2	21.4	28.3	17.2	19.0

Table 7.1: Changes in SUV_{peak} and SUV_{max} in all lesions, Patients A and C, and all types of model in AC PET.

to every other model, with SUV_{peak} and SUV_{max} increases of 36% and 43% respectively. Both SUV metric increases in lesions were significant when compared to the 1D-linear and 1D-poly models ($p < 0.05$), but not significant when compared with the 2D-poly model ($p > 0.05$), with the paired Wilcoxon signed rank test.

Visually, the motion-corrected images from the four types of motion model were comparable, with all lesions showing an increase in sharpness. Figures 7.8 and 7.9 show examples of the improvements in image quality apparent in the motion-corrected PET reconstructions, using the 2D model. For patient A (Figure 7.8), the blurring in the lesion marked in the uncorrected image has been reduced in the motion-corrected image and the lesion appears sharper.

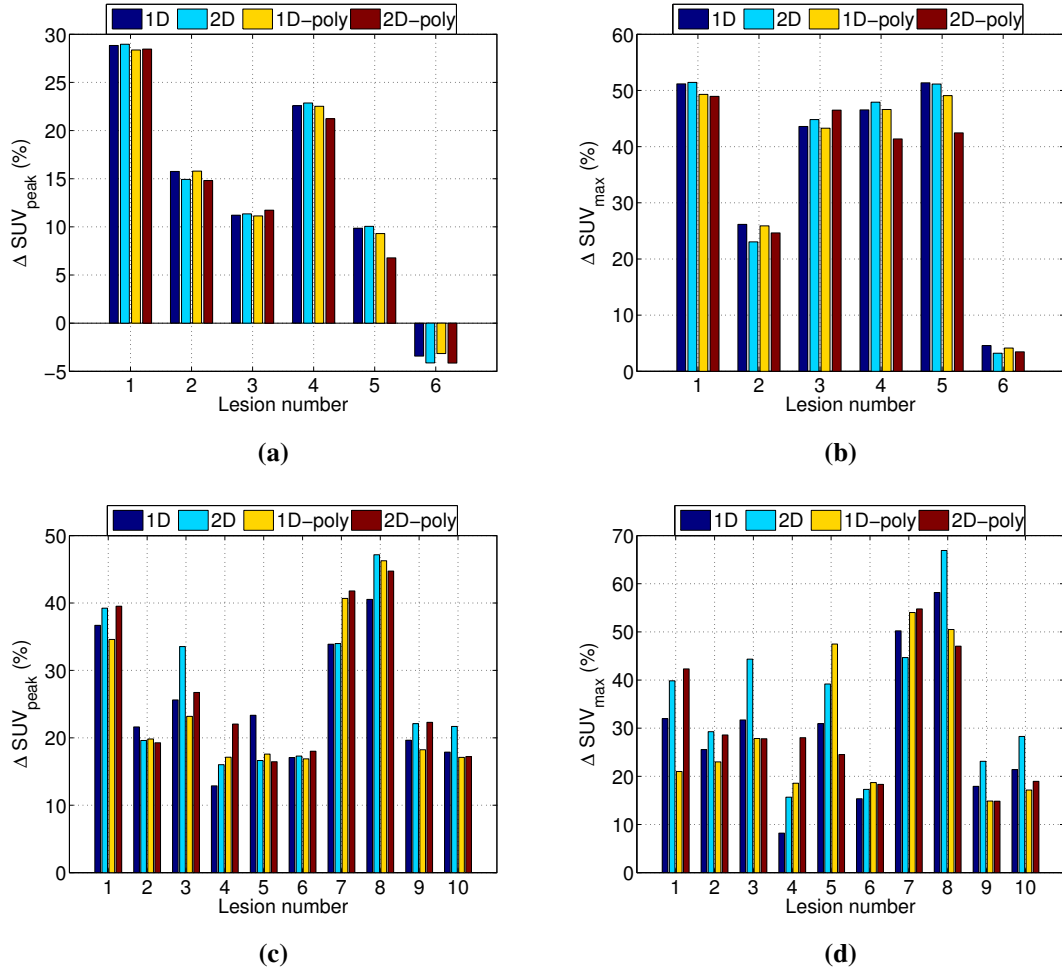


Figure 7.6: Mean SUV_{peak} and SUV_{max} changes in lesions in AC PET reconstructions. (a) and (b) Patient A, SUV_{peak} and SUV_{max}, (c) and (d) Patient C, SUV_{peak} and SUV_{max}.

For patient B (Figure 7.9), the MRAC was acquired at a deep inhale position (possibly due to the patient misunderstanding the instructions or difficulty holding breath due to illness), causing a mismatch between the attenuation μ -map and PET emission data. This in turn causes artefacts in the uncorrected images above the liver. In this example, the combination of misaligned μ -map, respiratory motion and avid lesions present at the top of the liver causes them to be almost invisible in the uncorrected image. Two lesions are marked on the sagittal image, and one of them is also marked on the coronal image. Both lesions are visible on the motion-corrected image. Both lesions, along with others that appear in the motion-corrected image were confirmed to be present in the patient using extra MR and CT information confirmed by an accredited radiologist.

It is clear from the PET images for patient B (Figure 7.9) that a large source of

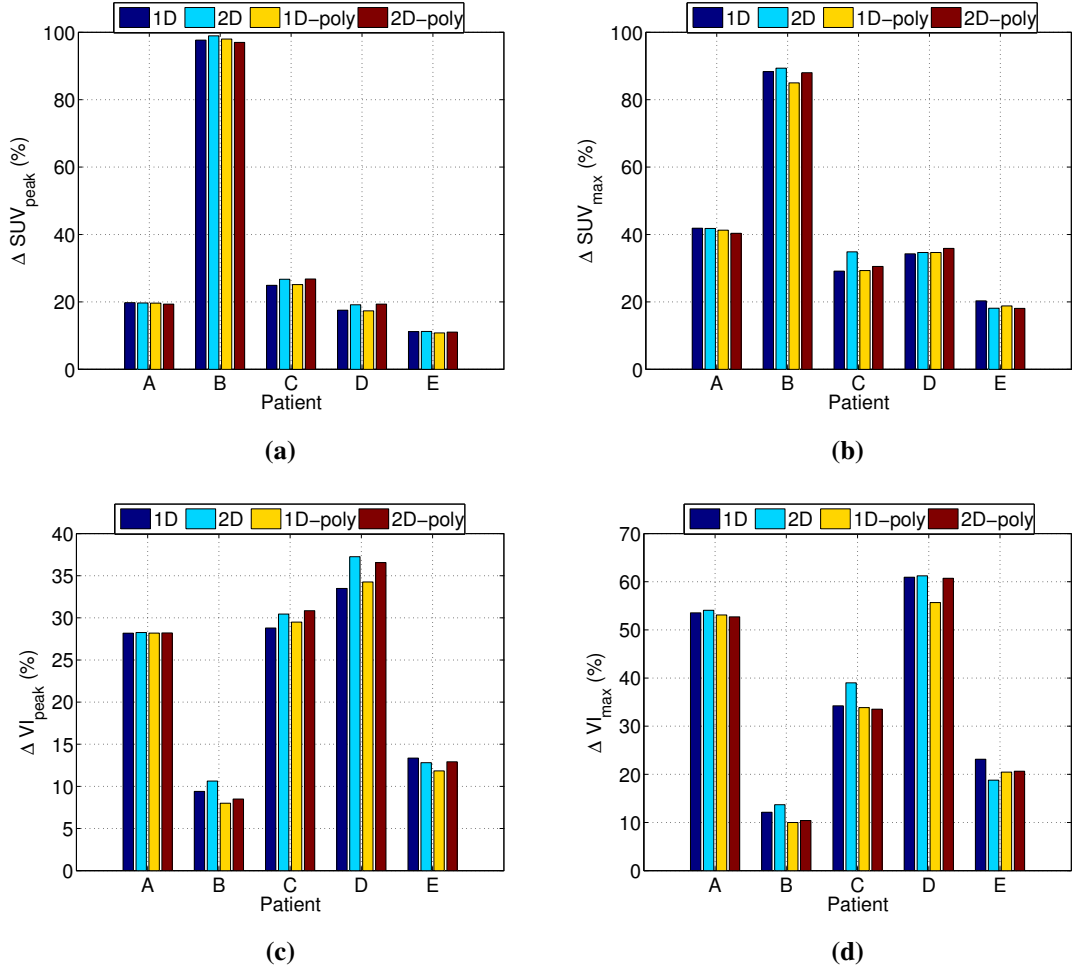


Figure 7.7: Mean SUV_{peak} and SUV_{max} changes in lesions in 5 patients. (a) SUV_{peak} AC, (b) SUV_{max} AC, (c) VI_{peak} NAC, (d) VI_{max} NAC

error in the uncorrected images of this patient stemmed from the μ -map being mismatched with the emission data. This is highlighted by the large increases in SUV_{peak} and SUV_{max} in the AC motion-corrected images for this patient (Figures 7.7a and 7.7b), whereas the increase is much smaller in the NAC images. The extent of the μ -map mismatch can be seen by looking at the original signal P for this patient, where it is clear that a deep inhalation was taken at the start of the scan where the MRAC was acquired (see Section 6.8.3).

7.7 Discussion

When applied to PET data, the models all showed sizeable and statistically significant improvements by using MCIR compared to a single uncorrected reconstruction. There were no statistically significant difference in the extent of improvement between one

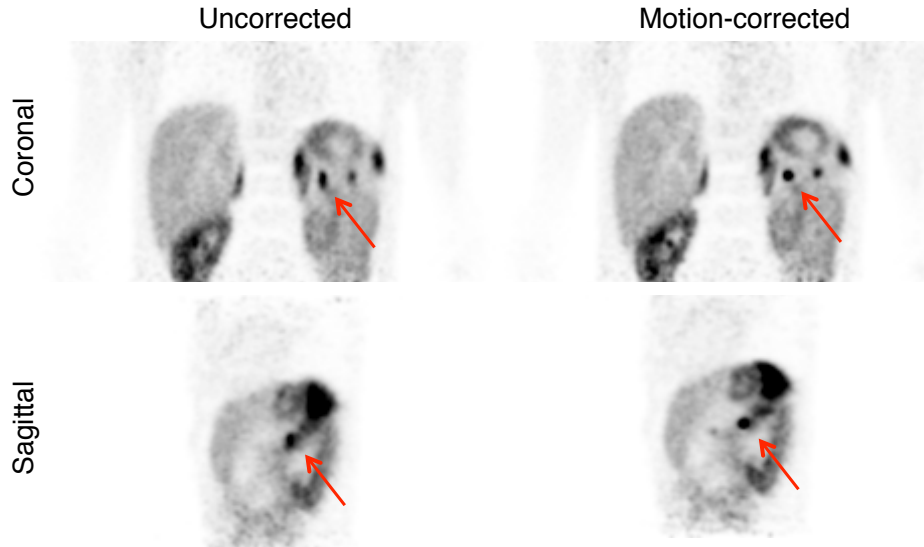


Figure 7.8: Uncorrected and motion-corrected (2D-linear model) PET reconstructions for patient A. Top row shows coronal slices and bottom row shows sagittal slices.

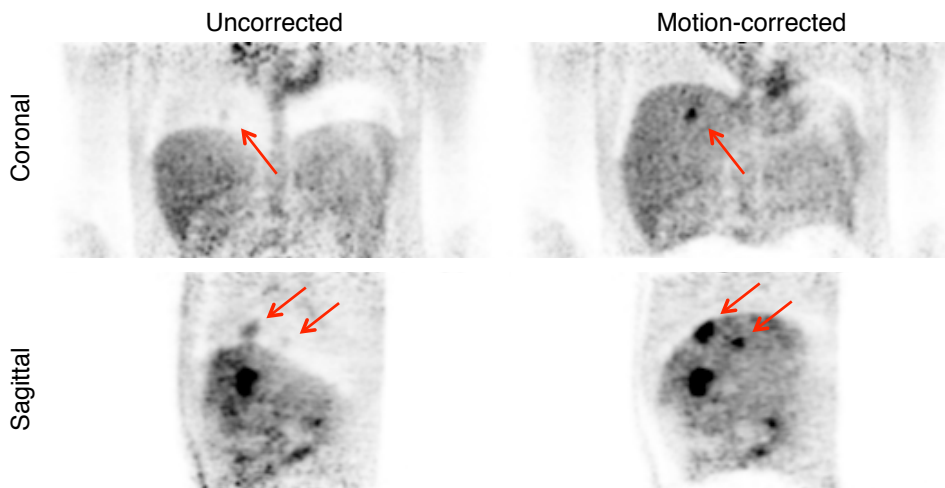


Figure 7.9: Uncorrected and motion-corrected (2D-linear model) PET reconstructions for patient B. Top row shows coronal slices and bottom row shows sagittal slices.

model and all other models, although over all lesions in all patients, the 2D-linear model performed best in AC PET, in terms of SUV_{peak} and SUV_{max} . It could be assumed that the quantitative evaluation on MR data gives a much better indication of model performance as three different global metrics were used, as opposed to only ROI based metrics in the PET. A higher number of MR data sets were used, and MR images are also of a much higher spatial resolution, so small discrepancies between the models would be more forthcoming. It should be noted that for the evaluation on PET data, we did not differentiate between model-fit and model-estimation as the whole four minute

PET acquisition was used in the reconstruction. However, as three of the four minutes of PET data were acquired outside of the model-building section, the reconstructions tested mainly model-prediction accuracy.

It is clear for Patient B in the detailed analysis of the five patients tested that the 2D and 2D-poly models performed best. This patient demonstrated the most hysteresis, apparent from the raw deformation data, and the high number of bins in the P' direction enforced by the gating scheme due to a large range of displacements in this direction.

By comparing average lesion SUV changes in AC and NAC PET, the results show that motion artefacts caused by the MRAC being acquired at the incorrect respiratory position can be reduced with the proposed methodology. This could be useful for patients with lung problems that find it difficult to hold their breath at exhale, or those with communication difficulties.

In terms of the final PET images produced with the MCIR reconstruction, it is clear that by warping the μ -map to each motion state, gaps can appear at the bottom of the image, as seen at the bottom of both coronal and sagittal views in Figure 7.9. This occurred as our methodology warped an MRAC image that exactly matched the FOV for the bed position to be analysed. This error could be removed by using an MRAC that extended the FOV for the bed position in question.

Overall, results indicate that the 2D linear PET-MR motion model performs best when predicting motion as measured by MR data, and is effective in PET motion correction, suggesting that in a clinical setting the 2D-linear model would be the best choice. Based on this we choose to use this model for estimation of deformation fields in a motion-compensated PET reconstruction in the next chapter, testing on a large clinical patient cohort. PET image results of patient B indicate the importance of proper motion correction through μ -map misalignment as it can lead to improved lesion detectability. A full quantitative assessment of lesion detectability will also be explored in the next chapter.

Chapter 8

Clinical Validation of Motion-Compensated PET: Pilot Study

8.1 Overview

In this final chapter of work, we validate the PET respiratory motion correction methodology based on a joint PET-MR motion model, on a large patient cohort. The results from the last two chapters suggested use of a 2D linear model with the respiratory signal and associated gradient as the surrogates to model motion. We apply the flexible binning scheme described in Section 7.4, using the motion model methodology described in Chapter 6, on 45 clinical patient data sets.

Although increases in quantitative metrics such as SUV in tracer-avid lesions (via motion correction) can be significant for patient management decisions, impact on detection by human observers is also important. First, we give some background on lesion detectability studies, traditionally carried out with Free-response Receiver Operating Characteristic (FROC) analysis [Bunch et al., 1977], and highlight the potential hazards of using this methodology when testing PET data.

For the clinical validation study, we first use some of the quantitative analysis methods explored in the last few chapters to measure performance of the motion correction, by comparing uncorrected (U) and motion-corrected (MC) images. We use the TVS sharpness measure on all non attenuation-corrected (NAC) PET patient datasets then use SUV metrics on the attenuation corrected (AC) PET reconstructions, where PET-avid lesions and 'hot spots' are selected by trained radiologists.

We then perform a lesion detectability study, where two readers examine each U

and MC image and mark suspected lesions with a confidence score of how sure they are that a lesion is present at the location. A reference read is done by the two readers in consensus with all other imaging modalities available (MR, CT, follow-up PET), and the rate of true-positive and false-positive detection can be calculated, as well as changes in confidence scores between U and MC images.

Finally, we present a number of illustrative examples, presenting data for a number of patients, to show how respiratory motion correction may have the potential to affect clinical patient management, for example, on patient staging, diagnosis and surgical planning.

8.2 Detectability Studies in PET

A traditional approach to test lesion detectability is FROC analysis, which is used to compare two types of images, in terms of a certain criteria, such as portraying a malignancy. Like Receiver Operating Characteristic (ROC) analysis [Swets and Pickett, 1982], where a reader will decide whether each image shows malignancy or not, a reader will also consider lesion location, by marking suspicious lesions on an image, along with an associated confidence rating that there is a lesion at the marked location. A reference standard is needed, that maps true lesion locations. With this information, lesions marked correctly (lesion localisation) can be compared with fractions of lesions marked incorrectly (non-lesion localisation). A FROC figure of merit compares fractions of these two metrics - lesion localisation fraction (LLF) and non-lesion localisation fraction (NLF) at different confidence levels.

We did not carry out a full FROC study due to two reasons. The first is the lack of a homogeneous reference standard. Previous FROC studies have been conducted with human observers, for example, locating lung lesions in MR images derived from different sequences [Burris et al., 2015]. In this case CT served as the reference standard as it is known to have far greater ability to show up lung lesions than any MR sequence, and the detection task is just to find a lesion structure. For our work, we collected all images available, including those from other hospitals, for the reference read. This means we have to rely on heterogeneous imaging data to derive the reference standard between the individual patients, and which often includes the PET study. This stems in part from practical/logistical and ethical constraint to have to rely

on standard of care clinical imaging data for such use. More importantly however, it reflects that in many cases referred for a PET study, the clinical context is such that there is no single imaging modality which can claim to robustly and consistently establish the ground truth, especially *a priori*, and that PET is often the most accurate method with all imaging data considered together. It is for this reason that in the literature, PET-based detection studies revolving around testing different reconstruction methods [Morey and Kadrmas, 2013], different acquisition times [Kadrmas et al., 2012], motion correction [Polycarpou et al., 2014], or time-of-flight impact [Kadrmas et al., 2009], use phantom or simulated PET data, where a ground truth is known.

The second reason is the lack of a definite method to identify false-positives. The information that PET provides is unique in that it is portraying tracer uptake, unique to the modality. For example a lesion may appear avid in a PET image but this does not mean it will necessarily be visible in an MR or CT image due to its believed highly sensitive nature, with the potential to detect lesion before structural changes, or lesions becoming apparent. This means for PET detection tasks it is not possible to be 100% certain of distinguishing completely between true-positives and false-positives.

It is for these reasons that we carry out a simple detectability study without FROC analysis, using the terminology of lesion localisations (LL) and non-lesion localisations (NLL), and examine these in isolation.

8.3 Data

8.3.1 Patients

Data was acquired for 45 patients undertaking a range of clinical or research PET/MR scans between February 2014 and November 2015. Patients were selected based on prior clinical information suggesting possible avid regions in the thorax or abdomen. Written informed consent was obtained from all patients for examinations and for the use of data for scientific purposes. Tracers used were ^{18}F -FDG (20 patients), ^{68}Ga -DOTATATE (23 patients) and ^{18}F (Florbetapir) (one patient). Mean patient age was 62 years (range, 36-85 years). The patient cohort consisted of 20 women (mean age, 63 years; range, 46-78 years) and 24 men (mean age, 61 years; range, 36-85 years). In total, there was 162 PET-positive lesions or 'hot spots' in the patient data, in the form

PET +ve Hot Spot	Number
Liver lesion	71
Pancreas lesion	22
Lung lesion	27
Abdomen node	6
Thorax node	29
Other (kidney, bowel etc.)	7
Total	162

Table 8.1: Lesion summary in patient cohort.

of liver, pancreas, kidney, bowel, rib and shoulder lesions, as well as an assortment of nodes and areas of benign uptake, spread across 32 patients. 12 patients had no identifiable 'hot spots' or lesions. From herein, we use the term 'lesion' to describe any of these marked areas of focal tracer uptake. These are summarised in table 8.1.

8.3.2 Protocol

After the main clinical/research scan, each patient underwent an extra four minute PET/MR acquisition to mimic a three minute single bed position in a whole-body scan, plus an extra one minute for motion modelling, as described in Section 7.5, consisting of PET list-mode (4 min), MR Dixon (18s) and MR GRE (1 min). The mean time interval from radiotracer injection to the extra PET/MR acquisition was 1 hour 39 minutes \pm 33 minutes.

8.3.3 Data Processing

A motion-compensated reconstruction of the extra four minute PET acquisition was carried out using deformation fields estimated by the 2D linear model, with PET data binned using the patient-specific scheme outlined in Section 7.5. The attenuation μ -map was warped to the exhale position with deformation fields estimated by the motion model and warped to each gate, using the values of the surrogate signals P and P' during the MRAC sequence acquisition, and randoms and scatter correction was again used. Each PET acquisition was reconstructed without motion correction, and with motion correction, and both with attenuation correction (AC) and without attenuation

correction (NAC). All images were then converted into DICOM format.

8.4 Methods

8.4.1 Global sharpness

Motion correction was assessed in all data sets with image sharpness using the Tenengrad Variance Sharpness (TVS) metric, as used in Section 7.3.1. This was done on NAC PET images, to avoid the confounding effects of the attenuation correction map also requiring motion correction.

8.4.2 SUV Analysis

Lesions were identified with a consensus read by two accredited radiologists, using combined reading of all imaging studies, including original uncorrected PET, diagnostic MR and CT, and follow-up PET at a later scan date where available. Change in SUV metrics, $\Delta\text{SUV}_{\text{peak}}$ and $\Delta\text{SUV}_{\text{max}}$ in AC PET images were assessed.

8.4.3 Lesion Detectability Study

The effect of motion correction on lesion detectability and localisation was assessed with a lesion detection study. Two accredited radiologists viewed the U and MC images for each patient data set, blinded. Images were read in two sets, with the U and MC images for each patient split between the two sets randomly, and with at least a two week interval between reads of each set to minimise recall bias. Each reader marked suspected lesions on each image, with a four-point confidence score χ . These were defined as the presence of a lesion at each location being either:

- $\chi=1$. questionable (<50% likely)
- $\chi=2$. possible (50-75% likely)
- $\chi=3$. probable (75-95% likely)
- $\chi=4$. definite (>95% likely)

Scores provided by reader 1 and reader 2 are referred to as χ_1 and χ_2 respectively. A lesion localisation was also attributed by the readers to each mark, identifying the assumed location of the lesion, as either 'liver', 'pancreas', 'lung', or 'other'.

The reference standard used to define the locations of true lesions was the consensus reading of all imaging studies defined previously, and was carried out after the individual lesion detection reads. Data was analysed in the style of a FROC study. Each marked lesion that matched a lesion in the reference (true-positive) was defined as a lesion localisation (LL), and any lesion in the reference that was not marked by the reader (false-negative) was given a score of 0. Each marked lesion that did not match a lesion in the reference (false-positive) was defined as a non-lesion localisation (NLL).

For all lesions in both the LL and NLL sets, change in confidence rating for each lesion, $\Delta\chi$ is defined as the χ score for the MC image minus the χ score for the U image. For readers 1 and 2 these are referred to as $\Delta\chi_1$ and $\Delta\chi_2$ respectively. An increase in these values represents an increase in detection confidence, and a decrease represents a decrease in detection confidence after motion correction.

8.4.4 Statistical Analysis

Significance of differences in image sharpness and lesion detection confidence scores between U and MC images was made with the Wilcoxon signed rank test. For SUV metrics of lesions a paired sample t-test test was used.

8.5 Results

A quantitative analysis summary is provided in Table 8.2. Each set of results is explained in more detail below. Two patient data sets were excluded from the SUV analysis and detectability study only. One was a sarcoidosis patient, where structural changes in the lung caused problems with the attenuation map and the PET image was therefore un-readable. For the other, Florbetapir was the administered tracer, giving unusual tracer distribution which the blinded readers would need to know to effectively read the image. One patient was removed from all studies due to non-respiratory bulk motion during the scan.

8.5.1 Global sharpness

Figure 8.1a shows a box plot of Δ TVS sharpness scores between U and MC NAC PET images in the 44 patient data sets. Overall, there was a significant increase in image sharpness in the NAC MC images compared to the NAC U images ($p < 0.0001$), with a

Metric	Uncorrected	Motion-corrected	Paired Significance
TVS sharpness	median 20.76×10^{-5}	median 21.25×10^{-5}	$p < 0.0001$ (Wilcoxon)
SUV_{peak}	mean 17.6 ± 18.0	mean 19.5 ± 20.1	$p < 0.0001$ (t-test)
SUV_{max}	mean 22.7 ± 22.6	mean 26.6 ± 29.9	$p < 0.002$ (t-test)
Detection score χ	2.67 ± 1.50	3.01 ± 1.29	$p < 0.0001$ (Wilcoxon)
LL (true-positive) rate	74%	84%	N/A
NLL (false-positive)	30 lesions	21 lesions	N/A

Table 8.2: Quantitative results summary. Image sharpness includes all data sets, SUV metrics include all lesions, and detectability metrics include all non-excluded data sets. The LL and NLL numbers are out of 84 data sets (42 patients \times 2 readers). Statistical significance is based on paired scores from uncorrected and motion-corrected data sets.

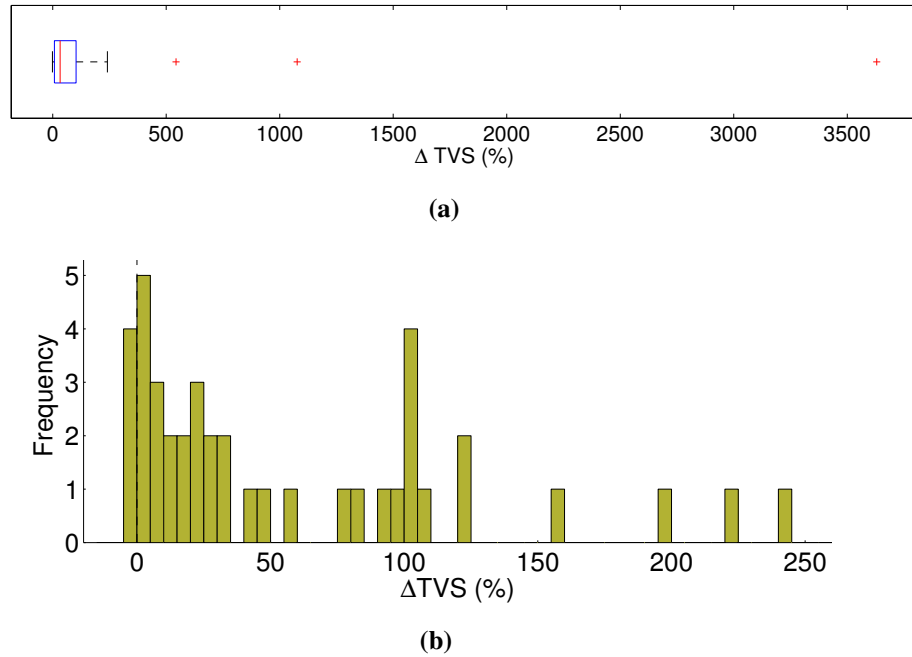


Figure 8.1: ΔTVS for all 44 patients. (a) box plot of all data points, (b) histogram with 3 outliers cut out. Positive change in TVS indicates an increase in image sharpness after motion correction.

mean increase of 173%. Figure 8.1b shows a histogram with 3 outliers cut out which show extreme increases in TVS of 540%, 1080% and 3630%. Without these outliers, ΔTVS is in the range of -1% to 241%, with a median of 33%.

8.5.2 SUV Analysis

All SUV analysis was done on lesions confirmed in the reference read as a consensus between the two readers. Of 162 confirmed lesions, 72 were confirmed with MR only, seven with CT only, and 62 with both. 21 lesions were confirmed either from PET follow-up, or from PET only, considering patient history and information.

Over all 162 confirmed lesions, there was a significant increase in both SUV_{peak} ($p < 0.0001$) and SUV_{max} ($p < 0.002$), with a mean increase of 12.4% for SUV_{peak} , and a mean increase of 17.6% for SUV_{max} , via motion-correction.

Figure 8.2 shows ΔSUV_{peak} and ΔSUV_{max} for all lesions, with 8.2a showing a histogram for all lesions, and 8.2b showing a close-up with some outliers excluded. Of all lesions, 14% (22 lesions) show a negative change, and 86% (140 lesions) show a positive change in SUV_{peak} , whilst 17% (27 lesions) show a negative change, and 83% (27 lesions) show a positive change in SUV_{max} .

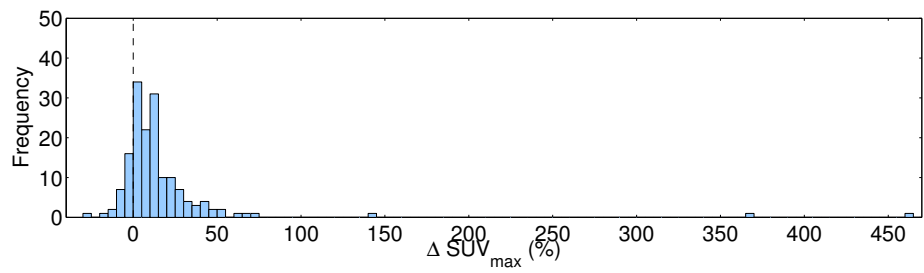
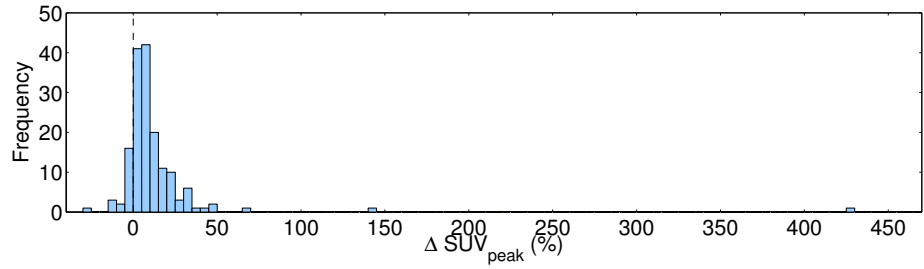
Defining 'considerable change' as only those with a magnitude of change greater than 5% for both ΔSUV_{peak} and ΔSUV_{max} ; 3% (five lesions) show considerable decrease, 43% (69 lesions) show inconsiderable change, and 54% (88 lesions) show considerable increase. The five lesions that showed considerable decrease were a lung node, lung lesion, rib lesion and two bowel lesions.

8.5.3 Lesion Detectability

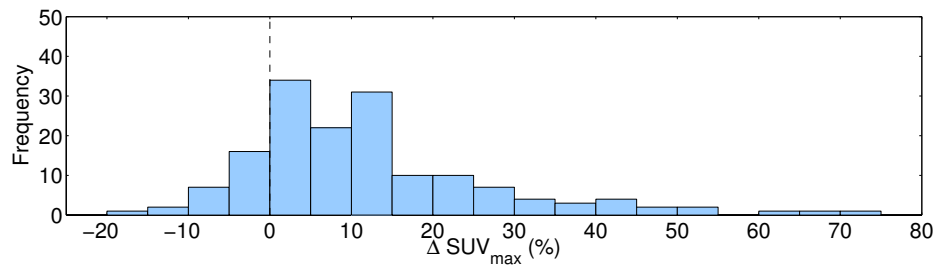
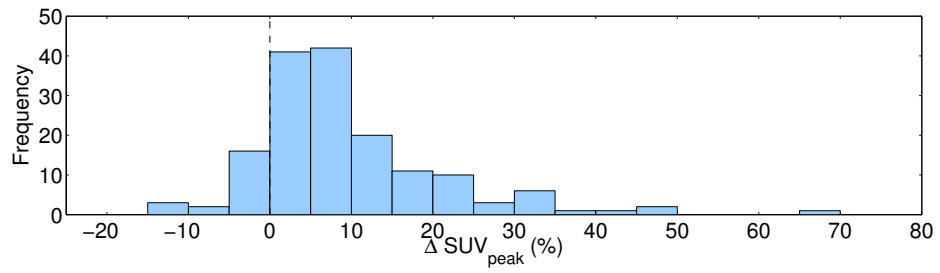
The LL rate (lesions positively identified with a score of 1 to 4), or sensitivity, for U and MC images was 85% and 95% for reader 1, and 62% and 73% for reader 2. In total, for 324 lesions (162 lesions x 2 readers), the LL rate was 74% (238 lesions) in the U images, rising to 84% (272 lesions) in the MC images.

Figure 8.3 shows $\Delta \chi$ scores for LL results. Figure 8.3a shows $\Delta \chi$ distribution for all 162 lesions, for each reader. Figure 8.3b shows the combined scores of $\Delta \chi_1$ and $\Delta \chi_2$ on one histogram, for 324 lesions. Overall, 8% (26 lesions) show a negative change, 69% (224 lesions) show no change, and 23% (74 lesions) show a positive change in confidence ratings.

Figure 8.3c shows the sum of detection scores $\Delta \chi_{1+2}$ for each lesion, with a possible range of scores of -8 to 8. Overall, 11% (18 lesions) show a negative change (range -4:-1), 53% (86 lesions) show no change, and 36% (58 lesions) show a positive



(a)



(b)

Figure 8.2: $\Delta\text{SUV}_{\text{peak}}$ and $\Delta\text{SUV}_{\text{max}}$. (a) histogram of all 162 lesions, (b) histogram with some outliers removed.

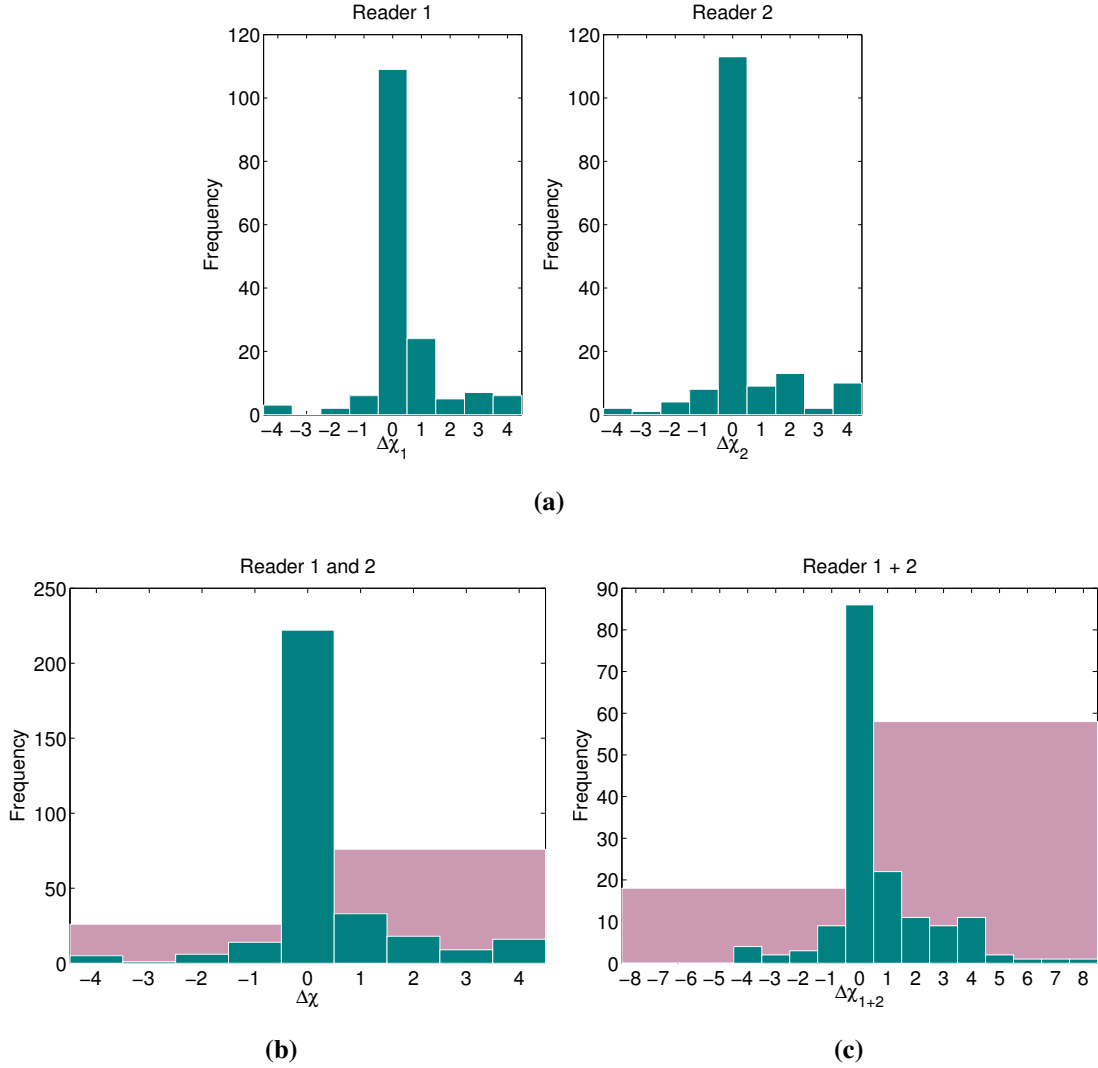


Figure 8.3: Change in confidence χ scores for true-positives (LL), for (a) reader 1 only and reader 2 only, (b) all reader 1 and 2 scores, (d) sum of reader 1 and 2 scores for each lesion. Green bars represent the number of lesions with specific values score changes. Pink bars represent the total number of lesions with negative or positive score changes, where positive change is 'good' - true lesions are more detectable after motion correction.

change (range +1:+8).

There was a significant increase in summed detection confidence scores, $\Delta\chi_{1+2}$ from the U images to the MC images, for the group of all reference lesions ($p < 0.0001$).

We aim to reduce the intrinsic intra- and inter-observer variability of the scoring test by examining score changes where $\Delta\chi_1$ and $\Delta\chi_2$ are either both positive or both negative; where the two readers are in agreement as to whether a lesion has increased or decreased in detectability. Figure 8.4 shows confidence scores for 14 lesions where this was the case, with one lesion showing negative change for both readers (range -

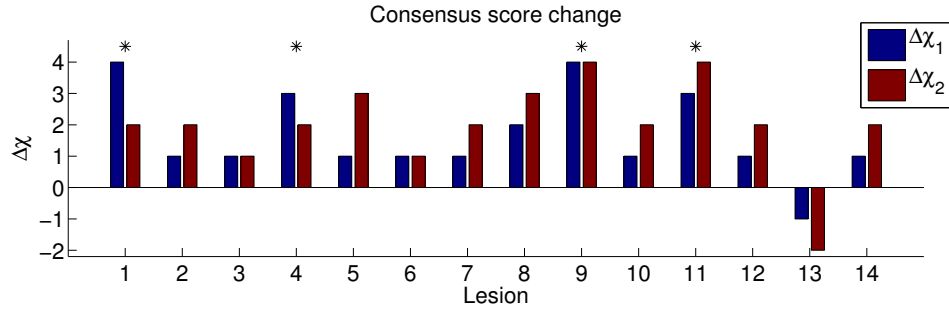


Figure 8.4: True-positive (LL) consensus scores (both positive or both negative change). The asterisk (*) denotes lesions which were not detected in the U image, then detected to some degree in the MC image by both readers.

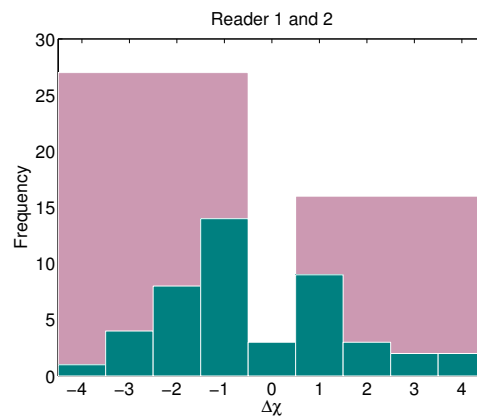


Figure 8.5: Change in confidence χ scores for false-positives (NLL) after motion correction. Green bars represent the number of lesions with specific values score changes. Pink bars represent the total number of lesions with negative or positive score changes, where negative change is 'good' - false lesions are less detectable after motion correction.

1:-2), and 13 lesions showing positive change for both lesions (range +1:+4). For four of these lesions, confidence scores changed from 0 in the U images for both readers, i.e. lesions which were invisible to both readers in U images, then detectable to some degree in the MC images to both readers.

The total number of non-lesion localisation (false-positive) detections, combining results from both readers was 30 in U images and 21 in MC images. Figure 8.5 shows the combined scores of $\Delta\chi_1$ and $\Delta\chi_2$ for NLL results. Overall, 27 lesions show a negative change, three lesions show no change, and 16 lesions show a positive change in confidence ratings, for marked areas assumed to not be true lesions from the reference read.

8.5.4 Cross-study Correlation

Overall, considering the three metrics of $\Delta\text{SUV}_{\text{peak}}$, $\Delta\text{SUV}_{\text{max}}$, and $\Delta\chi_{1+2}$, two lesions showed a negative change in all metrics and 49 showed a positive change in all metrics. Those that showed negative change were a mediastinal lymph node and a bowel lesion.

8.6 Clinical Case Studies

In this section we present a number of case study examples to show the effects of motion correction on AC PET images, considering potential to affect clinical patient management.

8.6.1 Case Study 1: New Lesions Detected with MR confirmation

Case study 1 is a ^{68}Ga -DOTATATE scan of a patient (age 70-80) who had undergone a partial liver resection. The referral stated that a previously acquired octreotide scan revealed a hot spot in liver, and MRI showed at least two suspicious lesions in liver and several smaller concerning deposits throughout the liver, suspected to be metastatic neuroendocrine disease. This prompted the request of a PET/MR scan.

In total, change in detection scores for three very small lesions was $\Delta\chi_{1+2} = [+1,+1,+1]$, with six of the total reads (3 lesions \times 2 readers) providing three newly detected lesions in the MC images. All three were confirmed to be present in the MR images during the consensus reference read. Figure 8.6 shows one of the lesions in both axial and coronal views on U and MC images, with the lesion contrast appearing much greater in the MC image. SUV results verify these results, with $\Delta\text{SUV}_{\text{peak}} = [+10\%,+5\%,+20\%]$ and $\Delta\text{SUV}_{\text{max}} = [+19\%,+14\%,+16\%]$. Absolute SUV values for the three lesions are shown in Figure 8.7.

In the context of the original doctor referral, it has been shown that at least three lesions demonstrate DOTATATE avidity, confirming that these are likely metastatic neuroendocrine lesions. This information would influence decision regarding choice of treatment, which may be drug treatment (e.g. octreotide analogue), percutaneous ablation or resection.

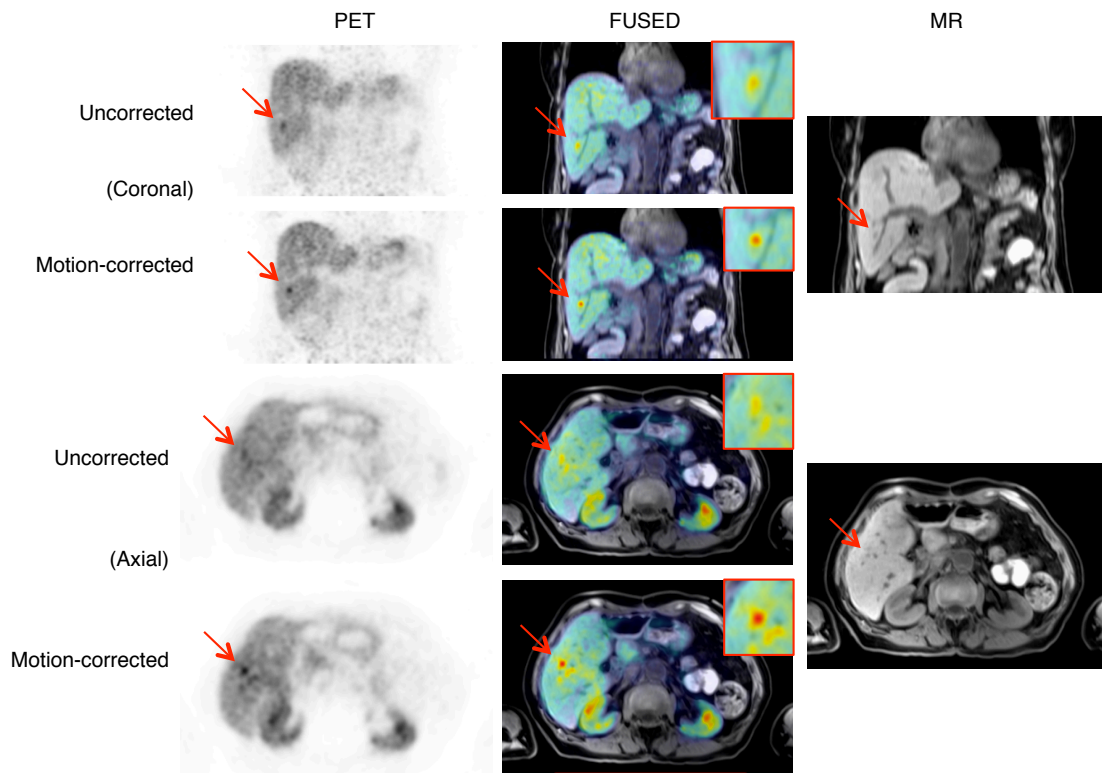


Figure 8.6: Case study 1. Lesion 1, coronal and axial slices of U and MC PET images, and fused with T1 Dixon VIBE MR.

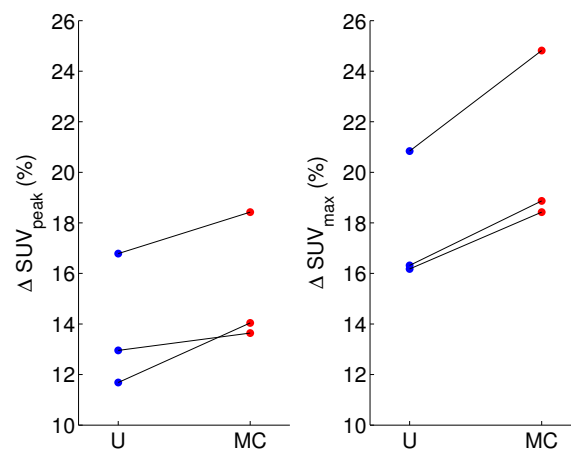


Figure 8.7: Absolute SUV_{peak} and ΔSUV_{max} values in U and MC images for three lesions.

8.6.2 Case Study 2: New Lesions Detected with PET Follow-up confirmation

Case study 2 is a ^{68}Ga -DOTATATE scan of a patient (age 40-50) with a previous scan showing pancreatic lesions were present. A PET/MR scan was requested to assess lesion uptake and determine possible surgical approach.

The detection results showed a total change in detection scores in six lesions of $\Delta\chi_{1+2} = [+3,+2,+5,+4,+4,+3]$. In the U image, readers 1 and 2 detected four lesions and one lesion respectively, and in the MC image readers 1 and 2 detected six lesions and five lesions respectively. Although the lesions were not verified in the MR images available, all six lesions were confirmed as present in the reference read due to also being visible in a follow-up scan carried out one year later. This would be in keeping with published data on superiority of PET in detection of neuroendocrine lesions over CT/MR. In the follow-up scan, total change in detection scores in the six lesions was $\Delta\chi_{1+2} = [0,+2,0,0,0,0]$. All six lesions were detected in both the U and MC images in the follow-up scan. The $\Delta\chi_{1+2}$ were lower in the follow-up, potentially due to the lesions growing in the time between scans and showing higher tracer uptake. At follow-up, all lesions still showed improvements in contrast, as visible in Figure 8.8.

SUV results verify this increase in lesion contrast, with lower absolute SUV values in the follow-up scan, shown in Figure 8.9. SUV increases were $\Delta\text{SUV}_{\text{peak}} = [+32\%,+3\%,+25\%,-5\%,+40\%,+10\%]$ at baseline and $\Delta\text{SUV}_{\text{peak}} = [+11\%,+22\%,+22\%,-4\%,+30\%,+16\%]$ at follow-up. The one lesion with a decrease in SUV_{peak} was located very close to the spleen, and still showed an increase in SUV_{max} in both baseline and follow-up.

The increased number of detected lesions in the baseline scan is crucial. Accurate mapping of the number and location of tumours in the pancreas would dictate the extent of pancreatectomy needed for curative surgery, which in turn influence decision of whether surgery should be the optimal treatment modality for this patient. The larger the extent of pancreatectomy, the more complex the surgery would be and the risk of subsequent diabetes as a complication.

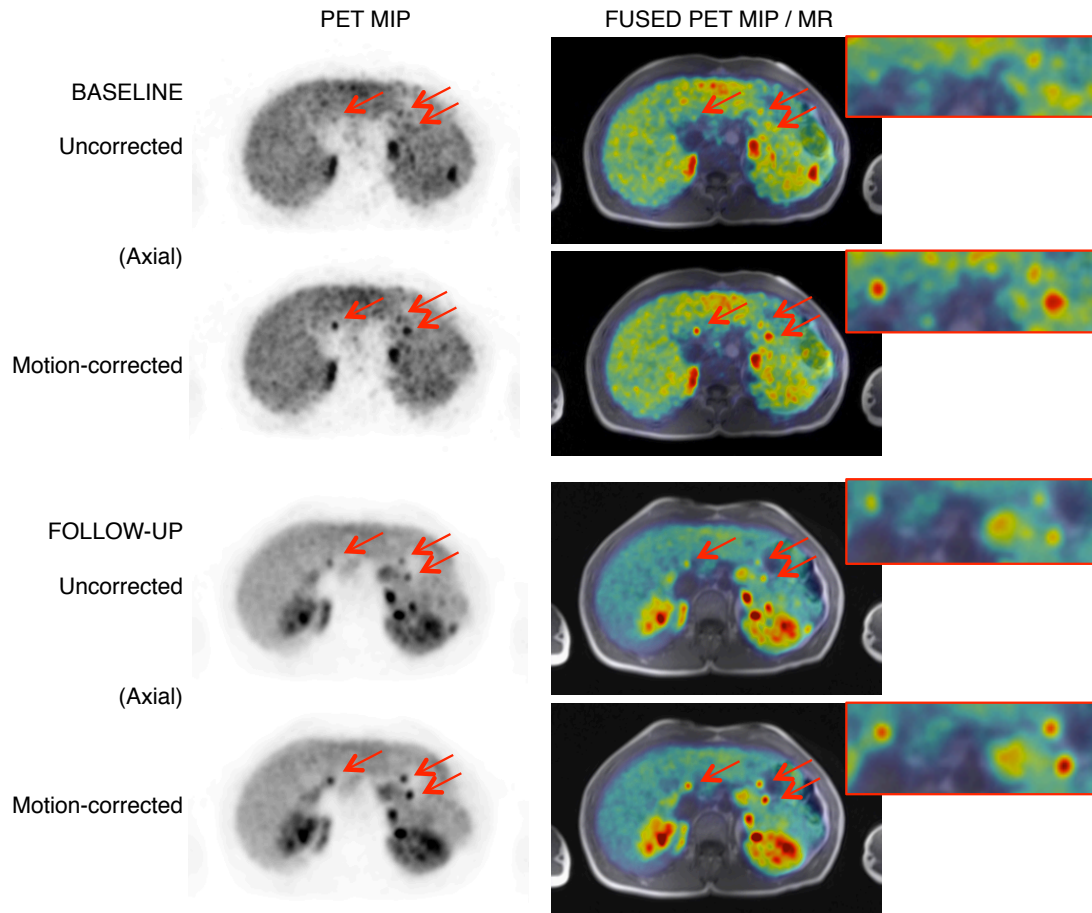


Figure 8.8: Case study 2. PET maximum intensity projection (MIP) image showing 3 pancreas lesions and axial views of U and MC PET images in both the baseline and follow-up PET scans, and fused with T1 Dixon VIBE MR.

8.6.3 Case Study 3: Lesion Localisation Change

Case study 3 is an ^{18}F -FDG scan for a patient (age 40-50) with known liver metastases found in a previously acquired CT scan, and a PET/MR scan was requested for staging.

Lesion localisation for one reader changed from lung to liver following motion correction. The reference read for this patient showed eight lesions, with all confirmed in the liver on the MR. This change in location is demonstrated in Figure 8.10a, showing a PET maximum intensity projection (MIP) of the U image. The location of the two lesions at the lung/liver interface is unclear in both the NAC and AC images, however in the MC image, it is clear that the lesions are located in the liver. The fused PET/MR images show better spatial alignment of the PET and MR images in the MC case in Figure 8.10b.

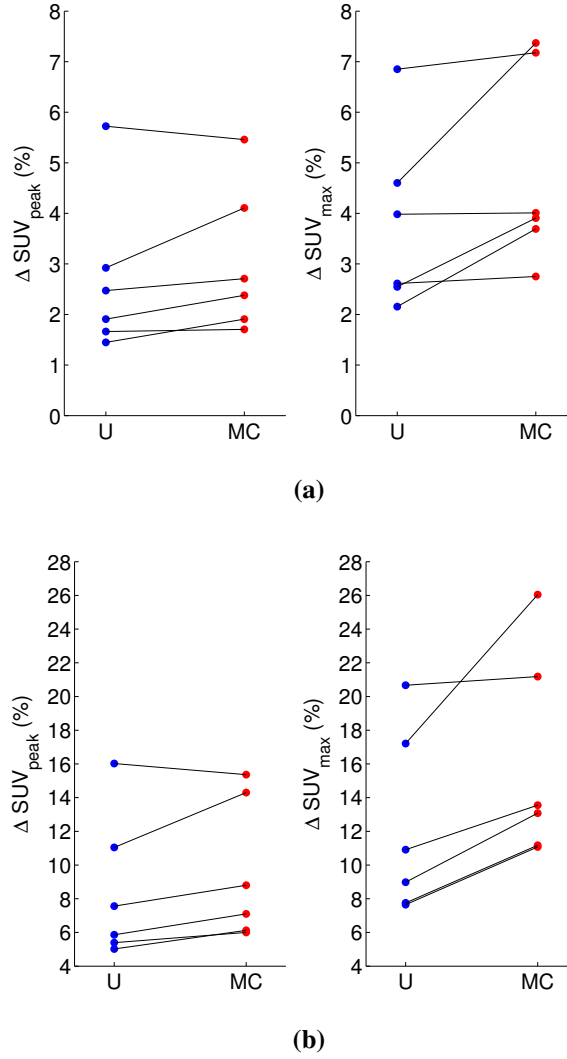


Figure 8.9: Absolute SUV_{peak} and $\Delta \text{SUV}_{\text{max}}$ values in U and MC images for six lesions in (a) baseline scan, and (b) follow-up scan.

This large change in location is due to the MRAC being acquired at deep exhale, and this being corrected for in the motion model, as discussed in Section 7.7. The re-alignment of the MRAC meant large changes in some SUV values, with $\Delta \text{SUV}_{\text{peak}} = [+142\%, +366\%]$ for the lesions which appeared to move from the lung in the U image to the liver in the MC image.

The correction of lesion localisation through motion correction is important for staging and treatment planning. Involvement of more organ systems by metastatic disease potentially escalates the disease stage, excludes the patient from surgical consideration and infers worse prognosis.

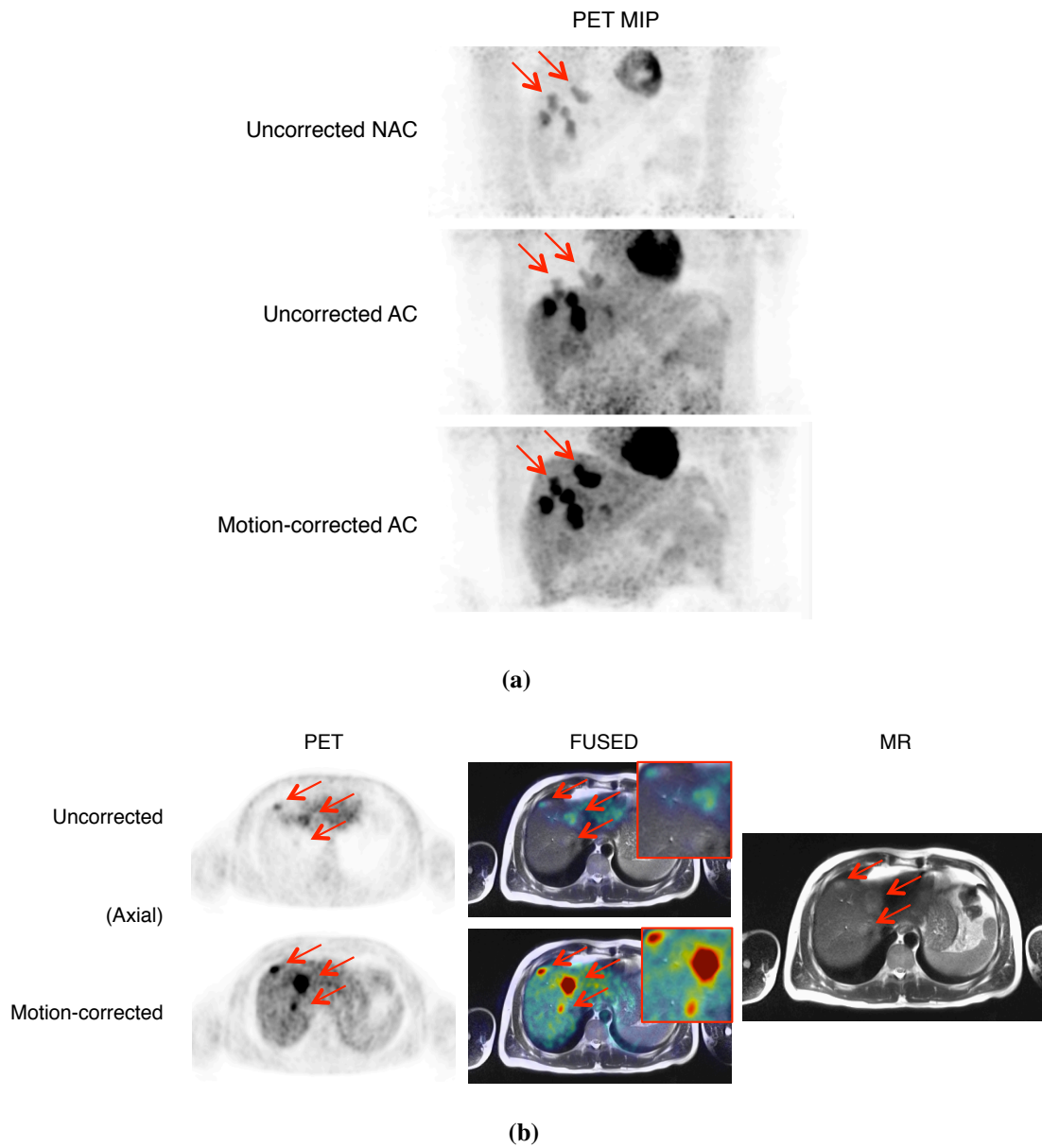


Figure 8.10: Case study 3. (a) MIP images for NAC and AC U images, and AC MC image. (b) axial PET slice with three lesions which wrongly appear in the lung in the U image and correctly in the liver in the MC image, and fused with T2 HASTE MR.

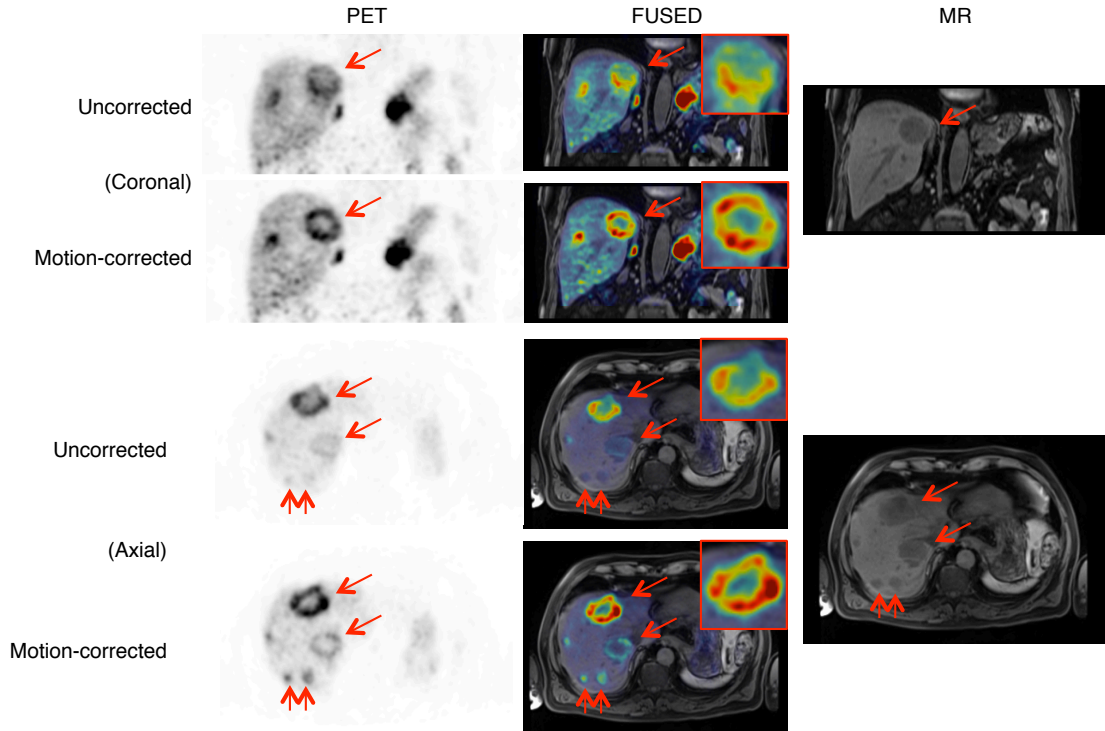


Figure 8.11: Case study 4. Coronal and axial slices of U and MC PET images, and fused with T1 VIBE SPAIR MR, showing change in shape of uptake in necrotic lesion.

8.6.4 Case Study 4: Lesion Shape Change

Case study 4 is a ^{68}Ga -DOTATATE scan (age 60-70). In this patient, detectability confidence scores showed either no change or a slight increase in all 11 lesions, with $\Delta\chi_{1+2} = [+1, +3, 0, +2, 0, 0, 0, 0, 0, 0, 0]$, with a $\Delta\text{SUV}_{\text{peak}}$ range of 0:+47% and a mean of 24%. The shape of the tracer uptake in three of these lesions was changed due to motion correction. These are necrotic lesions with uptake on the outer side of the lesion.

Although lesion detection and localisation has not been significantly changed, the uptake distribution within lesions could be of clinical importance. Specifically, this could affect perceived optimal site of any biopsy attempt (where most metabolically active area is generally believed to result in higher diagnostic yield) if biopsy is indicated. Intensity modulation of external beam radiotherapy based on metabolic information (from PET) or PET textural analysis could be grossly mis-informed without correction, although these latter are largely experimental currently.

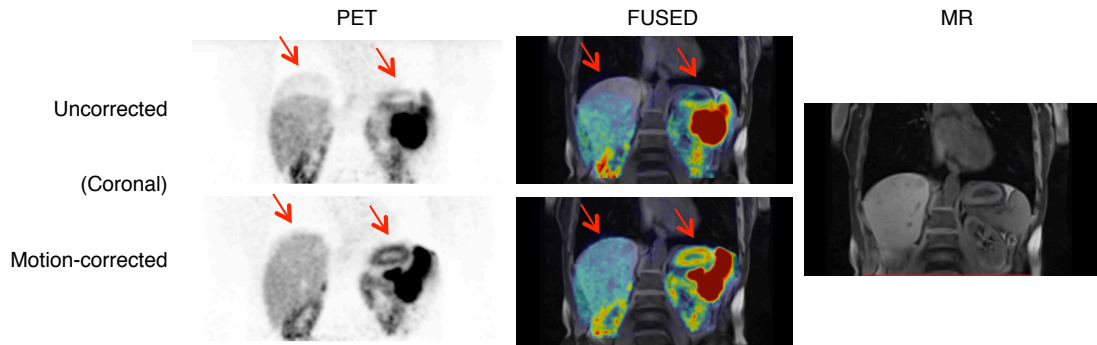


Figure 8.12: Case study 5. Coronal slice of U and MC PET images, and fused with T1 VIBE MR, showing a reduction in attenuation misalignment artefacts.

8.6.5 Case Study 5: Artefact Reduction

Case study 5 is a ^{68}Ga -DOTATATE scan (age 50-60). Previous CT showed a mass in the pancreatic tail, and a PET/MR scan was requested before consideration for surgery. In this patient there was 1 pancreas lesion that was correctly identified by both readers in both U and MC images, with $\Delta\chi_1=0$ and $\Delta\chi_2=0$. The artefact in the U image due to a mis-aligned attenuation map has been corrected in the MC image, as seen in Figure 8.12. In the PET images it is clear that the banana artefact at the top of the liver has been removed and the shape of high uptake in the stomach has been restored to match the shape of the stomach as seen in the MR. The MC PET image now spatially aligns better with the MR.

8.6.6 Case Study 6: Improved Cardiac Uptake

Case Study 6 is a ^{18}F -FDG scan (age 40-50). This patient had no lesions but has increased and sharper uptake in the heart in the MC image, as seen in Figure 8.13.

Although myocardial uptake in oncology FDG PET scans are generally non specific and usually non contributory, this case demonstrates the potential benefit of our technique in cases of dedicated cardiac PET, where distribution, degree of heterogeneity and intensity of uptake are integral to image interpretation; and which is the gold standard for non invasive assessment of myocardial inflammation and viability.

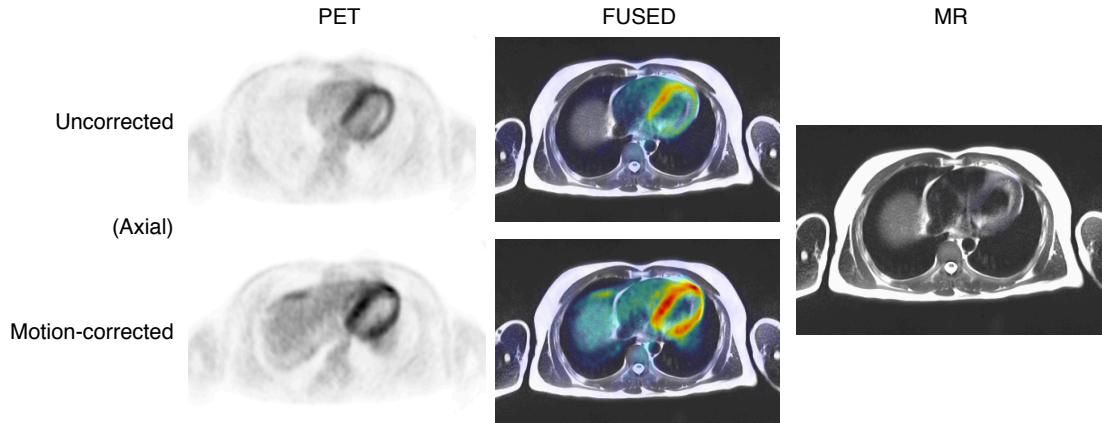


Figure 8.13: Case study 6. Axial slice of U and MC PET images, and fused with T2 HASTE MR, showing increased cardiac uptake.

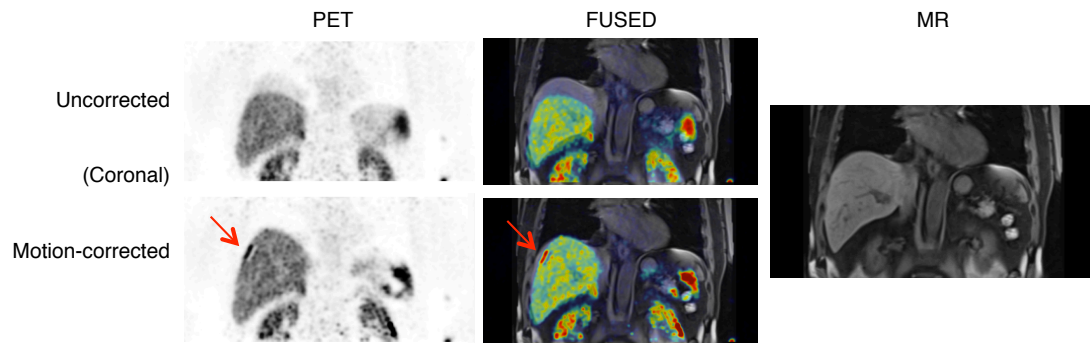


Figure 8.14: Case study 7. Coronal slice of U and MC PET images, and fused with T1 VIBE MR, showing an artefact introduced by motion correction.

8.6.7 Case Study 7: Motion-correction Induced Artefact

Case study 7 is a ^{68}Ga -DOTATATE scan (age 60-70). In this example it appears that although the attenuation-based artefact due to attenuation map misalignment has been removed, an extra artefact has been introduced at the top of the liver, at the side near the ribs. This was one of two data sets out of 42 that were noted by the readers during the detection reads that contained an artefact, which we later found were not present in the U images.

8.7 Discussion

This chapter has provided a pilot study for a clinical validation of our joint PET-MR model-based motion correction method. Significant increase in all tested metrics has been shown, with a median increase of 33% (excluding positive high outliers) in

overall image sharpness and mean increases of 12.4% and 17.6% in SUV_{peak} and SUV_{max} respectively. We also showed an increase in confidence scores of readers detecting avid lesions, with a mean score of 2.67 rising to 3.01 through motion correction, and an LL (true-positive) rate of 74% rising to 84%. We found only two lesions (out of 162) that showed a negative change in all three metrics SUV_{peak} , SUV_{max} and $\Delta\chi_{1+2}$, whilst 49 lesions showed a positive change in all metrics.

Through the case studies, a number of clinical examples were presented to understand the range of positive (and negative) effects that respiratory motion with our methodology correction can have. Examples were shown where motion correction lead to newly detected lesions, increased lesion sharpness and detectability, artefact reduction, and better lesion localisation and shape definition.

One patient was excluded from all studies due to bulk motion occurring during data acquisition, which the current methodology does not account for. Although this has been examined in other PET/MR studies [Kolbitsch et al., 2014], it is not a common occurrence during a short four minute bed position scan, as illustrated by the fact that it only happened to a single patient out of 45 in this work.

There are some limitations to the utilised quantitative metrics. Firstly, with TVS sharpness, although a positive change in TVS is seen in most patients, the large variance as seen in mean values in Table 8.2 show the unpredictability of the absolute values. Three data sets showed very large increases (above 500%), and although two of these show visual increases in sharpness, the largest of 3630% was possibly due to the addition of unwanted motion-correction induced artefacts, as seen in case study 7 (Section 8.6.7). Results like this that show positive change even though the motion-corrected image is corrupted are obviously misleading, however, the rest of the MC image is visually better due to attenuation map realignment, so it is possible that the large increase is still indicative of a 'generally' sharper image.

The introduction of this artefact at the edge of the liver (Figure 8.14) in two data sets possibly stems from discrepancies between the forward and backward motion models used to form deformation fields for the motion-corrected PET reconstruction. The absolute difference between these motion model coefficient matrices A_1^y for forward and backward models (as described in section 6.4.3) is also shown in Figure 8.14. For the MCIR method described in Section 5.4.7, the backwards warping matrix

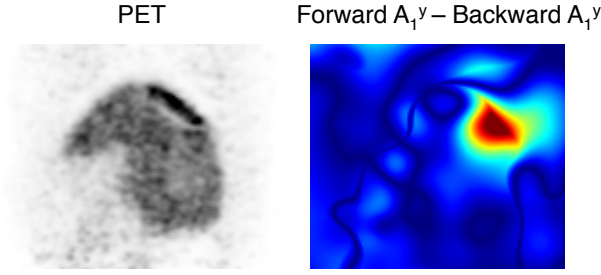


Figure 8.15: Sagittal PET slice from Case study 7, with the difference between coefficients for forward and backwards motion models.

W_g^{-1} is used. In our methodology, W_g and W_g^{-1} are calculated with independent registrations, and are not guaranteed to be inverse operations. This problem of independent registrations providing forward and backward models could be overcome by using the transpose W_g^T rather than an (approximation of an) inverse transformation, and will be discussed in the next chapter.

In the SUV analysis, outliers visible in Figure 8.2a arise from good results, where the large increases in lesion SUV_{peak} and SUV_{max} are due to attenuation map misalignment being corrected through motion correction, similar to the example seen in Section 7.6.2. The only five lesions that show considerable (more than 5%) decrease in SUV measurements could be due to the lesion locations. Two of these (including the largest decrease of 25%) were lesions located in the bowel, which is an area in which the motion model cannot predict motion due to bowel motion being sporadic and unrelated to respiration. Another was located on a rib, which could have suffered from poor deformation estimation due to the lack of sliding motion in the registration scheme, and the other two were in the lung of one patient with a very large lung mass, potentially causing unpredictable breathing patterns.

For the lesion detectability study, when considering combined lesion confidence scores from both readers, 11% of lesions showed negative change and 36% showed positive change, although the range is much smaller in the negative change set (-4:-1 vs. +1:+8). However, in reality both the number of positive and negatively changing lesions should be lower, with more lesions being unaffected in terms of human detectability due to motion correction. This is due to some limitations in the study.

The main limitation was intra- and inter- observer variability in interpretation of imaging studies. Figure 8.16a shows a lesion which visually becomes sharper and of

higher contrast in the MC image, yet one of the readers gave the lesion a lower confidence rating in the MC image than in the U image ($\Delta\chi = -1$). This in turn falsely adds to the number of lesions with decreasing confidence scores through motion correction.

The indeterminate nature of the consensus reference read for some lesions also adds more noise the detection results. For example, for some larger, coalescing or lobulated lesions it was ambiguous whether an area of high uptake should be marked as one or two lesions. This means that if the reference shows two lesions and a reader marks as only one then it will appear as if the lesion has been undetected. The images in Figure 8.16b show one such example where although the two lesions appear more separated in the MC image, one reader has marked it as only one lesion in the MC image, and marked two in the U image. We presume that this could happen either way round, causing lesions to be falsely given either a $\Delta\chi$ score of either -4 or +4.

Another limitation was the poor quality of the MR-based attenuation map used for attenuation correction, which includes no bone information. For the test, readers viewed the PET images in isolation, but for clinical reads the radiologists would often use the NAC PET images as artefacts often arise in the lungs due to attenuation correction problems. Figure 8.17 shows an example where the U and MC (not shown) PET images both portray two avid lung lesions. However, the CT only shows the upper lesion, whilst the lesion nearest the liver does not appear in the CT or NAC PET image. It seems that this lower lesion is falsely 'added' to the AC PET images due to segmentation error of the MR images in the generation of the μ -map for attenuation correction. This issue causes a higher NLL rate in both U and MC image sets. The un-natural way the readers were viewing the PET images, blinded to patient information, and without any other complimentary images such as MR or CT (intrinsic to hybrid PET/MR or PET/CT), also contributed to the low LL rates of 74% and 84% for U and MC.

We attempted to overcome intra- and inter- observer variability by analysing results from both readers together. For example, when looking at only results where $\Delta\chi$ was either positive or negative for both readers, 13 lesions showed an increase in detectability and only one showed a decrease. However, this single lesion had a higher SUV_{peak} and SUV_{max} in the MC image than the U image, meaning perhaps the

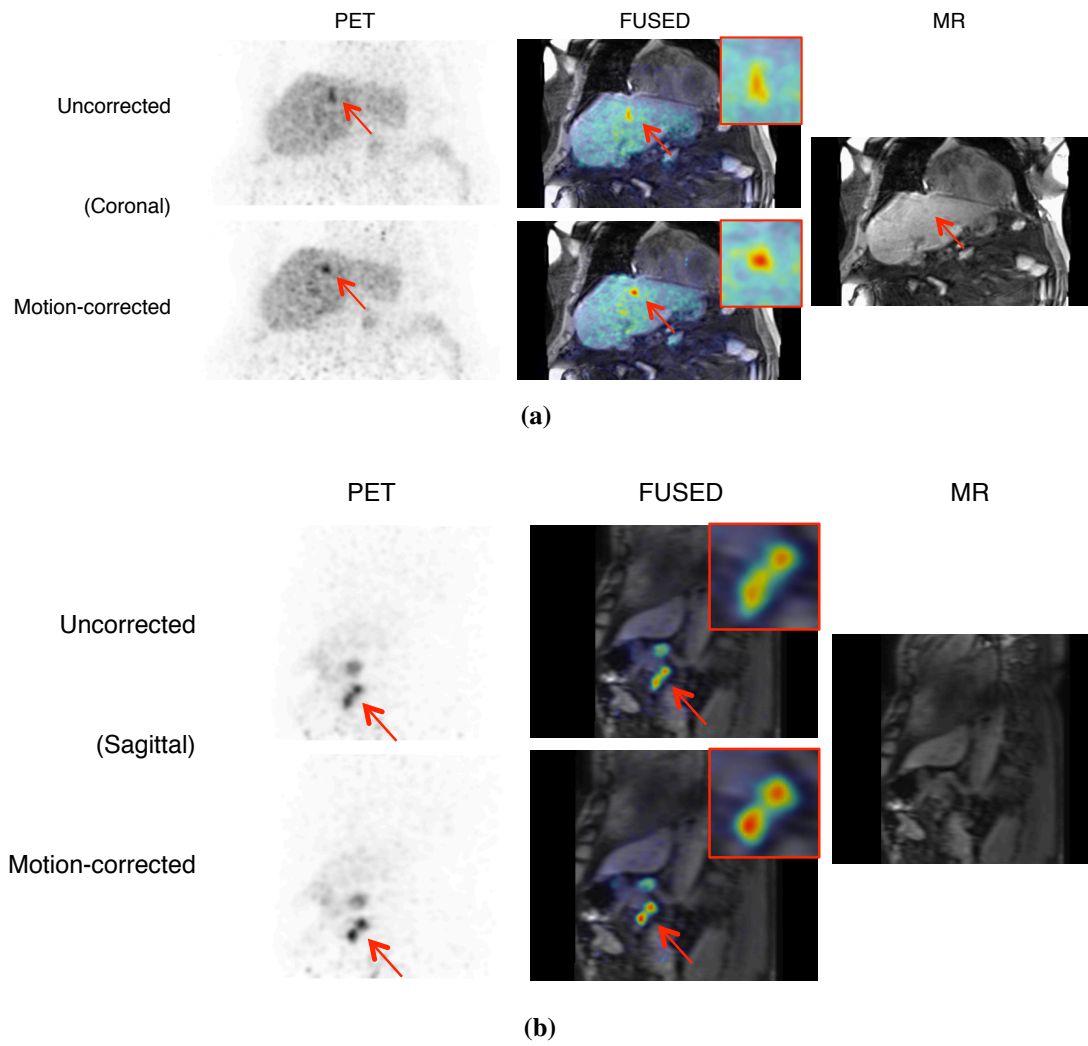


Figure 8.16: Examples of limitations in detectability study. (a) showing human error, where lesion given lower confidence score in MC image, and (b) area of high uptake marked as 1 lesion rather than 2.

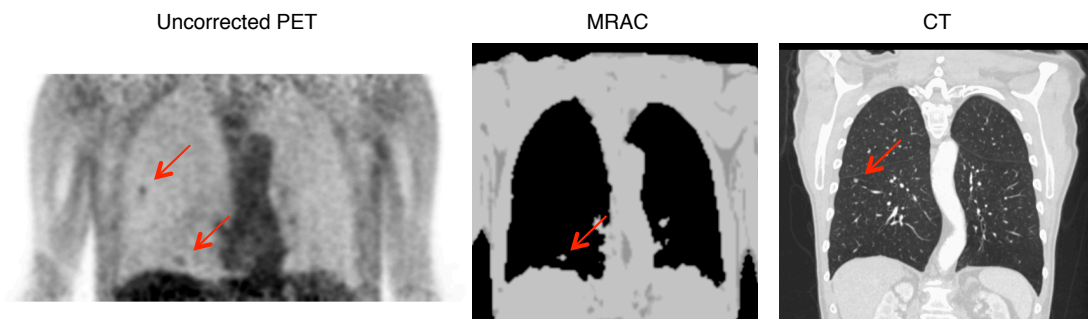


Figure 8.17: Lung lesion falsely 'added' to the uncorrected AC PET image due to segmentation error in the MRAC image. The CT image shows the location of the true lesion.

negative $\Delta\chi$ was also just due to human error.

The lack of a definite way to define false-positives (a PET avid lesion may not appear in MR or CT) applies to the results presented in this chapter for the NLL rate, where 30 lesions were detected in the U images and 21 in the MC images, from 84 data sets (42 patients \times 2 readers). These are marked as false-positives due to the lack of evidence in the patient information or other modality, but in reality some of these may be real lesions, and the NLL rate could therefore be lower.

At the start of this chapter we discussed the reasons for not carrying out a full FROC study. One possible way to conduct a proper FROC study with a homogeneous reference standard would be to use real patient dynamic MR and PET data, but with digitally inserted PET-avid lesions [Pet, 2011]. In theory, deformation fields found from MR registrations could be used to deform the PET data containing fake lesions. However, this would mean that the PET is perfectly deforming with the deformed fields used in the PET reconstruction, which would be unrealistic. On top of this, the deformation fields found with non-rigid MR registration are smooth and do not provide a perfect map of internal respiratory warping.

In conclusion, although some limitations to the study exist, we have demonstrated significant improvements in quantification and detection of PET-avid lesions in multiple tracers and multiple organ locations, with specific case study examples showing where motion-correction has the potential to have an affect on patient diagnosis or care. We consider the work in this chapter a pilot study as more data is needed, requiring a streamlined pipeline to process data efficiently, which will in turn allow practical use of the method in clinical practice. This is examined in the next chapter, along with other ideas for future work.

Chapter 9

Conclusions and Future Work

In this Chapter we review the main conclusions drawn from each chapter of work, and suggest possible routes for future work.

9.1 Conclusions

This thesis addressed the problem of motion blurring due to respiration in PET imaging, and explored methods to track and correct for this motion with a simultaneous PET/MR scanner. Chapter 1 described the motivation and plan for the thesis and outlined my contributions. In Chapter 2 we provided a brief description of the principles of PET and MR, the simultaneous PET/MR scanner, and how it is typically used in the clinic. Applications of PET in oncology were also considered, as many of these are affected by respiratory motion correction. Chapter 3 described the tools required for PET motion correction, from theory of respiratory mechanics and respiratory signals, to PET gating and image registration, including techniques described in the literature for PET, MR and PET/MR based motion correction.

In Chapter 4, we performed a validation of a PET-derived respiratory signal formed via low spatial resolution framing and Principal Component Analysis, by comparing with a respiratory cushion, and with an MR pencil-beam navigator which provided an absolute measure of diaphragmatic displacement. After an initial pilot study, PET and MR-derived signals were compared in nine patient data sets with a range of tracers and diseases, and a strong mean positive correlation was found ($\rho=0.89$). Simple gating of data sets by the two different signals also showed comparable results. This provided confirmation that the PET-derived signal could be used for motion tracking in further chapters, and provided an understanding of which

parameters should be used for extracting the signal.

The tools to carry out PET respiratory motion correction were described in Chapter 5, with a methodology for PET and MRI data acquisition and processing, binning, deformation field formation via MR image registration and motion-compensated PET reconstruction including attenuation, scatter and randoms correction. Many of these techniques were used in subsequent chapters. We showed via SUV_{peak} and SUV_{max} metrics, as well as visible artefact reduction, that motion correction of simultaneously acquired PET data, and PET data acquired (up to one hour) earlier during the clinical scan was possible. We also showed only one minute of the motion-capturing MR sequence was necessary with our 2D multi-slice sagittal GRE sequence. Mean increases in SUV_{peak} and SUV_{max} were demonstrated in a patient with four pancreatic lesions, of 23.1% and 34.5% in PET acquired simultaneously with motion-capturing MR, and 17.6% and 24.7% in PET acquired almost an hour prior as part of the clinical scan. A number of limitations of using a discrete binning approach were discussed, including the discarding of many of the MR images and relying on one image per bin to be representative, and also discarding of PET data that fell outside of the range of breathing observed during the MR acquisition.

A methodology for a continuous joint PET-MR continuous motion model was described in Chapter 6, using one minute of simultaneously acquired PET and MR data to provide a respiratory motion model that captured inter-cycle and intra-cycle breathing variations. The methodology addressed many of the limitations found with the discrete binning method used in the previous chapter. The continuous nature of the model allowed interpolation and extrapolation at any respiratory signal value, meaning 100% of PET data could be used in the reconstruction, and deformation fields could be estimated even at extreme values such as at deep inhale for the MRAC sequence. All slices of the MR acquisition were used, with an optimisation scheme to form the model that was robust to registration errors at single slices. The optimisation also accounts for the shift and drift between the PET and MR clocks. Various types of model were tested (one and two surrogates, linear and polynomial) on MR data for 45 patient data sets. We found that the 2-surrogate polynomial model performed best on MR data used to form the model, and the 2-surrogate linear model performed best when predicting

motion on MR data not used to form the model, in all image-based metrics.

In Chapter 7, the joint PET-MR motion models were used to estimate deformations during a PET scan, and account for the motion in the PET reconstruction for five patient data sets. A novel strategy to gate PET data depending on the breathing range of the patient during the scan was also outlined and used in the methodology. On average over all lesions in the five patients, the 2-surrogate linear model performed best with SUV metrics. Although this was not statistically significant, this combined with the fact the same model performed significantly better than the other models when tested on MR data, lead us to conclude that this model should be used for a clinical validation on a large patient cohort.

Finally, we tested the 2-surrogate linear joint PET-MR motion model in Chapter 8. A full quantitative assessment with 45 patient data sets was carried out by examining image sharpness in all NAC PET data sets, and with SUV metrics on 162 avid lesions. Mean increases of 12.4% for SUV_{peak} and 17.6% for SUV_{max} through motion correction were found. With a human detectability study, we also showed an increase in confidence scores for detecting avid lesions, with a mean score of 2.67 rising to 3.01 (out of 4) via motion correction, and a detection rate of 74% rising to 84%. Only two lesions showed a negative change in all three metrics SUV_{peak} , SUV_{max} and combined reader confidence scores, whilst 49 lesions showed positive change. We also presented a number of clinical case studies, demonstrating the effect respiratory motion correction of PET data can have on patient management, with increased numbers of lesions detected, improved lesion sharpness, localisation, and shape definition, as well as improved image sharpness and reduced attenuation based artefacts.

9.2 Future Work

9.2.1 Potential Improvements to Methodology

There are a number of aspects to the joint PET-MR motion model methodology used in Chapter 8 that could be improved upon, some of which were included in the discussions of previous chapters.

The first is the choice of MRI sequence used. In Chapter 5 the choice was explained, deciding on a 2D multi-slice GRE sequence, which provided good spatial

and temporal resolution, without suffering from the artefacts present in other sequences tested. The main limitation of using a 2D multi-slice sequence is the disregard of potential left-right motion. There are a few options to make the acquisition fully 3D. Sagittal slices could be acquired at more slice locations so they are contiguous [Würslin et al., 2013, Baumgartner et al., 2013]. However, with the current MR imaging parameters used, this would increase the acquisition time by a factor of around 2.5, so the 1 minute of MR would take 2.5 minutes to acquire to give the same number of images per slice location. Fast whole 3D volumes could be acquired but for each to appear static and contain no motion artefacts, spatial resolution would need to be compromised [King et al., 2012]. A 3D high resolution acquisition could also be used, through free breathing, with k-space lines retrospectively binned and then each bin reconstructed. This would give uneven k-space coverage within each bin, leading to artefacts which may adversely affect registration performance. One technique that has become more prominent in the literature is to use a golden-radial phase encoding MR k-space trajectory, with an iterative non-cartesian reconstruction, which would provide a more even coverage of k-space in each bin and reduce artefacts [Buerger et al., 2013, Kolbitsch et al., 2014], (see Section 3.6.2).

MR images were collected at nine sagittal slice locations but data at the outer locations are often redundant as they image only non-moving sections at the edges of the body. Fewer slice locations could be used, resulting in a more efficient acquisition reducing the additional scan time further to under one minute, or slice separation could be decreased allowing acquisition of contiguous slices, therefore obtaining 3D deformation information. As the GRE MR sequence covers a greater field of view in the superior-inferior direction than the PET FOV, motion information from this acquisition could be applied to multiple PET bed positions, enhancing efficiency further. However, as the PET-derived respiratory signals from different bed positions would be derived from different moving anatomies, this concept would need to be investigated further.

As discussed in several chapters, the registrations in our methodology were carried out with MIRT in Matlab, but this is a simple non-rigid scheme that does not deal with non-diffeomorphic transformations (sliding motion), as are present with respiration,

for example between at the liver/rib interface. This could be overcome by utilising a registration method that allows for non-smooth deformation fields at organ boundaries where sliding motion occurs, providing a piecewise-diffeomorphic deformation field [Risser et al., 2013].

In the methodology, one reference slice is chosen (at exhale) at each slice location for the subsequent registrations. Although this demonstrated no obvious problems, the individual slices may not have been acquired at the exact same respiratory state. One way to overcome this would be to do a breath-hold scan where a single image at each slice location would be acquired whilst the patient is still, then use these as the reference images. With the current MR sequence, this would be a short (under three seconds) breath-hold acquisition.

For the MCIR PET reconstruction outlined in Section 5.4.7, we showed in Chapter 8 that the approximation of the transpose of the deformation fields as separate reverse registrations can cause artefacts in resulting PET images. This occurred in some data sets as the forward and backward registration for each pair of images were carried out independently. This can be addressed by either using a registration scheme that ensures the forward and backward deformation fields are coupled (an image deformed forwards then backwards equals the original image), or by implementing an explicit calculation of the transpose as part of the reconstruction.

9.2.2 Development of Clinical Workflow

To allow our methodology to be used within the clinic, or for a larger scale validation study, a number of steps would need to be undertaken.

9.2.2.1 Protocol

The extra one minute motion model sequence utilised in the last few chapters could be acquired immediately after the routine clinical protocol (as per the methodology in this work), or could be incorporated within the clinical protocol. The duration of PET to be motion corrected can range from 3 minutes per bed position for whole-body scans, to up to 60-90 minutes for research studies with one bed position. For a whole-body scan with four bed positions, two of the positions adversely affected by motion (thorax and abdomen) may be extended from three minutes to four minutes each, with no change to the protocol for the initial three minute bed position (see Figure 9.1). In some clinical

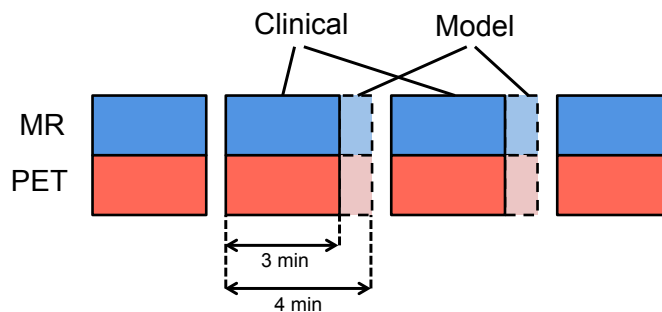


Figure 9.1: Proposed whole-body clinical workflow with extended PET bed position durations for motion model acquisitions.

protocols, the duration of MR acquisition may be shorter than the PET duration, in which case the motion-capturing MR sequence can be acquired with no time penalty. Acquiring the extra MR close in time to the clinical data reduces the effects of breathing style changes and tracer washout.

9.2.2.2 Computational Pipeline

Throughout this thesis, data processing has been carried out on a number of operating systems (Mac OS, Ubuntu, Windows) with various scripts in Matlab, STIR and bash. In order to produce results efficiently, a pipeline is required to automate processes, from raw data exported from the scanner to motion-compensated PET reconstruction. This will allow the method to be tested with a larger patient cohort or potentially to be used for specific research projects or clinical use.

9.2.2.3 Image Visualisation

For all motion correction work in this thesis, the resulting PET image has been warped to an 'exhale' state, and reference images for image registrations are chosen at exhale. For clinical use, it may be useful for the respiratory state of the motion-corrected PET image to be flexible, to allow for it to match the respiratory state of any of the diagnostic MR images from the same PET bed. For example, if a patient cannot successfully hold their breath at exhale for a breath-hold MR acquisition and does so at inhale (as seen for MRAC scans throughout the thesis), a motion-corrected PET image at inhale would be better for image visualisation, especially for fusion of PET and MR images.

An example is given in Figure 9.2, where the PET-derived signals $P(t)$ and $P'(t)$ are plotted for a four minute bed position, as part of a whole-body scan. Four diagnostic MR sequences are acquired throughout at various respiratory states, either at inhale

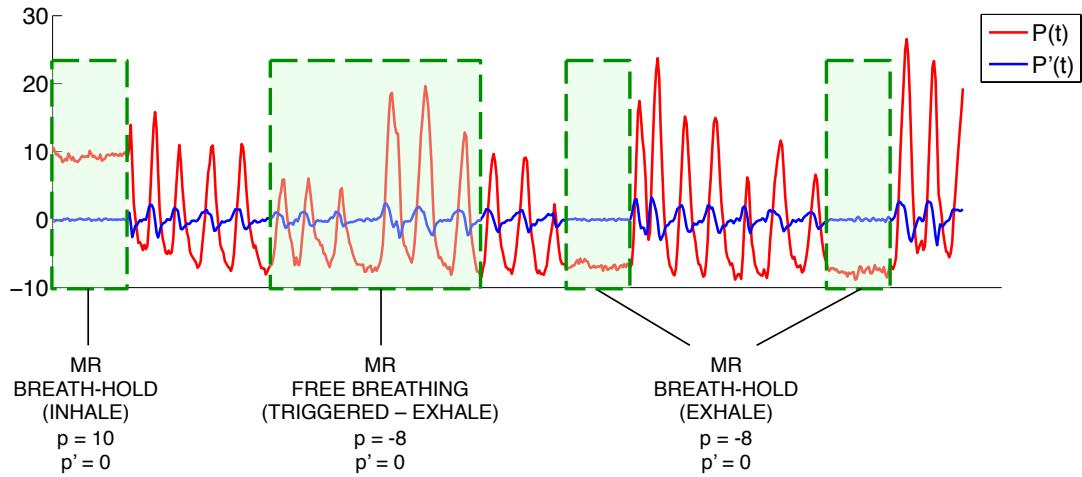


Figure 9.2: Typical 4 min PET/MR scan for a single bed position. Four different MR sequences acquired at either inhale breath-hold, exhale breath-hold or free breathing. Values of PET-derived signals can be used to warp motion-corrected PET images to spatially align with each MR acquisition.

or exhale breath-hold, or free-breathing, triggered to only acquire data at the exhale position. The values of signals during each MR acquisition can therefore be used as input to the motion model to estimate deformation fields, and a motion-corrected PET image can be reconstructed to spatially align with each MR acquisition. PET images could also be reconstructed at a respiratory state dependant on usage, e.g. at mid-cycle for certain types of radiation planning.

9.2.2.4 Metric for Motion Correction Performance

In general, clinicians have adapted to read PET images with artefacts known to be caused by respiration, and may not trust motion correction techniques due to a lack of robustness, clinical validation and clinical practicality [McClelland et al., 2013]. These issues have been addressed in this thesis, but examples have been shown where motion correction makes no significant change to images, or even adds artefacts in extreme cases. For clinical use, our proposal is that motion corrected PET is to be used alongside non motion-corrected AC and NAC PET images, rather than instead of. A metric to allow the clinician to understand how well the motion model performed, and therefore how much to 'trust' the motion corrected PET image would be useful.

One option would be to use a visual tool, showing a movie of MR slices at each slice location warped by model-estimated deformation fields. The more stationary the images appear, the better the model is performing. The drawback to this method is

that only MR images that were used to form the model can be tested, so data from the clinical section of the scan is untested. A movie of reconstructed PET gates could also be used as a visual tool, but a simplified version of the model would need to be used with a low number of gates to ensure high enough contrast in each.

Other image-based quantitative measures used throughout the thesis such as Euclidean Distance and Mutual Information on MR data, and Tenengrad Variance Sharpness on PET data could be utilised, but absolute values may be difficult to interpret.

9.2.3 Improving the PET-derived Signal

There are a number of ways to potentially improve the quality of the respiratory signal. The signal may be adversely affected if avid areas within the PET FOV move out of phase with each other, or areas move in and out of the FOV. One way to counteract this problem is to mask out certain areas in the sinogram series before extracting the respiratory signal with PCA. For example the heart could be masked so only signal from a moving lung lesion in the SI direction will be picked up, or vice versa. This could be done with the following steps:

- Reconstruct PET image
- Form binary mask in 3D space of image
- Forward project mask into sinogram space
- Unlist PET into 0.5sec sinogram series
- Multiply each sinogram in series by mask
- Extract signal with PCA

Respiratory signals could either be picked based on the anatomy of interest, or compared with the MR data to find which best compared to diaphragmatic displacement.

9.2.4 Multi-surrogate Motion Model

The joint PET-MR motion model formation uses the PET data in the form of the 1st PC weights $w_1(t)$ as a simple 1D respiratory signal, linked to imaging data from the

MR. It could be possible to utilise multiple PCs in the motion model, where each extra PC provides an extra surrogate signal $w_2(t)$, $w_3(t)$ etc. One benefit of a multi-PC approach is to capture a better measure of respiration, as not all the respiratory motion will necessarily be captured in the 1st PC, and different elements of the motion will be spread across multiple PCs. If PET-avid regions physically move out of phase to each other, these motions will also appear in different principal components, and with this method, all components could be used in the model.

This method could also capture other explicit types of motion such as cardiac contractions, to allow for dual gating respiratory-cardiac gating, as previously demonstrated with PET data [Klein et al., 1997, Kokki et al., 2010] . If the heart is avid to the tracer in the raw PET data, the motions of cardiac beating and respiratory motion may show up as separate principal components with the technique [Thielemans et al., 2014]. Figure 9.3a shows view 1 for the first five PCs for one tested cardiac data set, where the shape of the black/white areas in the first two components suggest SI motion and contracting motion respectively. Also presented is a section of the corresponding PC weights that provide the signals for PC 1 and 2 (figure 9.3b), and a plot showing a spectral analysis of the signals (figure 9.3c). From these plots it is clear that the two signals have strong frequency peak rates of around 0.2 and 1.5; approximately what is expected of cardiac and respiratory cycles. Typical cardiac gating of PET data would cut out data at systole (contraction) to only keep the remaining data including diastole (filling and relaxing). Using both signals in the motion model would allow all PET data to be utilised. However, computational expense will increase with number of surrogate signals as PET data will need to be binned based on a combination of each. This frequency information could also be used to select which PC most resembles respiratory motion, if only one surrogate was to be used in the model.

9.2.5 Other

Currently PET and MR data are binned based on the respiratory signal but only the MR is used to model respiratory motion and provide deformation fields between respiratory bins. It could be possible to reconstruct images from the binned PET data and use these images along with the MR images for a dual registration that uses both modalities to

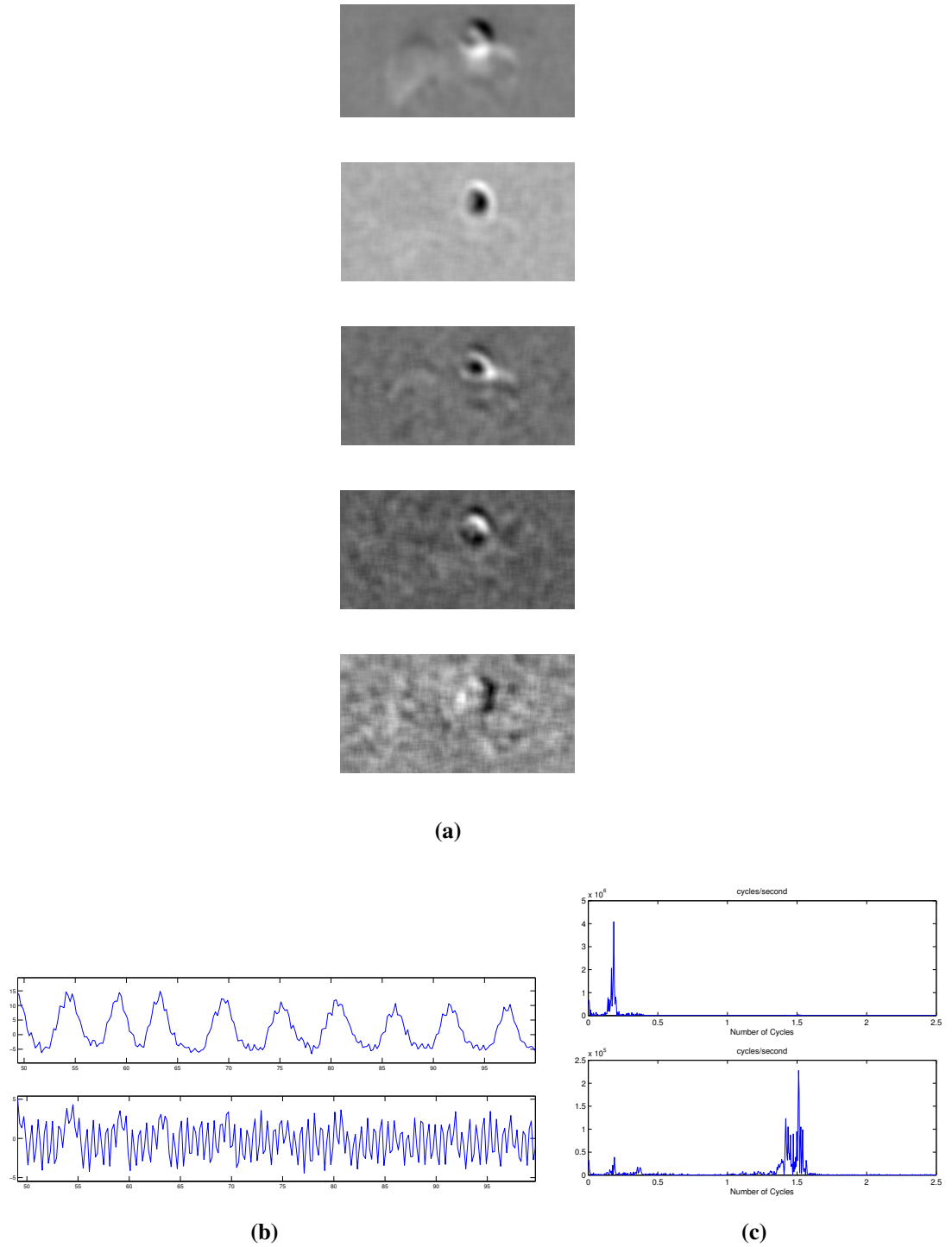


Figure 9.3: Multiple PET-derived signals for cardiac scan, (a) Principal components 1-5, (b) Associated weights for PC1 (top) and PC2 (bottom), (c) Frequency distribution of signals for PC1 (top) and PC2 (bottom).

find deformation parameters between bins. As the MR sequence is based at sagittal slices with gaps, adding PET information could help to provide motion information in these gaps.

As most PET/MR motion correction techniques in the literature use MR to correct PET, it would be of interest to use PET to correct MR. A respiratory signal is difficult to obtain in an MR scan without hardware or some compromise in the sequence, but a signal is necessary for MR respiratory motion correction. We have demonstrated the use of PCA for a PET-derived respiratory signal in PET motion correction, but there is potential to use this signal for MR motion correction with simultaneous PET/MR scanners. For example, the PET-derived respiratory signal could bin 3D MR data through a free-breathing acquisition. Each bin could then be reconstructed, registered, then warped and combined to form an image comparable to a breath-hold MR acquisition. This could be useful for paediatric, elderly or patients with breathing problems who find it difficult to hold their breath for prolonged periods.

References

- [Acton et al., 2004] Acton, P. D., Zhuang, H., and Alavi, A. (2004). Quantification in PET. *Radiol. Clin. North Am.*, 42(6):1055–1062.
- [Alessio and Kinahan, 2006] Alessio, A. and Kinahan, P. (2006). PET image reconstruction. In *Nucl. Med.*, volume 1, pages 1–22.
- [Ambwani et al., 2011] Ambwani, S., Karl, W. C., Tawakol, A., and Pien, H. (2011). Joint cardiac and respiratory motion correction and super-resolution reconstruction in coronary PET/CT. In *Proc. - Int. Symp. Biomed. Imaging*, pages 1702–1705. IEEE.
- [Atkinson et al., 1997] Atkinson, D., Hill, D. L., Stoye, P. N., Summers, P. E., and Keevil, S. F. (1997). Automatic correction of motion artifacts in magnetic resonance images using an entropy focus criterion. *IEEE Trans. Med. Imaging*, 16(6):903–10.
- [Alvarez-Borrego, 2005] Alvarez-Borrego, J. (2005). Fast autofocus algorithm for automated microscopes. *Opt. Eng.*, 44(6):063601.
- [Badawi et al., 2000] Badawi, R. D., Ferreira, N. C., Kohlmyer, S. G., Dahlbom, M., Marsden, P. K., and Lewellen, T. K. (2000). A comparison of normalization effects on three whole-body cylindrical 3D PET systems. *Phys. Med. Biol.*, 45(11):3253–3266.
- [Badawi et al., 1998] Badawi, R. D., Lodge, M. a., and Marsden, P. K. (1998). Algorithms for calculating detector efficiency normalization coefficients for true coincidences in 3D PET. *Phys. Med. Biol.*, 43(1):189–205.

- [Bai and Brady, 2011] Bai, W. and Brady, M. (2011). Motion correction and attenuation correction for respiratory gated PET images. *IEEE Trans. Med. Imaging*, 30(2):351–365.
- [Balfour et al., 2015] Balfour, D. R., Marsden, P. K., Polycarpou, I., Kolbitsch, C., and King, A. P. (2015). Respiratory motion correction of PET using MR-constrained PET-PET registration. *Biomed. Eng. Online*, 14(1):85.
- [Batchelor et al., 2005] Batchelor, P. G., Atkinson, D., Irarrazaval, P., Hill, D. L. G., Hajnal, J., and Larkman, D. (2005). Matrix description of general motion correction applied to multishot images. *Magn. Reson. Med.*, 54(5):1273–1280.
- [Baumgartner et al., 2013] Baumgartner, C. F., Kolbitsch, C., McClelland, J. R., Rueckert, D., and King, A. P. (2013). Groupwise simultaneous manifold alignment for high-resolution dynamic MR imaging of respiratory motion. In *Lect. Notes Comput. Sci. (including Subser. Lect. Notes Artif. Intell. Lect. Notes Bioinformatics)*, volume 7917 LNCS, pages 232–243.
- [Bert and Durante, 2011] Bert, C. and Durante, M. (2011). Motion in radiotherapy: particle therapy. *Phys. Med. Biol.*, 56(16):R113–R144.
- [Boellaard R, Delgado-Bolton R, Krause B, 2015] Boellaard R, Delgado-Bolton R, Krause B, E. A. (2015). FDG PET/CT: EANM procedure guidelines for tumour imaging: version 2.0. *Eur J Nucl Med Mol Imaging*, 42(2):328–354.
- [Bolos et al., 2009] Bolus, N. E., George, R., Washington, J., and Newcomer, B. R. (2009). PET/MRI: The Blended-Modality Choice of the Future? *J. Nucl. Med. Technol.*, 37(2):63–71.
- [Boucher et al., 2004] Boucher, L., Rodrigue, S., Lecomte, R., and Bénard, F. (2004). Respiratory gating for 3-dimensional PET of the thorax: feasibility and initial results. *J. Nucl. Med.*, 45(2):214–9.
- [Buerger et al., 2012] Buerger, C., Clough, R. E., King, a. P., Schaeffter, T., and Prieto, C. (2012). Nonrigid motion modeling of the liver from 3-D undersampled self-gated golden-radial phase encoded MRI. *IEEE Trans. Med. Imaging*, 31(3):805–815.

- [Buerger et al., 2013] Buerger, C., Prieto, C., and Schaeffter, T. (2013). Highly efficient 3D motion-compensated abdomen MRI from undersampled golden-RPE acquisitions. *Magn. Reson. Mater. Physics, Biol. Med.*, 26(5):419–429.
- [Bunch et al., 1977] Bunch, P. C., Hamilton, J. F., Sanderson, G. K., and Simmons, A. H. (1977). A free response approach to the measurement and characterization of radiographic observer performance. In Gray, J. E. and Hendee, W. R., editors, *Appl. Opt. Instrum. Med. VI*, volume 4, pages 124–135.
- [Bundschuh et al., 2007] Bundschuh, R. a., Martínez-Moeller, A., Essler, M., Martínez, M.-J., Nekolla, S. G., Ziegler, S. I., and Schwaiger, M. (2007). Postacquisition Detection of Tumor Motion in the Lung and Upper Abdomen Using List-Mode PET Data: A Feasibility Study. *J. Nucl. Med.*, 48(5):758–763.
- [Burris et al., 2015] Burris, N. S., Johnson, K. M., Larson, P. E. Z., Hope, M. D., Nagle, S. K., Behr, S. C., and Hope, T. a. (2015). Detection of Small Pulmonary Nodules with Ultrashort Echo Time Sequences in Oncology Patients by Using a PET/MR System. *Radiology*, 278(1):150489.
- [Catana et al., 2011] Catana, C., Benner, T., van der Kouwe, A., Byars, L., Hamm, M., Chonde, D. B., Michel, C. J., El Fakhri, G., Schmand, M., and Sorensen, a. G. (2011). MRI-Assisted PET Motion Correction for Neurologic Studies in an Integrated MR-PET Scanner. *J. Nucl. Med.*, 52(1):154–161.
- [Chawla et al., 2010] Chawla, S. C., Federman, N., Zhang, D., Nagata, K., Nuthakki, S., McNitt-Gray, M., and Boechat, M. I. (2010). Estimated cumulative radiation dose from PET/CT in children with malignancies: A 5-year retrospective review. *Pediatr. Radiol.*, 40(5):681–686.
- [Chen et al., 2008] Chen, K., Blebea, J., Laredo, J. D., Chen, W., Alavi, A., and Torigian, D. A. (2008). Evaluation of Musculoskeletal Disorders with PET, PET/CT, and PET/MR Imaging. *PET Clin.*, 3(3):451–465.
- [Chun et al., 2012] Chun, S. Y., Reese, T. G., Ouyang, J., Guerin, B., Catana, C., Zhu, X., Alpert, N. M., and El Fakhri, G. (2012). MRI-Based Nonrigid Motion Correction in Simultaneous PET/MRI. *J. Nucl. Med.*, 53(8):1284–1291.

- [Coleman and Li, 1996] Coleman, T. F. and Li, Y. (1996). An Interior Trust Region Approach for Nonlinear Minimization Subject to Bounds. *SIAM J. Optim.*, 6(2):418–445.
- [Coombs et al., 1997] Coombs, B. D., Szumowski, J., and Coshov, W. (1997). Two-point Dixon technique for water-fat signal decomposition with B0 inhomogeneity correction. *Magn. Reson. Med.*, 38(6):884–9.
- [Daftary, 2010] Daftary, A. (2010). PET-MRI: Challenges and new directions. *Indian J. Nucl. Med.*, 25(1):3–5.
- [Danas et al., 1997] Danas, P. G., McConnell, M. V., Khasgiwala, V. C., Chuang, M. L., Edelman, R. R., and Manning, W. J. (1997). Prospective navigator correction of image position for coronary MR angiography. *Radiology*, 203(3):733–736.
- [Danas et al., 1999] Danas, P. G., Stuber, M., Botnar, R. M., Kissinger, K. V., Edelman, R. R., and Manning, W. J. (1999). Relationship between motion of coronary arteries and diaphragm during free breathing: Lessons from real-time MR imaging. *Am. J. Roentgenol.*, 172(4):1061–1065.
- [Daube-Witherspoon and Muehllehner, 1987] Daube-Witherspoon, M. E. and Muehllehner, G. (1987). Treatment of axial data in three-dimensional PET. *J. Nucl. Med.*, 28(11):1717–1724.
- [Delso et al., 2011] Delso, G., Fürst, S., Jakoby, B., Ladebeck, R., Ganter, C., Nekolla, S. G., Schwaiger, M., and Ziegler, S. I. (2011). Performance Measurements of the Siemens mMR Integrated Whole-Body PET/MR Scanner. *J. Nucl. Med.*, 52(12):1914–1922.
- [Dixon, 1984] Dixon, W. T. (1984). Simple proton spectroscopic imaging. *Radiology*, 153(1):189–194.
- [El Naqa et al., 2009] El Naqa, I., Grigsby, P. W., Apte, a., Kidd, E., Donnelly, E., Khullar, D., Chaudhari, S., Yang, D., Schmitt, M., Laforest, R., Thorstad, W. L., and Deasy, J. O. (2009). Exploring feature-based approaches in PET images for predicting cancer treatment outcomes. *Pattern Recognit.*, 42(6):1162–1171.

- [Fayad et al., 2010] Fayad, H., Pan, T., Roux, C., and Visvikis, D. (2010). A generic respiratory motion model for motion correction in PET/CT. In *IEEE Nucl. Sci. Symp. Conf. Rec.*, pages 2455–2458. IEEE.
- [Fayad et al., 2015] Fayad, H., Schmidt, H., Wuerslin, C., and Visvikis, D. (2015). Reconstruction-Incorporated Respiratory Motion Correction in Clinical Simultaneous PET/MR Imaging for Oncology Applications. *J Nucl Med*, 56:884–889.
- [Fieseler et al., 2014] Fieseler, M., Gigengack, F., Jiang, X., and Schäfers, K. P. (2014). Motion Correction of Whole-Body PET Data with a Joint PET-MRI Registration Functional. *Biomed. Eng. Online*, 13 Suppl 1(Suppl 1):S2.
- [Fulton et al., 2002] Fulton, R. R., Meikle, S. R., Eberl, S., Pfeiffer, J., and Constable, C. J. (2002). Correction for head movements in positron emission tomography using an optical motion-tracking system. *IEEE Trans. Nucl. Sci.*, 49,(1):116–123.
- [Gierga et al., 2005] Gierga, D. P., Brewer, J., Sharp, G. C., Betke, M., Willett, C. G., and Chen, G. T. Y. (2005). The correlation between internal and external markers for abdominal tumors: Implications for respiratory gating. *Int. J. Radiat. Oncol. Biol. Phys.*, 61(5):1551–1558.
- [Guérin et al., 2011] Guérin, B., Cho, S., Chun, S. Y., Zhu, X., Alpert, N. M., El Fakhri, G., Reese, T., and Catana, C. (2011). Nonrigid PET motion compensation in the lower abdomen using simultaneous tagged-MRI and PET imaging. *Med. Phys.*, 38(6):3025–38.
- [Hamberg et al., 1994] Hamberg, L. M., Hunter, G. J., Alpert, N. M., Choi, N. C., Babich, J. W., and Fischman, a. J. (1994). The dose uptake ratio as an index of glucose metabolism: useful parameter or oversimplification? *J Nucl Med*, 35(8):1308–1312.
- [He et al., 2008] He, J., O’Keefe, G. J., Gong, S. J., Jones, G., Saunder, T., Scott, A. M., and Geso, M. (2008). A novel method for respiratory motion gated with geometric sensitivity of the scanner in 3D PET. *IEEE Trans. Nucl. Sci.*, 55(5):2557–2565.

- [Hickeson et al., 2002] Hickeson, M., Yun, M., Matthies, A., Zhuang, H., Adam, L. E., Lacorte, L., and Alavi, A. (2002). Use of a corrected standardized uptake value based on the lesion size on CT permits accurate characterization of lung nodules on FDG-PET. *Eur. J. Nucl. Med.*, 29(12):1639–1647.
- [Higashi et al., 2003] Higashi, T., Saga, T., Nakamoto, Y., Ishimori, T., Fujimoto, K., Doi, R., Imamura, M., and Konishi, J. (2003). Diagnosis of pancreatic cancer using fluorine-18 fluorodeoxyglucose positron emission tomography (FDG PET) – usefulness and limitations in ”clinical reality”. *Ann. Nucl. Med.*, 17(4):261–79.
- [Holland and Welsch, 1977] Holland, P. W. and Welsch, R. E. (1977). Robust regression using iteratively reweighted least-squares. *Commun. Stat. - Theory Methods*, 6(9):813–827.
- [Hubner et al., 1996] Hubner, K. F., Buonocore, E., Gould, H. R., Thie, J., Smith, G. T., Stephens, S., and Dickey, J. (1996). Differentiating benign from malignant lung lesions using ”quantitative” parameters of FDG PET images. *Clin Nucl Med*, 21(12):941–949.
- [Jacobson and Fessler, 2003] Jacobson, M. and Fessler, J. (2003). Joint estimation of image and deformation parameters in motion-corrected PET. In *2003 IEEE Nucl. Sci. Symp. Conf. Rec. (IEEE Cat. No.03CH37515)*, volume 5, pages 3290–3294. IEEE.
- [Kadrmas et al., 2009] Kadrmas, D. J., Casey, M. E., Conti, M., Jakoby, B. W., Lois, C., and Townsend, D. W. (2009). Impact of time-of-flight on PET tumor detection. *J. Nucl. Med.*, 50(8):1315–23.
- [Kadrmas et al., 2012] Kadrmas, D. J., Oktay, M. B., Casey, M. E., and Hamill, J. J. (2012). Effect of scan time on oncologic lesion detection in whole-body PET. *IEEE Trans. Nucl. Sci.*, 59(5 PART 1):1940–1947.
- [Kaufmann and Camici, 2005] Kaufmann, P. a. and Camici, P. G. (2005). Myocardial blood flow measurement by PET: technical aspects and clinical applications. *J. Nucl. Med.*, 46(1):75–88.

- [King et al., 2012] King, a. P., Buerger, C., Tsoumpas, C., Marsden, P. K., and Schaeffter, T. (2012). Thoracic respiratory motion estimation from MRI using a statistical model and a 2-D image navigator. *Med. Image Anal.*, 16(1):252–264.
- [Klein et al., 1997] Klein, G., Reutter, B., Ho, M., Reed, J., and Huesman, R. (1997). Real-time system for respiratory-cardiac gating in positron tomography. *1997 IEEE Nucl. Sci. Symp. Conf. Rec.*, 2(4):1284–1287.
- [Klein et al., 1996] Klein, G. J., Reutter, B. W., and Huesman, R. H. (1996). Non-rigid summing of gated PET via optical flow. In *Nucl. Sci. Symp. 1996. Conf. Rec. 1996 IEEE*, volume 2, pages 1339–1342. IEEE.
- [Kokki et al., 2010] Kokki, T., Sipilä, H. T., Teräs, M., Noponen, T., Durand-Schaefer, N., Klén, R., and Knuuti, J. (2010). Dual gated PET/CT imaging of small targets of the heart: Method description and testing with a dynamic heart phantom. *J. Nucl. Cardiol.*, 17(1):71–84.
- [Kolbitsch et al., 2014] Kolbitsch, C., Prieto, C., Tsoumpas, C., and Schaeffter, T. (2014). A 3D MR-acquisition scheme for nonrigid bulk motion correction in simultaneous PET-MR. *Med. Phys.*, 41(8):082304.
- [Krak et al., 2005] Krak, N. C., Boellaard, R., Hoekstra, O. S., Twisk, J. W. R., Hoekstra, C. J., and Lammertsma, A. a. (2005). Effects of ROI definition and reconstruction method on quantitative outcome and applicability in a response monitoring trial. *Eur. J. Nucl. Med. Mol. Imaging*, 32(3):294–301.
- [Kruis et al., 2013] Kruis, M. F., Van De Kamer, J. B., Houweling, A. C., Sonke, J. J., Belderbos, J. S. a., and Van Herk, M. (2013). PET motion compensation for radiation therapy using a CT-based mid-position motion model: Methodology and clinical evaluation. *Int. J. Radiat. Oncol. Biol. Phys.*, 87(2):394–400.
- [Langen and Jones, 2001] Langen, K. M. and Jones, D. T. L. (2001). Organ motion and its management. *Int. J. Radiat. Oncol. Biol. Phys.*, 50(1):265–278.
- [Livieratos et al., 2005] Livieratos, L., Stegger, L., Bloomfield, P. M., Schafers, K., Bailey, D. L., and Camici, P. G. (2005). Rigid-body transformation of list-mode

- projection data for respiratory motion correction in cardiac PET. *Phys. Med. Biol.*, 50(14):3313–3322.
- [Low et al., 2005] Low, D. A., Parikh, P. J., Lu, W., Dempsey, J. F., Wahab, S. H., Hubenschmidt, J. P., Nystrom, M. M., Handoko, M., and Bradley, J. D. (2005). Novel breathing motion model for radiotherapy. *Int. J. Radiat. Oncol. Biol. Phys.*, 63(3):921–929.
- [Malone et al., 2000] Malone, S., Crook, J. M., Kendal, W. S., and Zanto, J. S. (2000). Respiratory-induced prostate motion: Quantification and characterization. *Int. J. Radiat. Oncol. Biol. Phys.*, 48(1):105–109.
- [Manber et al., 2014a] Manber, R., Atkinson, D., Hutton, B., Barnes, A., Ourselin, S., Arridge, S., O’Meara, C., and Thielemans, K. (2014a). Validation of a PET-derived Respiratory Signal by Comparison with an MRI Pencil-Beam Navigator Signal in Simultaneous PET/MR. In *ISMRM*, volume 44, page 1396.
- [Manber et al., 2015a] Manber, R., Atkinson, D., Thielemans, K., Hutton, B., Barnes, A., O’Meara, C., Wan, S., Ourselin, S., and Arridge, S. (2015a). Practical PET respiratory motion correction in clinical simultaneous PET/MR. In *Proc. - Int. Symp. Biomed. Imaging*, volume 2015-July, pages 1580–1583. IEEE.
- [Manber et al., 2014b] Manber, R., Thielemans, K., Hutton, B., Barnes, A., Ourselin, S., Arridge, S., O’Meara, C., and Atkinson, D. (2014b). Initial evaluation of a practical PET respiratory motion correction method in clinical simultaneous PET/MRI. *EJNMMI Phys.*, 1(Suppl 1):A40.
- [Manber et al., 2015b] Manber, R., Thielemans, K., Hutton, B., Barnes, A., Ourselin, S., Arridge, S., Wan, M. Y. S., O’Meara, C., and Atkinson, D. (2015b). MR Image-based PET Respiratory Motion Correction in PET/MR. *J. Nucl. Med.*, 56:98.
- [Manber et al., 2016] Manber, R., Thielemans, K., Hutton, B., Wan, M. Y. S., McClelland, J. R., Barnes, A., Arridge, S., Ourselin, S., and Atkinson, D. (2016). Joint PET-MR Respiratory Motion Models for Clinical PET Motion Correction. *Phys. Med. Biol.*, 6515(17):6515–6530.

- [Manber et al., 2015c] Manber, R., Thielemans, K., Hutton, B. F., Barnes, A., Ourselin, S., Arridge, S., O'Meara, C., Wan, S., and Atkinson, D. (2015c). Practical PET Respiratory Motion Correction in Clinical PET/MR. *J. Nucl. Med.*, 56(6):890–896.
- [Manduca et al., 2000] Manduca, a., McGee, K. P., Welch, E. B., Felmlee, J. P., Grimm, R. C., and Ehman, R. L. (2000). Autocorrection in MR imaging: adaptive motion correction without navigator echoes. *Radiology*, 215(3):904–909.
- [Martinez-Möller et al., 2009] Martinez-Möller, A., Souvatzoglou, M., Delso, G., Bundschuh, R. a., Ched'hotel, C., Ziegler, S. I., Navab, N., Schwaiger, M., and Nekolla, S. G. (2009). Tissue classification as a potential approach for attenuation correction in whole-body PET/MRI: evaluation with PET/CT data. *J. Nucl. Med.*, 50(4):520–526.
- [Martinez-Möller et al., 2007] Martinez-Möller, A., Zikic, D., Botnar, R. M., Bundschuh, R. a., Howe, W., Ziegler, S. I., Navab, N., Schwaiger, M., and Nekolla, S. G. (2007). Dual cardiac-respiratory gated PET: Implementation and results from a feasibility study. *Eur. J. Nucl. Med. Mol. Imaging*, 34(9):1447–1454.
- [Matsunari et al., 2003] Matsunari, I., Taki, J., Nakajima, K., Tonami, N., and Hisada, K. (2003). Myocardial viability assessment using nuclear imaging. *Ann. Nucl. Med.*, 17(3):169–179.
- [McClelland et al., 2014] McClelland, J. R., Champion, B. A. S., and Hawkes, D. J. (2014). Combining image registration, respiratory motion modelling, and motion compensated image reconstruction. In *Lect. Notes Comput. Sci. (including Subser. Lect. Notes Artif. Intell. Lect. Notes Bioinformatics)*, volume 8545 LNCS, pages 103–113. Springer International Publishing.
- [McClelland et al., 2013] McClelland, J. R., Hawkes, D. J., Schaeffter, T., and King, a. P. (2013). Respiratory motion models: A review. *Med. Image Anal.*, 17(1):19–42.
- [McLeish et al., 2002] McLeish, K., Hill, D. L. G., Atkinson, D., Blackall, J. M., and Razavi, R. (2002). A study of the motion and deformation of the heart due to respiration. *IEEE Trans. Med. Imaging*, 21(9):1142–1150.

- [Moghari et al., 2013] Moghari, M. H., Roujol, S., Chan, R. H., Hong, S. N., Bello, N., Henningsson, M., Ngo, L. H., Goddu, B., Goepfert, L., Kissinger, K. V., Manning, W. J., and Nezafat, R. (2013). Free-breathing 3D cardiac MRI using iterative image-based respiratory motion correction. *Magn. Reson. Med.*, 70(4):1005–1015.
- [Montgomery et al., 2006] Montgomery, A. J., Thielemans, K., Mehta, M. a., Turkheimer, F., Mustafovic, S., and Grasby, P. M. (2006). Correction of head movement on PET studies: comparison of methods. *J. Nucl. Med.*, 47(12):1936–1944.
- [Morey and Kadrmas, 2013] Morey, a. M. and Kadrmas, D. J. (2013). Effect of varying number of OSEM subsets on PET lesion detectability. *J. Nucl. Med. Technol.*, 41(4):268–73.
- [Myronenko and Song, 2010] Myronenko, A. and Song, X. (2010). Intensity-based image registration by minimizing residual complexity. *IEEE Trans. Med. Imaging*, 29(11):1882–1891.
- [NCI Breast Cancer, 2013] NCI Breast Cancer (2013). National Cancer Institute.
- [Nehmeh et al., 2002] Nehmeh, S. a., Erdi, Y. E., Ling, C. C., Rosenzweig, K. E., Schoder, H., Larson, S. M., Macapinlac, H. a., Squire, O. D., and Humm, J. L. (2002). Effect of respiratory gating on quantifying PET images of lung cancer. *J. Nucl. Med.*, 43(7):876–881.
- [Nehmeh et al., 2004] Nehmeh, S. a., Erdi, Y. E., Pan, T., Yorke, E., Mageras, G. S., Rosenzweig, K. E., Schoder, H., Mostafavi, H., Squire, O., Pevsner, a., Larson, S. M., and Humm, J. L. (2004). Quantitation of respiratory motion during 4D-PET/CT acquisition. *Med. Phys.*, 31(2004):1333–1338.
- [Nuyts et al., 2013] Nuyts, J., Bal, G., Kehren, F., Fenchel, M., Michel, C., and Watson, C. (2013). Completion of a truncated attenuation image from the attenuated PET emission data. In *IEEE Trans. Med. Imaging*, volume 32, pages 237–246. IEEE.
- [Odille et al., 2010] Odille, F., Uribe, S., Batchelor, P. G., Prieto, C., Schaeffter, T., and Atkinson, D. (2010). Model-based reconstruction for cardiac cine MRI without ECG or breath holding. *Magn. Reson. Med.*, 63(5):1247–1257.

- [Odille et al., 2008] Odille, F., Vuissoz, P. a., Felblinger, J., and Atkinson, D. (2008). Generalized Reconstruction by Inversion of Coupled Systems (GRICS) applied to parallel MRI. *2008 5th IEEE Int. Symp. Biomed. Imaging From Nano to Macro, Proceedings, ISBI*, 60(1):1019–1022.
- [Osman et al., 2000] Osman, N. F., McVeigh, E. R., and Prince, J. L. (2000). Imaging heart motion using harmonic phase MRI. *IEEE Trans. Med. Imaging*, 19(3):186–202.
- [Ozhasoglu and Murphy, 2002] Ozhasoglu, C. and Murphy, M. J. (2002). Issues in respiratory motion compensation during external-beam radiotherapy. *Int. J. Radiat. Oncol. Biol. Phys.*, 52(5):1389–1399.
- [Patz et al., 1993] Patz, E. F., Lowe, V. J., Hoffman, J. M., Paine, S. S., Burrowes, P., Coleman, R. E., and Goodman, P. C. (1993). Focal pulmonary abnormalities: evaluation with F-18 fluorodeoxyglucose PET scanning. *Radiology*, 188(2):487–90.
- [Pépin et al., 2014] Pépin, A., Daouk, J., Bailly, P., Hapdey, S., and Meyer, M.-E. (2014). Management of respiratory motion in PET/computed tomography: the state of the art. *Nucl. Med. Commun.*, 35(2):113–22.
- [Pet, 2011] Pet, O. T.-o.-f. (2011). Improvement in Lesion Detection with Whole-Body Oncologic Time-of-Flight PET. *J. Nucl. Med.*, 52(3):347–353.
- [Petibon et al., 2013] Petibon, Y., Ouyang, J., Zhu, X., Huang, C., Reese, T. G., Chun, S. Y., Li, Q., and El Fakhri, G. (2013). Cardiac motion compensation and resolution modeling in simultaneous PET-MR: A cardiac lesion detection study. *Phys. Med. Biol.*, 58(7):2085–2102.
- [Picard and Thompson, 1997] Picard, Y. and Thompson, C. J. (1997). Motion correction of PET images using multiple acquisition frames. *IEEE Trans. Med. Imaging*, 16(2):137–144.
- [Polycarpou et al., 2014] Polycarpou, I., Tsoumpas, C., King, A. P., and Marsden, P. K. (2014). Impact of respiratory motion correction and spatial resolution on lesion detection in PET: a simulation study based on real MR dynamic data. *Phys. Med. Biol.*, 59(3):697–713.

- [Polycarpou et al., 2012] Polycarpou, I., Tsoumpas, C., and Marsden, P. K. (2012). Analysis and comparison of two methods for motion correction in PET imaging. *Med. Phys.*, 39(10):6474.
- [Qiao et al., 2006] Qiao, F., Pan, T., Clark, J. W., and Mawlawi, O. R. (2006). A motion-incorporated reconstruction method for gated PET studies. *Phys. Med. Biol.*, 51(15):3769–3783.
- [Quick et al., 2011] Quick, H. H., Ladebeck, R., and Georgi, J. C. (2011). Whole-Body MR/PET Hybrid Imaging: Technical Considerations, Clinical Workflow, and Initial Results. *MAGNETOM Flash*, 1:88–100.
- [Rahmim et al., 2007] Rahmim, A., Rousset, O., and Zaidi, H. (2007). Strategies for Motion Tracking and Correction in PET. *PET Clin.*, 2(2):251–266.
- [Rank et al., 2015] Rank, C. M., Heuß er, T., Wetscherek, A., and Kachelrieß, M. (2015). Respiratory Motion Compensation for Simultaneous PET / MR based on strongly undersampled radial MR data. *EJNMMI Phys.*, 2(Suppl 1):A24.
- [Ratib and Beyer, 2011] Ratib, O. and Beyer, T. (2011). Whole-body hybrid PET/MRI: Ready for clinical use? *Eur. J. Nucl. Med. Mol. Imaging*, 38(6):992–995.
- [Risser et al., 2013] Risser, L., Vialard, F. X., Baluwala, H. Y., and Schnabel, J. a. (2013). Piecewise-diffeomorphic image registration: Application to the motion estimation between 3D CT lung images with sliding conditions. *Med. Image Anal.*, 17(2):182–193.
- [Rohren et al., 2004] Rohren, E. M., Turkington, T. G., and Coleman, R. E. (2004). Clinical applications of PET in oncology. *Radiology*, 231(2):305–332.
- [Ruan et al., 2008] Ruan, D., Fessler, J. a., Balter, J. M., Berbeco, R. I., Nishioka, S., and Shirato, H. (2008). Inference of hysteretic respiratory tumor motion from external surrogates: a state augmentation approach. *Phys. Med. Biol.*, 53(11):2923–36.

- [Schleyer et al., 2009] Schleyer, P. J., O'Doherty, M. J., Barrington, S. F., and Marsden, P. K. (2009). Retrospective data-driven respiratory gating for PET/CT. *Phys. Med. Biol.*, 54(7):1935–1950.
- [Schwenzer et al., 2012] Schwenzer, N. F., Stegger, L., Bisdas, S., Schraml, C., Kolb, a., Boss, a., Müller, M., Reimold, M., Ernemann, U., Claussen, C. D., Pfannenberger, C., and Schmidt, H. (2012). Simultaneous PET/MR imaging in a human brain PET/MR system in 50 patients - Current state of image quality. *Eur. J. Radiol.*, 81(11):3472–3478.
- [Seppenwoolde et al., 2002] Seppenwoolde, Y., Shirato, H., Kitamura, K., Shimizu, S., Van Herk, M., Lebesque, J. V., and Miyasaka, K. (2002). Precise and real-time measurement of 3D tumor motion in lung due to breathing and heartbeat, measured during radiotherapy. *Int. J. Radiat. Oncol. Biol. Phys.*, 53(4):822–834.
- [Shukla and Kumar, 2006] Shukla, A. and Kumar, U. (2006). Positron emission tomography: An overview. *J. Med. Phys.*, 31(1):13.
- [Sureshbabu and Mawlawi, 2005] Sureshbabu, W. and Mawlawi, O. (2005). PET/CT Imaging Artifacts. *J. Nucl. Med. Technol.*, 33(3):156–161.
- [Swets and Pickett, 1982] Swets, J. a. and Pickett, R. M. (1982). *Evaluation of diagnostic systems: Methods from signal detection theory*. Academic Press, New York :.
- [Teppema and Berendsen, 2014] Teppema, L. J. and Berendsen, R. R. (2014). Control of Breathing.
- [Teymurazyan et al., 2013] Teymurazyan, a., Riauka, T., Jans, H. S., and Robinson, D. (2013). Properties of noise in positron emission tomography images reconstructed with filtered-backprojection and row-action maximum likelihood algorithm. *J. Digit. Imaging*, 26(3):447–456.
- [Thielemans et al., 2007] Thielemans, K., Mustafovic, S., and Tsoumpas, C. (2007). STIR: Software for tomographic image reconstruction release 2. *IEEE Nucl. Sci. Symp. Conf. Rec.*, 4(4):2174–2176.

- [Thielemans et al., 2012] Thielemans, K., Rathore, S., Engbrant, F., and Razifar, P. (2012). Device-less gating for PET/CT using PCA. *IEEE Nucl. Sci. Symp. Conf. Rec.*, pages 3904–3910.
- [Thielemans et al., 2013] Thielemans, K., Schleyer, P., Dunn, J., Marsden, P. K., and Manjeshwar, R. M. (2013). Using PCA to detect head motion from PET list mode data. *IEEE Nucl. Sci. Symp. Conf. Rec.*
- [Thielemans et al., 2014] Thielemans, K., Schleyer, P., Marsden, P. K., Teuho, J., Teras, M., Bettinardi, V., Menezes, L., Manjeshwar, R., and Stearns, C. (2014). Data-driven dual-gating for cardiac PET data. pages 2–5. MIC proceedings.
- [Tixier et al., 2011] Tixier, F., Le Rest, C. C., Hatt, M., Albarghach, N., Pradier, O., Metges, J.-P., Corcos, L., and Visvikis, D. (2011). Intratumor Heterogeneity Characterized by Textural Features on Baseline 18F-FDG PET Images Predicts Response to Concomitant Radiochemotherapy in Esophageal Cancer. *J. Nucl. Med.*, 52(3):369–378.
- [Tomasi et al., 2012] Tomasi, G., Turkheimer, F., and Aboagye, E. (2012). Importance of quantification for the analysis of PET data in oncology: Review of current methods and trends for the future. *Mol. Imaging Biol.*, 14(2):131–136.
- [Torigian et al., 2013] Torigian, D. a., Zaidi, H., Kwee, T. C., Saboury, B., Udupa, J. K., Cho, Z.-H., and Alavi, A. (2013). PET/MR imaging: technical aspects and potential clinical applications. *Radiology*, 267(1):26–44.
- [Tsoumpas et al., 2013] Tsoumpas, C., Polycarpou, I., Thielemans, K., Buerger, C., King, a. P., Schaeffter, T., and Marsden, P. K. (2013). The effect of regularization in motion compensated PET image reconstruction: a realistic numerical 4D simulation study. *Phys. Med. Biol.*, 58(6):1759–1773.
- [Tsui et al., 1981] Tsui, B. M., Beck, R. N., Doi, K., and Metz, C. E. (1981). Analysis of recorded image noise in nuclear medicine. *Phys. Med. Biol.*, 26(5):883–902.
- [Ullisch, 2012] Ullisch, M. G. (2012). *A NavigatorBased Rigid Body Motion Correction for Magnetic Resonance Imaging*. PhD thesis.

- [Ullisch et al., 2012] Ullisch, M. G., Scheins, J. J., Weirich, C., Kops, E. R., Celik, A., Tellmann, L., Stöcker, T., Herzog, H., and Shah, N. J. (2012). MR-Based PET Motion Correction Procedure for Simultaneous MR-PET Neuroimaging of Human Brain. *PLoS One*, 7(11):e48149.
- [Vardi et al., 1985] Vardi, Y., Shepp, L., and Kaufman, L. (1985). A statistical model for Positron Emission Tomography. *J. Am. Stat. Assoc.*, 80(389):8–20.
- [Visvikis et al., 2003] Visvikis, D., Barret, O., Fryer, T., Turzo, A., Lamare, F., Rest, C. C. L., and Bizais, Y. (2003). A posteriori respiratory motion gating of dynamic PET images. In *2003 IEEE Nucl. Sci. Symp. Conf. Rec. (IEEE Cat. No.03CH37515)*, volume 5, pages 3276–3280.
- [Wade, 1954] Wade, O. L. (1954). Movements of the thoracic cage and diaphragm in respiration. *J. Physiol.*, 124(2):193–212.
- [Wang et al., 1995] Wang, Y., Riederer, S. J., and Ehman, R. L. (1995). Respiratory motion of the heart: kinematics and the implications for the spatial resolution in coronary imaging. *Magn. Reson. Med.*, 33(5):713–9.
- [Watson, 2000] Watson, C. C. (2000). New, faster, image-based scatter correction for 3D PET. In *IEEE Trans. Nucl. Sci.*, volume 47, pages 1587–1594.
- [Weissman et al., 2013] Weissman, N. J., Soman, P., and Shah, D. J. (2013). Multimodality imaging: Opportunities and challenges. *JACC Cardiovasc. Imaging*, 6(9):1022–1023.
- [Würslin et al., 2013] Würslin, C., Schmidt, H., Martirosian, P., Brendle, C., Boss, A., Schwenzer, N. F., and Stegger, L. (2013). Respiratory motion correction in oncologic PET using T1-weighted MR imaging on a simultaneous whole-body PET/MR system. *J. Nucl. Med.*, 54(3):464–71.
- [Yankeelov et al., 2012] Yankeelov, T. E., Peterson, T. E., Abramson, R. G., Garcia-Izquierdo, D., Arlinghaus, L. R., Li, X., Atuegwu, N. C., Catana, C., Manning, H. C., Fayad, Z. a., and Gore, J. C. (2012). Simultaneous PET-MRI in oncology: A solution looking for a problem? *Magn. Reson. Imaging*, 30(9):1342–1356.

- [Zerhouni et al., 1988] Zerhouni, E. a., Parish, D. M., Rogers, W. J., Yang, a., and Shapiro, E. P. (1988). Human heart: tagging with MR imaging—a method for noninvasive assessment of myocardial motion. *Radiology*, 169(1):59–63.